

**Satellite-based Estimates of Net Radiation and  
Modeling the Role of Topography and Vegetation on  
Inter-annual Hydro-climatology**

by

Gautam Bisht

M. S. Hydrology, University of Cincinnati (2004)  
B. Tech., Indian Institute of Technology, Kanpur (2002)

Submitted to the Department of Civil and Environmental Engineering  
in partial fulfillment of the requirements for the degree of

Doctor of Philosophy

at the

Massachusetts Institute of Technology

June 2010

© 2010 Massachusetts Institute of Technology. All rights reserved.

Author .....  
Department of Civil and Environmental Engineering  
April 16, 2010

Certified by .....  
Rafael Luis Bras  
Edward Abdun-Nur Professor of Civil and Environmental Engineering  
Thesis Supervisor

Accepted by .....  
Daniele Veneziano  
Chairman, Departmental Committee for Graduate Students



# Satellite-based Estimates of Net Radiation and Modeling the Role of Topography and Vegetation on Inter-annual Hydro-climatology

by

Gautam Bisht

Submitted to the Department of Civil and Environmental Engineering  
on April 16, 2010, in partial fulfillment of the  
requirements for the degree of  
Doctor of Philosophy in the Field of Hydrology

## Abstract

The Fourth Assessment Report of the Intergovernmental Panel on Climate Change acknowledged that the lack of relevant observations in various regions of the world is a crucial gap in understanding and modeling impacts of climate change related to hydrologic cycle. The Surface Radiation Budget (SRB) is an important component in the study of land surface processes. Existing SRB retrieval algorithms generally suffer from two major shortcomings: difficulty in dealing with cloudy sky conditions and reliance on study-site specific ancillary ground data. In this work, a framework of estimating net radiation from the MODerate-resolution Imaging Spectroradiometer (MODIS) data is presented that is applicable under all-sky conditions, while solely relying on satellite data. The results from the proposed methodology are compared against several ground measurements within the United States for the entire 2006. Finally, monthly radiation maps for the Continental United States are produced.

Modeling, similar to observations, is critical to the Earth Sciences and the second part of this work focuses on the impact of incorporating vegetation dynamics and topography in modeling hydro-climatology over large river basins. Land and atmosphere are coupled with each other through the exchange of heat, momentum and water at the boundary. This work involves coupling of a physically-based, fully distributed ecohydrology model with a numerical atmospheric model, using high performance computing. The ability of the ecohydrology model (in an offline mode) to accurately resolve hydro-climatic signatures and vegetation dynamics is first examined. The ecohydrology model is applied in a highly instrumented catchment, Walnut Gulch Experimental Watershed (WGEW) in Arizona, for a period of 11-years (1997-2007). The ecohydrology model is able to capture the behavior of several key hydrologic variables and vegetation dynamics within the WGEW.

A series of three synthetic experiments are conducted with a coupled land-atmosphere model. The anomalies of various simulated quantities between the synthetic experiments are

examined within the rainfall-soil moisture feedback hypothesis proposed by Elathir [1998]. The results from the experiments highlight the need to explicitly account for vegetation dynamics and topography within a numerical atmospheric model. The thesis concludes with a discussion of contributions, and future directions for this work.

Thesis Supervisor: Rafael Luis Bras

Title: Edward Abdun-Nur Professor of Civil and Environmental Engineering

## Acknowledgments

I am truly indebted to my advisor, Dean Rafael L. Bras, whose support and guidance over the years. His supervision has helped me to not only focus on the imminent research questions at hand, but simultaneously keep the bigger picture in perspective. Rafael has been very supportive and patient, which lead to a truly enjoyable graduate journey at MIT. I am also very grateful to my thesis committee members for providing invaluable support and research insights that went beyond the thesis work. Prof. Dara Entekhabi gave me a teaching opportunity for a undergraduate hydrology class; Prof. Elfatih Eltahir's two introductory courses help lay the foundation of hydrology principles; Prof. Enrique R. Vivoni provided me with three excellent opportunities to participate in field campaigns in New Mexico; and Prof. Valeriy Y. Ivanov was more than eager to share and help me get started with the tRIBS+VEGGIE model.

I would also like to thank various members of the research group, with whom I interacted during different stages of my graduate life at MIT: Ryan Knox, Gajan Sivandran, Homero Flores, Chiara Lepore, Tony Parolari, Jingfeng Wang, Lejo Flores, Ujjwal Narayan, Frederic Chagnon, Valeri Ivanov, Daniel Collions, Jean Fitzmaurice, Erkan Istanbuluoglu and Hanan Karam. I appreciate the suggestions and critique that you all provided during the marathon-group meetings, which helped me better define my research work. I owe a special thanks to Ryan Knox. Over the years, we took many graduate courses together, were called *24-hour boys* in our first year, and spent a summer at the Oak Ridge National Laboratory (ORNL).

The other fellow Parsons lab members to whom I'm thankful are: Pierre Gentine, Mack Durham, Sara Friedman, Amy Muller, Jon Winter, Crystal Ng, Arne Bomblies, Rebecca Neumann, Piyatida Hoisungwan, Behnam Jafarpour, Adel Ahanin, Marc Marcella, Rebecca Gianotti, Sara Jane White and Moji Bateni. Gayle Sherman, Vicky Murphy, Shelia Frankel, Jim Long, Kris Kipp and Cynthia Stewart, who helped me at the Parsons and Building 1, I am thankful to you all. I would like to extend my gratitude to Amanda Garcia and Dawn Tsuyuki at UCI, who have in the last two years helped the group at MIT keep track of Dean Bras' whereabouts.

Two individuals outside MIT, to whom I'm grateful are Dr. David C. Goodrich and Dr. Auroop Ganguly. Dr. Goodrich was gracious enough to help me during my trip to the Walnut Gulch Experimental Watershed in Arizona in the summer of 2006, and provided access to their observation dataset. Dr. Ganguly presented at an excellent summer opportunity to visit the ORNL, and helped me in exploring various potential employment options after graduate school.

I am also thankful to my friend, Mukesh Kumar, with whom I did my undergraduate

together from the Indian Institute of Technology, Kanpur (IITK)<sup>1</sup>. Interestingly enough, we both ended up in the field of hydrology. I have developed a sincere respect for his research perspectives and whenever I was stuck in my research, discussion with him was often helpful in trouble-shooting the problem.

Over the years, following funding sources have supported this research work: MIT Presidential Fellowship, Martin Family Sustainability Fellowship, National Aeronautics and Space Agency grant (NNG05GA17G) and National Oceanic and Atmospheric Administration grant (NA06OAR4310059). I am appreciative of the financial support that the above-mentioned research sponsors provided.

To mom and dad, I don't think any words can express my gratitude to the sacrifices you both endured in giving me the best possible opportunities. Thank you.

Lastly, I would like to thank my wife, Eva. Your unconditional support, academically and emotionally, over the years has helped me in completing this thesis and none of it would be feasible without it.

---

<sup>1</sup>Along with Eva and Ujjwal

कर्मण्येवाधिकारस्ते मा फलेषु कदाचन ।  
मा कर्मफलहेतुर्भूर्मा ते संगोऽस्त्वकर्मणि ॥ ४७ ॥

I would like to dedicate this thesis to my family.

Mom, Dad & Eva



# TABLE OF CONTENTS

<b>1</b>	<b>Introduction</b>	<b>29</b>
<b>I</b>	<b>Estimation of net radiation under all-sky conditions</b>	<b>37</b>
<b>2</b>	<b>Literature Review</b>	<b>39</b>
2.1	Surface radiation budget . . . . .	39
2.2	Remote sensing of surface radiation budget . . . . .	43
2.2.1	Shortwave radiation . . . . .	45
2.2.2	Longwave radiation . . . . .	52
2.3	Conclusion . . . . .	57
<b>3</b>	<b>Development and assessment of an algorithm to estimate net radiation under all-sky conditions</b>	<b>61</b>
3.1	Methodology to Estimate Net Radiation . . . . .	62
3.1.1	Instantaneous net radiation: clear sky pixels with 1-km MOD11.L2 LST available . . . . .	62
3.1.2	Instantaneous net radiation: cloudy pixels with 1-km MOD11.L2 LST unavailable . . . . .	65
3.1.3	Daily average net radiation . . . . .	66
3.1.4	Adaptations to the algorithm for estimating surface radiation budget over the Continental United States . . . . .	67

3.2	Study site and data used . . . . .	69
3.2.1	Southern Great Plains . . . . .	70
3.2.2	Surface Radiation Budget network . . . . .	70
3.2.3	MODIS data products . . . . .	73
3.3	Results: Over the Southern Great Plains . . . . .	74
3.3.1	Temperatures: land surface, air and dew . . . . .	74
3.3.2	Instantaneous and daily average net radiation: under cloudy-skies condition . . . . .	79
3.3.3	Instantaneous estimates of net radiation: Under all sky-conditions . . . . .	83
3.4	Results: Over the Continental United States . . . . .	89
3.4.1	Instantaneous surface energy budget . . . . .	89
3.4.2	Daily average net shortwave and net radiation . . . . .	96
3.4.3	Net shortwave and net radiation over CONUS . . . . .	100
3.5	Conclusion . . . . .	103

**II Role of topography and vegetation dynamics in seasonal to inter-annual hydro-climatology 105**

<b>4</b>	<b>Literature Review and Scope of Research</b>	<b>107</b>
4.1	Motivation . . . . .	107
4.1.1	The global hydrologic cycle . . . . .	108
4.1.2	Soil moisture-rainfall feedback . . . . .	111
4.1.3	Bidirectional feedbacks between soil moisture and vegetation in the presence of topography . . . . .	113
4.1.4	The role of high performance computing in Earth system models . . . . .	115
4.2	Modeling overview of land surface processes . . . . .	116
4.2.1	Land surface models in climate models . . . . .	116
4.2.2	Distributed hydrologic models . . . . .	119
4.3	Conclusion . . . . .	121

<b>5</b>	<b>Models</b>	<b>125</b>
5.1	tRIBS+VEGGIE Model . . . . .	125
5.2	Weather Research and Forecasting Model . . . . .	129
5.3	Domain Representation . . . . .	129
5.3.1	Domain decomposition for tRIBS+VEGGIE . . . . .	129
5.3.2	Domain decomposition for Parallel tRIBS+VEGGIE . . . . .	131
5.3.3	Domain representation for WRF - <i>pt</i> RIBS+VEGGIE . . . . .	133
5.4	Ground heat flux . . . . .	135
5.5	Conclusion . . . . .	138
<b>6</b>	<b>Application of <i>pt</i>RIBS+VEGGIE over a semi-arid region</b>	<b>139</b>
6.1	Walnut Gulch Experimental Watershed . . . . .	139
6.1.1	Hydro-Meteorological in situ data . . . . .	143
6.1.2	Remote sensing data . . . . .	143
6.2	Model setup and calibration . . . . .	144
6.3	Model evaluation . . . . .	151
6.3.1	Energy fluxes . . . . .	151
6.3.2	Soil moisture . . . . .	158
6.3.3	Land surface temperature . . . . .	160
6.3.4	Vegetation dynamics . . . . .	165
6.4	Conclusion . . . . .	166
<b>7</b>	<b>WRF - <i>pt</i>RIBS+VEGGIE simulations</b>	<b>171</b>
7.1	Synthetic experiments . . . . .	171
7.1.1	Design of synthetic experiments . . . . .	171
7.1.2	Nested domains . . . . .	174
7.1.3	Topography data . . . . .	175
7.1.4	Soils and vegetation type . . . . .	175
7.2	Results . . . . .	177

7.2.1	Flat Earth with static vegetation experiment . . . . .	177
7.2.2	TOPO-STAT: Observed topography with static vegetation experiment	183
7.2.3	Observed topography with dynamic vegetation experiment . . . . .	188
7.3	Discussion . . . . .	197
<b>8</b>	<b>Conclusions</b>	<b>201</b>
8.1	Contribution . . . . .	201
8.1.1	Satellite-based estimates of surface radiation budget . . . . .	201
8.1.2	Coupled WRF - <i>pt</i> RIBS+VEGGIE modeling framework . . . . .	202
8.2	Future research . . . . .	204
8.2.1	Satellite-based estimates of surface radiation budget . . . . .	204
8.2.2	Coupled WRF - <i>pt</i> RIBS+VEGGIE modeling framework . . . . .	206
<b>A</b>	<b>1-D Heat Diffusion Model</b>	<b>211</b>
A.1	Spatial discretization . . . . .	212
A.2	Temporal discretization . . . . .	213
A.3	Derivation for the system of equations . . . . .	214
<b>B</b>	<b>Results from the WRF - <i>pt</i>RIBS+VEGGIE simulation in 2003</b>	<b>217</b>

# LIST OF FIGURES

1-1 Interactions among human and Earth systems. Energy is the predominant human system represented in Integrated Assessment Models, but many systems - from the economy to managed ecosystems - are included. Earth systems encompass the atmosphere, oceans, fresh water, the carbon and nitrogen cycles, and ecosystems. (Adapted from [Janetos, 2009]) . . . . . 30

1-2 Historical and projected performance of top 500 supercomputers in the world (From <http://www.top500.org>). . . . . 32

1-3 Performance gaps between GPUs (shown as squares) and CPUs (shown as triangles) (Adapted from [Kirk and Hwu, unpublished]). . . . . 33

2-1 Black-body radiance curve for the Sun (at 6000K) and the Earth (at 295K), with 36 MODIS spectral bands superimposed. (Adapted from [Chagnon, 2005]) 40

2-2 Illustration of sun-satellite geometry.  $\theta_s$  is the solar zenith angle,  $\theta_v$  is the satellite zenith angle,  $\phi_s$  is the solar azimuth angle, and  $\phi_v$  is the viewing azimuth angle . . . . . 48

2-3 Weighting functions ( $dT/dlnP$ ) for the MODIS infrared channels 27-36 (shown with different lines) as functions of atmospheric pressure, calculated from MODTRAN4 using sensor viewing angle of  $0^\circ$  (From Tang and Li [2008]) . . 54

3-1 Division of the Continental United States domain into  $5^0 \times 5^0$  regions over which temperature offsets, required to estimate near-surface air and dew temperatures from 5-km LST given by the cloud product, are computed. . . . . 68

3-2	Map of the Continental United States showing SURFRAD sites and ARM SGP network. ARM SGP ground stations in circles, triangle and squares had SIRS station only, EBBR station only and both SIRBS and EBBR stations, respectively. . . . .	69
3-3	Comparison of 5-km land surface temperature (LST) from the MODIS cloud data product (MOD06_L2): panels (a) and (b) are comparison of MOD06_L2 LST against observation during day- and night-overpasses, respectively; panels (c) and (d) are comparison of MOD06_L2 LST against observed air temperature during day- and night-overpasses; and; panels (e) and (f) are comparison of MOD06_L2 LST against observed dew temperature during day- and night-overpasses. Bias is computed as LST-MOD06_L2 minus Observed values. . .	76
3-4	Comparison of 5-km land surface temperature (LST) from the MOD06_L2 product with near-surface air and obtained from the MOD07_L2 product under hydrostatic atmosphere assumption. Panels (a) and (b) are comparison of MOD06_L2 with near-surface air temperature from MOD07_L2 during day- and night-overpass; panels (c) and (d) are comparison of MOD06_L2 with near-surface dew temperature from MOD07_L2 during day- and night-overpass.	77
3-5	Error histograms between observed and estimated components of net radiation for cloudy overpasses: (a) Downwelling longwave; (b) Upwelling longwave; (c) Net longwave; (d) Downwelling shortwave; (e) Upwelling shortwave; and (f) Net shortwave radiation. Bias is computed as estimated minus observed values.	80
3-6	Comparison of estimated and observed net radiation for cloudy overpasses. Circles and triangles represents day- and night-overpasses of the MODIS. Bias is computed as estimated minus observed values. . . . .	82
3-7	Comparison of daily average estimated and observed net radiation for cloudy overpasses. Bias is computed as estimated minus observed values. . . . .	82

3-8	Error histograms between observed and estimated radiations for clear-sky overpasses: (a) Downwelling longwave; (b) Upwelling longwave; (c) Net longwave; (d) Downwelling shortwave; (e) Upwelling shortwave; and (f) Net shortwave radiation. Bias is computed as estimated minus observed values. . . . .	84
3-9	Comparison of estimated and observed net radiation for clear-sky overpasses. Circles and triangles represents day- and night-overpasses of the MODIS. Bias is computed as estimated minus observed values. . . . .	85
3-10	Comparison of daily average estimated and observed net radiation for clear-sky overpasses. Bias is computed as estimated minus observed values. . . . .	85
3-11	Flowchart to estimate instantaneous and daily average net radiation from the MODIS data for all sky conditions. . . . .	86
3-12	Instantaneous estimation of net radiation ( $R_n$ ) from the MODIS-Terra for all sky conditions on 24 <sup>th</sup> July, 2006 at 17:35UTC. (a) Cloud fraction from MOD06_L2 data over the SGP; (b) Estimate of $R_n$ using clear sky algorithm (White region represents no data due to cloud cover); (c) Estimate of $R_n$ using cloudy-sky algorithm for the cloud covered portion only; (d) Estimate of $R_n$ for all sky conditions obtained by merging (b) and (c). . . . .	87
3-13	Same as Figure 3-12 except for the MODIS-Terra overpass on 6 <sup>th</sup> July, 2006 at 17:45UTC. . . . .	88
3-14	Comparison of estimated and observed instantaneous downwelling shortwave radiation at all study sites. Bias is computed as estimated minus observed values. . . . .	90
3-15	Same as Figure 3-14 except for instantaneous upwelling shortwave radiation.	91
3-16	Same as Figure 3-14 except for instantaneous downwelling longwave radiation.	91
3-17	Same as Figure 3-14 except for instantaneous upwelling longwave radiation. .	92
3-18	Same as Figure 3-14 except for instantaneous net shortwave radiation. . . . .	92
3-19	Same as Figure 3-14 except for instantaneous net radiation. . . . .	95
3-20	Same as Figure 3-14 except for daily average net shortwave radiation. . . . .	97

3-21	Same as Figure 3-14 except for daily average net radiation. . . . .	97
3-22	Time series of net radiation at Bondville, IL from 10-15 April, 2006. Instantaneous net radiation estimates, along with the sinusoidal model fitted through those estimates, are shown for the Terra and Aqua overpasses in (a) and (b), respectively. . . . .	99
3-23	Monthly estimated net shortwave radiation maps for the CONUS. . . . .	101
3-24	Same as Figure 3-23 except for net radiation. . . . .	102
4-1	Estimates of the global water resources . . . . .	108
4-2	Schematic representation of global hydrologic cycle showing fluxes and storages of water (From [Oki and Kanae, 2006]). . . . .	110
4-3	Estimate of the Earth’s annual and global mean energy balance (From [Treut et al., 2007]) . . . . .	111
4-4	Computational resources tradeoff (From [Washington et al., 2008]) . . . . .	116
4-5	A schematic representation of land-atmosphere modeling, illustrating how the feedbacks (one- or two-way) within the various land surface components (topography, soil moisture and vegetation) are considered. (a) Within climate models (regional or global), the atmosphere, soil moisture and vegetation are two-way coupled; while role of topography in lateral redistribution and surface radiation is neglected. (b) In hydrologic modeling, the atmospheric forcings drive the model, and topography influences soil moisture and vegetation dynamics. (c) The proposed model of regional climate will explicitly account for the role of topography in the evolution of soil moisture and vegetation. . . .	122
5-1	A schematic representation of the fully distributed eco-hydrology model: the tRIBS+VEGGIE is shown. (a) The various hydrologic process represented in tRIBS and the TIN representation of the surface, (b) The basic computational voronoi element of tRIBS, (c) The partitioning of radiation fluxes, and (d) The carbon fluxes simulated by the model (tRIBS+VEGGIE). [Adapted from Ivanov [2006]] . . . . .	127



5-2	(a) Domain representation for the Walnut Gulch Experimental Watershed, AZ. The computational elements in black are the stream nodes, while elements with same color belong to a common reach. (b) Delineation of reaches within the watershed. (c) Directed graph that shows the connectivity of reaches and contains weights at the vertices. The weights corresponds to the number of computational elements draining into a given reach. (d) Partition of the WGEW domain for a simulation with three processors. . . . .	132
5-3	Performance of the <i>ptRIBS+VEGGIE</i> model for a 240-hours simulation experiment. . . . .	132
5-4	Horizontal domain representation for WRF and <i>ptRIBS+VEGGIE</i> model. WRF employs a rectangular grid, while <i>ptRIBS+VEGGIE</i> works on a watershed domain. . . . .	134
5-5	A schematic representation of WRF <i>ptRIBS+VEGGIE</i> coupling for a simulation run with 4 processors (P0, P1, P2 and P3). . . . .	136
6-1	(a) Location of the USDA-ARS Walnut Gulch Experimental Watershed in southeast Arizona and the digital elevation map of the WGEW along with rain gage locations from which data is used. Kendall and Lucky Hills are station 82 and 83, respectively. (b) Soil types within the Walnut Gulch Experimental Watershed provided by Soil Survey Geographic (SSURGO) database. (c) Spatial distribution of the two dominant vegetation types, grass and shrub, within the WGEW. . . . .	140
6-2	Illustrations of surface conditions at sites Kendall (grass-dominated) and Lucky Hills (shrub-dominated), respectively. [Pictured in June, 2008] . . . . .	141
6-3	Domain discretization of the WGEW (a) Horizontal discretization (19,443 Voronoi polygons); and (b) Vertical discretization (25 exponentially varying soil layers) . . . . .	145

6-4	Hourly difference between <i>ptRIBS</i> + <i>VEGGIE</i> model and observations at grass-dominated Kendall station for (a) Net radiation; (b) Latent heat flux; (c) Ground heat flux; and (d) Sensible heat flux. . . . .	152
6-5	Same as Figure 6-4, except for shrub-dominated Lucky Hills station. . . . .	153
6-6	Hourly time-series for August, 2006 simulated by the <i>ptRIBS</i> + <i>VEGGIE</i> model (red) and observations (blue) at grass-dominated Kendall station for (a) Net radiation, (b) Latent heat flux (c) Sensible heat flux; and (d) Ground heat flux.	154
6-7	Same as Figure 6-6 except for Lucky Hills station. . . . .	155
6-8	Monthly energy fluxes at grass-dominated Kendall: (a) Net radiation; (b) Latent heat flux; (c) Ground heat flux; and (d) Sensible heat flux . . . . .	156
6-9	Same as Figure 6-8, except for shrub-dominated Lucky Hills station. . . . .	157
6-10	Time-series of (a) daily rainfall; and daily volumetric soil moisture, modeled along with observations, at Kendall station at varying soil depths: (b) 5cm; (c) 15cm; and (d) 30cm respectively. . . . .	161
6-11	Same as Figure 6-10, except for Lucky Hills. . . . .	162
6-12	Hourly surface temperature comparison between the modeled and ground observations. Scatter plots and error histogram during daytime are shown in (a) and (b), respectively; while (c) and (d) comparison during nighttime. . . . .	163
6-13	Evaluation of the MODIS-derived land surface temperature (LST) product. Error histogram for the MODIS-LST with respect to ground observations for day and night overpasses shown in (a) and (b) respectively; while (c) and (d) show the error histogram for the MODIS-LST with respect to upscaled modeled surface temperature for day and night overpasses. . . . .	164
6-14	Comparison between modeled leaf area index (LAI) and MODIS-LAI for grass-dominated Kendall and shrub-dominated Lucky-Hills sites. . . . .	167

7-1	Schematic representation of physical processes accounted within the three synthetic experiments. (a) Static vegetation with flat Earth assumption. (b) Topographic effects on surface radiation and lateral redistribution of moisture (above- and below-ground) are accounted, while keeping static vegetation cover. (c) Accounting for both, vegetation dynamics and topographic effects.	172
7-2	Modeling domain over the Southwestern United States. (a) One-way nested domains for simulations. Domain 1 (D01), Domain 2 (D02) and Domain 3 (D03) have grid spacing of 27-km, 9-km and 4.5-km, respectively. (b) Delineated watersheds used by the <i>ptRIBS+VEGGIE</i> model for D03. . . . .	173
7-3	Timeseries of various simulated quantities for 2001 by the WRF - <i>ptRIBS+VEGGIE</i> model. Panel (a) shows domain average simulated monthly precipitation, along with the estimates obtained from the PERSIANN data over the same region. Panel (b) shows simulated domain average latent and sensible heat fluxes, along with the estimates from the NARR data. . . . .	176
7-4	Spatial distribution of simulated monthly precipitation for 2001 by the WRF - <i>ptRIBS+VEGGIE</i> model for the FLAT-STAT case. . . . .	179
7-5	Spatial distribution of simulated monthly volumetric root-zone soil moisture for 2001 by the WRF - <i>ptRIBS+VEGGIE</i> model for the FLAT-STAT case. . . . .	180
7-6	Spatial distribution of simulated monthly downwelling surface shortwave radiation for 2001 by the WRF - <i>ptRIBS+VEGGIE</i> model for the FLAT-STAT case. . . . .	181
7-7	Correlation coefficient for various months in 2001 simulated by the WRF - <i>ptRIBS+VEGGIE</i> model for FLAT-STAT case among the following quantities: (i) rainfall and downwelling surface shortwave radiation; and (ii) rainfall and soil moisture. . . . .	182

7-8	Monthly average anomalies between the TOPO-STAT and the FLAT-STAT case during the months of June, July and August, 2001 for: (a) Rainfall; (b) Latent heat flux; and (c) Sensible heat flux. (Percentage anomalies are computed as the TOPO-STAT value minus the FLAT-STAT value with respect to the FLAT-STAT value). . . . .	184
7-9	Soil moisture-rainfall feedback hypothesis proposed by Eltahir [1998]. . . . .	185
7-10	Correlation coefficient in June, July and August, 2001, among anomalies between the TOPO-STAT and the FLAT-STAT case for various quantities: rainfall, 10-cm soil moisture (SM), Bowen ratio (BR), surface temperature ( $T_s$ ), planetary boundary layer height (PBLH), and wet-bulb depression (WBD). . . . .	186
7-11	Monthly average anomalies between TOPO-DYN and FLAT-STAT case during the months of June, July and August, 2001 for: (a) Rainfall; (b) Latent heat flux; and (c) Sensible heat flux. (Percentage anomalies are computed as TOPO-DYN minus FLAT-STAT with respect to FLAT-STAT). . . . .	189
7-12	Spatial distribution of simulated monthly average leaf area index for 2001 by the WRF - <i>ptRISB+VEGGIE</i> model for the TOPO-DYN case. . . . .	190
7-13	Spatial distribution of simulated monthly average downwelling surface shortwave radiation for 2001 by the WRF - <i>ptRISB+VEGGIE</i> model for the TOPO-DYN case. . . . .	191
7-14	Spatial distribution of simulated monthly average rainfall for 2001 by the WRF - <i>ptRISB+VEGGIE</i> model for the TOPO-DYN case. . . . .	192
7-15	Simulated monthly average LAI for June, 2001, along with three sub-regions within the domain. . . . .	193
7-16	Timeseries of simulated (a) LAI; (b) Cumulative rainfall; and (c) Monthly average downwelling shortwave radiation for three sub-regions within the D03 domain. . . . .	194
7-17	Average diurnal cycle for (a) Net radiation; (b) Latent heat flux; and (c) Sensible heat flux for June, July and August, 2001. . . . .	196

8-1	Global locations of Baseline Surface Radiation Network. (Obtained from <a href="http://www.gewex.org/bsrn.html">http://www.gewex.org/bsrn.html</a> ) . . . . .	206
8-2	Spatial distribution of soil and vegetation types within the D03 domain, as obtained from the NARR data. . . . .	207
A-1	Vertical mesh used of soil profile used in solving 1-D heat diffusion model . .	212
B-1	Timeseries of various simulated quantities for 2003 by the WRF - <i>ptRISB+VEGGIE</i> model. Panel (a) shows domain average simulated monthly precipitation, along with the estimates obtained from the PERSIANN data over the same region. Panel (b) shows simulated domain average latent and sensible heat fluxes, along with the estimates from the NARR data. . . . .	218
B-2	Spatial distribution of simulated monthly precipitation for 2003 by the WRF - <i>ptRISB+VEGGIE</i> model for the FLAT-STAT case. . . . .	219
B-3	Spatial distribution of simulated monthly volumetric root-zone soil moisture for 2003 by the WRF - <i>ptRISB+VEGGIE</i> model for the FLAT-STAT case. .	220
B-4	Spatial distribution of simulated monthly downwelling surface shortwave radiation for 2003 by the WRF - <i>ptRISB+VEGGIE</i> model for the FLAT-STAT case. . . . .	221
B-5	Monthly average anomalies between the TOPO-STAT and the FLAT-STAT case during the months of June, July and August, 2003 for: (a) Rainfall; (b) Latent heat flux; and (c) Sensible heat flux. (Percentage anomalies are computed as the TOPO-STAT value minus the FLAT-STAT value with respect to the FLAT-STAT value). . . . .	222
B-6	Monthly average anomalies between the TOPO-DYN and the FLAT-STAT case during the months of June, July and August, 2003 for: (a) Rainfall; (b) Latent heat flux; and (c) Sensible heat flux. (Percentage anomalies are computed as the TOPO-DYN value minus the FLAT-STAT value with respect to the FLAT-STAT value). . . . .	223

B-7	Spatial distribution of simulated monthly average leaf area index for 2003 by the WRF - <i>pt</i> RISB+VEGGIE model for the TOPO-DYN case. . . . .	224
B-8	Spatial distribution of simulated monthly average downwelling surface short-wave radiation for 2003 by the WRF - <i>pt</i> RISB+VEGGIE model for the TOPO-DYN case. . . . .	225
B-9	Spatial distribution of simulated monthly average rainfall for 2003 by the WRF - <i>pt</i> RISB+VEGGIE model for the TOPO-DYN case. . . . .	226

# LIST OF TABLES

- 2.1 MODIS Spectral bands specifications [Obtained from MODIS-website] . . . . . 44
- 2.2 Number of clear sky days (i.e. 75% or more of study site had no cloud cover) for the MODIS onboard the Terra satellite for the Southern Great Plains (SGP) during 2006. Values in the parenthesis indicate the total number of the MODIS-Terra overpasses for the SGP region. . . . . 58
- 3.1 Geographic locations of SURFRAD and ARM ground stations. . . . . 71
- 3.2 The MODIS products used in this study . . . . . 72
- 3.3 Bias, Root Mean Square Errors (RMSE), correlation ( $R^2$ ) and number of data points for following quantities given or derived from the MODIS data and ground observations: (i) Land surface temperature (LST); (ii) Near-surface air temperature ( $T_a$ ); (iii) Near-surface dew temperature ( $T_d$ ); (iv) Near-surface air temperature derived from MOD07\_L2 product; and (v) Near-surface dew temperature derived from MOD07\_L2 product. Bias is computed as the MODIS data minus observed data. . . . . 78
- 3.4 Bias, Root Mean Square Errors (RMSE), correlation ( $R^2$ ) and number of data points for various quantities given or derived from the MODIS data and ground observations. Bias is computed as MODIS data minus observed data. 81
- 3.5 Bias, Root Mean Square Errors (RMSE), and correlation ( $R^2$ ) for various components of surface radiation budget estimated. Bias is computed as MODIS data minus observed data. . . . . 93

3.6	Comparison of results obtained from proposed methodology with four published studies. For description about the published studies see Section 3.4.1	94
3.7	Bias, Root Mean Square Errors (RMSE), and correlation ( $R^2$ ) for various components of surface radiation budget estimated. Bias is computed as MODIS data minus observed data. . . . .	98
4.1	Storage volume (absolute and percentage) and residence time of the various components of the global hydrologic cycle (Obtained from [Oki and Kanae, 2006] and [Shiklomanov, 1999]). . . . .	109
5.1	Various physics options available in WRF-ARW v3.0 . . . . .	130
6.1	Station number in Walnut Gulch and data type used either for model forcing or evaluation. . . . .	142
6.2	Soil parameterizations: Saturated hydraulic conductivity in the surface normal direction, $K_{sn}$ [mm hr <sup>-1</sup> ]; saturation moisture content, $\theta_s$ [mm <sup>3</sup> mm <sup>-3</sup> ]; residual moisture content, $\theta_r$ [mm <sup>3</sup> mm <sup>-3</sup> ]; pore size distribution, $\lambda_o$ [dimensionless]; air entry bubbling pressure, $\psi_b$ [mm]; dry soil thermal conductivity, porosity, $n$ [mm <sup>3</sup> mm <sup>-3</sup> ]; $k_{s,dry}$ [J m <sup>-1</sup> K <sup>-1</sup> ]; saturated soil thermal conductivity, $k_{s,sat}$ [J m <sup>-1</sup> K <sup>-1</sup> ]; and soil heat capacity $C_{s,soi}$ [J m <sup>-3</sup> K <sup>-1</sup> ]. . . . .	147
6.3	Vegetation biophysical and interception parameters: $\chi_L$ is departure of leaf angles from a random distribution; Leaf reflectance and transmittance, $\alpha_{\Lambda}^{leaf}$ [-] and $\tau_{\Lambda}^{leaf}$ [-] respectively; Stem reflectance and transmittance, $\alpha_{\Lambda}^{stem}$ [-] and $\tau_{\Lambda}^{stem}$ [-] respectively; VIS and NIR denote visible and near-infrared spectral bands; Canopy water drainage rate coefficient, $K_c$ [mm h <sup>-1</sup> ]; Exponential decay parameter of canopy water drainage rate, $g_c$ [mm <sup>-1</sup> ]; and Specific leaf area, $S_{la}$ [m <sup>2</sup> leaf area kg C <sup>-1</sup> ] (For detail descriptions of the parameters, the reader is referred to Ivanov et al. [2008a].) . . . . .	148



6.4 Biochemical parameters: Maximum catalytic capacity of Rubisco at 25<sup>0</sup>C,  $V_{max,25}$  [ $\mu\text{mol CO}_2 \text{ m}^{-2} \text{ leaf s}^{-1}$ ]; Mean time PAR extinction coefficient parameterizing decay of nitrogen content in canopy,  $\bar{K}$  [-]; Slope parameter,  $m$ [-]; Minimum stomatal conductance,  $b$  [ $\mu\text{mol CO}_2 \text{ m}^{-2} \text{ leaf s}^{-1}$ ]; Intrinsic quantum efficiency for CO<sub>2</sub> uptake for C<sub>3</sub> and C<sub>4</sub> plants,  $\epsilon_{3,4}$  [ $\mu\text{mol CO}_2 \mu\text{mol}^{-1}$  photons]; Sapwood and root tissue respiration at 10<sup>0</sup>C,  $r_{sapw}$  [ $\text{g C g C}^{-1} \text{ s}^{-1}$ ] and  $r_{root}$  [ $\text{g C g C}^{-1} \text{ s}^{-1}$ ], respectively; Fraction of canopy assimilation less maintenance respiration utilized for tissue growth,  $\omega_{sapw}$  [-]; Leaf turnover rate,  $d_{leaf}$  [ $\text{year}^{-1}$ ]; Stem turnover rate,  $d_{stem}$  [ $\text{year}^{-1}$ ]; and Root turnover rate,  $d_{root}$  [ $\text{year}^{-1}$ ]. (For detail descriptions of the parameters, the reader is referred to Ivanov et al. [2008a].) . . . . . 149

6.5 Vegetation allocation, phenology and water uptake parameters: Maximum drought induced foliage,  $\gamma_{Wmax}$  [ $\text{day}^{-1}$ ]; Maximum cold induced foliage,  $\gamma_{Cmax}$  [ $\text{day}^{-1}$ ]; Shape parameter reflecting sensitivity for drought,  $b_W$  [-], and cold,  $b_C$  [-]; Temperature threshold below which cold-induced leaf loss begins,  $T_{cold}$  [<sup>0</sup>C]; Base allocation fraction for canopy,  $e_{leaf}$  [-], sapwood,  $e_{sapw}$  [-] and root,  $e_{root}$  [-]; Sensitivity parameter of allocation fractions to changes in light and soil availability,  $\varpi$  [-]; Parameters controlling the relation between carbon content in the above and below ground biomass,  $\xi$  [-] and  $\epsilon_s$  [-]; Mean daily soil temperature,  $\bar{T}_{soil}$  [<sup>0</sup>C], and day length,  $D_{LH}^C$  [hour], that have to be exceeded for the growing season to start; Minimum duration of period for which the conditions of transition from/to the dormant season have to be continuously met,  $\Delta T_{min,Fav}$  [day]; Faction of structural biomass,  $f_{C,init}$  [-], and leaf area index,  $L_{init}$  [-], used to initiate the leaf onset; Soil matric potential at which stomatal closure,  $\Psi^*$  [Mpa], and plant wilting,  $\Psi_w$  [MPa], begins. (For detail descriptions of the parameters, the reader is referred to Ivanov et al. [2008a].) 150

6.6	Bias, RMSE and $R^2$ for hourly net radiation ( $R_{net}$ ), latent heat flux (LH), ground heat flux (G) and sensible heat flux (H) for Kendall and Lucky Hills between the hourly observations and <i>ptRIBS+VEGGIE</i> simulations for 1997-2007. . . . .	158
6.7	Bias, RMSE and $R^2$ for the daily volumetric soil moisture between modeled and observations for 2002-2007 at various soil depths. The comparison was carried for all station within each of the four soil-type classes and separately for Kendall and Lucky Hills site. . . . .	159
6.8	Bias, RMSE and $R^2$ for land surface temperature: (a) <i>ptRIBS+VEGGIE</i> modeled output against ground observations at hourly interval (2004-2007); (b) MODIS LST product against ground observation for day and night overpasses (2004-2007); and (c) <i>ptRIBS+VEGGIE</i> modeled output against MODIS LST product for day and night overpasses (2001-2007); (d) Upscaled <i>ptRIBS+VEGGIE</i> modeled output at 1km resolution against MODIS LST product for day and night overpasses (2001-2007). . . . .	165
7.1	Description of synthetic experiments . . . . .	171
7.2	Soil hydraulic and thermal properties: Saturated hydraulic conductivity in the surface normal direction, $K_{sn}$ [mm hr <sup>-1</sup> ]; saturation moisture content, $\theta_s$ [mm <sup>3</sup> mm <sup>-3</sup> ]; residual moisture content, $\theta_r$ [mm <sup>3</sup> mm <sup>-3</sup> ]; pore size distribution, $\lambda_o$ [dimensionless]; air entry bubbling pressure, $\psi_b$ [mm]; dry soil thermal conductivity, $k_{s,dry}$ [J m <sup>-1</sup> K <sup>-1</sup> ]; saturated soil thermal conductivity, $k_{s,sat}$ [J m <sup>-1</sup> K <sup>-1</sup> ]; and soil heat capacity $C_{s,soi}$ [J m <sup>-3</sup> K <sup>-1</sup> ] (Obtained from Ivanov [2006]).	175

7.3	Average correlation during June, July and August, 2001, among the various anomalies: rainfall, 10-cm soil moisture (SM), Bowen ratio (BR), surface temperature ( $T_s$ ), planetary boundary layer height (PBLH), and wet-bulb depression (WBD). The first and second column corresponds to anomalies between the TOPO-STAT and the TOPO-DYN cases with respect to the FLAT-STAT case. The third column corresponds to anomalies in the TOPO-DYN with respect to the FLAT-STAT case, after neglecting the “radiation-limited” points within the domain (see Section 7.2.3) . . . . .	187
B.1	Average correlation during June, July and August, 2003, among the various anomalies: rainfall, 10-cm soil moisture (SM), bowen ratio (BR), surface temperature ( $T_s$ ), planetary boundary layer height (PBLH), and wet-bulb depression (WBD). The first and second column corresponds to anomalies between the TOPO-STAT and the TOPO-DYN cases with respect to the FLAT-STAT case. The third column corresponds to anomalies in the TOPO-DYN with respect to the FLAT-STAT case, after neglecting the “radiation-limited” points within the domain (see Section 7.2.3) . . . . .	227



# CHAPTER 1

## INTRODUCTION

Many changes in global climate have been observed and documented by a variety of reports published by the Intergovernmental Panel on Climate Change (IPCC) and the U.S. Climate Change Science Program (CCSP). On the one hand, human activities have increased the concentration of “greenhouse” gases in the Earth’s atmosphere, which absorb heat radiated from the Earth’s surface, thereby causing Earth’s surface temperature to rise. On the other hand, emission of aerosols, produced by burning of coal products, reflect incoming solar radiation and thus offset some of the warming caused by greenhouse gases. Human activities are also responsible for major land-use changes such as burning of forests, replacing natural vegetation with agricultural fields and large-scale irrigation.

Earth system researchers study the Earth’s atmosphere, oceans, ice and lands; and the consequences of anthropogenic climate change on these various components. The global and regional Earth system models represent natural systems interactions and circulations affecting the climate system. Ultimately, scientists and modelers engaged in impacts, adaptation, and vulnerability (IAV) studies are interested in the consequences of changes to Earth’s climate for humans. IAV modelers depend on output from climate models to project the impact of climate change under various scenarios. Usually the IAV models are sector-specific, focusing on topics such as energy, forestry, transportation, agriculture, health, and more, as shown in Figure 1-1. Recently, in a report on future research directions for climate change

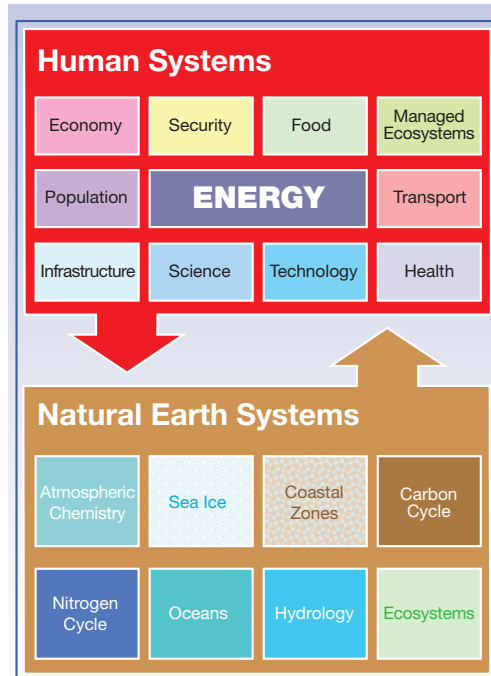


Figure 1-1: Interactions among human and Earth systems. Energy is the predominant human system represented in Integrated Assessment Models, but many systems - from the economy to managed ecosystems - are included. Earth systems encompass the atmosphere, oceans, fresh water, the carbon and nitrogen cycles, and ecosystems. (Adapted from [Janetos, 2009])

integrated assessment, the U.S. Department of Energy has stressed the importance of treating the Earth and human system as a “single, integrated” system to identify vulnerabilities arising from climate change [Janetos, 2009].

## Progress in Earth System Modeling

The integration of both human and climate systems would be a very valuable tool for policy makers to manage risks of climate change. Janetos [2009] emphasized the need for development/improvement of current generation climate models. Incorporation of previously unaccounted physical/biological processes within the models of the Earth system leads to new insights. An example is the explicit accounting of nitrogen cycling within a Dynamic Global Vegetation Models (DGVMs) and Atmosphere Ocean General Circulation Model (AOGCM)

[Thornton et al., 2007, Sokolov et al., 2008, Thornton et al., 2009]. Plants require nutrients such as nitrogen to support growth and several studies have shown that limitations of available mineral nitrogen hinders primary production in many natural and managed ecosystem [Vitousek and Howarth, 1991, Elser et al., 2007, LeBauer and Treseder, 2008]. Thornton et al. [2007] demonstrated that the Carbon-Nitrogen (C-N) interaction fundamentally alters the land surface response to interannual variability in temperature and precipitation by coupling the biophysical Community Land Model (CLM) to terrestrial biogeochemistry model (Biome-BGC). The C-N simulations (forced by a reanalysis of historical near-surface atmospheric conditions without feedback to the atmosphere) showed a 74% reduction in global terrestrial carbon uptake in response to increasing atmospheric CO<sub>2</sub> concentration when compared against simulations that included C-only model. Sokolov et al. [2008] coupled a climate model of intermediate complexity, MIT Integrated Global Systems Model (IGSM), to the Terrestrial Ecosystem Model (TEM) and further demonstrated that explicit accounting of the N cycle changes terrestrial C uptake with increased surface temperature. Recently, Thornton et al. [2009] introduced terrestrial C-N interactions explicitly within a fully-coupled AOGCM; and supported conclusion of previous studies that the capacity of the land ecosystem for net carbon uptake is reduced when C-N interactions are taken into account. Vegetation dynamics is another crucial biophysical processes that the current generation terrestrial models simulate. The inclusion of of the terrestrial carbon cycle introduces feedbacks into the climate system on the timescales of decades to centuries [Randall et al., 2007]. Major advancement in this research area have been made since the Third Assessment Report (TAR) was published by IPCC in 2001. Yet, all of the participating climate models in IPCC's Fourth Assessment Report (AR4) included prescribed static vegetation types because the dynamic vegetation modeling components at the time of AR4 were not routinely incorporated within the AOGCMs. It is expected that explicit account of vegetation dynamics would be among various additions to the models for the Fifth Assessment Report.

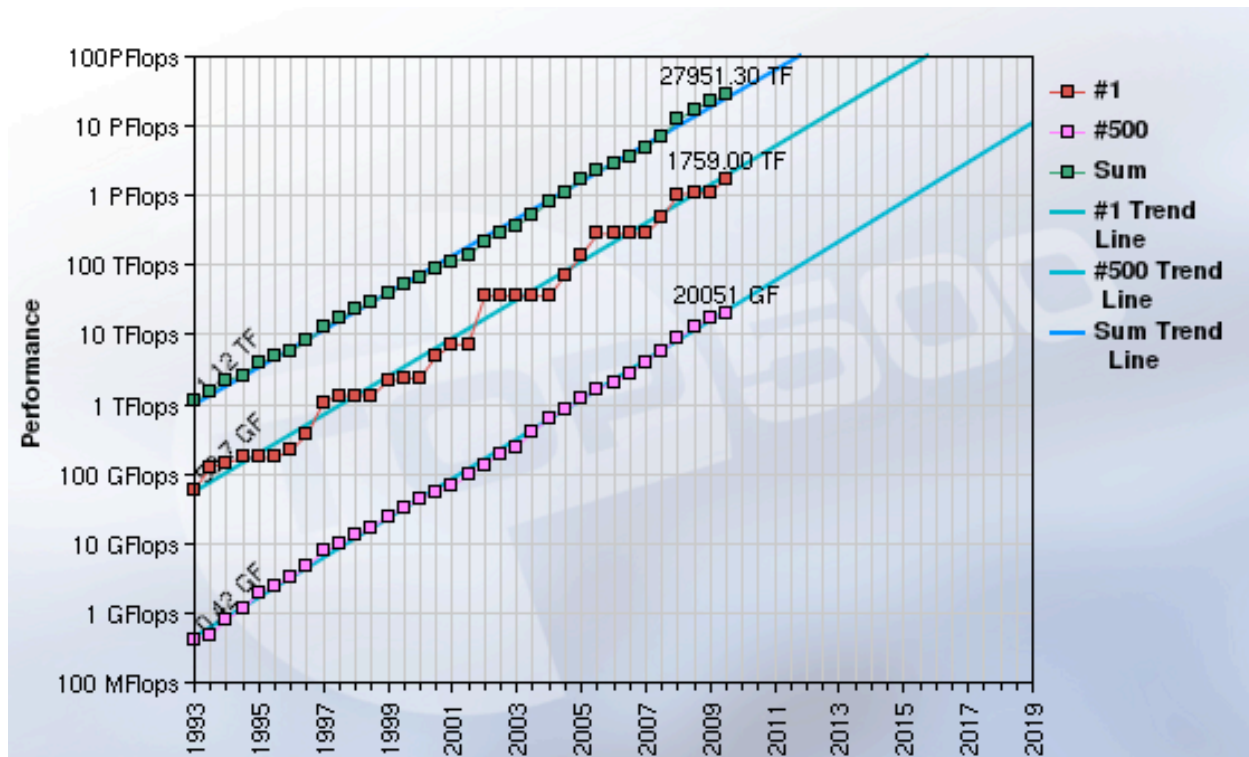


Figure 1-2: Historical and projected performance of top 500 supercomputers in the world (From <http://www.top500.org>).

## Advances in computational resources

One of the key drivers responsible for the development of more sophisticated climate models is the recent advancement in computer hardware. The computational performance of first, last and aggregate of all supercomputers on the list of fastest 500 supercomputers in the world is shown in Figure 1-2. In June 2008, IBM's Roadrunner machine of the Los Alamos National Laboratory became the first ever computer to cross the petaflop/s ( $10^{15}$  floating point operations per second) barrier, while as of Nov., 2009 the Oak Ridge National Laboratory's (ORNL's) Jaguar supercomputer is fastest in the world. Multi-core (dual, quad and six) processors by Intel and Advance Micro Devices are becoming a norm in computer hardware. Recently, Nvidia corporation, which specializes in the development of graphics processing units (GPUs) and chipsets for computers, has shown that GPUs can be used as



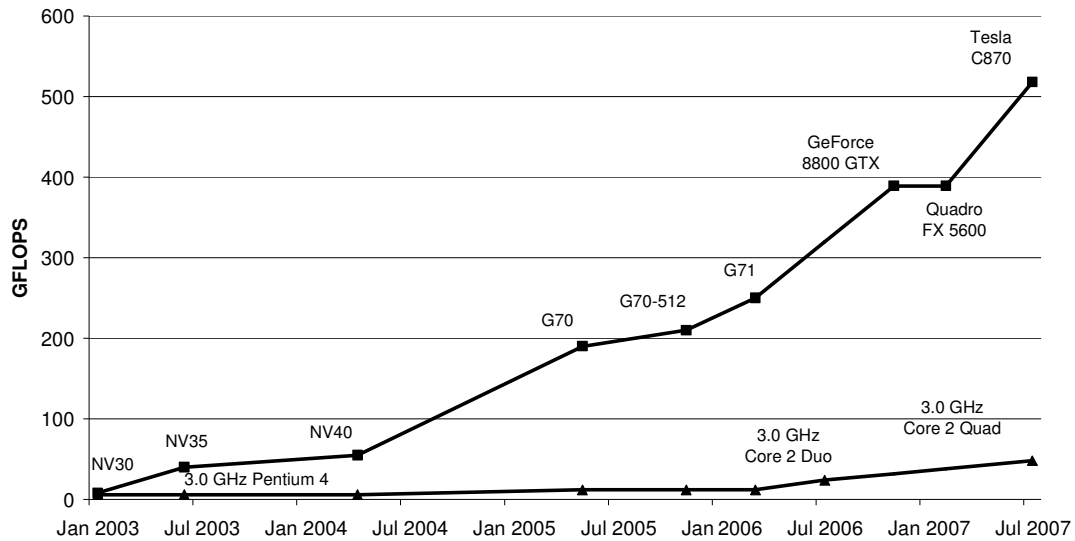


Figure 1-3: Performance gaps between GPUs (shown as squares) and CPUs (shown as triangles) (Adapted from [Kirk and Hwu, unpublished]).

alternates to traditional central processing units (CPUs) in parallel computing. Nvidia has developed the Compute Unified Device Architecture (CUDA) framework for programming on GPUs. Figure 1-3 shows the evolution of performance of GPUs against CPUs over time. Though, the GPUs are clearly faster than CPUs, they do have certain drawbacks when compared with CPUs such as limited memory, lower performance with double precision computing and lack of error-correcting code (ECC). The next generation CUDA architecture, code named “Fermi”, will overcome some above mentioned shortcomings and ORNL has already disclosed plans of using it for their new supercomputer. These breakthroughs in computer industry present excellent opportunities for researchers to develop new Earth system models capable of conducting simulations at higher spatial and temporal resolutions, while simultaneously incorporating more feedbacks among various physical processes.

## Need for new satellite-based observations

Development of more complex climate models alone cannot lead to improvement in the understanding of Earth systems. Observations, equally vital as the models, are not only helpful in evaluating and improving models; but can be used separately to gain improved understanding about the Earth system. Satellite-based observations have been routinely used to forecast weather, climate and natural hazards over the past 50 years [Minster et al., 2008]. Both active and passive remote sensing sensors have provided measurements related to several components of the Earth system such as radiation budget, atmospheric composition, precipitation, land/sea surface temperature, ocean color, surface winds, topography, etc. Observations from satellites are also continuously assimilated into weather prediction models, so as to improve the agreement between model forecasts and observations. There exists a need for developing new types of data products from satellite data, while simultaneously improving existing data products.

## Scope of work

This work can be separated in two distinct parts. The first part focuses on developing a new data product, surface radiation budget, from existing satellite data. Numerous studies have developed retrieval algorithms to estimate net radiation or its components from the MODIS data [Bisht et al., 2005, Wang et al., 2005, Tang et al., 2006, Zhou et al., 2007, Tang and Li, 2008, Kim and Hogue, 2008, Wang and Liang, 2009, Wang et al., 2009, Formann and Margulis, 2009]. Such retrieval algorithms to estimate the surface radiation budget (SRB) generally suffer from two major shortcomings: difficulty in dealing with cloudy-sky conditions and reliance on study-site specific ancillary ground data.

*Chapter 2* of this work provides a brief overview of the basics of surface radiation budget. A review of existing remote sensing methodologies to estimate shortwave and longwave radiation is covered. The chapter concludes by enumerating the shortcomings of existing SRB retrieval algorithms and outlines the desired objectives of the new proposed SRB algorithm.

*Chapter 3* presents the retrieval algorithm to estimate various components of SRB under all sky conditions. Comparison of estimated SRB components is carried out against ground measurements from both the Department of Energy' (DOE's) Atmospheric Radiation Measurement (ARM) program in the Southern Great Plains and the National Oceanic and Atmospheric Administration's (NOAA's) Surface Radiation (SURFRAD) budget network for the entire 2006. The remotely sensed data from the MODIS sensor from both Aqua and Terra satellites is used. Finally, monthly radiation maps for the Continental United States are presented.

The second part of this work focuses on effects of incorporating vegetation dynamics and topography on hydro-climatology over large river basins. Land and atmosphere are fundamentally coupled with each other through the exchange of heat, momentum and water at the boundary. Prior studies have looked at feedbacks between soil, vegetation, topography and climate by considering either two or three of the components coupled together. This research would investigate the regional scale feedbacks between the atmosphere and vegetation, controlled by topography and soil moisture. The contrast between static and dynamic modeling approaches on these feedbacks is also examined. The work involves coupling of a physically-based, fully distributed ecohydrology model with a regional climate model, using high performance computing. Vegetation dynamics and topography play an important role in land-atmosphere interactions and this work examines their importance by explicitly accounting for them.

*Chapter 4* presents the soil moisture in the context of global hydrological cycle and illustrates that vegetation and topography are key factors determining its evolution. A historical treatment of land surface processes within climate and distributed hydrologic models is introduced next.

*Chapter 5* introduces the two numerical models, an ecohydrology model and a numerical atmospheric model, used in the study; along with a description of the model coupling. In order to utilize high performance computing, the treatment of the domain within the ecohydrology model is modified. Additionally, a new one-dimensional ground heat flux scheme

that is incorporated within the ecohydrology model is also presented.

*Chapter 6* assessed how capable the ecohydrology model (in an offline mode), which explicitly accounts for hydrologic processes in a complex terrain, is in accurately resolving hydro-climatic signatures and vegetation dynamics in a semiarid region. The ecohydrology model is applied in a highly instrumented semiarid catchment, Walnut Gulch Experimental Watershed in Arizona for a period of 11 years (1997-2007). The model performance is examined with respect to several key hydrologic variables: energy fluxes, distributed soil moisture within the watershed at three depths and land surface temperature. Additionally, the model's capability to capture vegetation dynamics for two generic plant functional types, C4 grass and shrubs, is also evaluated against the MODIS leaf area index product.

*Chapter 7* describes a series of three synthetic experiments that are performed to investigate the effect of incorporating vegetation dynamics and topography on hydro-climatology over large river basins. Configuration of the three synthetic experiments conducted, along with a description of the coupled model (WRF - *pt*RIBS+VEGGIE) setup is also presented. Results demonstrate the role of explicitly accounting for topography and vegetation dynamics in coupled land-atmosphere model.

Finally, *Chapter 8* summarizes the original contribution of this work, along with some potential future research directions to extend the current work.

# Part I

## Estimation of net radiation under all-sky conditions



# CHAPTER 2

# LITERATURE REVIEW

## 2.1 Surface radiation budget

The Sun is the dominant source of energy supporting life on the Earth. Incoming solar radiation is transmitted, reflected, scattered and absorbed through the Earth's atmosphere. The terrestrial radiative processes allow loss of energy to space and is the ultimate energy sink. Radiation budgets at the surface and in the atmosphere drive the global hydrologic cycle. The net radiation,  $R_n$  [ $\text{Wm}^{-2}$ ], at the Earth's surface can be expressed as:

$$\begin{aligned} R_n &= R_S^\downarrow - R_S^\uparrow + R_L^\downarrow - R_L^\uparrow \\ &= R_S^\downarrow(1 - \alpha_{srf}) + R_L^\downarrow - R_L^\uparrow \end{aligned} \quad (2.1)$$

where  $R_S^\downarrow$ ,  $R_S^\uparrow$ ,  $R_L^\downarrow$  and  $R_L^\uparrow$  are downwelling shortwave radiation [ $\text{Wm}^{-2}$ ], upwelling shortwave radiation [ $\text{Wm}^{-2}$ ], downwelling longwave radiation [ $\text{Wm}^{-2}$ ] and upwelling longwave radiation [ $\text{Wm}^{-2}$ ], respectively; and  $\alpha_{srf}$  [-] is land surface albedo.

Electromagnetic radiation is the primary process responsible for energy transfer in the Earth's atmosphere [Liou, 2002]. Planck's law is often used to model radiation from the Sun and the Earth; and it describes the monochromatic radiance (or intensity),  $I_\lambda(T)$  [ $\text{Wm}^{-2} \text{sr}^{-2} \text{m}^{-2}$ ], emitted by a black-body as a function of temperature,  $T$  [K], and wavelength,  $\lambda$  [ $\mu\text{m}$ ], as:

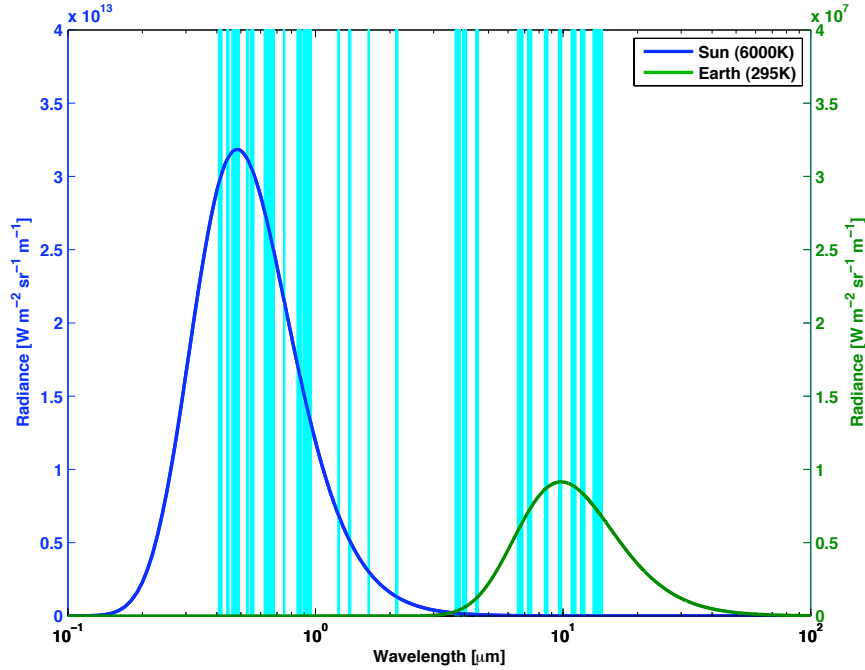


Figure 2-1: Black-body radiance curve for the Sun (at 6000K) and the Earth (at 295K), with 36 MODIS spectral bands superimposed. (Adapted from [Chagnon, 2005])

$$I(\lambda, T) = \frac{2h^2c}{\lambda^5 \left( e^{\frac{hc}{KT\lambda}} - 1 \right)} \quad (2.2)$$

where  $h = 6.626 \times 10^{-34}$  [J s] is the Planck's constant,  $c = 2.998 \times 10^8$  [m s] is the speed of light and  $K = 1.38062 \times 10^{-23}$  [J K<sup>-1</sup>] is the Boltzmann's constant. Black-body emitted radiance given by the Planck's law for the Sun (at 6000K) and the Earth (at 295K) are shown in Figure 2-1, with the MODerate-resolution Imaging Spectroradiometer (MODIS) spectral bands superimposed on it. It is evident from the Figure 2-1 that most of the Sun's energy lies in the shorter wavelength region ( $0.3 - 4.0\mu m$ ) and is thus accordingly termed *shortwave radiation*; while energy emitted by the Earth lies in  $4.0 - 10.0\mu m$  wavelength band and called *longwave radiation*. The balance of incoming and outgoing shortwave and longwave radiation at the Earth's surface is the net radiation and drives the process of evaporation, photosynthesis, heating of soil and air, melting of ice and development of the planetary



boundary-layer.

The various gases (water vapor, carbon dioxide, ozone, oxygen, methane and others) present in the Earth's atmosphere absorb the incoming shortwave radiation from the Sun. The knowledge about atmospheric transmittance through various regions within the electromagnetic spectrum is useful in designing remote sensing instruments with bands that lie within (for atmospheric composition studies) or outside (for estimating land surface conditions) the absorption bands. Atmospheric scattering by gases and aerosols (volcanic dust, windblown dust, smoke from forest fires and anthropogenic combustion processes) is also responsible for attenuation of the shortwave radiation and results in diffuse sky radiation reaching the surface. Surface reflectivity or albedo determines the net amount of shortwave radiation available at the surface and varies with the type of surface. The albedo for water is about 0.06-0.09; while it ranges from 0.10 to 0.40 over land surfaces (deserts have higher value compared to vegetated surfaces). Snow and ice covered surface have albedo values greater than 0.40. The absorption of outgoing longwave radiation by atmospheric gasses plays an important role in sustaining life on Earth by raising its temperature from a below-freezing temperature of 255[K] (predicted by simple energy equilibrium black-body radiation model) to 295[K] [Liou, 2002].

The IPCC's AR4 has shown widespread warming of the Earth system by temperature observations taken at the surface, in the atmosphere and in the oceans [Bates et al., 2008]. IPCC-AR4 states:

It is *very likely* that anthropogenic greenhouse gas increases caused most of the observed increase in global average temperatures since the mid-20th century. Without the cooling effect of atmospheric aerosols, it is *likely* that greenhouse gases alone would have caused a greater global mean temperature rise than that observed during the last 50 years.

Since global energy and hydrologic cycle are intertwined, changes in the radiative flux at the Earth's surface would affect the surface heat and moisture budgets, thereby altering the hydrologic cycle. Recent studies indicate that the interaction of some forcing agents

with clouds and aerosols can influence the hydrologic cycle in unforeseen ways. Quantification of the Surface Radiation Budget (SRB) at the Earth's surface is essential for the study of land surface processes and land-atmosphere interactions. Estimates of the SRB and its components (upwelling or downwelling longwave and/or shortwave radiation) have applications in hydrology [Jacobs et al., 2002, Nishida et al., 2003, Norman et al., 2003, Batra et al., 2006, Venturini et al., 2008, Kim and Hogue, 2008], climate research [Li et al., 2005], agriculture [Hunt et al., 1998, Diak et al., 2000] and renewable energy [Myers, 2005]. Climate change elevates the significance of studying the surface radiation budget (SRB). One of the scientific questions to be investigated in Phase II (2003-2012) of the Global Energy and Water Cycle Experiment (GEWEX) is whether the Earth's energy and water cycle are changing [see [http://www.gewex.org/gewex\\_overview.html](http://www.gewex.org/gewex_overview.html)]. The AR4 report, while addressing potential impacts of climate change on freshwater resources, acknowledged the lack of observations as a crucial gap to improve understanding and modeling of climate changes related to hydrological cycle. Records of hydrometeorological variables, such as actual and potential evapotranspiration, are short and sparse globally, thereby hindering global analysis of droughts [Rind et al., 1990, Anderson and Kustas, 2008]. Remote sensing data from polar-orbiting and geostationary satellites provide high spatial and temporal coverage of land, atmosphere and ocean. Numerous studies have attempted to compute the SRB from remotely sensed data. SRB estimates can be used as forcings to drive the existing physically-based hydrologic models [Formann and Margulis, 2009] and also serve to evaluate the model performance. Additionally, data assimilation of the SRB or its components within a numerical weather prediction and hydrologic models could lead to improvements in forecast [Lakshmi, 2000, Kumar and Kaleita, 2003, Huang et al., 2008]. A brief overview of remote sensing methodologies aiming to estimate the SRB and its various components is presented next.

## 2.2 Remote sensing of surface radiation budget

Remote sensing is most commonly a framework of collecting and interpreting data related to electromagnetic radiation in various wavelength regions from an object of interest, while not being in physical contact with the object. The remote sensing platforms include aircrafts and satellites. The remote sensing instrument records an electromagnetic signal and fundamental radiative transfer theories are employed to invert the signal to infer states of atmosphere, land and ocean. Different electromagnetic regions are well-suited for distinct applications and an example of 36 spectral bands of the MODIS, with their primary use, are summarized in Table 2.1. Remote sensing techniques can be classified based on the source of radiant energy into two fundamental types: active and passive. In active remote sensing, an artificial source of radiation (such as lasers in lidar or microwaves in radar) sends energy within a specific wavelength band to a target and a detector records the intensity of the backscattered energy. Passive remote sensing measures natural radiation emitted or reflected by a target. The most common sources of radiation recorded by passive sensors include reflected solar radiation and thermal radiation emitted by the Earth and its atmosphere. Space-borne remote sensing satellites provide can be classified on the basis of their orbit: geostationary and polar-orbiting. Geostationary satellites remain virtually stationary above a point on the equator and orbit the Earth at an altitude of  $\approx 36,000$  km. Since geostationary satellites are stationary, they provide a continuous stream of data regarding the region of interest with only one set of zenith and azimuthal angles. Polar-orbiting or sun-synchronous satellites are typically at an altitude of 870 km above the Earth's surface and generally provide data about every location on the Earth twice each day. Numerous studies have used various remote sensing platforms including Geostationary Operational Environmental Satellites (GOES), the Advanced Very High Resolution Radiometer (AVHRR), Landsat and the MODIS to estimate components of the SRB [Gautier et al., 1980, Diak and Gautier, 1983, Gratton et al., 1993, Li et al., 1993, Jacobs et al., 2002, Ma et al., 2002, Lee and Ellingson, 2002, Nishida et al., 2003, Bisht et al., 2005, Wang et al., 2005, Tang et al., 2006, Zhou et al., 2007, Tang and Li, 2008, Wang and Liang, 2009, Wang et al., 2009, Formann and Margulis,

Table 2.1: MODIS Spectral bands specifications [Obtained from MODIS-website]

Primary Use	Band	Bandwidth [ $\mu m$ ]	Primary Use	Band	Bandwidth [ $\mu m$ ]
Land/Cloud/Aerosol Boundaries	1	0.620 - 0.670	Surface/Cloud Temperature	20	3.660 - 3.840
	2	0.841 - 0.876		21	3.929 - 3.989
Land/Cloud/Aerosol Properties	3	0.459 - 0.479		22	3.929 - 3.989
	4	0.545 - 0.565	23	4.020 - 4.080	
	5	1.230 - 1.250 $\Psi$	24	4.433 - 4.498	
	6	1.628 - 1.652	25	4.482 - 4.549	
Ocean color/ Phytoplankton/ Biogeochemistry	7	2.105 - 2.155	Cirrus Clouds	26	1.360 - 1.390
	8	0.405 - 0.420		27	6.535 - 6.895
	9	0.438 - 0.448	Water Vapor	28	7.175 - 7.475
	10	0.483 - 0.493	Cloud Properties	29	8.400 - 8.700
	11	0.526 - 0.536	Ozone	30	9.580 - 9.880
	12	0.546 - 0.556	Surface/Cloud Temperature	31	10.780 - 11.280
	13	0.662 - 0.672		32	11.770 - 12.270
	14	0.673 - 0.672	Cloud Top Altitude	33	13.185 - 13.485
15	0.743 - 0.753	34		13.485 - 13.785	
16	0.862 - 0.877	35		13.785 - 14.085	
17	0.890 - 0.920	36		14.085 - 14.385	
Atmospheric Water Vapor	18	0.931 - 0.941			
	19	0.915 - 0.965			

2009].

The remote sensing methodologies developed for estimating the SRB can be broadly classified into two categories on the basis of data used and they are: (i) parameterization schemes that use near-surface conditions (eg. land surface temperature, surface albedo, near-surface air and dew temperature) to estimate SRB; and (ii) statistical regressions which relate the Top Of the Atmosphere (TOA) data to surface radiation measurements. The parameterization schemes are based on radiative transfer theories that utilize near-surface conditions to estimate various components on the SRB and vary in their level of complexity. For statistical regression approaches, the first step involves using a radiative transfer model (eg. MODTRAN), to simulate the TOA radiance or reflectance observed by a particular sensor for varying surface radiation and atmospheric conditions. The next step is to then establish a statistical relationship, that incorporates dependence on solar zenith angle and/or satellite viewing angle, between the TOA radiance/reflectance in various satellite channels and SRB components. A review of methodologies estimating satellite-derived shortwave and longwave radiation is presented in Schmetz [1989], Ellingson [1995], Pinker et al. [1995], Niemelä et al. [2001a,b] and Diak et al. [2004]. A separate review of the theory and retrieval algorithms for estimating surface shortwave and longwave radiation estimates from satellite data are presented next.

### **2.2.1 Shortwave radiation**

The incoming TOA solar radiation is absorbed, scattered and reflected as it passes through the Earth's atmosphere, before reaching the surface. The radiation emitted by the atmospheric constituents does not contribute in the solar or shortwave region ( $0.3 - 4.0\mu m$ ), as evident from Figure 2-1. Fritz et al. [1964] reported a correlation of -0.9 between the TOA solar flux estimated from the third Television Infrared Observation Satellite (TIROS III) and ground measurements in the United States. Hanson [1971] provided early quantification of solar irradiance from satellite measurements.

The downwelling shortwave flux,  $R_s^\downarrow$ , reaching the surface can be expressed as:

$$R_S^\downarrow = S_0 \Gamma_{atm} \cos \theta_s \quad (2.3)$$

where  $S_0 = 1367 \text{ [Wm}^{-2}\text{]}$  is the solar constant,  $\theta_s \text{ [rad]}$  is the solar zenith angle and  $\Gamma_{atm}$  is broadband atmospheric transmissivity. (The term “broadband” refers to integrated value over all wavelengths; in contrast to “narrowband”, where integration is confined over a smaller wavelength window, usually the range of the satellite channel). Thus, accurate estimation of  $\Gamma_{atm}$  is critical for retrieving  $R_S^\downarrow$  from satellite-based observations. At the Earth’s surface, the upwelling shortwave radiation flux,  $R_S^\uparrow$ , can be expressed in terms of downwelling shortwave radiation and the surface albedo,  $\alpha_{srf} \text{ [-]}$ , as:

$$R_S^\uparrow = \alpha_{srf} R_S^\downarrow \quad (2.4)$$

Next, an overview of the algorithms to estimate  $R_S^\downarrow$  using the TOA satellite data is given. Later, the parameterization schemes based on near-surface conditions to estimate downwelling surface shortwave radiation is presented.

## TOA broadband albedo

The first step in estimate  $R_S^\downarrow$  using the TOA data is developing a linear regression between the broadband atmospheric transmissivity and the TOA broadband albedo. The second step involves estimating the TOA broadband albedo from narrowband albedos obtained by the satellite’s various channels. The shortwave radiation budget for the Earth-atmosphere system can be written as [Schmetz, 1989]:

$$\alpha_{TOA} + \beta_{atm} + (1 - \alpha_{srf}) \Gamma_{atm} = 1 \quad (2.5)$$

where  $\alpha_{TOA} \text{ [-]}$ ,  $\beta_{atm} \text{ [-]}$  and  $\alpha_{srf} \text{ [-]}$  are broadband albedo at the TOA, fractional total absorption within the atmosphere and the surface albedo, respectively. Schmetz [1989] showed that atmospheric absorption can be expressed as a linear function of the TOA broadband albedo.

$$\beta_{atm} - \beta_{atm}^{clear} = \xi(\alpha_{TOA} - \alpha_{TOA}^{clear}) \quad (2.6)$$

where  $\xi$  is a constant. Substituting Eq. 2.6 in Eq. 2.5 and rearranging, the broadband atmospheric transmissivity can be expressed as linear function of broadband albedo:

$$\begin{aligned} \Gamma_{atm} &= \frac{1 - \beta_{atm}^{clear} + \xi\alpha_{TOA}^{clear}}{1 - \alpha_{srf}} - \frac{1 + \xi}{1 - \alpha_{srf}}\alpha_{TOA} \\ &= a - b\alpha_{TOA} \end{aligned} \quad (2.7)$$

$a$  and  $b$  are constants and can be obtained as intercept and slope of the scatter plot between  $\Gamma_{atm}$  and  $\alpha_{TOA}$ . Li et al. [1993], Masuda et al. [1995] and Tang et al. [2006] incorporated dependance on solar zenith angle and precipitable water in the atmosphere while estimating  $a$  and  $b$ . An atmospheric radiation model is generally used to estimate  $a$  and  $b$  based on a wide range of simulations that vary surface and atmospheric conditions (LOWTRAN-6, LOWTRAN-7 and MODTRAN by Li et al. [1993], Masuda et al. [1995] and Tang et al. [2006], respectively). The TOA data obtained from a satellite in various channels are narrowband quantities, while it should be noted that  $\alpha_{TOA}$  is a broadband quantity. Thus, a narrowband-to-broadband albedo conversion is necessary and presented next.

### **Narrowband-to-broadband albedo conversion**

Before proceeding to present the narrowband-to-broadband albedo conversion, it is useful to take a detour to get a theoretical foundation about exactly what a spaceborne remote sensing platforms measures.

The reflected radiance,  $I^\uparrow$ , at the Earth's surface in the direction of zenith and azimuth angle given by  $(\theta_r, \phi_r)$  and at a particular wavelength,  $\lambda$ , can be expressed as:

$$I^\uparrow(\lambda; \theta_r, \phi_r) = \int_0^{2\pi} \int_0^{\frac{\pi}{2}} I^\downarrow(\lambda, \theta_i, \phi_i) \gamma_r(\theta_i, \phi_i; \theta_r, \phi_r) \cos\theta_i \sin\theta_i d\theta_i d\phi_i \quad (2.8)$$

where subscript i and r denotes “incoming” and “reflected” direction, respectively (see Fig. 2-

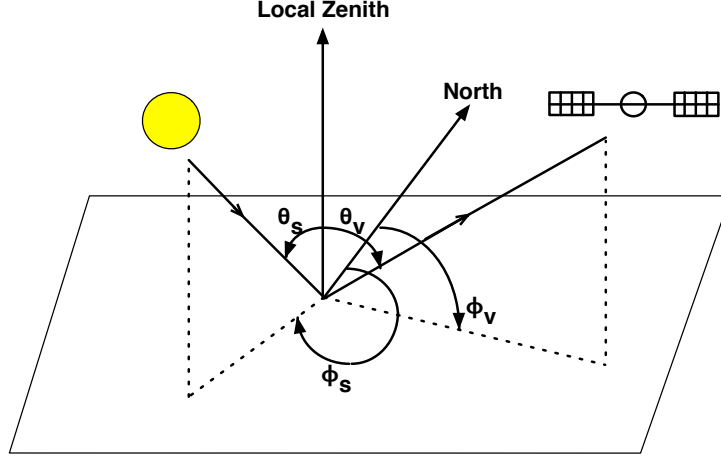


Figure 2-2: Illustration of sun-satellite geometry.  $\theta_s$  is the solar zenith angle,  $\theta_v$  is the satellite zenith angle,  $\phi_s$  is the solar azimuth angle, and  $\phi_v$  is the viewing azimuth angle

2).  $\gamma_r(\theta_i, \phi_i; \theta_r, \phi_r)$  is the Bi-Directional Reflectance Function (BRDF) and represents the relative amount of radiation coming from the direction  $(\theta_i, \phi_i)$  being reflected in the direction  $(\theta_r, \phi_r)$ . For a Lambertian surface, which reflects incoming radiation equally in all direction, the BRDF can be written as:

$$\gamma_r(\theta_i, \phi_i; \theta_r, \phi_r) = \frac{\rho}{\pi} \quad (2.9)$$

Radiation from the Sun is the only source of shortwave radiation at the TOA and can be expressed as delta function of magnitude  $I_s(\lambda)$  in the direction given by  $(\theta_s, \phi_s)$ , where the subscript 's' denotes the sun.

$$I^\downarrow(\lambda, \theta_i, \phi_i) = \begin{cases} I_s(\lambda) & (\theta_i, \phi_i) = (\theta_s, \phi_s); \\ 0 & \text{otherwise.} \end{cases} \quad (2.10)$$

Substituting Eq. 2.9 and 2.10 in Eq. 2.8 and integrating, we obtained:

$$I^\uparrow(\lambda; \theta_v, \phi_v) = I_s(\lambda) \Omega_s \cos \theta_s \frac{\rho}{\pi} \quad (2.11)$$

The Sensor Response Function (SRF) of a satellite in the  $k$ -th channel with a band



$[\lambda_k^{min}, \lambda_k^{max}]$ , is usually a non-linear function that can be written as:

$$w_k(\lambda) = \begin{cases} 0 & \lambda < \lambda_k^{min}; \\ f(\lambda) & \lambda_k^{min} \leq \lambda \leq \lambda_k^{max}; \\ 0 & \lambda > \lambda_k^{max}. \end{cases} \quad (2.12)$$

The measurement by the remote sensing platform at the TOA in the  $k$ -th channel is weighted by the SRF as:

$$\int_{\lambda_k^{min}}^{\lambda_k^{max}} I^\uparrow(\lambda; \theta_v, \phi_v) w_k(\lambda) d\lambda = \cos\theta_s \frac{\rho}{\pi} \Omega_s \int_{\lambda_k^{min}}^{\lambda_k^{max}} I_s(\lambda) w_k(\lambda) d\lambda \quad (2.13)$$

The terms on the right and left side of Eq. 2.13 can be normalized by the integral of the SRF and defined as radiance measured by the satellite in the  $k$ -th channel,  $L_k$ , and solar irradiance,  $F_\odot$ , in the same channel.

$$L_k \equiv \frac{\int_{\lambda_k^{min}}^{\lambda_k^{max}} I^\uparrow(\lambda; \theta_v, \phi_v) w_k(\lambda) d\lambda}{\int_{\lambda_k^{min}}^{\lambda_k^{max}} w_k(\lambda) d\lambda} \quad (2.14)$$

$$F_\odot \equiv \Omega_s \frac{\int_{\lambda_k^{min}}^{\lambda_k^{max}} I_s(\lambda) w_k(\lambda) d\lambda}{\int_{\lambda_k^{min}}^{\lambda_k^{max}} w_k(\lambda) d\lambda} \quad (2.15)$$

Thus, Eq. 2.13 can be expressed as:

$$\rho_k = \frac{\pi L_k}{F_\odot (r_0/r)^2 \cos\theta_s} \quad (2.16)$$

where  $\rho_k$  is the reflectance in the  $k$ -th channel at the TOA. A correction factor  $(r_0/r)$  is applied to incorporate seasonal variation in the Earth-Sun distance. It should be noted that reflectance is a narrowband quantity (as it is computed over the spectral band of  $[\lambda_k^{min}, \lambda_k^{max}]$ ) and the derivation of the TOA albedo involves narrowband-to-broadband conversion. A linear conversion of narrowband reflectance in  $N$  bands can be expressed as:

$$\alpha_{TOA} = \sum_{k=1}^N c_k \rho_k + c_0 \quad (2.17)$$

where  $c_k$  ( $k = 0, 1, \dots, N$ ) are the conversion coefficients. Similar to the approach of estimating linear coefficients for the relationship between the TOA albedo and atmospheric transmissivity (Eq. 2.7),  $c_k$  are obtained based on multiple simulation runs of a radiative transfer model. Tang et al. [2006] used 158,976 MODTRAN simulation runs and developed a non-linear relationship based on solar zenith and satellite view angle to estimate  $c_k$  for seven MODIS shortwave bands. Once  $\alpha_{TOA}$  is obtained from Eqn. 2.17, broadband transmissivity can be estimated using Eqn. 2.7; and finally the downwelling shortwave radiation can be estimated from Eqn. 2.3.

### Parameterization schemes

Numerous simple parameterizations have been presented in the literature to estimate  $R_S^{\downarrow clear}$  by providing an empirical relationship for the atmospheric transmissivity (see Eq. 2.3). The parameterizations vary in the level of complexity and a review of such schemes are presented in Pinker et al. [1995] and Niemelä et al. [2001b]. A few parameterizations of  $R_S^{\downarrow}$  are mentioned briefly below. The first three schemes are the simplest parameterizations that depend only on the cosine of the solar zenith angle.

- Bennett [1982]:

$$R_S^{\downarrow clear} = 0.72 S_0 \cos \theta_s \quad (2.18)$$

- Paltridge and Platt [1976]:

$$R_S^{\downarrow clear} = 10 + 1411 \cos \theta_s - 310 \sqrt{\cos \theta_s} \quad (2.19)$$

- Moritz [1978]:

$$R_S^{\downarrow clear} = S_0 \cos \theta_s (0.47 + 0.47 \cos \theta_s) \quad (2.20)$$

- Zillman [1972] used screen level water vapor pressure,  $e_a$  [hPa], along with solar zenith angle to estimate downwelling surface shortwave radiation.

$$R_S^{\downarrow clear} = \frac{S_0 \cos^2 \theta_s}{1.085 \cos \theta_s + e_a (2.7 + \cos \theta_s) \times 10^{-3} + 0.10} \quad (2.21)$$

- Iqbal [1983] presented a parameterization that estimated the direct,  $R_{S, dir}$ , and diffuse,  $R_{S, dif}$ , component of solar radiation separately.

$$R_S^{\downarrow clear} = R_{S, dir}^{\downarrow} + R_{S, dif}^{\downarrow} \quad (2.22a)$$

$$R_{S, dir}^{\downarrow} = 0.9751 S_0 T_r T_g T_w T_a T_o \cos \theta_s \quad (2.22b)$$

$$R_{S, dif}^{\downarrow} = D_R + D_a + D_m \quad (2.22c)$$

where  $T_r$ ,  $T_g$ ,  $T_w$ ,  $T_a$  and  $T_o$  are transmittance by Rayleigh scattering, gases, water vapor, aerosols and ozone respectively;  $D_R$ ,  $D_a$  and  $D_m$  are Rayleigh-scattered, aerosol-scattered and multiple-reflected irradiance, respectively (see Iqbal [1983] for details).

Under cloudy conditions, a correction factor is applied to clear-sky shortwave radiation reaching the surface that depends on fraction of cloud cover,  $f_c$ , as proposed by Berliand [1960]:

$$R_S^{\downarrow cloudy} = R_S^{\downarrow clear} [(1 - f_c) + f_c T_c] \quad (2.23)$$

where  $T_c$  is the transmittance through the cloud. Laevastu [1960] proposed a correction factor that was a cubic function of amount of cloud cover, as indicated by:

$$R_S^{\downarrow cloudy} = R_S^{\downarrow clear} (1 - 0.6 f_c^3) \quad (2.24)$$

While, Niemelä et al. [2001b] proposed a parameterization that partitions total cloud fraction,  $f_c$ , into low cloud,  $f_{c,low}$  and “other clouds”,  $f_{c,oth}(= f_c - f_{c,low})$ , as:

$$R_S^{\downarrow cloudy} = R_S^{\downarrow clear} \left( 1 - f_c^{\left[4.7 - 2.24 \frac{f_{c,low}}{f_c + 10^{-3}}\right]} + 0.31 f_{c,low}^{2.46} + 0.73 f_{c,oth}^{4.7} \right) \quad (2.25)$$

Stephens [1978] suggested a parameterization to estimate cloud optical depth,  $\tau_c$ , (which is related to cloud transmittance by  $T_c = e^{-\tau_c}$ ) as a function of cloud optical properties, such as effective cloud droplet size and cloud water path. A detail analysis of Stephens’ [1978] scheme is beyond the scope of this text and interested readers are referred to Stensrud [2007] for details.

## 2.2.2 Longwave radiation

Unlike the shortwave radiation, which has the incoming solar radiation at the TOA as the only source, the longwave radiation reaching the surface is the aggregate result of atmospheric absorption, emission and scattering of the entire atmospheric column. Schmetz [1989], Ellingson [1995], Niemelä et al. [2001a] and Diak et al. [2004] have presented reviews of methods to estimate longwave radiation from the satellite data. Schmetz [1989] showed that nearly 80% of the longwave radiation reaching the surface is emitted by the lowest 500 m of the atmosphere. It thus follows that accurate retrieval of downwelling longwave radiation at the surface crucially depends on accurate estimation of near-surface temperature and humidity, amount of cloud cover, cloud height and cloud base temperature. Recent studies have alternatively estimated surface longwave budget using the TOA radiance from the MODIS data for clear sky conditions [Tang and Li, 2008, Wang and Liang, 2009, Wang et al., 2009]. The rationale behind the using the TOA satellite radiance to estimate components of longwave radiations is presented next, followed by parameterization schemes that rely on near-surface data.

## TOA radiance

In clear-sky conditions, the longwave (or thermal infrared) radiance reaching at the TOA,  $I_{TOA}$ , can be written as the contribution from the Earth's surface and all levels of the atmosphere as [Tang and Li, 2008]:

$$\begin{aligned}
 I_{TOA}(\lambda) = & \epsilon_{srf} I(\lambda, T_{srf}) \Gamma(\lambda, \theta_v, \phi_v, P_{srf} \rightarrow 0) + \int_{P_{srf}}^0 I(\lambda, T_P) \frac{d\Gamma(\lambda, \theta_v, \phi_v, P \rightarrow 0)}{d \ln P} d \ln P \\
 & + \frac{1 - \epsilon_{srf}}{\pi} \int_0^{2\pi} \int_0^{\pi/2} \int_0^{P_{srf}} I(\lambda, T_P) \frac{d\Gamma(\lambda, \theta_v, \phi_v, P \rightarrow 0)}{d \ln P} \cos \theta' \sin \theta' d \ln P d \theta' d \phi' \\
 & \cdot \Gamma(\lambda, \theta_v, \phi_v, P_{srf} \rightarrow 0)
 \end{aligned} \tag{2.26}$$

where  $T_{srf}$  [K] and  $\epsilon_{srf}$  [-] are surface temperature and surface emissivity, respectively;  $P_{srf}$  is the surface pressure;  $\theta_v$  and  $\phi_v$  are satellite viewing and zenith angle, respectively; and  $\Gamma(\lambda, \theta_v, \phi_v, P \rightarrow 0)$  denotes atmospheric transmittance from a pressure level  $P$ , with a temperature  $T_p$ , to the top of the atmosphere. The first and second term on the right hand side of the Eq. 2.26 represents transmittance of longwave radiation through the atmosphere emitted by the Earth's surface and atmosphere, respectively. The third term represents the downwelling atmospheric longwave radiation that is reflected from the surface and transmitted through the atmosphere to reach the TOA. It should be noted that Eq. 2.26 represents the radiance reaching the TOA that is dependent on wavelength  $\lambda$ . The measurement recorded by the satellite in a particular channel can be obtained by integrating  $I_{TOA}(\lambda)$  with the sensor response function similar to Eq. 2.13. The term  $dT/d \ln P$  is known as the channel weighting function. An example of the MODIS infrared channels obtained by Tang and Li [2008] is shown in Figure 2-3. The weighting function determines the measured channel radiance by giving relative importance to the emitted radiation from various atmospheric levels and the surface. As clearly evident from the Figure 2-3, channels 31 and 32 provide radiance measurements that are mainly based on the Earth's surface; while channel 33 gives information about near-surface conditions.

Several regression techniques have been developed to estimate surface longwave radiation

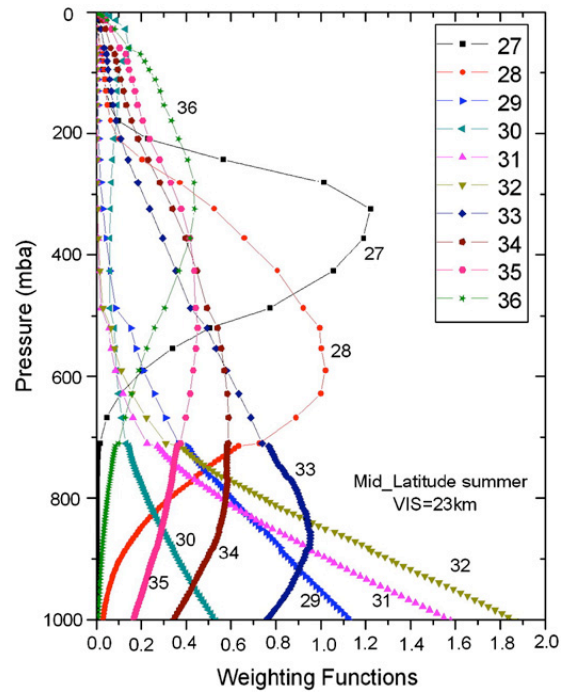


Figure 2-3: Weighting functions ( $dT/d\ln P$ ) for the MODIS infrared channels 27-36 (shown with different lines) as functions of atmospheric pressure, calculated from MODTRAN4 using sensor viewing angle of  $0^\circ$  (From Tang and Li [2008])

from the TOA satellite radiance. Even though Eq. 2.26 is highly non-linear, Tang and Li [2008] used a linear regression for the MODIS channels 28, 29, 31, 33, 34 and 36 to estimate  $R_L^\downarrow$ ; while Wang and Liang [2009] developed linear and non-linear regressions to compute  $R_L^\downarrow$  from radiance in MODIS channels 27-34. Similarly, Wang et al. [2009] obtained upwelling longwave radiation as a linear combination of the TOA radiance in channel 29, 31 and 32 of the MODIS. The coefficients of linear and non-linear regression analysis by Wang and Liang [2009] incorporated a dependance on satellite viewing angle. The attempts of using the TOA to estimate downwelling and upwelling longwave radiation have been until now limited to cloud-free conditions. Next, parameterizations schemes are presented that estimate longwave radiation based on near-surface conditions.

### Parameterization schemes

The total energy emitted by a perfect black-body at a given temperature  $T$  can be obtained by integrating the emitted radiation over all wavelengths using Eq. 2.2 as:

$$\begin{aligned}
 R_{blackbody} &= \pi \int_0^\infty I(\lambda, T) d\lambda \\
 &= \pi \left( \frac{2\pi^4 K^4}{15c^2 h^3} \right) T^4 \\
 &= \sigma T^4
 \end{aligned} \tag{2.27}$$

where  $\sigma = \frac{2\pi^5 K^4}{15c^2 h^3} = 5.67 \times 10^{-8} \text{ [W m}^{-2} \text{ K}^{-4}]$  is the Steffan-Boltzmann constant. However, most objects do not behave as perfect black-bodies and the emitted energy is lower than in the ideal case. Energy emission from a real body is described as:

$$R_{greybody} = \epsilon \sigma T^4 \tag{2.28}$$

where  $\epsilon [-]$  is the surface emissivity (less than unity) and this is often called a grey-body emission. Nearly all downwelling longwave parameterization schemes under clear-sky conditions use a grey-body emission formulation, which uses screen level air temperature,  $T_a$

[K], and develop empirical relationships for air emissivity based near-surface atmospheric conditions (such as, vapor pressure,  $e_a$ , [hPa] and  $T_a$ ). Examples of few parameterizations are presented below:

- Ångström [1918]

$$R_L^{\downarrow,clear} = (0.83 - 0.18 \times 10^{-0.067e_a}) \sigma T_a^4 \quad (2.29)$$

- Brunt [1932]

$$R_L^{\downarrow,clear} = (0.52 - 0.065\sqrt{e_a})^{1/7} \sigma T_a^4 \quad (2.30)$$

- Brutsaert [1975]

$$R_L^{\downarrow,clear} = 1.24 \left( \frac{e_a}{T_a} \right)^{1/7} \sigma T_a^4 \quad (2.31)$$

- Idso [1981]

$$R_L^{\downarrow,clear} = \left[ 0.7 + 5.95 \times 10^{-5} e_a \exp\left(\frac{1500}{T_a}\right) \right]^{1/7} \sigma T_a^4 \quad (2.32)$$

- Prata [1996]

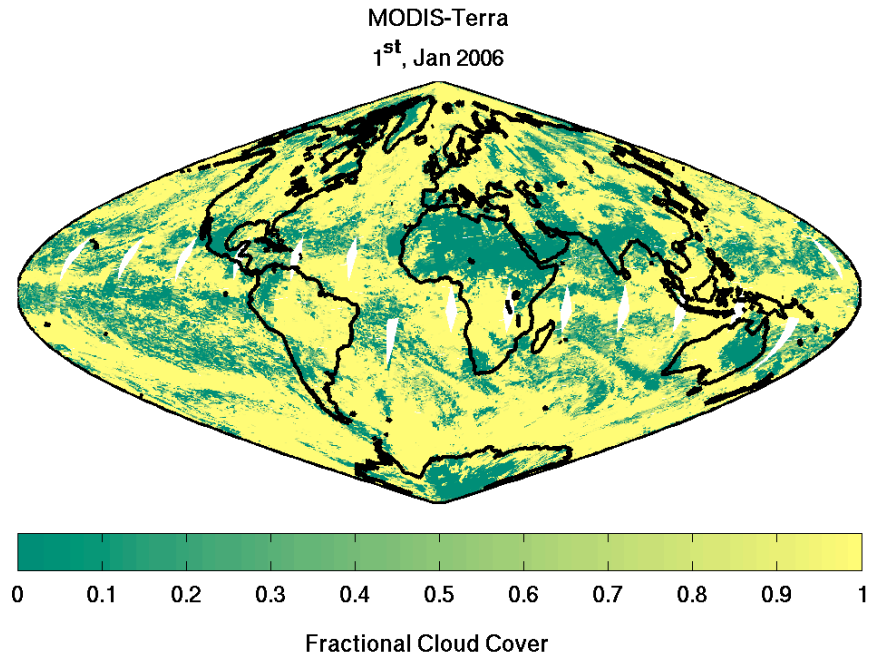
$$R_L^{\downarrow,clear} = \left[ 1 - (1 + \xi) \exp(-\sqrt{(1.2 + 3\xi)}) \right] \sigma T_a^4 \quad (2.33)$$

$$\xi = \frac{46.5}{T_a} e_a \quad (2.34)$$

During cloudy conditions, parameterization schemes included the influence of clouds by incorporating cloud fraction,  $f_c$ , cloud temperature,  $T_c$ , and cloud emissivity,  $\epsilon_c$  as:

- Jacobs [1978]





$$R_L^{\downarrow, \text{cloudy}} = (1 + 0.26f_c)R_L^{\downarrow, \text{clear}} \quad (2.35)$$

- Maykut and Church [1973]

$$R_L^{\downarrow, \text{cloudy}} = (1 + 0.22f_c^{2.75})R_L^{\downarrow, \text{clear}} \quad (2.36)$$

- Formann and Margulis [2009]

$$R_L^{\downarrow, \text{cloudy}} = \sigma\epsilon_a T_a^4 + (1 - \epsilon_a)\epsilon_c T_c^4 \quad (2.37)$$

## 2.3 Conclusion

Recently numerous studies have developed retrieval algorithms to estimate net radiation or its components from the MODIS data [Bisht et al., 2005, Wang et al., 2005, Tang et al.,

Table 2.2: Number of clear sky days (i.e. 75% or more of study site had no cloud cover) for the MODIS onboard the Terra satellite for the Southern Great Plains (SGP) during 2006. Values in the parenthesis indicate the total number of the MODIS-Terra overpasses for the SGP region.

Month	Number of clear day-overpasses	Number of clear night-overpasses
January	09 (40)	04 (41)
February	08 (38)	00 (39)
March	06 (42)	02 (44)
April	14 (40)	06 (43)
May	12 (42)	06 (44)
June	08 (38)	04 (38)
July	09 (42)	03 (44)
August	01 (40)	01 (43)
September	14 (40)	02 (41)
October	15 (39)	04 (39)
November	14 (41)	05 (42)
December	09 (41)	05 (42)
Full-year	118 (483)	43 (500)

2006, Zhou et al., 2007, Tang and Li, 2008, Kim and Hogue, 2008, Wang and Liang, 2009, Wang et al., 2009, Formann and Margulis, 2009]. Retrieval algorithms to estimate the SRB generally suffer from two major shortcomings: difficulty in dealing with cloudy-sky conditions and reliance on study-site specific ancillary ground data. Figure 2.3 is a composite of fractional cloud cover (where a value 1.0 denotes total cloud cover) for all MODIS overpasses on 1<sup>st</sup> Jan., 2006. It is clearly evident that a large portion of remotely sensed data is obtained under cloudy conditions. Table 2.2 the number of clear sky and total overpasses for the MODIS-Terra over the Southern Great Plains (SGP) in the United States during 2006, where an overpass is deemed to be under clear skies if 75% of the SGP was cloud free. Only 24% and 9% of the MODIS-Terra overpassed during the day and night, respectively, were under clear sky conditions. Thus, a retrieval algorithm applicable under clear-sky days only omits a large portion of remote sensing data. Dependence on additional study-site specific data in estimating the SRB from remotely sensed data, curtails the global applicability of the retrieval algorithm. Thus, the research objective of the present work can be summarized as:

Accurate retrieval of instantaneous and daily average estimates of the SRB under *all sky* conditions, while relying *solely* on remote sensing data.

The proposed retrieval algorithm to estimate various components of SRB under all sky conditions is presented in the following chapter. Comparison of the estimated SRB components against ground measurements within the Southern Great Plains and seven additional stations within United States for entire 2006 is carried out.



# **DEVELOPMENT AND ASSESSMENT OF AN ALGORITHM TO ESTIMATE NET RADIATION UNDER ALL-SKY CONDITIONS**

## **CHAPTER 3**

This chapter presents the algorithm to estimate all components of the surface energy budget using the MODIS data under all-sky conditions. The current work extends the Bisht et al. [2005] framework that estimated net radiation from the MODIS data under clear sky conditions only and is briefly summarized in Section 3.1.1. The extension of the retrieval algorithm for cloudy sky conditions using various cloud parameters from the MODIS cloud product (MOD06\_L2 and MYD06\_L2) is outlined in Section 3.1.2. Two adaptations are also presented to make the estimation of net radiation over the Continental United States (CONUS) feasible. The study sites (Southern Great Plains and Surface Radiation Budget network in the U.S.) over which the proposed retrieval algorithm is applied, as well as, the ground measurement and the MODIS data products used are described in Section 3.2. The results for various components of the SRB estimated by the proposed methodology for the Southern Great Plains and Surface Radiation Budget network are presented in Section 3.3 and 3.4, respectively. Finally the chapter concludes with a summary of the current methodology.

## 3.1 Methodology to Estimate Net Radiation

### 3.1.1 Instantaneous net radiation: clear sky pixels with 1-km MOD11\_L2 LST available

Estimation of net radiation for clear sky pixels uses the algorithm of Bisht et al. [2005]. At the Earth's surface, instantaneous  $R_n^{clear}$  [ $\text{Wm}^{-2}$ ] for clear sky conditions can be expressed in terms of downwelling and upwelling radiations as:

$$\begin{aligned} R_n^{clear} &= R_S^{\downarrow clear} - R_S^{\uparrow clear} + R_L^{\downarrow clear} - R_L^{\uparrow clear} \\ &= R_S^{\downarrow clear}(1 - \alpha) + R_L^{\downarrow clear} - R_L^{\uparrow clear} \end{aligned} \quad (3.1)$$

where  $R_S^{\downarrow clear}$ ,  $R_S^{\uparrow clear}$ ,  $R_L^{\downarrow clear}$  and  $R_L^{\uparrow clear}$  are downwelling shortwave radiation [ $\text{Wm}^{-2}$ ], upwelling shortwave radiation [ $\text{Wm}^{-2}$ ], downwelling longwave radiation [ $\text{Wm}^{-2}$ ] and upwelling longwave radiation [ $\text{Wm}^{-2}$ ] for clear sky respectively; and  $\alpha$  [-], is land surface albedo.

A parameterization scheme developed by Zillman [1972] is used to estimate downwelling shortwave radiation using near-surface vapor pressure,  $e_0$  [hPa], and solar zenith angle,  $\theta$  [rad], as

$$R_S^{\downarrow clear} = \frac{S_0 \cos^2(\theta)}{1.085 \cos(\theta) + e_0(2.7 + \cos(\theta)) \times 10^{-3} + \beta} \quad (3.2)$$

where  $\beta$  is 0.1 and  $S_0$ , is the solar constant at the top of atmospheric, is 1367 [ $\text{Wm}^{-2}$ ]. Niemelä et al. [2001a] and Bisht et al. [2005] have shown that Zillman's [1972] scheme tends to overestimate the downwelling shortwave radiation, thus a  $\beta$  value of 0.2 is proposed.

Downwelling longwave radiation is obtained from air emissivity,  $\varepsilon_a$ , and air temperature,  $T_a$  [K], at near-surface; while upwelling longwave requires surface emissivity,  $\varepsilon_s$  [-], and surface temperature,  $T_s$  [K]. Air emissivity is parameterized using a scheme proposed by Prata [1996]. Near-surface vapor pressure,  $e_0$  [hPa], is computed from dew point temperature,  $T_d$  [K], using

the Clausius-Clapeyron equation [Rogers and Yau, 1989].

$$R_L^{\downarrow clear} = \sigma \varepsilon_a T_a^4 \quad (3.3a)$$

$$\varepsilon_a = 1 - (1 + \xi) \exp(-\sqrt{(1.2 + 3\xi)}) \quad (3.3b)$$

$$\xi = \frac{46.5}{T_a} e_0 \quad (3.3c)$$

$$e_0 = 6.11 \exp \left[ \frac{L_v}{R_v} \left( \frac{1}{273.15} - \frac{1}{T_d} \right) \right] \quad (3.3d)$$

$$R_L^{\uparrow clear} = \sigma \varepsilon_s T_s^4 \quad (3.3e)$$

where  $\sigma = 5.67 \times 10^{-8}$  [W m<sup>-2</sup> K<sup>-4</sup>] is the Steffan-Boltzmann constant,  $L_v = 2.5 \times 10^6$  [J kg<sup>-1</sup>] is the latent heat of vaporization and  $R_v = 461$  [J kg<sup>-1</sup> K<sup>-1</sup>] is the gas constant for water vapor.

Bisht et al. [2005] used the following MODIS data products: geolocation data (MOD03 at 1-km); aerosol depth (MOD04.L2 at 10-km); atmospheric profile data (MOD07.L2 at 5-km); land surface temperature and surface emissivity (MOD11.L2 at 1-km); and land surface albedo (MOD43B1 at 1-km). The methodology of Bisht et al. [2005] used air and dew point temperatures from the MOD07.L2 at the vertical pressure level of 1000 hPa as surrogates for near-surface temperatures. The land surface temperature and surface emissivity were obtained from the MOD11.L2 product. The land surface albedo was computed as a linear combination of black-sky albedo,  $\alpha_{bs}$  and white-sky albedo,  $\alpha_{ws}$ , provided in the MOD43B1 data product as [Lucht et al., 2000]:

$$\alpha = [1 - S(\theta, \tau)] \alpha_{bs} + S(\theta, \tau) \alpha_{ws} \quad (3.4)$$

where  $\tau$  [-] is the aerosol depth and  $S(\theta, \tau)$  is the isotropic fraction representing the state of the atmosphere between the extreme cases of completely direct (black-sky) and diffuse (white-sky) illumination. A look up table for computing the isotropic fraction was available from the MODIS albedo products homepage. The solar zenith angle and aerosol optical depth are obtained from the MOD03.L2 and MOD04.L2 data products, respectively. For a

detailed description of the algorithm to estimate clear sky net radiation, readers are referred to Bisht et al. [2005].

Tang and Li [2008] argued that approximating air and dew temperatures at 1000 hPa as near-surface temperatures maybe inappropriate due to variations caused by Earth's terrain and suggested using the hydrostatic assumption in the atmosphere to estimate near-surface temperatures. Thus, in this study, we assume a hydrostatic atmosphere assumption to extrapolate  $T_a$  and  $T_d$  provided at the lowest vertical pressure level from the MODIS atmospheric profile product to estimate near-surface  $T_a$  and  $T_d$ . The hydrostatic atmospheric assumption can be written as:

$$\begin{aligned}\frac{dp}{dz} &= -\rho g \\ \frac{P^L - P^S}{\Delta z} &= -\rho g\end{aligned}\tag{3.5}$$

where  $P^L$  is the lowest pressure level of the MODIS atmospheric profile measurement; while  $P^S$  is the surface pressure level obtained from the MODIS data. The ambient lapse rate is assumed to be equal to  $-6.5^0\text{K/km}$  [Cosgrove et al., 2003] and can be used to relate temperature at the lowest pressure level,  $T_a^L$ , and near-surface temperature,  $T_a^S$ , as:

$$\begin{aligned}\frac{dT}{dz} &= -6.5^0\text{K/km} \\ \frac{T_a^L - T_a^S}{\Delta z} &= -6.5^0\text{K/km}\end{aligned}\tag{3.6}$$

Combining equation 3.5 and 3.6 and rearranging the terms, near-surface air temperature can be estimated as:

$$T_a^S = T_a^L + \frac{6.5^0\text{K/km}}{\rho g}(P^S - P^L)\tag{3.7}$$

Even though the above equation is strictly applicable to air temperature, we additionally



use it to estimate near-surface dew temperature. Near-surface  $T_d$  is used to compute air-emissivity through Eq. 3.3b, 3.3c and 3.3d; which is eventually used to estimate downwelling longwave radiation as Eq 3.3a. Thus, the retrieval of  $R_L^{\downarrow clear}$  is not very sensitive to near-surface dew temperature and justifies our estimation of near-surface  $T_d$  using an identical approach as given by Eq 3.7.

### 3.1.2 Instantaneous net radiation: cloudy pixels with 1-km MOD11\_L2 LST unavailable

The net radiation,  $R_n^{cloudy}$  [ $\text{Wm}^{-2}$ ], for cloudy pixels is defined as:

$$R_n^{cloudy} = R_S^{\downarrow cloudy}(1 - \alpha) + R_L^{\downarrow cloudy} - R_L^{\uparrow cloudy} \quad (3.8)$$

Under cloudy-skies, the downwelling shortwave radiation,  $R_S^{\downarrow cloudy}$  [ $\text{Wm}^{-2}$ ], is estimated as a linear combination of the fluxes from clear sky and cloudy sky, weighted by cloud fraction, according to the parameterization proposed by Slingo [1989] as:

$$R_S^{\downarrow cloudy} = R_S^{\downarrow clear} [(1 - f_c) + f_c e^{-\tau_c / \cos(\theta)}] \quad (3.9)$$

where  $f_c$  [-] is the cloud fraction and  $\tau$  [-] is cloud optical thickness. The downwelling longwave radiation for cloudy conditions,  $R_L^{\downarrow cloudy}$  [ $\text{Wm}^{-2}$ ], is estimated as a combination of downwelling radiation from near-surface conditions and clouds as proposed by Formann and Margulis [2009]; while the upwelling longwave radiation,  $R_L^{\uparrow cloudy}$  [ $\text{Wm}^{-2}$ ], for cloudy conditions follows the similar approach as during clear sky conditions given by:

$$R_L^{\downarrow cloudy} = \sigma \varepsilon_a T_a^4 + \sigma (1 - \varepsilon_a) \varepsilon_c T_c^4 \quad (3.10a)$$

$$R_L^{\uparrow cloudy} = \sigma \varepsilon_s T_s^4 \quad (3.10b)$$

where  $\varepsilon_c$  [-] and  $T_c$  [K] are cloud emissivity and cloud temperature, respectively.

The proposed methodology of estimating  $R_n^{cloudy}$  requires numerous parameters regarding

clouds. The MODIS cloud product provides cloud optical depth at 1-km spatial resolution (for Eqn 3.9); while cloud emissivity (for Eqn 3.10a), cloud top temperature (for Eqn 3.10a) and land surface temperature (for Eqn 3.10b) are available at the 5-km spatial resolution. Computation of downwelling longwave radiation requires surface air and dew temperature (Eqn 3.3b, 3.3c, 3.3d and 3.10a), which under clear sky are available at 5-km resolution from the MOD07.L2. For cloudy conditions,  $T_a$  and  $T_d$  are estimated by subtracting offsets from 5-km LST provided by the MOD06.L2 product,  $T_s^{06.L2}$ , as:

$$T_a = T_s^{06.L2} - \delta_a^{day} \quad \text{if day-overpass} \quad (3.11a)$$

$$= T_s^{06.L2} - \delta_a^{night} \quad \text{if night-overpass} \quad (3.11b)$$

$$T_d = T_s^{06.L2} - \delta_d^{day} \quad \text{if day-overpass} \quad (3.11c)$$

$$= T_s^{06.L2} - \delta_d^{night} \quad \text{if night-overpass} \quad (3.11d)$$

where  $\delta_a^{day}$  [K] and  $\delta_a^{night}$  [K] are offset for air temperature during day- and night-overpass; while  $\delta_d^{day}$  [K] and  $\delta_d^{night}$  [K] are offset for dew temperature during day- and night-overpass. The procedure to estimate the temperature offsets are presented in Section 3.3.1.

### 3.1.3 Daily average net radiation

Daily average net radiation estimates are more meaningful totals than instantaneous net radiation estimates. Methodologies aimed to estimate evapotranspiration from remote sensing data require daily average net radiation values [Nishida et al., 2003, Norman et al., 2003, Batra et al., 2006, Venturini et al., 2008]. Bisht et al. [2005] suggested a sinusoidal model to estimate the diurnal cycle of net radiation, which closely follows the framework for retrieving the diurnal cycle of surface temperature proposed by Lagouarde and Brunet [1983]. The daily average net radiation,  $R_n^{avg}$  [ $\text{Wm}^{-2}$ ], in terms of the instantaneous (clear or cloudy) net radiation estimate obtained at local satellite overpass time,  $t_{ovp}$ , is given as [Bisht et al., 2005]:

$$R_n^{avg} = \frac{2R_n}{\pi \sin \left[ \pi \left( \frac{t_{ovp} - t_{rise}^*}{t_{set}^* - t_{rise}^*} \right) \right]} \quad (3.12)$$

where  $t_{rise}^*$  and  $t_{set}^*$  corresponds to local time when  $R_n$  becomes positive and negative, respectively. It should be pointed out that  $t_{rise}^*$  and  $t_{set}^*$  are related to the local sunrise and sunset time; and are approximated as one hour after local sunrise time and one hour before local sunset time, respectively. Similarly, daily average net shortwave radiation can be estimated as:

$$R_{S,net}^{avg} = \frac{2R_{S,net}}{\pi \sin \left[ \pi \left( \frac{t_{ovp} - t_{rise}}{t_{set} - t_{rise}} \right) \right]} \quad (3.13)$$

where  $t_{rise}$  and  $t_{set}$  corresponds to the local sunrise and sunset time, respectively.

### 3.1.4 Adaptations to the algorithm for estimating surface radiation budget over the Continental United States

In order to estimate net radiation over the CONUS using the proposed algorithm, two adaptations have been incorporated. The first is related to the computation of temperature offsets (eq. 3.11a and 3.11c) necessary for estimating near-surface air and dew temperatures from 5-km LST given by the cloud product; while the second addresses the issue of missing surface albedo values in the MOD43B2 product. Under cloudy sky conditions, the atmospheric profile data is unavailable and the proposed methodology relies on estimating near-surface temperatures (air and dew) by subtracting offsets from  $T_s^{06.L2}$ . Explicit computation of temperature offsets for the CONUS at 1 km spatial resolutions is computationally expensive, thus the CONUS domain was divided into sub-domains of  $5^0 \times 5^0$  (as shown in Figure 7-15). Temperature offsets for each sub-domains are computed separately for the Aqua and Terra overpasses; and then applied to all the 1-km MODIS pixels that lie within the sub-domain.

The MODIS surface albedo product (MCD43B3) is a combined Aqua and Terra 16-day product, produced every 8 days, that supplies black-sky and white-sky albedo for seven

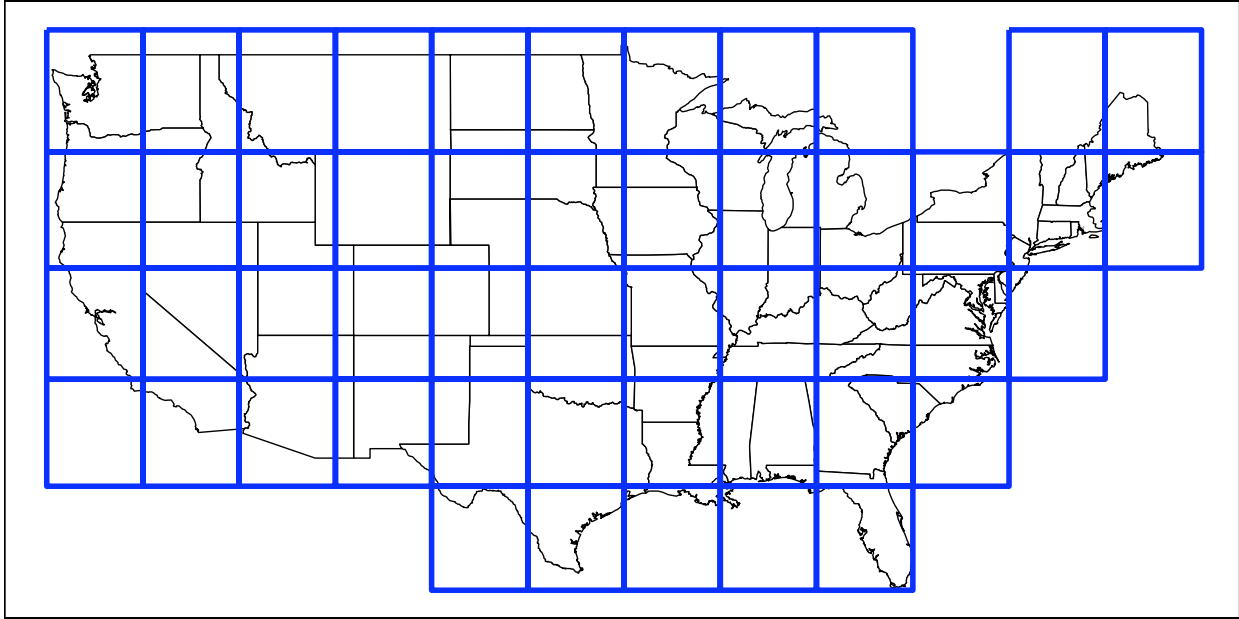


Figure 3-1: Division of the Continental United States domain into  $5^{\circ} \times 5^{\circ}$  regions over which temperature offsets, required to estimate near-surface air and dew temperatures from 5-km LST given by the cloud product, are computed.

spectral bands ( $0.47\text{-}2.10 \mu\text{m}$ ) and three broad bands ( $0.3\text{-}0.7$ ,  $0.7\text{-}3.0$  and  $0.3\text{-}5.0 \mu\text{m}$ ) at 1 km resolution [Schaaf and coauthors, 2002]. Due to weather, corrupt satellite data and requirements of retrieval algorithm, the MODIS albedo products often has gaps. Fang et al. [2007] reported that 13.3% of land pixels did not contain any valid retrieval values during 2000-2004. In order to estimate  $R_n$  over the CONUS at 1 km, a spatially gap-free surface albedo product is a necessary requirement. Since the primary focus here is to demonstrate the applicability of a framework to estimate net radiation over the CONUS domain, while relying entirely on remotely sensed data, a simple spatial-temporal interpolation scheme to fill missing albedo values is adopted. The first step of our simple spatio-temporal approach involves taking the MODIS surface albedo data at a given julian day and filling the missing values with data available 8 days earlier or later than the julian day in consideration. In the second step, the remaining missing albedo values, for which no valid albedo values were available 8 days earlier or later, are filled using a nearest-neighbor approach. The

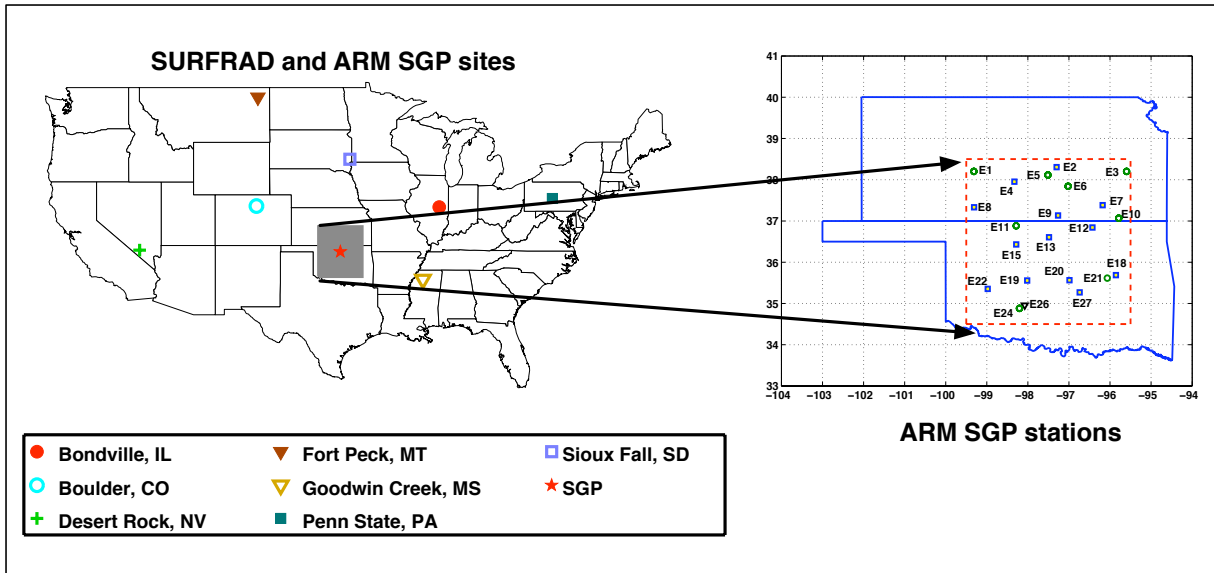


Figure 3-2: Map of the Continental United States showing SURFRAD sites and ARM SGP network. ARM SGP ground stations in circles, triangle and squares had SIRS station only, EBBR station only and both SIRBS and EBBR stations, respectively.

MODIS land surface albedo team is developing a more sophisticated approach of producing continuous 1 km surface albedo product using multiyear observations [Fang et al., 2007] and once such a product is available, it can be readily used in our methodology to estimate  $R_n$ . These two above-mentioned adaptations to the proposed methodology enable the estimation of the SRB over the CONUS feasible.

## 3.2 Study site and data used

In this study, ground measurement data is used from both the Department of Energy's (DOE's) Atmospheric Radiation Measurement (ARM) program in the Southern Great Plains and the National Oceanic and Atmospheric Administration's (NOAA's) Surface Radiation budget (SURFRAD) network.

### 3.2.1 Southern Great Plains

The Southern Great Plains (SGP) region covers southern part of Kansas and most of Oklahoma, extending from  $34.5^{\circ}$  to  $38.5^{\circ}$ N and  $95.5^{\circ}$  to  $99.5^{\circ}$ W, as shown in Figure 3-2. The dashed box in Figure 3-2 corresponds to the grid, with interval of  $0.009^{\circ}$ . The region has a relatively flat terrain with heterogenous land cover [Batra et al., 2006]. The Atmospheric Radiation Measurement (ARM) program funded by the U.S. Department of Energy, maintains continuous measurements of various meteorological and surface variables. In this study, data from Energy Balance Bowen Ratio (EBBR) stations and Solar and Infrared Radiation Stations (SIRS) is utilized. The radiation system uses Eppley Normal Incidence Pyrheliometers (NIP) and Precision Spectral Pyranometers (PSP) to measure direct and diffuse downwelling shortwave radiation; upwelling shortwave radiation is measured by Eppley PSP; while downwelling and upwelling longwave radiation are measured by Eppley Precision Infrared Radiometer (PIR). The spatial distribution of ground stations within the SGP, along with the data-type measured at each location, is shown in Figure 3-2. EBBR stations provided measurements of air temperature and vapor pressure (which is used to compute dew-temperature) at 2.05 m above the land surface; while SIRS recorded upwelling and downwelling shortwave, as well as, longwave radiation. The 1-minute SIRS data, along with details about the instruments, are available from the ARM website (<http://www.arm.gov>). The local sunrise and sunset times for the study region are obtained from the website of US Naval Observatory, Astronomical Application Department (<http://aa.usno.navy.mil/>), which are used in estimating daily average net radiation.

### 3.2.2 Surface Radiation Budget network

The NOAA's SURFRAD network has been operational since 1995 and includes seven sites: Bondville, Illinois; Boulder, Colorado; Desert Rock, Nevada; Fort Peck, Montana; Goodwin Creek, Mississippi; Penn State, Pennsylvania; and Sioux Falls, South Dakota (see Figure 3-2 and Table 3.1). Primary measurements at the SURFRAD sites involve upwelling and downwelling solar and infrared radiations, direct and diffuse solar radiations, photosyn-

Table 3.1: Geographic locations of SURFRAD and ARM ground stations.

Network	Site identification	Name	Latitude (N)	Longitude (W)
SURFRAD	BON	Bondville, IL	40.05 <sup>0</sup>	88.37 <sup>0</sup>
	TBL	Table Mountain, CO	40.13 <sup>0</sup>	105.24 <sup>0</sup>
	DRA	Desert Rock, NV	36.63 <sup>0</sup>	116.02 <sup>0</sup>
	FPK	Fort Peck, MT	48.31 <sup>0</sup>	105.10 <sup>0</sup>
	GWN	Goodwin Creek, MS	34.25 <sup>0</sup>	89.87 <sup>0</sup>
	PSU	Penn State, PA	40.72 <sup>0</sup>	77.93 <sup>0</sup>
	SXF	Sioux Falls, SD	43.73 <sup>0</sup>	96.62 <sup>0</sup>
ARM SGP	E01	Larned, KS	38.20 <sup>0</sup>	99.32 <sup>0</sup>
	E02	Hillsboro, KS	38.31 <sup>0</sup>	97.30 <sup>0</sup>
	E03	LeRoy, KS	38.20 <sup>0</sup>	95.60 <sup>0</sup>
	E04	Plevna, KS	37.95 <sup>0</sup>	98.33 <sup>0</sup>
	E05	Halstead, KS	38.11 <sup>0</sup>	97.51 <sup>0</sup>
	E06	Towanda, KS	37.84 <sup>0</sup>	97.01 <sup>0</sup>
	E07	Elk Falls, KS	37.38 <sup>0</sup>	96.18 <sup>0</sup>
	E08	Coldwater, KS	37.33 <sup>0</sup>	99.31 <sup>0</sup>
	E09	Ashton, KS	37.13 <sup>0</sup>	97.27 <sup>0</sup>
	E10	Tyro, KS	37.07 <sup>0</sup>	95.79 <sup>0</sup>
	E11	Byron, OK	36.88 <sup>0</sup>	98.29 <sup>0</sup>
	E12	Pawhuska, OK	36.84 <sup>0</sup>	96.43 <sup>0</sup>
	E13	Lamont, OK	36.61 <sup>0</sup>	97.49 <sup>0</sup>
	E15	Ringwood, OK	36.43 <sup>0</sup>	98.28 <sup>0</sup>
	E18	Morris, OK	35.69 <sup>0</sup>	95.86 <sup>0</sup>
	E19	El Reno, OK	35.56 <sup>0</sup>	98.02 <sup>0</sup>
	E20	Meeker, OK	35.56 <sup>0</sup>	96.99 <sup>0</sup>
E21	Okmulgee, OK	35.62 <sup>0</sup>	96.07 <sup>0</sup>	
E22	Cordell, OK	35.35 <sup>0</sup>	98.98 <sup>0</sup>	
E24	Cyril, OK	34.88 <sup>0</sup>	98.21 <sup>0</sup>	

Table 3.2: The MODIS products used in this study

MODIS product	Short name	Spatial resolution	Temporal resolution	Parameters used	Clear sky algorithm	Cloudy-sky algorithm
Geolocation Product	MODD03 MYD03	1-km	1/4 day	Solar zenith angle, Latitude and Longitude	x	x
Aerosol Product	MODD04_L2 MYD04_L2	10-km	1/4 day	Optical depth	x	
Cloud Product	MODD06_L2 MYD06_L2	1-km	1/4 day	Cloud optical depth Cloud emissivity, Cloud fraction, Cloud top temperature, and Land surface temperature		x
		5-km	1/4 day			
Atmospheric Profile Product	MODD07_L2 MYD07_L2	5-km	1/4 day	Air temperature and Dew temperature	x	
Land Surface Temperature and Emissivity	MOD11_L2 MYD11_L2	1-km	1/4 day	Surface temperature and Surface emissivity	x	
		1-km	8-day			
Albedo Product	MCD43B3	1-km	8-day	White- and Black-sky albedo	x	x



thetically active radiation, ultraviolet radiation and meteorological parameters [Augustine et al., 2000, 2005]. The SURFRAD data is available at a 3-minute temporal resolution from <ftp://ftp.srrb.noaa.gov/pub/data/surfrad/>. The direct and diffuse component of incoming solar radiation are measured with an Eppley Normal Incidence Pyrheliometers (NIP) and shaded Eppley Black and White (B&V) pyranometers, respectively; while Spectolab pyranometer, mounted on a 10-m tower, measures upwelling solar radiation. The downwelling and upwelling longwave radiation are measured with the Epply Precision Infrared Radiometer (PIR). A detail description about the instruments used for measuring various components of surface radiation budget and quality control of the data are presented in Augustine et al. [2000, 2005] and Long et al. [2009]. The measurement data from both, SURFRAD and SGP, are aggregated to 15-minute interval when comparing with estimates of various SRB components presented in Section 3.3 and 3.4.

### 3.2.3 MODIS data products

The MODIS data products used in this study for clear sky and cloudy conditions consist of: geolocation product (MOD03 and MYD03)<sup>1</sup>, aerosol product (MOD04\_L2 and MYD04\_L2), cloud product (MOD06\_L2 and MYD06\_L2), atmospheric profile product (MOD07\_L2 and MYD07\_L2), land surface temperature and emissivity product (MOD11\_L2 and MYD11\_L2) and albedo product (MCD43B3). A detail descriptions about all the MODIS data products, except the cloud product, is presented in Bisht et al. [2005]. In the MOD06\_L2 and MYD06\_L2 product, cloud top temperature, cloud emissivity and cloud fraction are estimated at 5-km resolution from a CO<sub>2</sub> slicing technique using the MODIS channels 31 (11.03  $\mu\text{m}$ ), 33 (13.34  $\mu\text{m}$ ), 34 (13.64  $\mu\text{m}$ ), 35 (13.94  $\mu\text{m}$ ) and 36 (14.24  $\mu\text{m}$ ) [Menzel et al., 2006]. Cloud optical thickness is estimated at 1 -km resolution from the MODIS channel 1 (0.645  $\mu\text{m}$ ) which exploits the fact that the reflection function of clouds at a nonabsorbing band in the visible wavelength region is primarily a function of the cloud optical thickness [King et al., 1998]. The various MODIS data products, along with their spatial resolution and

---

<sup>1</sup>MOD and MYD refers to the MODIS data products obtained from Terra and Aqua satellites, respectively

parameters used, are summarized in Table 3.2. All the MODIS data products are available in Hierarchical Data Format (HDF) and are obtained from the NASA’s Warehouse Inventory Search Tool (WIST) website. Next the comparison of estimated SRB components obtained from the proposed methodology with ground measurements are presented.

### 3.3 Results: Over the Southern Great Plains

In this section, the applicability of the retrieval algorithm is tested over the SGP region using only MODIS-Terra data for both day and night overpasses during 2006.

#### 3.3.1 Temperatures: land surface, air and dew

In this section, a comparison of the 5-km land surface temperature obtained from the MOD06.L2 product against ground measurements. Furthermore, the temperature offsets mentioned in equations 3.11a, 3.11b, 3.11c and 3.11d to estimate air and dew temperature under cloudy conditions are also obtained. Direct measurements of LST were not available, thus measurements of upwelling longwave by the SIRS stations were converted to obtain surrogate observations of LST using Eqn 3.3e, while assuming a constant surface emissivity of 0.98. The scatter plot between  $T_s^{06.L2}$  and ground observations is shown in Figure 3-3(a) and (b) for day- and night-overpasses. The bias, root mean square error (RMSE) and correlation ( $R^2$ ) between  $T_s^{06.L2}$  and ground observations are summarized in Table 3.3. In this study, the bias is computed as the MODIS data minus in-situ observations (the same definition is also used while reporting values of bias from any other study). Recently Wang et al. [2008] compared clear sky nighttime surface temperatures provided by another the MODIS product, MOD07.L2 over eight ground locations (six in U.S. and two in Germany). They reported biases in MOD07.L2 LST that varied between -3.38 [K] to 3.14 [K]; while RMSE ranged from 1.97 [K] to 4.10 [K]. Thus, the surface temperature estimates from the MOD06.L2 are not only comparable to those obtained from the MOD07.L2, but have an advantage of being available for all sky conditions, while the MOD07.L2 LST are produced

for only clear sky pixels.

Air and dew temperatures, needed to compute downwelling longwave radiation, are estimated as offsets from  $T_s^{06.L2}$ . EBBR measurements of vapor pressure at 2.05 m above land surface are converted to  $T_d$  measurements for comparison purposes. Scatter plot of  $T_s^{06.L2}$  and  $T_a$  during day- and night-overpasses is shown in Figure 3-3(c) and (d); while Figure 3-3(e) and (f) show the scatter plot between  $T_s^{06.L2}$  and  $T_d$  for day- and night-overpasses. Bias, RMSE and  $R^2$  are summarized in Table 3.3. The RMSE and  $R^2$  between  $T_s^{06.L2}$  and  $T_a$  for both day- and night-overpasses are better than to those between  $T_s^{06.L2}$  and  $T_s$ ; while statistical agreement between  $T_s^{06.L2}$  and  $T_d$  is not as strong (higher RMSE and lower  $R^2$ ). The temperature offsets used in Eqn 3.11a, 3.11b, 3.11c and 3.11d are estimated as biases from scatter plots as:

$$\delta_a^{day} = 4.35 \text{ [K]} \quad (3.14a)$$

$$\delta_a^{night} = -0.51 \text{ [K]} \quad (3.14b)$$

$$\delta_d^{day} = 16.01 \text{ [K]} \quad (3.14c)$$

$$\delta_d^{night} = 7.18 \text{ [K]} \quad (3.14d)$$

The above estimates of temperature offsets rely on ancillary surface measurements and such measurements are sparse globally. An alternate approach to estimate temperature offsets that does not require surface measurements is also proposed. Thus, the proposed framework of estimating  $R_n$  can rely exclusively on remote sensing information when surface measurements regarding air and dew temperatures are absent. The comparison of near-surface air and dew temperatures (using a hydrostatic assumption in the atmosphere) from the MOD07\_L2 data with  $T_s^{06.L2}$ , under clear-sky conditions, are shown in Figure 3-4. The

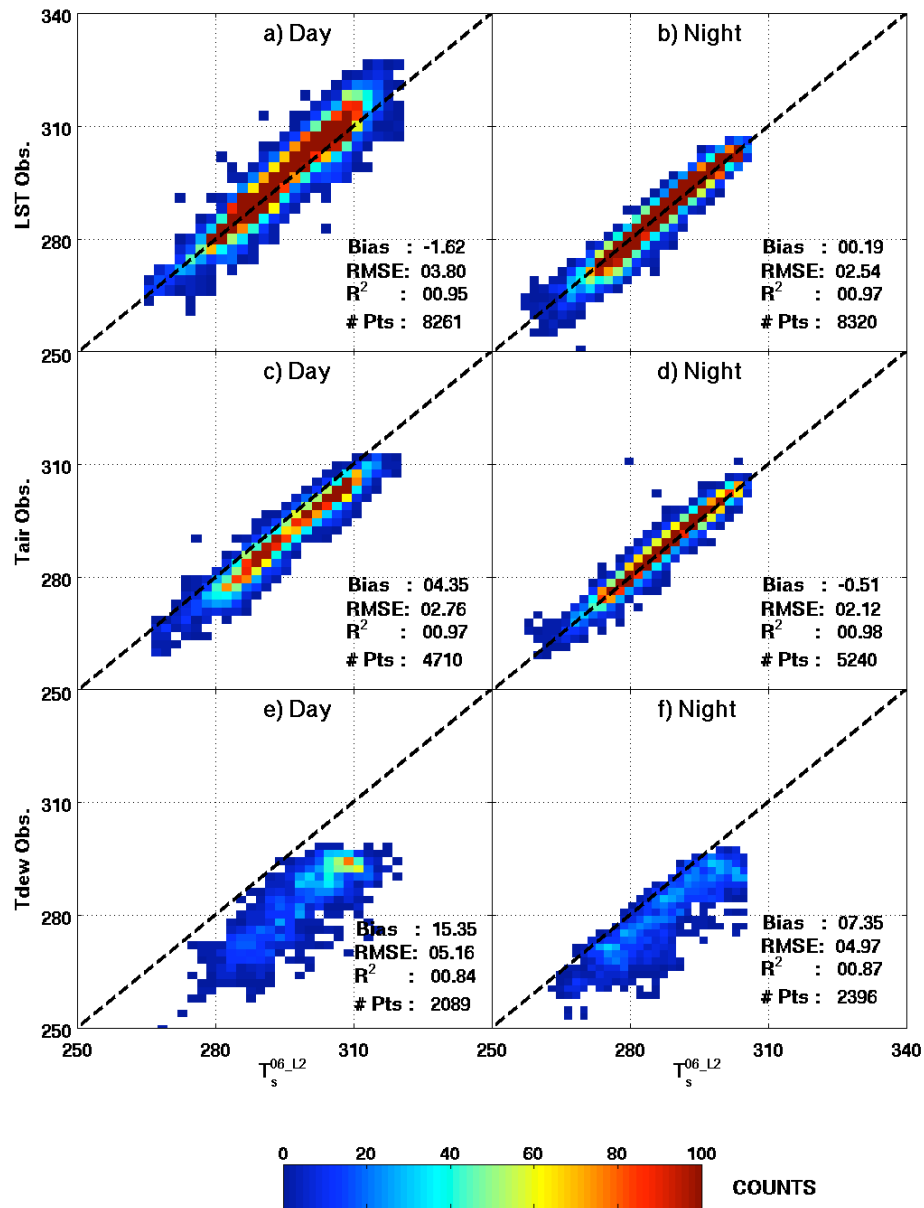


Figure 3-3: Comparison of 5-km land surface temperature (LST) from the MODIS cloud data product (MOD06\_L2): panels (a) and (b) are comparison of MOD06\_L2 LST against observation during day- and night-overpasses, respectively; panels (c) and (d) are comparison of MOD06\_L2 LST against observed air temperature during day- and night-overpasses; and; panels (e) and (f) are comparison of MOD06\_L2 LST against observed dew temperature during day- and night-overpasses. Bias is computed as LST-MOD06\_L2 minus Observed values.

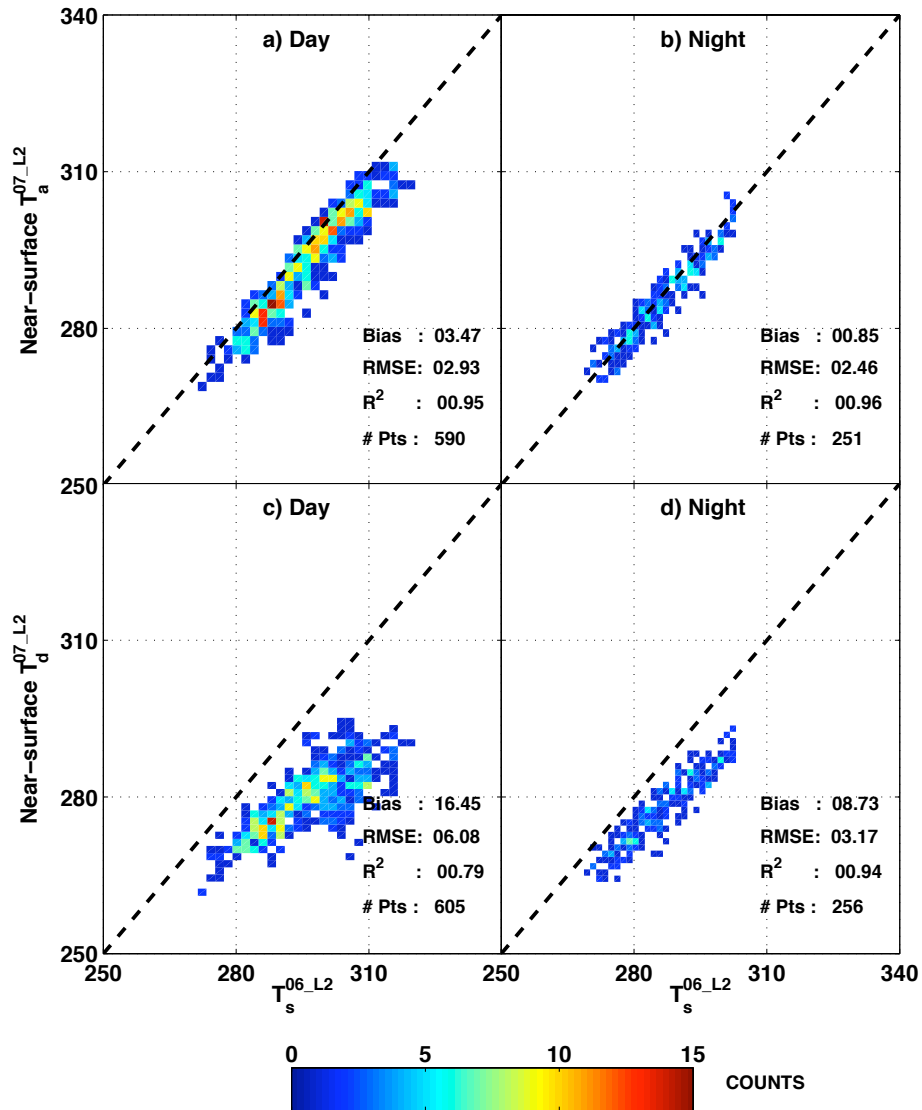


Figure 3-4: Comparison of 5-km land surface temperature (LST) from the MOD06.L2 product with near-surface air and obtained from the MOD07.L2 product under hydrostatic atmosphere assumption. Panels (a) and (b) are comparison of MOD06.L2 with near-surface air temperature from MOD07.L2 during day- and night-overpass; panels (c) and (d) are comparison of MOD06.L2 with near-surface dew temperature from MOD07.L2 during day- and night-overpass.

Table 3.3: Bias, Root Mean Square Errors (RMSE), correlation ( $R^2$ ) and number of data points for following quantities given or derived from the MODIS data and ground observations: (i) Land surface temperature (LST); (ii) Near-surface air temperature ( $T_a$ ); (iii) Near-surface dew temperature ( $T_d$ ); (iv) Near-surface air temperature derived from MOD07\_L2 product; and (v) Near-surface dew temperature derived from MOD07\_L2 product. Bias is computed as the MODIS data minus observed data.

MODIS data	Observation data	Overpass Time	Sky Condition	Bias	RMSE	$R^2$	# of points
5-km Land surface temperature from MOD06_L2	LST	Day	Clear and	-1.62	3.80	0.95	8261
		Night	Cloudy	0.19	2.54	0.97	8320
	$T_a$	Day	Clear and	4.5	2.76	0.97	4710
		Night	Cloudy	-0.51	2.12	0.98	5240
	$T_d$	Day	Clear and	16.01	5.00	0.86	3347
		Night	Cloudy	7.18	4.94	0.87	2927
	$T_a$ from MOD07_L2	Day	Clear	3.47	2.93	0.95	590
		Night	Clear	0.85	2.46	0.96	251
	$T_d$ from MOD07_L2	Day	Clear	16.45	6.08	0.79	605
		Night	Clear	8.73	3.17	0.94	256

temperature offsets computed as biases from the scatter plot as:

$$\delta_a^{day, clear} = 3.47 \text{ [K]} \quad (3.15a)$$

$$\delta_a^{night, clear} = 0.85 \text{ [K]} \quad (3.15b)$$

$$\delta_d^{day, clear} = 16.45 \text{ [K]} \quad (3.15c)$$

$$\delta_d^{night, clear} = 8.73 \text{ [K]} \quad (3.15d)$$

where the superscript emphasizes that these offsets are obtained under clear-sky conditions. The difference in temperature offsets obtained from surface measurements and the MOD07\_L2 product during the day and night are  $\approx 1$  [K] and  $\approx 1.5$  [K], respectively. In Section 3.3.2, the results regarding various components of the surface energy budget under cloudy-skies use temperature offsets obtained from surface measurements, as presented in Eqn 3.14. The overall impact of using temperature offsets obtained under clear-sky conditions (Eqn 3.15) to estimate net radiation is also presented in Section 3.3.2.

### 3.3.2 Instantaneous and daily average net radiation: under cloudy-skies condition

In this section, we present the results of instantaneous  $R_n$  obtained using data about cloud properties and 5-km surface temperature from the MOD06\_L2 product; along with geolocation (MOD03), surface albedo data (MCD43B3) and temperature offsets obtained in Section 3.3.1. Under clear sky conditions, a higher resolution 1-km LST MOD11\_L2 product is available and the MOD07\_L2 provides direct estimates of  $T_a$  and  $T_d$  at 20 vertical pressure levels. The MODIS overpasses that were deemed as under clear-sky (i.e. 75% of the SGP domain was cloud free) in 2006 were omitted from the analysis presented in this section.

The error histogram between estimated and in-situ measurements of downwelling, upwelling and net radiation for shortwave and longwave is shown in Figure 3-5; while the summary of bias, RMSE and  $R^2$  are presented in Table 3.4. Tang and Li [2008] reported an overall bias, RMSE and  $R^2$  for clear sky  $R_L^\downarrow$  for the SURFRAD locations in U.S. as -20.3 [ $\text{Wm}^{-2}$ ], 30.1 [ $\text{Wm}^{-2}$ ] and 0.91, respectively; while clear sky net longwave radiation,  $R_L^{net}$ , statistics were -11.7 [ $\text{Wm}^{-2}$ ], 26.1 [ $\text{Wm}^{-2}$ ] and 0.94. Wang and Liang [2009] similarly estimated clear sky  $R_L^\downarrow$  and clear sky  $R_L^{net}$  for SURFRAD locations in U.S. from the Terra and Aqua satellites. Overall bias by Wang and Liang [2009] for  $R_L^\downarrow$  and  $R_L^{net}$  from the Terra satellite were -0.40 [ $\text{Wm}^{-2}$ ] and -2.80 [ $\text{Wm}^{-2}$ ]; while RMSE were 17.60 [ $\text{Wm}^{-2}$ ] and 17.72 [ $\text{Wm}^{-2}$ ]. Thus, the longwave radiation estimates presented in this section are comparable to those reported in literature, while having an added advantage of being available under cloudy conditions, though at a coarse 5-km resolution. Wang et al. [2008] estimated net surface shortwave radiation using the TOA reflectance and obtained RMSE under clear and cloudy skies of 20 [ $\text{Wm}^{-2}$ ] and 35 [ $\text{Wm}^{-2}$ ], respectively.

The comparison of instantaneous  $R_n$  estimates with ground measurements during day- and night-overpasses are shown in Figure 3-6. The bias, RMSE and  $R^2$ , including day- and night-overpasses, are 10.46 [ $\text{Wm}^{-2}$ ], 38.70 [ $\text{Wm}^{-2}$ ] and 0.99. The  $R^2$  between estimated and measured  $R_n$  during the night-overpass is significantly lower (0.32) when compared to day-overpasses (0.95), as summarized in Table 3.4. The use of temperature offsets obtained under

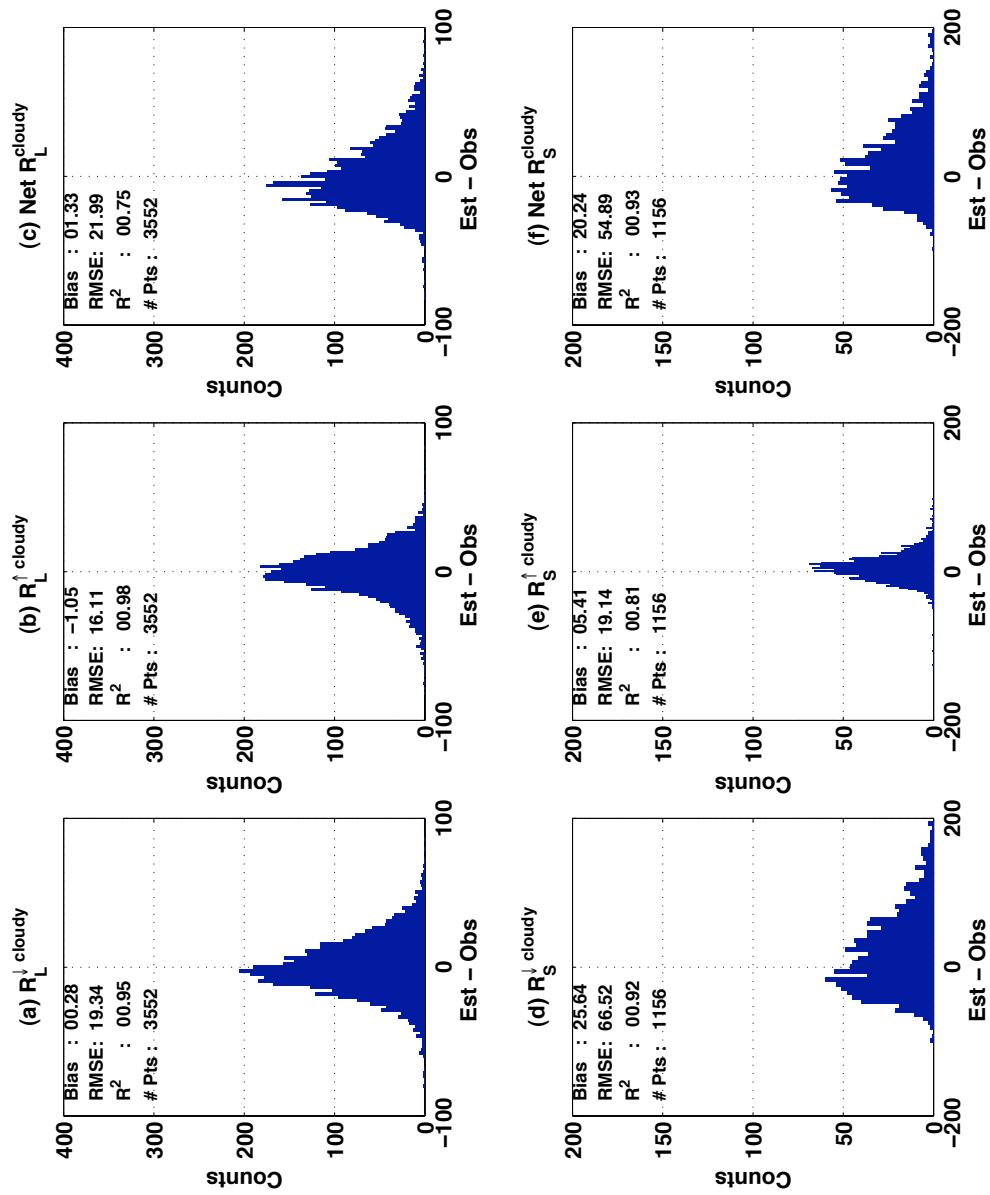


Figure 3-5: Error histograms between observed and estimated components of net radiation for cloudy overpasses: (a) Downwelling longwave; (b) Upwelling longwave; (c) Net longwave; (d) Downwelling shortwave; (e) Upwelling shortwave; and (f) Net shortwave radiation. Bias is computed as estimated minus observed values.



Table 3.4: Bias, Root Mean Square Errors (RMSE, correlation ( $R^2$ )) and number of data points for various quantities given or derived from the MODIS data and ground observations. Bias is computed as MODIS data minus observed data.

Sky Condition	Component of the the surface energy budget	Overpass time	Bias	RMSE	$R^2$	# of data points
Cloudy	$R_L^\downarrow$	Day+Night	0.28	19.34	0.95	3552
	$R_L^\uparrow$	Day+Night	-1.05	16.11	0.98	3552
	Net $R_L^\uparrow$	Day+Night	1.33	21.99	0.75	3552
	$R_S^\downarrow$	Day	25.64	66.52	0.92	1156
	$R_S^\uparrow$	Day	5.41	19.14	0.81	1156
	Net $R_S^\uparrow$	Day	20.24	54.89	0.93	1156
	Instantaneous $R_n$	Day	35.16	50.58	0.95	1156
		Night	-5.23	17.72	0.33	2396
		Day+Night	7.91	37.44	0.99	3552
	Daily average $R_n$	-	34.00	37.72	0.93	1152
Clear	$R_L^\downarrow$	Day+Night	3.87	20.79	0.93	1653
	$R_L^\uparrow$	Day+Night	-2.50	15.76	0.98	1653
	Net $R_L^\uparrow$	Day+Night	6.37	19.37	0.86	1653
	$R_S^\downarrow$	Day	17.82	42.05	0.96	1097
	$R_S^\uparrow$	Day	-17.40	17.79	0.79	1097
	Net $R_S^\uparrow$	Day	35.22	40.78	0.96	1097
	Instantaneous $R_n$	Day	23.08	39.34	0.96	1118
		Night	-3.72	11.51	0.51	476
		Day+Night	16.19	34.60	0.99	1594
	Daily average $R_n$	-	11.27	31.98	0.93	991

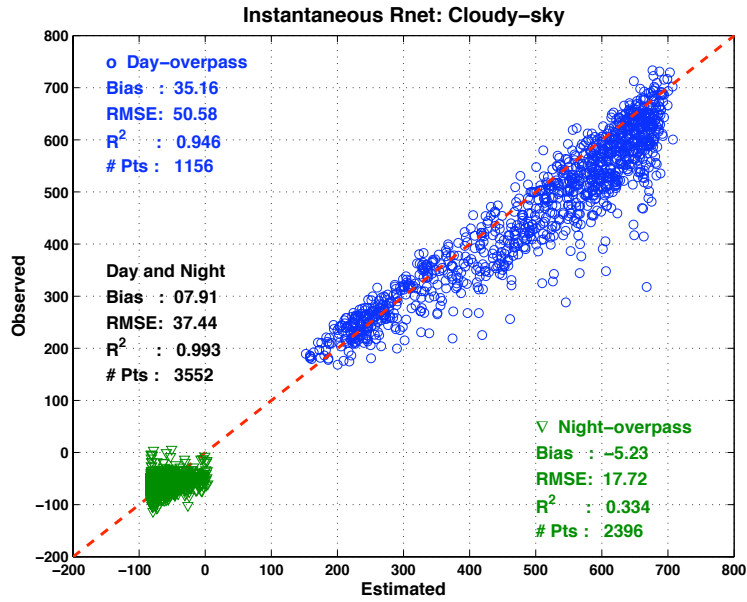


Figure 3-6: Comparison of estimated and observed net radiation for cloudy overpasses. Circles and triangles represents day- and night-overpasses of the MODIS. Bias is computed as estimated minus observed values.

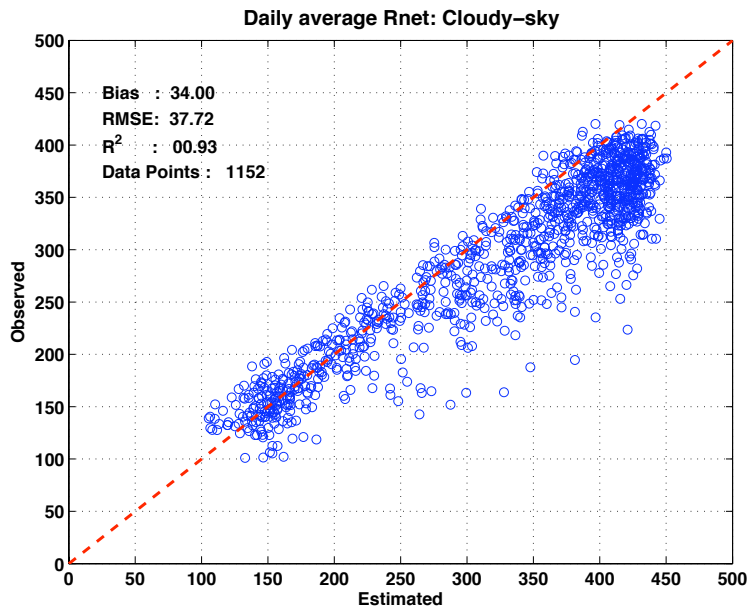


Figure 3-7: Comparison of daily average estimated and observed net radiation for cloudy overpasses. Bias is computed as estimated minus observed values.

clear-sky conditions only (Eqs 3.15(a)-3.15(d)) has little impact on  $R_n$  estimates, including day- and night-overpasses, with an overall bias, RMSE and  $R^2$  as 3.28 [ $\text{Wm}^{-2}$ ], 40.49 [ $\text{Wm}^{-2}$ ] and 0.99, respectively. Figure 3-7 shows the scatter plot between estimated daily average net radiation and ground observations. The bias, RMSE and  $R^2$  between estimated daily average net radiation and ground observations were 22.75 [ $\text{Wm}^{-2}$ ], 34.11 [ $\text{Wm}^{-2}$ ] and 0.95. Overall the proposed methodology is successfully able to estimate instantaneous and daily average net radiation from the MOD06.L2 product for 2006. Furthermore, when the use of ancillary ground measurements in estimating temperature offsets is excluded, the impact on  $R_n$  estimates is minor.

### 3.3.3 Instantaneous estimates of net radiation: Under all sky-conditions

In 2006, a large portion of the MODIS-Terra overpasses over the SGP were contaminated by the presence of clouds. Only 24% of day-overpasses and 9% of night-overpasses had 75% or more of the SGP region as cloud free. Thus, the methodologies that focus on retrieving net radiation during clear sky days are not applicable to a large portion of the MODIS overpasses. In the previous section, it was successfully demonstrated that for cloudy days the MOD06.L2 product can be used to estimate  $R_n$ , albeit at a coarser 5-km spatial resolution when compared to 1-km  $R_n$  estimates available under clear sky conditions. Before proceeding to present the framework of estimating  $R_n$  for all sky conditions, the results obtained using the approach of Bisht et al. [2005] under clear-sky conditions for 2006 over the SGP are presented for the sake of completeness. Figure 3-8 shows the error histograms between estimate and in-situ measurements for the various components of longwave and shortwave energy budget; while Figure 3-9 and 3-10 present results for instantaneous and daily average  $R_n$ . The statistical summary of the results for components of the surface energy budget under clear-sky conditions is given in Table 3.4.

It is then possible to use the high resolution (1-km) clear skies algorithm with the lower resolution (5-km) cloudy skies algorithm to suggest an all-sky conditions methodology to estimate instantaneous and daily net radiation as shown in Figure 3-11. An example of this

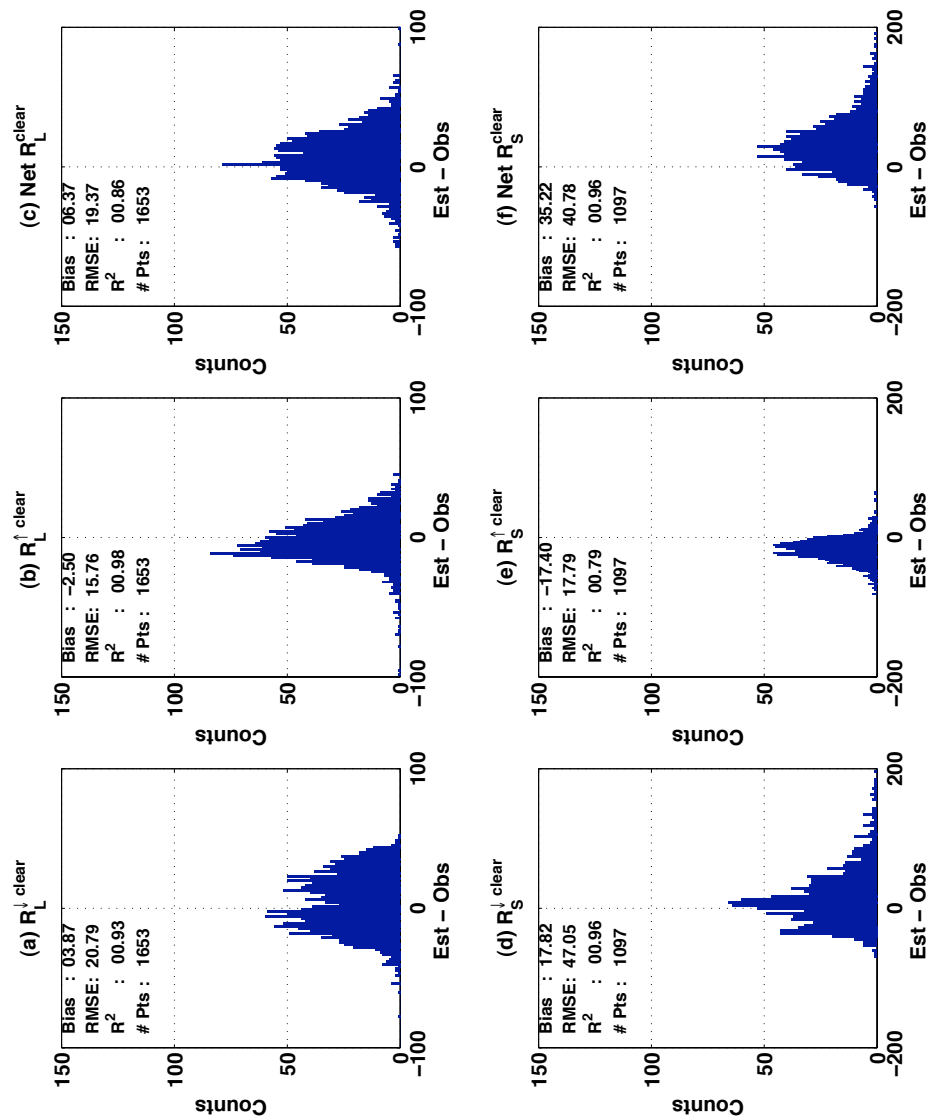


Figure 3-8: Error histograms between observed and estimated radiations for clear-sky overpasses: (a) Downwelling longwave; (b) Upwelling longwave; (c) Net longwave; (d) Downwelling shortwave; (e) Upwelling shortwave; and (f) Net shortwave radiation. Bias is computed as estimated minus observed values.

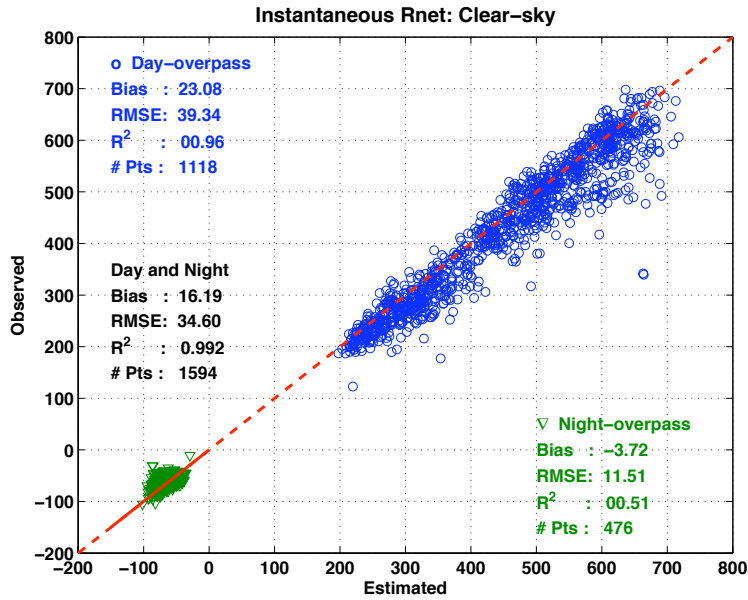


Figure 3-9: Comparison of estimated and observed net radiation for clear-sky overpasses. Circles and triangles represents day- and night-overpasses of the MODIS. Bias is computed as estimated minus observed values.

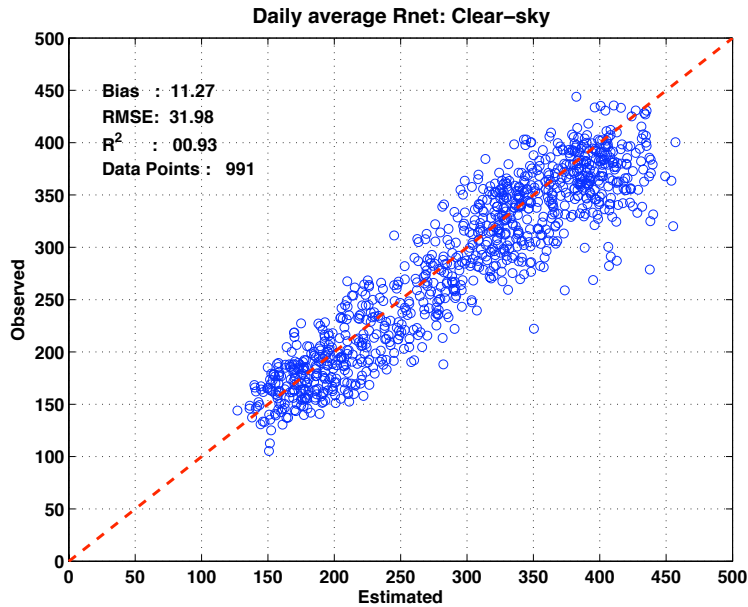
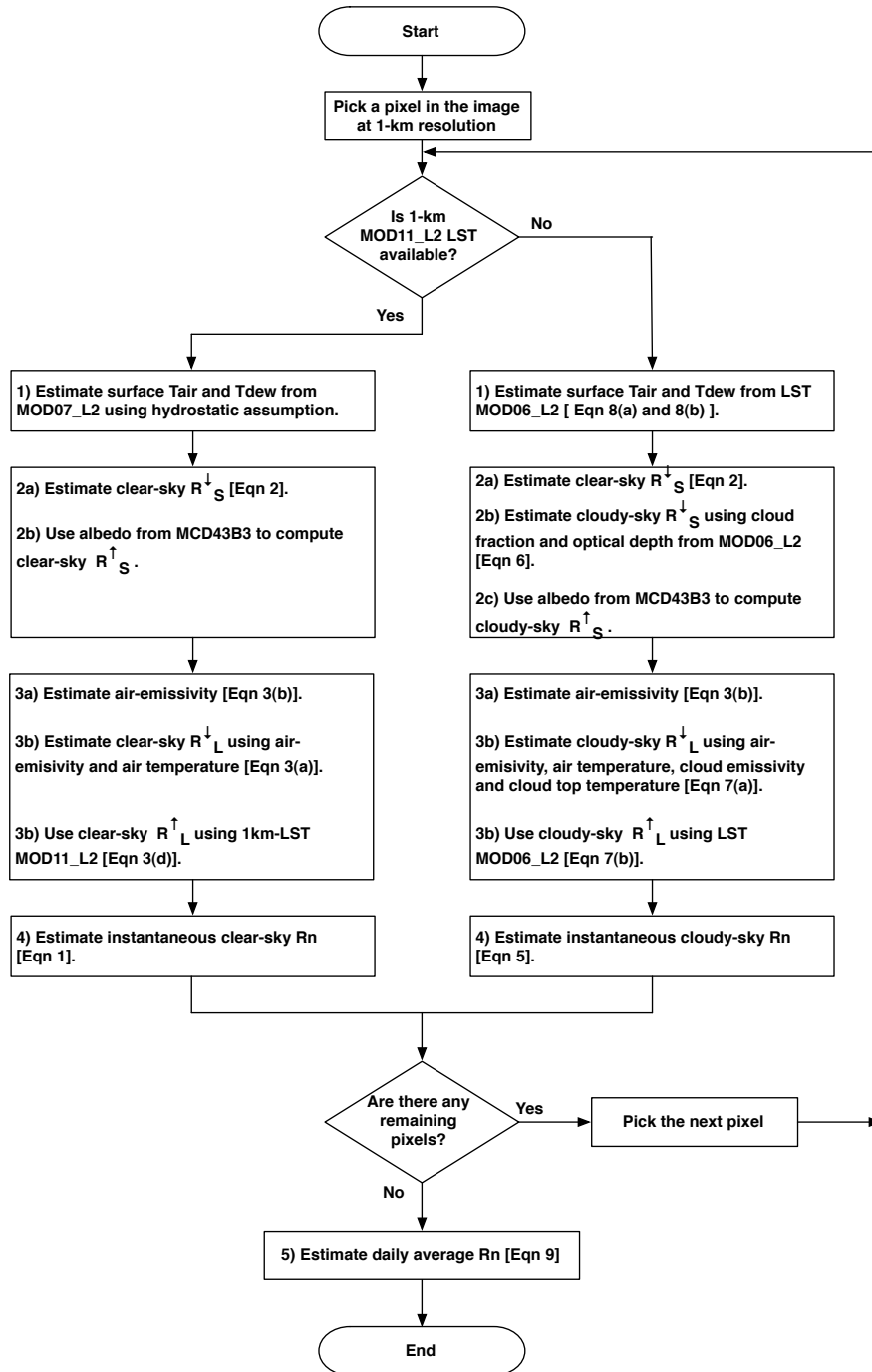


Figure 3-10: Comparison of daily average estimated and observed net radiation for clear-sky overpasses. Bias is computed as estimated minus observed values.



**NOTE:**

(1) 5-km data products are converted to 1-km by assuming homogenous values over 5x5-km grid.

(2) Similar approach is adopted to convert 10-km data products to 1-km.

Figure 3-11: Flowchart to estimate instantaneous and daily average net radiation from the MODIS data for all sky conditions.

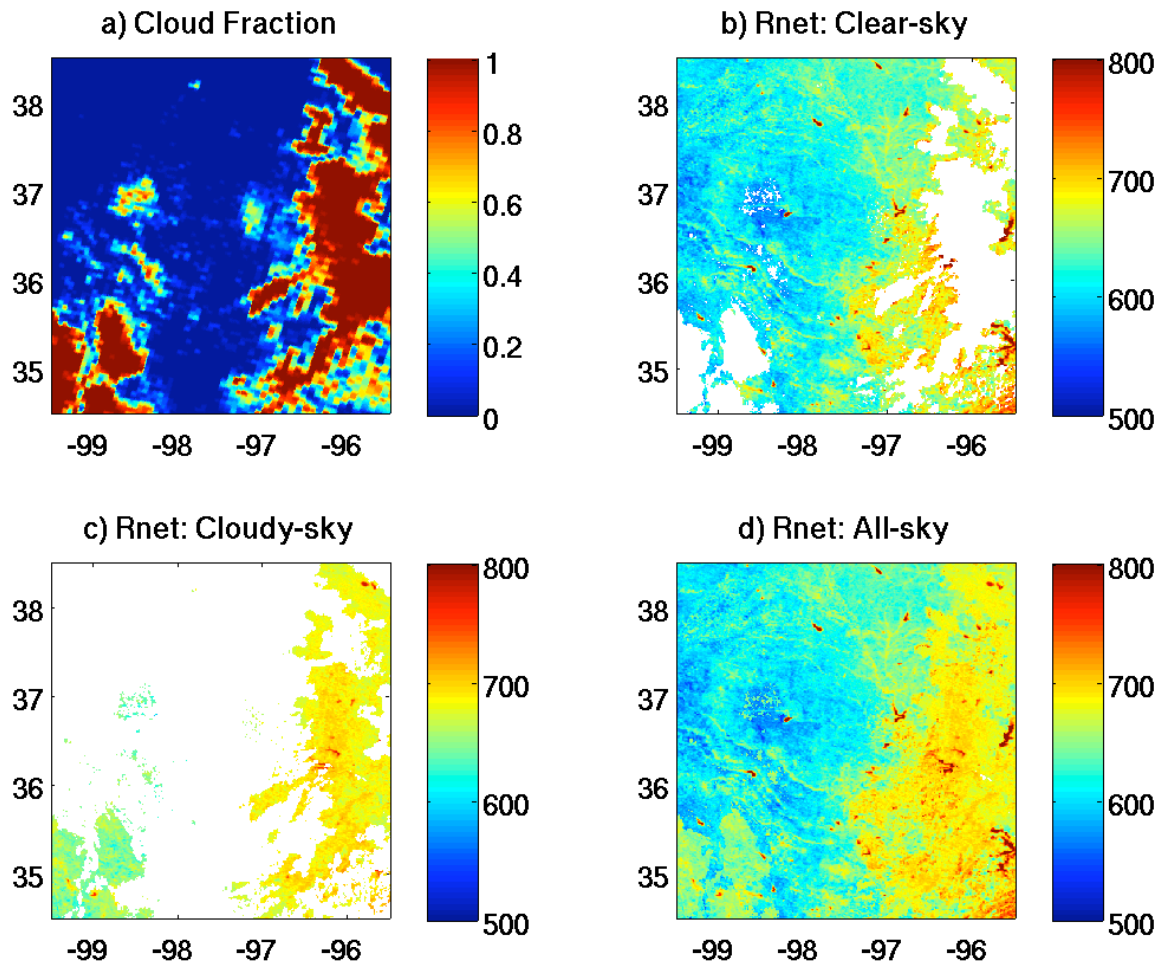


Figure 3-12: Instantaneous estimation of net radiation ( $R_n$ ) from the MODIS-Terra for all sky conditions on 24<sup>th</sup> July, 2006 at 17:35UTC. (a) Cloud fraction from MOD06\_L2 data over the SGP; (b) Estimate of  $R_n$  using clear sky algorithm (White region represents no data due to cloud cover); (c) Estimate of  $R_n$  using cloudy-sky algorithm for the cloud covered portion only; (d) Estimate of  $R_n$  for all sky conditions obtained by merging (b) and (c).

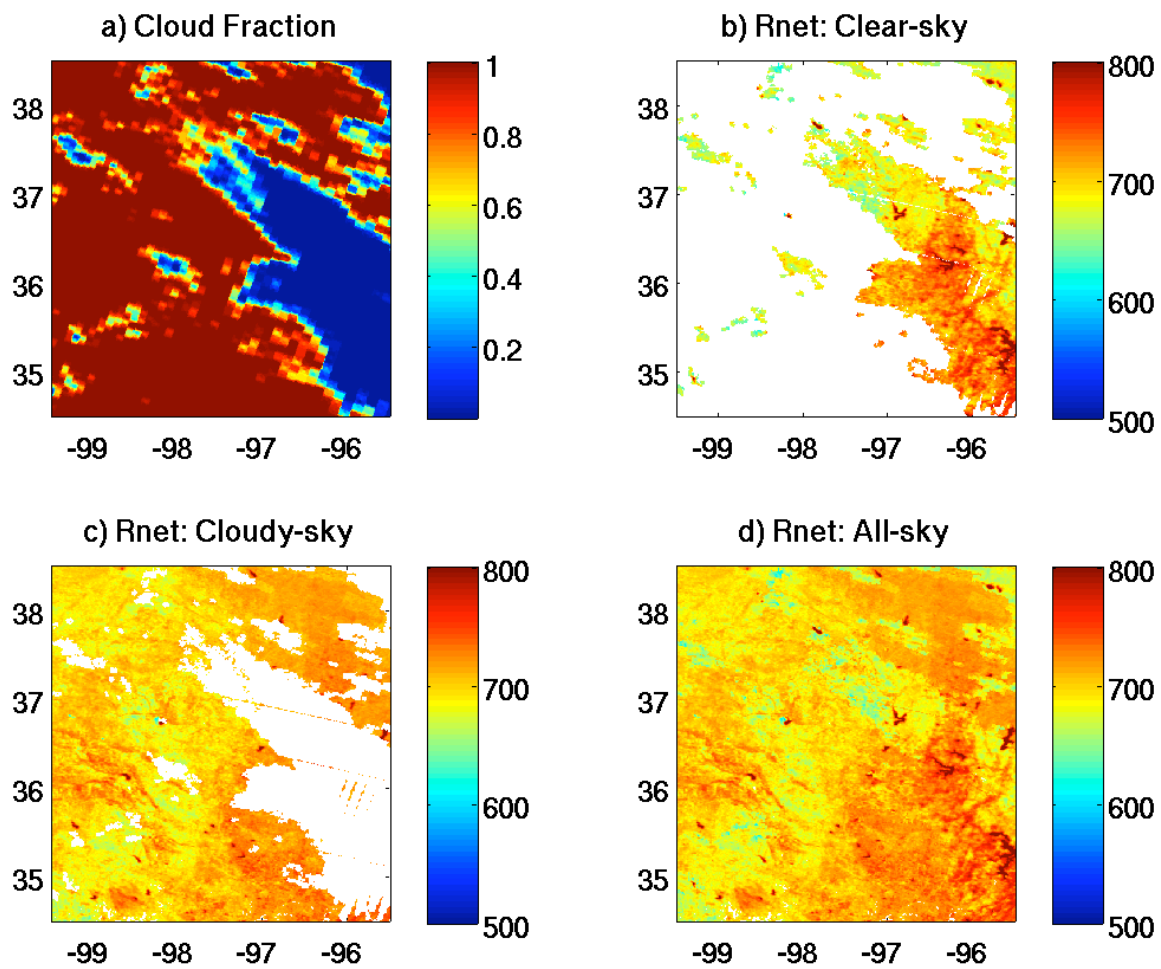


Figure 3-13: Same as Figure 3-12 except for the MODIS-Terra overpass on 6<sup>th</sup> July, 2006 at 17:45UTC.



merged framework to the MODIS-Terra overpass on 24<sup>th</sup> July, 2006, at 17:35 UTC is shown in Figure 3-12. Clouds are present in eastern and south-western part of the SGP and occupy  $\approx 23\%$  the SGP domain. In Figure 3-12(b) and (c), estimates of  $R_n$  are shown for the clear sky and cloudy region of the image. Finally the merged  $R_n$  map is shown in Figure 3-12(d). Similarly, Figure 3-13 demonstrates the application of merged framework to estimate  $R_n$  when  $\approx 71\%$  of the SGP was covered with clouds for the MODIS-Terra overpass on 6<sup>th</sup> July, 2006 at 17:45UTC. The strength of the proposed approach is that it can rely solely on remote sensing data and thus can be applied to globally.

## 3.4 Results: Over the Continental United States

The SURFRAD network provides additional radiation observations at seven locations within the U.S.; while data from MODIS-Aqua is further source of remotely sensed data. Thus, in this section applicability of the proposed methodology is explored while comparing the SRB estimates against SURFRAD and SGP measurements. MODIS data from Aqua and Terra is used for entire 2006, while limiting the analysis to day-overpasses only.

### 3.4.1 Instantaneous surface energy budget

In this section, the results of comparison between estimated instantaneous components of the SRB using the MODIS data (Aqua and Terra) and ground measurements at the SURFRAD and the SGP-ARM sites is presented. The results presented here encompass all the MODIS day overpasses during 2006, except when there was error in the satellite data or ground observations. The scatter plot between the estimated and observed quantities of the SRB are shown in Figure 3-14 - 3-19, while the the summary of bias,  $RMSE$  and  $R^2$  at individual study sites are presented in Table 3.5.

A comparison of results obtained from four other studies, which similarly estimated various components of the SRB using the MODIS data, along with the results obtained in this study are presented in Table 3.6. Tang et al. [2006], Tang and Li [2008] and Wang

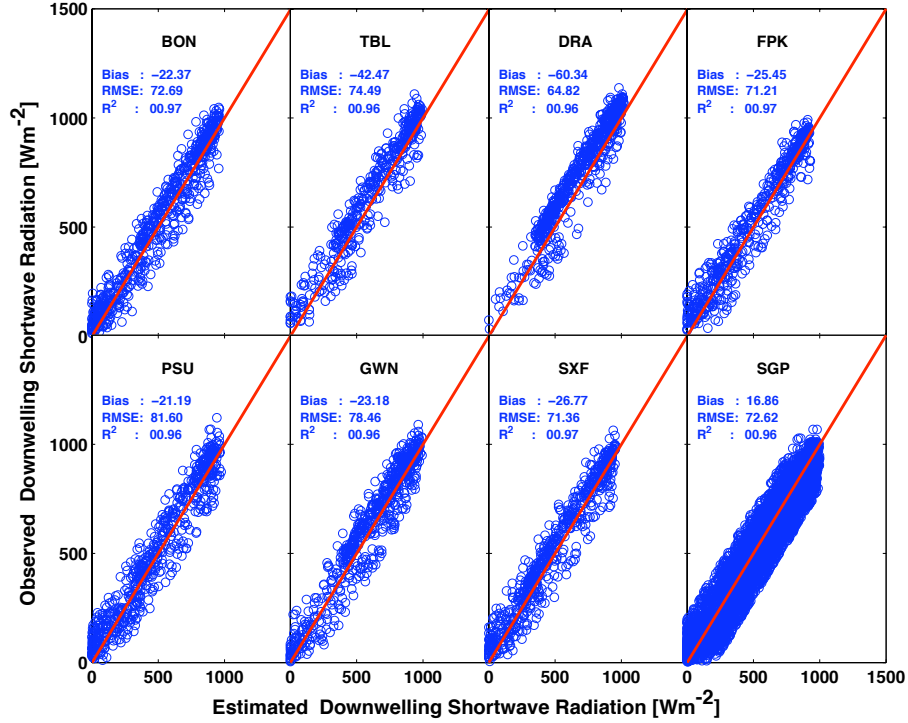


Figure 3-14: Comparison of estimated and observed instantaneous downwelling shortwave radiation at all study sites. Bias is computed as estimated minus observed values.

and Liang [2009] developed a statistical regression analysis between the MODIS TOA radiance/reflectance to estimate components of the SRB; while Kim and Hogue [2008] and the proposed algorithm uses near-surface and cloud data products to estimate the SRB. Tang et al. [2006] and Kim and Hogue [2008] applied their methodology under all sky conditions, while other two studies were limited to clear sky conditions only. Tang and Li [2008] and Wang and Liang [2009] computed longwave radiation; while Tang et al. [2006] produced net shortwave radiation estimates. Kim and Hogue [2008] reported all components of SRB as produced by the proposed algorithm using the proposed methodology, except for instantaneous upwelling shortwave and instantaneous net radiation. The time period, study sites and satellite used to obtain the MODIS data for each study are summarized in Table 3.6.

Errors in instantaneous downwelling shortwave radiation obtained from the proposed methodology range between 8.7%-16.5% of its mean value; while errors in upwelling shortwave radiation were higher, between 15.3%-38.0% across the study-sites. Instantaneous up-

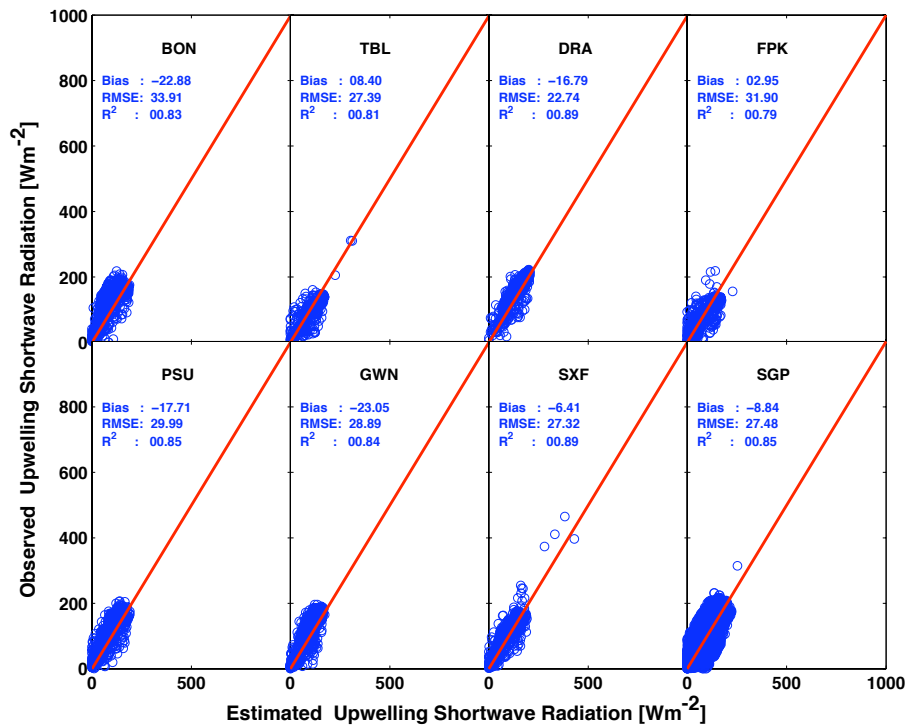


Figure 3-15: Same as Figure 3-14 except for instantaneous upwelling shortwave radiation.

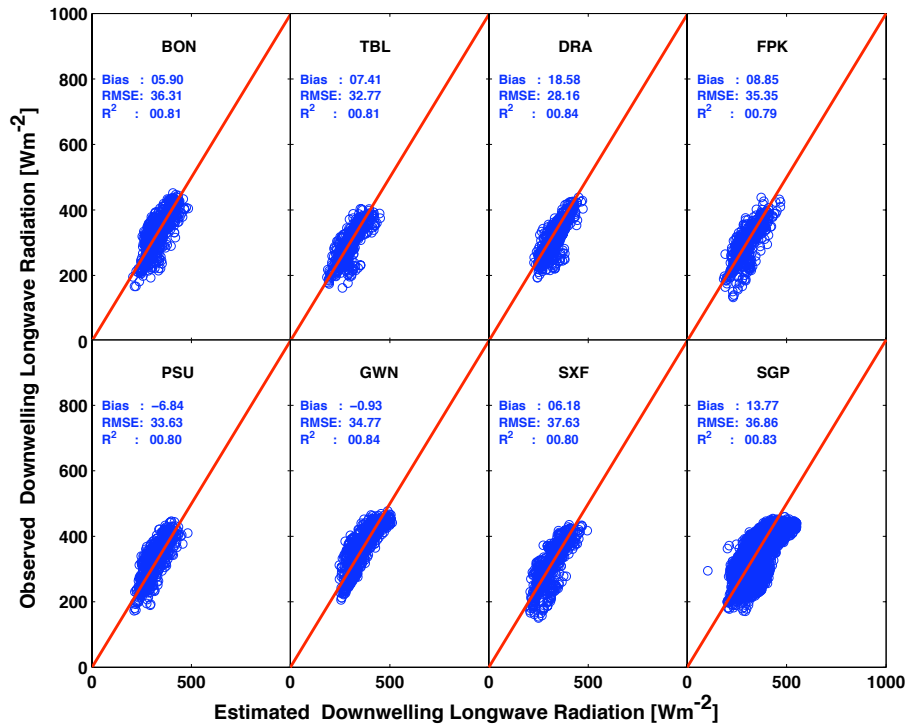


Figure 3-16: Same as Figure 3-14 except for instantaneous downwelling longwave radiation.

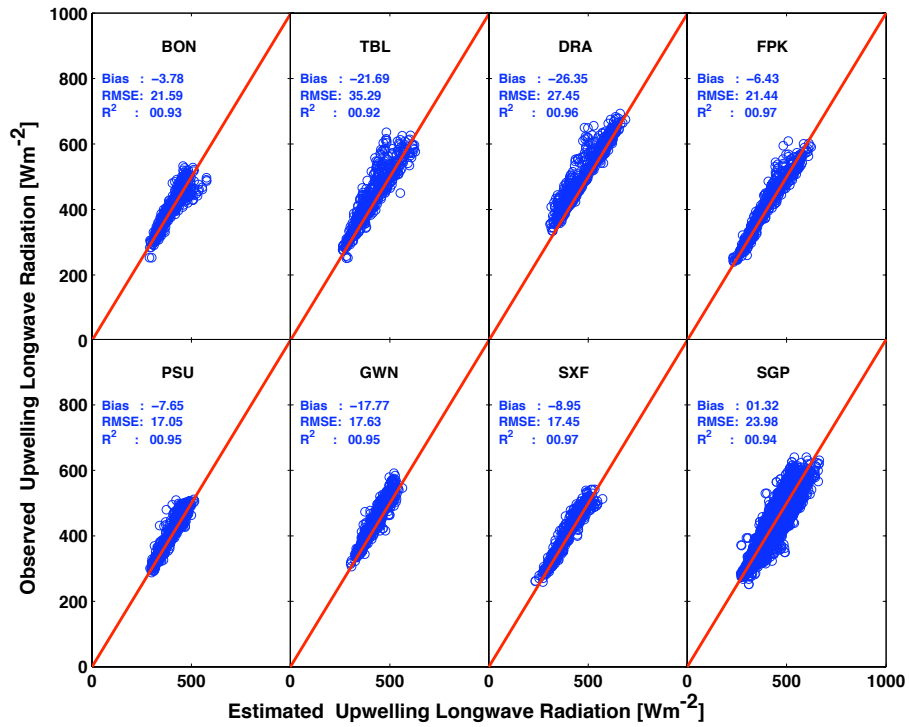


Figure 3-17: Same as Figure 3-14 except for instantaneous upwelling longwave radiation.

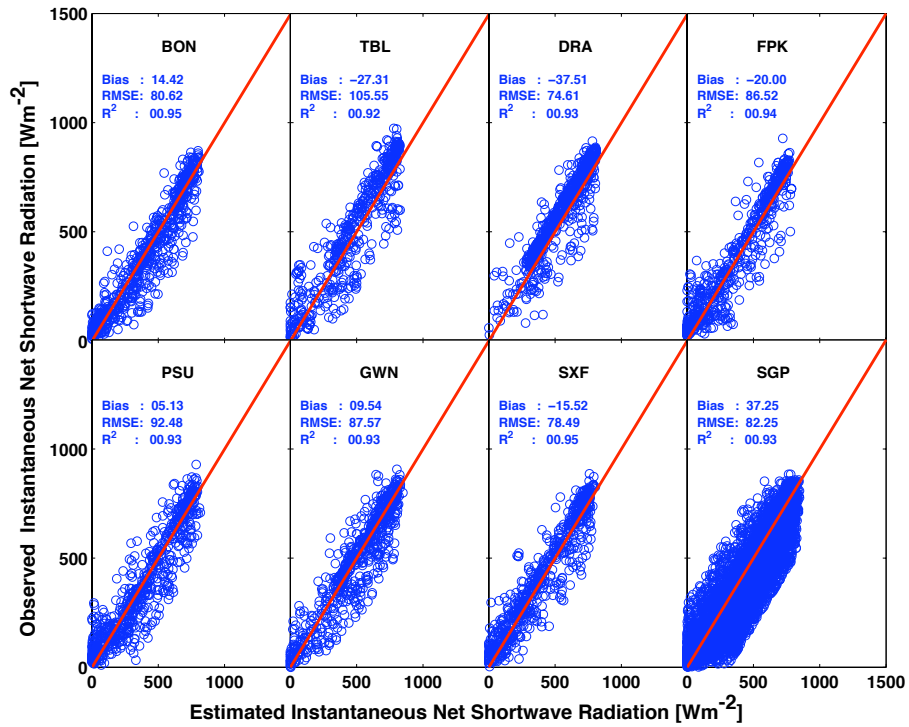


Figure 3-18: Same as Figure 3-14 except for instantaneous net shortwave radiation.

Table 3.5: Bias, Root Mean Square Errors (RMSE), and correlation ( $R^2$ ) for various components of surface radiation budget estimated. Bias is computed as MODIS data minus observed data.

		BON	TBL	DRA	FPK	GWN	PSU	SXF	SGP
Instantaneous $R_S^\downarrow$	Bias [ $Wm^{-2}$ ]	-22.37	-42.47	-60.34	-25.45	-21.19	-23.18	-26.77	16.86
	RMSE [ $Wm^{-2}$ ]	72.69	74.49	64.82	71.21	81.60	78.46	71.36	72.62
	$R^2$ [-]	0.97	0.96	0.96	0.97	0.96	0.96	0.97	0.96
	Mean [ $Wm^{-2}$ ]	519	633	749	504	495	608	505	582
Instantaneous $R_S^\uparrow$	Bias [ $Wm^{-2}$ ]	-22.88	8.40	-16.79	2.95	-17.71	-23.05	-6.41	-8.84
	RMSE [ $Wm^{-2}$ ]	33.91	27.39	22.74	31.90	29.99	28.89	27.32	27.48
	$R^2$ [-]	0.83	0.81	0.89	0.79	0.85	0.084	0.89	0.85
	Mean [ $Wm^{-2}$ ]	106	91	148	83	98	112	99	114
Instantaneous $R_L^\downarrow$	Bias [ $Wm^{-2}$ ]	5.90	7.41	18.58	8.85	-6.84	-0.93	6.18	13.77
	RMSE [ $Wm^{-2}$ ]	36.31	32.77	28.16	35.35	33.63	34.77	37.63	36.86
	$R^2$ [-]	0.81	0.81	0.84	0.79	0.80	0.84	0.80	0.83
	Mean [ $Wm^{-2}$ ]	334	294	308	298	325	362	311	337
Instantaneous $R_L^\uparrow$	Bias [ $Wm^{-2}$ ]	-3.78	021.69	-26.35	-6.43	-7.65	-17.77	-8.95	1.32
	RMSE [ $Wm^{-2}$ ]	21.59	35.29	27.45	21.44	17.05	17.63	17.45	23.98
	$R^2$ [-]	0.93	0.92	0.96	0.97	0.95	0.95	0.97	0.94
	Mean [ $Wm^{-2}$ ]	405	440	502	4000	399	452	396	435
Instantaneous $R_{S,net}$	Bias [ $Wm^{-2}$ ]	14.42	-27.31	37.51	-20.00	5.13	9.54	-15.52	37.25
	RMSE [ $Wm^{-2}$ ]	80.62	105.55	74.61	86.52	92.48	87.57	78.49	82.25
	$R^2$ [-]	0.95	0.92	0.92	0.93	0.94	0.93	0.95	0.93
	Mean [ $Wm^{-2}$ ]	401	501	598	403	389	486	398	453
Instantaneous $R_n$	Bias [ $Wm^{-2}$ ]	25.51	-9.81	-2.26	-0.60	12.41	27.85	3.43	47.59
	RMSE [ $Wm^{-2}$ ]	72.62	82.83	61.10	73.88	72.01	66.76	67.87	69.77
	$R^2$ [-]	0.94	0.90	0.91	0.93	0.94	0.94	0.95	0.93
	Mean [ $Wm^{-2}$ ]	357	397	403	332	355	424	338	374

Table 3.6: Comparison of results obtained from proposed methodology with four published studies. For description about the published studies see Section 3.4.1

	This study	WL	TL	KH	T
Study	7 SURFRAD sites and SGP	6 SURFRAD sites	6 SURFRAD sites	2 SURFRAD and 2 other sites in U.S.	YuCheng site in China
Time-period	2006	2005-06	2000	2001-04	2003
Sky condition	Clear + Cloudy	Clear	Clear	Clear + Cloudy	Clear + Cloudy
Satellites used	Aqua + Terra	Aqua + Terra	Terra	Terra	Terra
INST. $R_S^{\downarrow}$	4.05, $\pm 76.26$ , 0.96			-27.9, $\pm 76.4$ , 0.89*	
INST. $R_S^{\uparrow}$	-9.75, $\pm 28.49$ , 0.84				
INST. $R_L^{\downarrow}$	11.54, $\pm 36.57$ , 0.83	1.63, $\pm 16.89$ , NA	20.3, $\pm 30.1$ , 0.91	25.6, $\pm 38.3$ , 0.88*	
Inst. $R_L^{\uparrow}$	-2.52, $\pm 24.86$ , 0.94			-6.63, $\pm 19.5$ , 0.97*	
INST. $R_{S,net}$	24.76, $\pm 86.37$ , 0.93				11.45, $\pm 23.25$ , NA
INST. $R_n$	37.36, $\pm 72.30$ , 0.93			27.2, $\pm 83.0$ , 0.78*	
DA $R_{S,net}$	15.00, $\pm 52.21$ , 0.94			3.27, $\pm 64.5$ , 0.91**	
DA $R_n$	17.83, $\pm 54.42$ , 0.91			2.4, $\pm 53.8$ , 0.86**	

WL: Wang and Liang [2009]

TL: Tang and Li [2008]

KH: Kim and Hogue [2008]

T: Tang et al. [2006]

INST: Instantaneous estimates

DA: Daily average

NA: Not Available

\*: Under clear-sky conditions

\*\* : Under clear and cloudy conditions

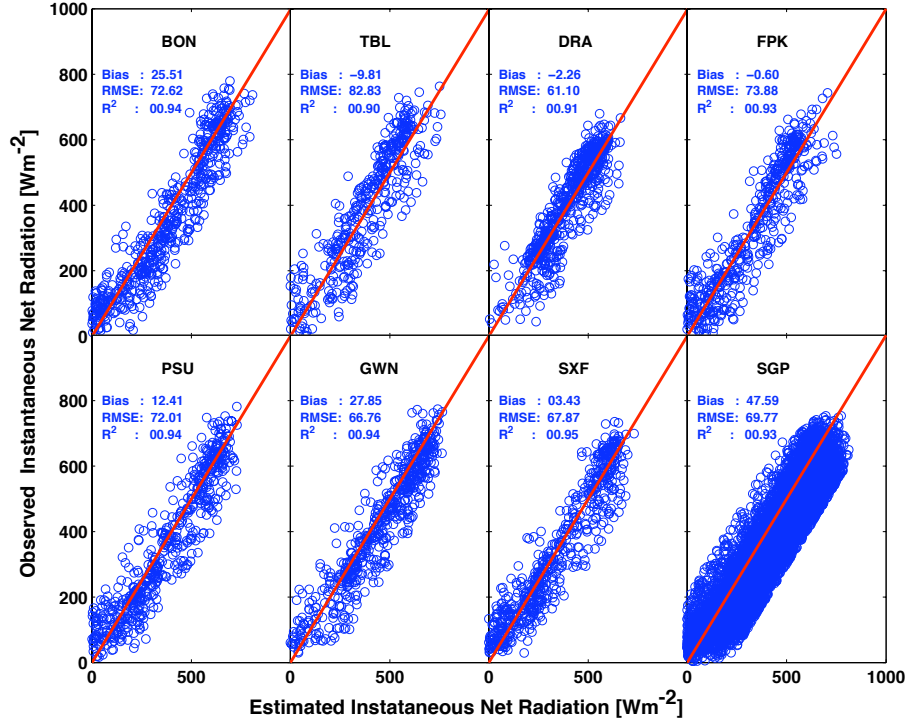


Figure 3-19: Same as Figure 3-14 except for instantaneous net radiation.

welling and downwelling longwave radiation had errors between 9.1%-12.1% and 3.9%-8.0% respectively. Overall errors in instantaneous net shortwave and net radiation ranged between 15.2%-22.2% and 12.7-23.8%, respectively. Among the various components of SRB, instantaneous downwelling shortwave radiation has the largest overall RMSE of 76.26 [Wm<sup>-2</sup>]. Thus, a more accurate retrieval of instantaneous downwelling shortwave radiation will lead to an overall improvement in estimation of instantaneous net radiation.

The RMSE of the various components of instantaneous SRB from the proposed methodology are similar to those obtained from other studies reported in Table 3.6. Tang et al. [2006] converted narrowband reflectance to broadband albedo at the TOA and used statistical regression to estimate net shortwave radiation from the TOA broadband albedo. Results of instantaneous  $R_{S,net}$  obtained by Tang et al. [2006] under all sky conditions show significantly lower RMSE than those from the proposed methodology. This suggest that an approach to estimate  $R_n$  from remotely sensed data could benefit by using hybrid data types: near-surface data products for longwave radiation; and TOA data for shortwave radiation.

### 3.4.2 Daily average net shortwave and net radiation

Daily average net radiation is more useful than instantaneous values for methodologies estimating evapotranspiration from remote sensing data [Nishida et al., 2003, Norman et al., 2003, Batra et al., 2006, Venturini et al., 2008]. A sinusoidal model was used to estimate both the daily average net shortwave and net radiation. The sinusoidal model used information about local sunrise and sunset times. The daily averages radiation quantities are obtained from both Aqua and Terra satellites; and the mean of the two estimates is used in comparison against the ground measurements. The scatter plots between the estimated and measured daily average  $R_{S,net}^{avg}$  and  $R_n^{avg}$  for all study sites are shown in Figure 3-20 and 3-21, respectively. The statistical summary of the daily average radiation quantities at the various locations is given in Table 3.7; while an overall comparison with other studies is presented in Table 3.6. The daily average of net shortwave and net radiation have better agreement than the instantaneous estimates and are comparable with those obtained by Kim and Hogue [2008].

An example of the estimated net radiation values from the Terra and Aqua satellite is shown in Figure 3-22 (a) and (b) at Bondville, IL site from 10-15 April, 2006. Ground observation is shown with a solid line; while instantaneous estimates of net radiation from the Terra and Aqua are shown as circles and triangles, respectively. The sinusoidal model fitted to the retrieved instantaneous  $R_n$  values is shown with a dashed line. The instantaneous estimates agree well with the ground observations. The sinusoidal model is able to capture the diurnal variation of the net radiation during clear sky days (i.e 4/11, 4/12 and 4/14). For the two cloudy days, especially for 4/14, the diurnal cycle of net radiation is not well captured with the sinusoidal model, even though the instantaneous values from both satellites agree well. This highlights the limitation of using polar-orbiting satellites only to retrieve the diurnal cycle of  $R_n$ . Recently, Formann and Margulis [2009] presented a methodology to estimate the diurnal cycle of downwelling radiation (longwave and shortwave) from satellite data by combining data from geostationary and polar-orbiting satellites. A limitation of the Formann and Margulis [2009] methodology to be applicable globally is its reliance of



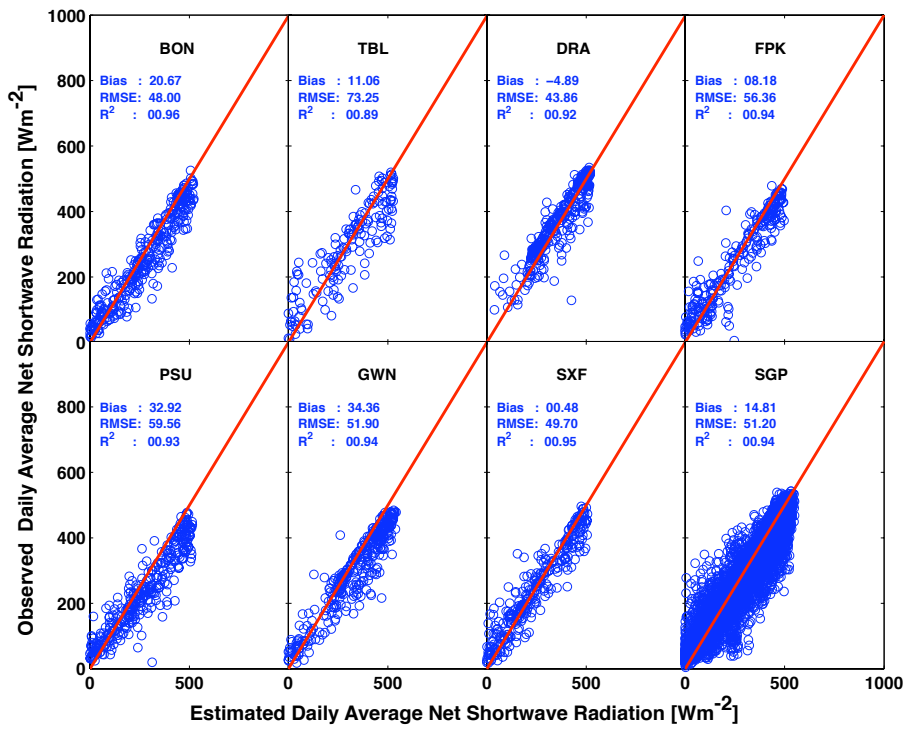


Figure 3-20: Same as Figure 3-14 except for daily average net shortwave radiation.

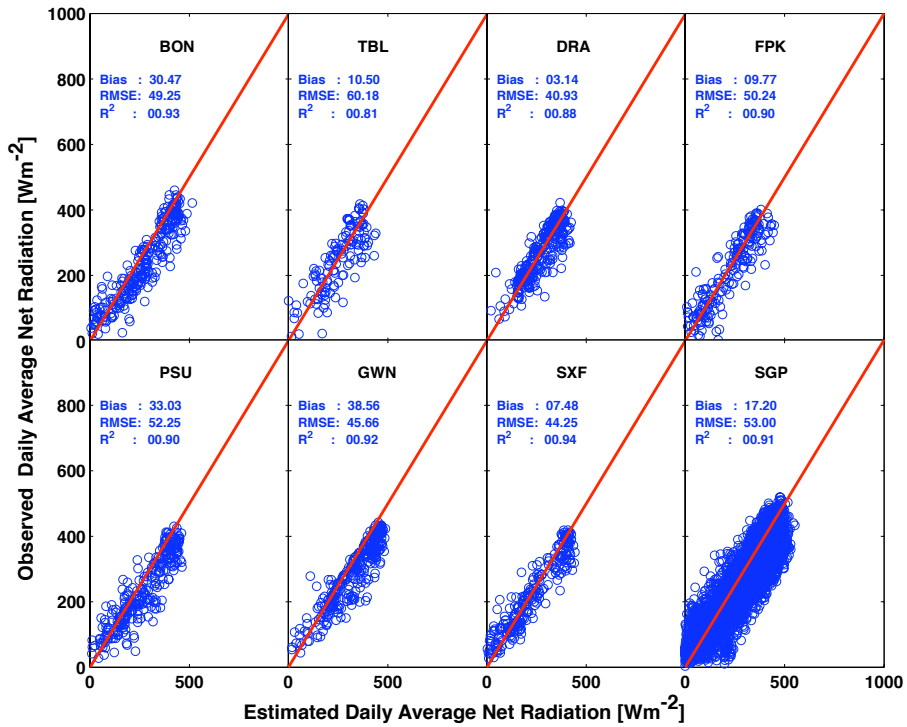


Figure 3-21: Same as Figure 3-14 except for daily average net radiation.

Table 3.7: Bias, Root Mean Square Errors (RMSE), and correlation ( $R^2$ ) for various components of surface radiation budget estimated. Bias is computed as MODIS data minus observed data.

	BON	TBL	DRA	FPK	GWN	PSU	SXF	SGP	
Daily-average $R_{S,net}$	Bias [ $Wm^{-2}$ ]	20.67	11.06	-4.89	8.18	32.92	34.36	0.48	14.81
	RMSE [ $Wm^{-2}$ ]	48.00	73.25	43.86	56.36	59.56	51.90	49.70	51.20
	$R^2$ [-]	0.96	0.89	0.92	0.94	0.93	0.94	0.95	0.94
	Mean [ $Wm^{-2}$ ]	257	289	374	244	232	302	245	315
Daily-average $R_n$	Bias [ $Wm^{-2}$ ]	30.47	10.50	3.14	9.77	33.03	38.56	7.48	17.20
	RMSE [ $Wm^{-2}$ ]	49.25	60.18	40.93	50.24	52.25	45.66	44.25	53.0
	$R^2$ [-]	0.93	0.81	0.88	0.90	0.90	0.92	0.94	0.91
	Mean [ $Wm^{-2}$ ]	242	246	277	220	234	287	223	272

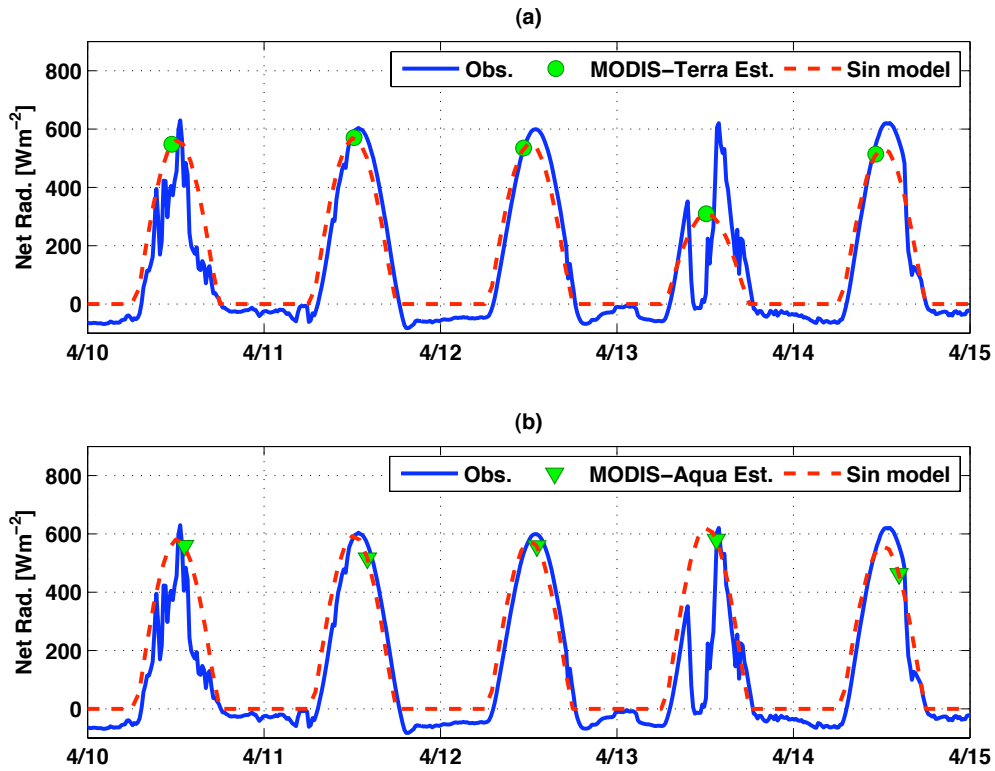


Figure 3-22: Time series of net radiation at Bondville, IL from 10-15 April, 2006. Instantaneous net radiation estimates, along with the sinusoidal model fitted through those estimates, are shown for the Terra and Aqua overpasses in (a) and (b), respectively.

a climatological lookup table derived from a regional climate model over the study site. Nonetheless, it presents a way to use satellite data from different platforms and can serve as a guidance to extend the proposed methodology, that relies solely on satellite data, to retrieve the diurnal cycle of net radiation.

### **3.4.3 Net shortwave and net radiation over CONUS**

A data analysis study of the measurements at SURFRAD and ARM sites from 1995-2007, showed an occurrence of widespread decadal brightening of shortwave over the CONUS [Long et al., 2009]. One of the advantages of the proposed methodology is that it can be potentially used to detect spatial patterns of such a shortwave brightening over the CONUS. The proposed methodology was applied to produce daily maps of net shortwave and net radiation daily from both the Aqua and Terra satellites. All the MODIS data products (listed in Table 3.2) are Level-2 swaths, except surface albedo, which is a tiled Level-3 product. The MODIS tiles are  $10^0 \times 10^0$  at the equator and 14 of them cover the CONUS domain. Each swath overpass data was reprojected onto the tiles and then the SRB estimates were computed. As mentioned in Section 3.1.4, two adaptations allow estimation of the SRB feasible over the CONUS. The first adaptation of the algorithm (see Section 3.1.4) reduces the computational cost of estimating temperature offsets at 1 km spatial resolution for the entire CONUS domain by splitting the CONUS in  $5^0 \times 5^0$  sub-domains. Temperature offsets computed at the aggregated sub-domain scale and then applied to all 1-km MODIS pixels that lie within the sub-domain. It is acknowledged that this level of aggregation could introduce errors because of difference in land cover type. An alternate approach could involve computing separate temperature offsets for the various vegetation types present within the  $5^0 \times 5^0$  sub-domain. Information regarding the vegetation types can be obtained from the MODIS Land Cover Type product (MCD12Q1), a combined Aqua and Terra product, produced yearly. The second adaptation to the proposed methodology involved filling the missing surface albedo values in the MCD43B3 data product. During the entire 2006, the minimum coverage of surface albedo product was 80% the CONUS domain; and more than 85% of

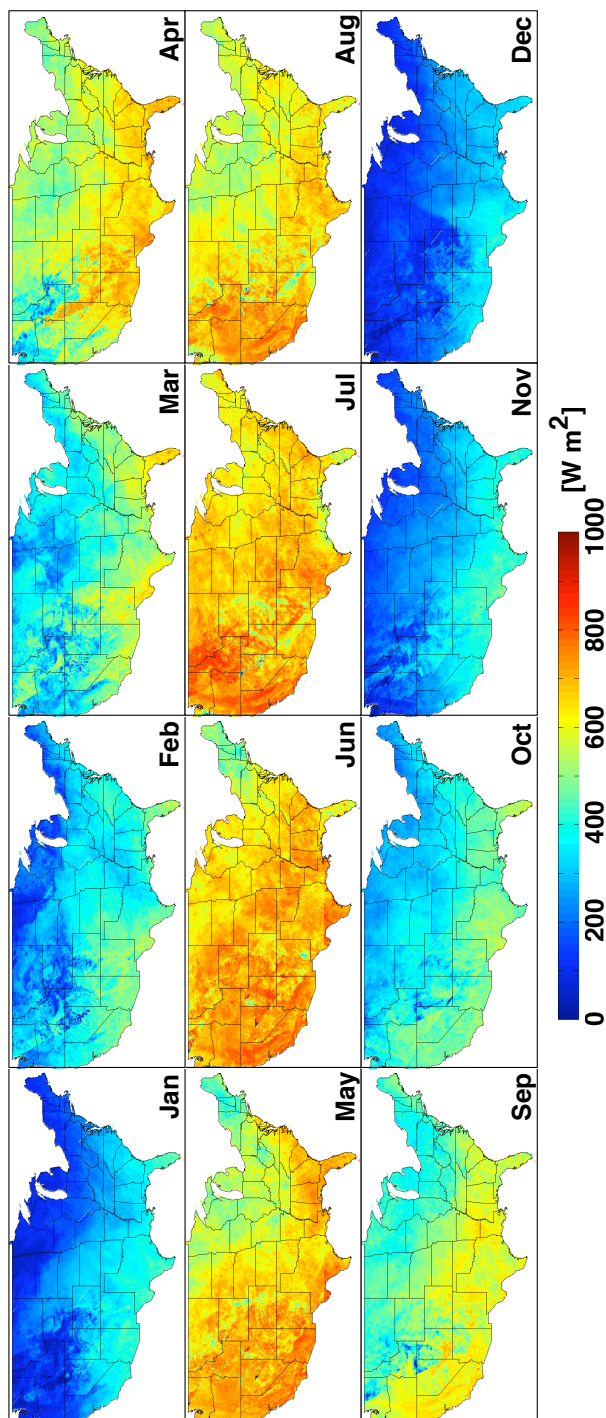


Figure 3-23: Monthly estimated net shortwave radiation maps for the CONUS.

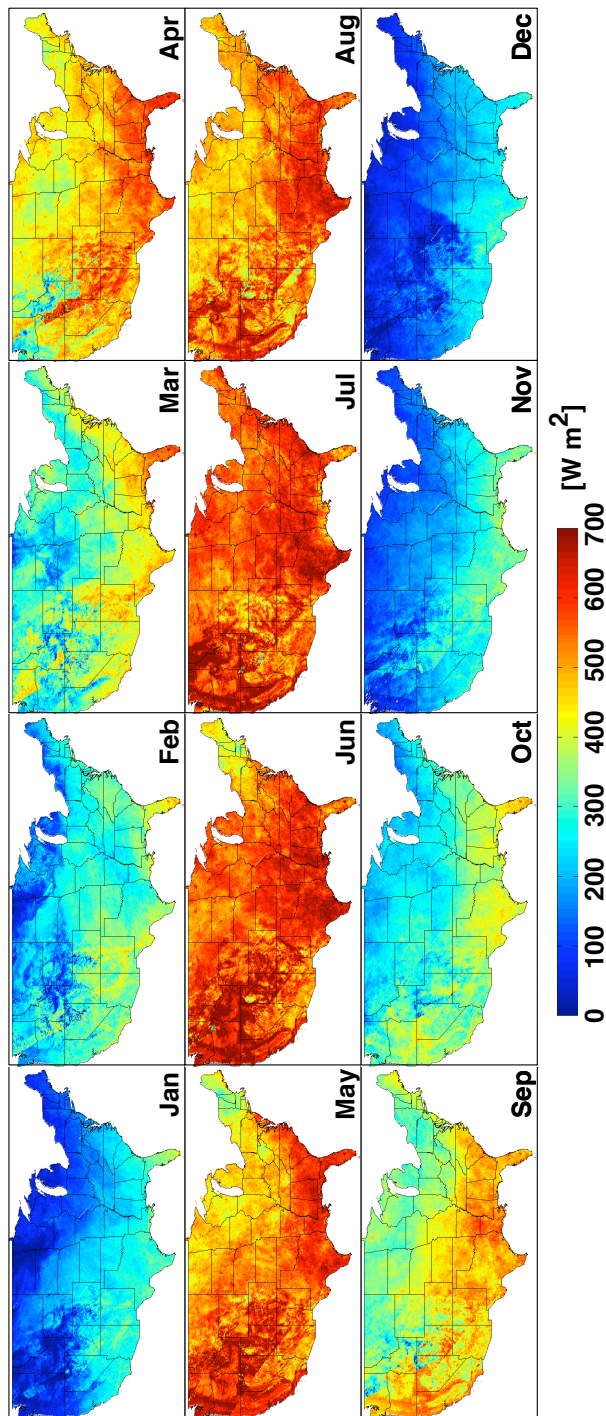


Figure 3-24: Same as Figure 3-23 except for net radiation.

the CONUS had valid surface albedo for 95% of the year. Daily average  $R_{S,net}^{avg}$  and  $R_n^{avg}$  are used to produce monthly maps as shown in Figure 3-23 and 3-24.

### 3.5 Conclusion

The MODIS sensor on the Aqua and Terra satellites provides various data products about the Earth's land surface, atmosphere, cryosphere and ocean. The MODIS data products have large spatial footprint as compared to sparse ground-observations. The surface energy budget plays a significant role in land-atmosphere interactions, thus numerous studies have attempted to estimate the surface energy budget or its components from the MODIS data. Such attempts until now have been mostly limited to cloud-free days and thus a large share of the MODIS overpasses are discarded. The proposed  $R_n$  estimation methodology overcomes the restriction of cloud-free condition to estimate net radiation using the MODIS-Terra data. The MODIS cloud product is employed to provide information about cloud top temperature, cloud fraction, cloud emissivity, cloud optical thickness and land surface temperature for cloud covered regions within a MODIS overpass. A statistical regression, using ancillary ground measurements, is applied to 5-km MOD06\_L2-LST in order to obtain near-surface air and dew temperatures. In absence of ancillary ground measurements, a similar statistical regression can be obtained by using the MOD07\_L2 product, thus presenting a framework that can exclusively utilize remote sensing information. The MODIS geolocation and surface albedo data products are used under both sky conditions. Downwelling shortwave radiation is obtained as a linear combination of cloud-free and cloudy radiation weighted by cloud fraction following the approach of Slingo [1989]. The estimate of downwelling longwave radiation has a component dependent on near-surface conditions along with an influence of clouds as suggested by Formann and Margulis [2009]. Upwelling shortwave and longwave radiation uses land surface albedo data and 5-km MOD06\_L2-LST data.

In order to appraise how well the estimates of  $R_n$  from the MOD06\_L2 perform, the methodology is first applied over the SGP for 2006, as presented in Section 3.3. The  $R_n$  estimates from this study are shown to be comparable to other existing methodologies, while

apparently having an advantage of being applicable to cloudy days. Finally, a framework of to estimate  $R_n$  from the MODIS under all sky conditions is proposed by merging the higher resolution methodology (1-km) outlined by Bisht et al. [2005] for clear sky pixels of the overpass and the present low resolution methodology (5-km) for cloudy pixels. Two applications of the proposed methodology are demonstrated for the MODIS-Terra overpass on 6<sup>th</sup> July, 2006 and 24<sup>th</sup> July, 2006 that had 71% and 23% cloud cover for the SGP respectively.

Section 3.4 explored the global applicability of the proposed methodology in estimating instantaneous SRB components, along with daily net shortwave and net radiation. The study site comprises of seven sites of SURFRAD network and twenty one stations within the SGP for all seasons of 2006 using data from the Aqua and Terra satellites. The results at the various study sites and a comparison with similarly published approaches is presented. Instantaneous downwelling shortwave radiation has the largest RMSE. Overall, the proposed methodology is successfully able to estimate SRB at different study sites. Adaptation related to estimation of temperature offsets and missing surface albedo values is incorporated in the proposed methodology, to produce daily SRB estimates over the CONUS. A simple spatio-temporal approach was used to produced gap-free surface albedo product. Finally, monthly average net shortwave and net radiation over the CONUS are presented.

In summary, the applicability of the proposed methodology to retrieve instantaneous and daily average components of the SRB over the CONUS had been demonstrated. The proposed methodology relies only on remotely sensed data and is applicable under all sky conditions. Future research efforts would be aimed at enhancing the accuracy and usefulness of the present methodology.



## Part II

# Role of topography and vegetation dynamics in seasonal to inter-annual hydro-climatology



## CHAPTER 4

# LITERATURE REVIEW AND SCOPE OF RESEARCH

The land and atmosphere are fundamentally coupled. The source of this coupling lies in the exchange of heat, momentum and water at the boundary, which are affected by land characteristics such as soils, vegetation and topography. In the second part of this thesis, we focus on the effects of vegetation dynamics and topography on hydro-climatology over large river basins. We begin this chapter by studying soil moisture in the context of global hydrological cycle. The role of soil moisture in feedbacks to the climate system through rainfall; and the importance of vegetation and topography in determining the evolution soil moisture is presented. The crucial role played by high performance computing in Earth systems modeling is briefly covered. A historical overview regarding the treatment of land surface processes within climate and distributed hydrologic models is presented next. Finally, the chapter concludes with an outline of the research for this part of thesis work.

### 4.1 Motivation

The Earth's atmosphere and terrestrial ecosystem interact with each other in a nonlinear way through the exchange of energy, water, momentum and carbon flux by physical and biological processes. The feedbacks between the ecosystem and climate occur at varying timescales, ranging from seconds to millions of years [Sellers et al., 1995]. Understanding

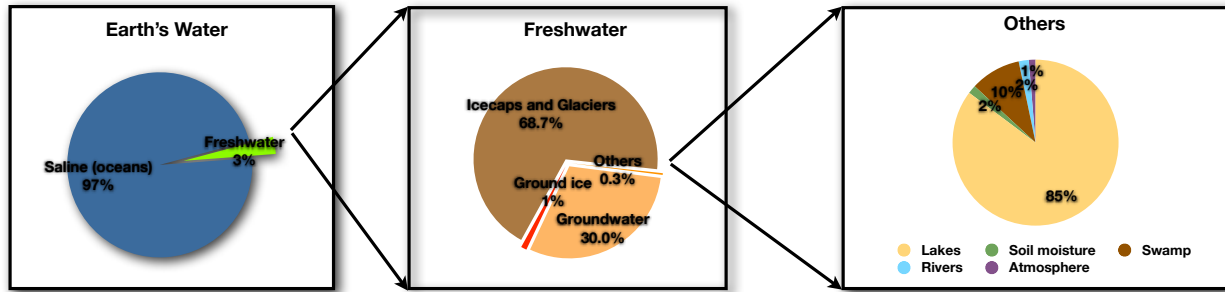


Figure 4-1: Estimates of the global water resources

and quantification of feedbacks between the atmospheric boundary layer and the land surface are critical to the study of land surface processes. Several studies have demonstrated the importance of land-atmosphere interactions in both long-term climate simulations, as well as, short-term weather forecasting applications [Eltahir, 1996, Wang and Eltahir, 2000, Dickinson, 2000, Pielke, 2001]. The role of the land surface, after sea surface temperature, as a key component in enhancing seasonal climate prediction has been recognized in the recent years [Dirmeyer, 2006]. Among the various land surface states (soil moisture, temperature, snow-depth and presence/absence of vegetation), soil moisture has been identified as potentially the most crucial [Dirmeyer, 1995]. The strength of the soil moisture coupling to precipitation has been suggested, by numerical modeling studies to be weakest near the ocean and equator; and highest in interior semiarid regions [Koster et al., 2004a]. Before embarking on a discussion about the role of soil moisture on various feedback pathways for land-atmosphere coupling, it is beneficial to study soil moisture within the context of the global hydrological cycle.

#### 4.1.1 The global hydrologic cycle

Water is a naturally circulating resource and is essential for all living organisms, including humans. The majority of the water on Earth is in the oceans (97%) and is not fit for human consumption. The Fourth Assessment Report (AR4) by the Intergovernmental Panel on Climate Change (IPCC) concluded that *all regions of the world show an overall net negative*

Table 4.1: Storage volume (absolute and percentage) and residence time of the various components of the global hydrologic cycle (Obtained from [Oki and Kanae, 2006] and [Shiklomanov, 1999]).

Reservoir	Estimate Volume [10 <sup>3</sup> km <sup>3</sup> ]	Percentage volume [%]	Residence time
<hr/>			
Saltwater			
Oceans	1,338,000	96.5376	4,000 years
Freshwater			
Glaciers, snow and Permafrost	24,364	1.7579	1,000-10,000 years
Groundwater	23,400	1.6883	100-10,000 years
Lakes	175	0.0126	10 years
Soil moisture	17	0.0012	2 weeks to 1 year
Atmosphere	13	0.0009	1.5 weeks
Rivers and Streams	2	0.0001	2 to 6 months
<hr/>			
Total	1,385,971		

*impact of climate change on water resources and freshwater ecosystems.* Thus, ensuring adequate supplies of freshwater are available in the future is a critical task. Based on the synthesis from various sources [Korzun, 1978, Church, 1996, Shiklomanov, 1997, Oki, 2005, Oki and Kanae, 2006], the estimated global water resources are schematically shown in Figure 4-1, while the breakdown of volume and residence time for each storage reservoir within the global hydrologic cycle is summarized in Table 4.1. The largest portion of the freshwater is stored in glaciers and snow cover ( $\approx 69\%$ ); while groundwater is the second largest source of freshwater. Soil moisture accounts for only one-thousandth of one percent of the global water budget and it has about 25% more water than in the global atmosphere (see Table 4.1). Oki and Kanae [2006] suggested that instead of focusing on the amount of water stored within various reservoirs, one should concentrate on the fluxes in and out of individual reservoirs (as shown with arrows in Figure 4-2). The residence time, which is the average time a water molecule spends in a given reservoir, is estimated by dividing the volume of the reservoir by the mean flux into and out of it. Residence time is on the order of 100 to 10,000 years for groundwater and oceans; while it is about 9 days for water in the atmosphere and ranges from 2 weeks to 1 year for soil moisture (see Table 4.1). It is the

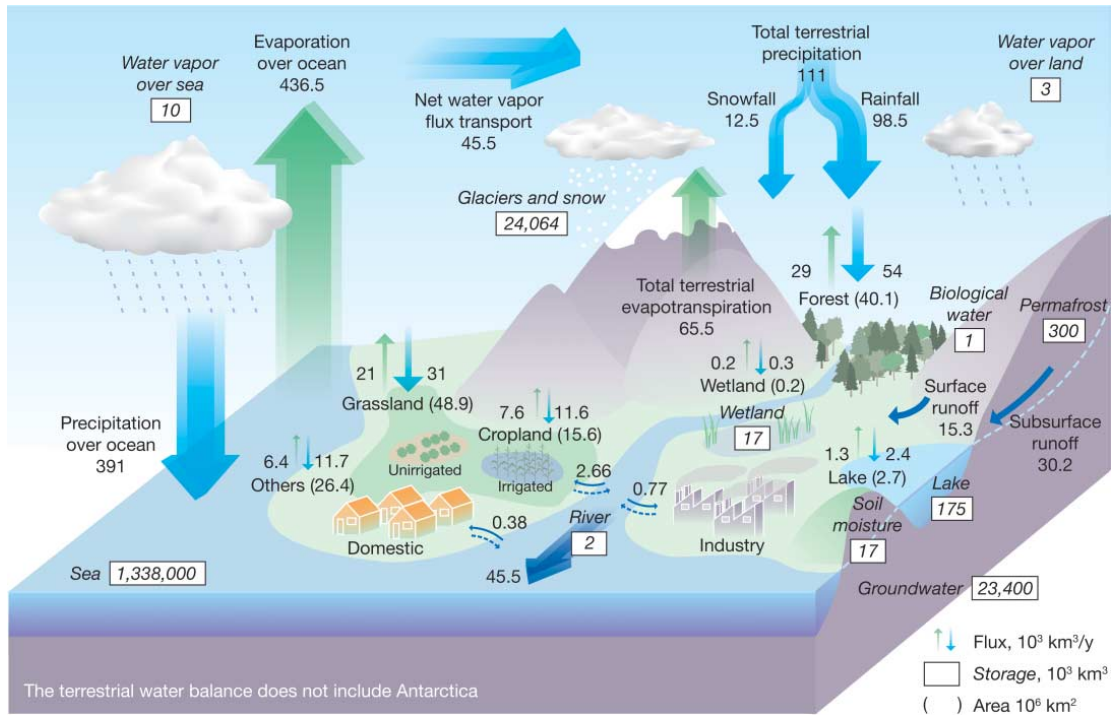


Figure 4-2: Schematic representation of global hydrologic cycle showing fluxes and storages of water (From [Oki and Kanae, 2006]).

more dynamic nature of atmospheric water vapor, leading to precipitation, which impacts evolution of soil moisture at the land surface.

The global hydrologic cycle is connected with the global radiation cycle, which is shown in Figure 4-3. Evaporation from water bodies (rivers, lakes and oceans) and terrestrial evapotranspiration (from bare soil and vegetation) replenishes water in the atmosphere, which gets depleted by condensation processes in the form of rain and snow. The state change of water from liquid to vapor, through the process of evapotranspiration, requires an input of energy (latent heat); while condensation and sublimation processes in the atmosphere release energy. Thus, the global hydrologic and energy cycles are intertwined together. Incoming solar radiation reaching the surface is the main driver of the hydrologic cycle and is converted into latent ( $\lambda E$ ), sensible ( $H$ ) and ground ( $G$ ) heat flux at the land surface (see Figure 4-3). Three factors that control the amount of latent heat flux at the land surface include: (1) the

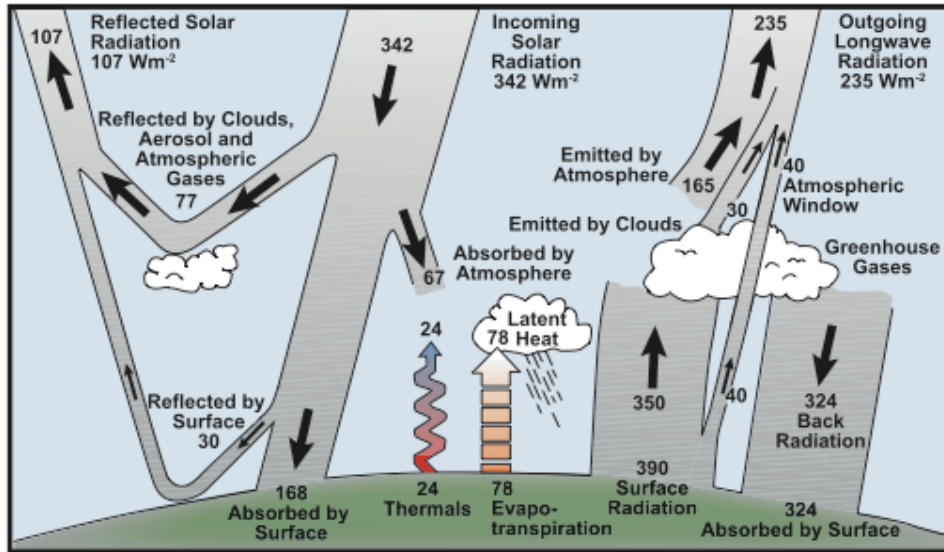


Figure 4-3: Estimate of the Earth's annual and global mean energy balance (From [Treat et al., 2007])

availability of energy, (2) the availability of water, and (3) transport mechanism to remove the moist air. It is via the availability of water that soil moisture directly exerts control on the amount of  $\lambda E$ , thereby affecting the partitioning of energy at the land surface. The energy partition at the land surface, serves as a forcing at the bottom boundary of the atmospheric column and depending on atmospheric conditions, can eventually lead to precipitation.

#### 4.1.2 Soil moisture-rainfall feedback

The feedback mechanisms between soil moisture and rainfall has been of a point of interest for numerous studies related to land-atmosphere interactions. The hypothesis that soil moisture could sustain month-to-month persistence in climatic anomalies was proposed by Namias [1952]. Several simple water balance models have demonstrated positive soil moisture-rainfall feedbacks on the basis of precipitation recycling [Eltahir, 1989, Rodriguez-Iturbe et al., 1991, Eltahir and Bras, 1994, Savenije, 1995]. Entekhabi et al. [1996] proposed theoretical feedback pathways between soil moisture and atmospheric phenomenon on multiple space and time

scales. Net radiation, surface heat fluxes ( $\lambda E$  and  $H$ ) and convective potential energy were identified as mechanisms through which soil moisture and rainfall interacted. Brubaker and Entekhabi [1995a,b, 1996] using a nonlinear stochastic model of the land-atmosphere boundary, concluded that soil moisture and temperature anomalies could be self-reinforcing causing persistence of hydrologic conditions.

Findell and Eltahir [1997] analyzed 14 years soil moisture and provided observational evidence of low, but statistically significant positive correlation between average soil moisture saturation and subsequent summer rainfall over Illinois, USA. Eltahir [1998] proposed a hypothesis about positive feedback between soil moisture and precipitation. Wetter soil moisture conditions, decreased both surface albedo and bowen ratio (the ratio of  $H$  to  $\lambda E$ ). This leads to a decrease in surface temperature, an increase in atmospheric water vapor, an increase in net radiation at the surface, a decrease in depth of planetary boundary layer (PBL), which eventually results in an increase in moist static energy in the PBL leading to more rainfall. Findell and Eltahir [1999] presented a followup analysis of their earlier work [Findell and Eltahir, 1997] to gain further understanding of the physical processes associated with the feedback mechanism. The average soil moisture and near-surface meteorological conditions did not exhibit the expected correlation as suggested by theory; though available surface moisture conditions strongly impacted wet-bulb depression of near-surface air during mid-May to end of August.

Numerical modeling approaches, in lieu of limited data, have been an alternative tool to explore linkages between soil moisture and precipitation using climate models at global [Shukla and Minz, 1982, Rind, 1982, Oglesby et al., 2002] and regional spatial scales [Seth and Giorgi, 1998, Lu et al., 2001, Pal and Eltahir, 2001]. The strength of the soil moisture-precipitation feedback varies geographically. Koster and Suarez [2001] documented significant soil moisture persistence over regions including central United States was by analyzing the lagged autocorrelation of soil moisture over the globe based on results from the National Aeronautics and Space Administration (NASA) Seasonal-to-Interannual Precipitation Project. Entin et al. [2000] used in-situ soil moisture observations from the United States



(in Illinois and Iowa), Russia, Mongolia and China, to evaluate the observed temporal and spatial scales of soil moisture variations. Their results showed persistence in the top 1-m soil moisture is approximately 2 months. Betts [2004] found the strong evaporation-precipitation feedback during the summer over the continents of the Northern Hemisphere in the ERA40-model. This is supported by Koster et al. [2004a, 2006], who identified different regions on the continent that exhibited a strong coupling between soil moisture and precipitation. Numerical modeling studies have also shown that the persistence in soil moisture transforms into persistence in droughts as well as floods [Bonan and Stillwell-Soller, 1998]. Various studies have focused on the role of soil moisture in the 1988 summer drought [Oglesby and Erickson III, 1989, Oglesby, 1991, Sud et al., 2003] and the 1993 summer flood [Bosilovich and Sun, 1999, Paegle et al., 1996] in the United States.

Soil moisture initialization within climate models has been shown to significantly affect their forecasts and a proper initialization can potentially improve precipitation predictability [Mahfouf, 1991, Beljaars et al., 1996, Schär et al., 1999, Koster et al., 2004b, Mo et al., 2006, Aligo et al., 2007, Vivoni et al., 2009]. The spatial structure of initial soil moisture has also been shown to impact precipitation patterns at the regional scales [Avisar and Liu, 1996, Georgescu et al., 2003, Weaver, 2004, Taylor et al., 2007, Kim and Wang, 2007]. The physical parameterization related to convection has been shown to influence simulated rainfall [Xu and Small, 2002, Gochis et al., 2002, 2003, Ratnam and Kumar, 2005]. Findell and Eltahir [2003a,b] investigated the interaction between soil moisture and the boundary layer and showed that the variability of soil moisture conditions over large regions has a direct influence on important processes associated with rainfall in the boundary layer. Thus, numerous studies have suggested coupling of soil moisture and precipitation.

### **4.1.3 Bidirectional feedbacks between soil moisture and vegetation in the presence of topography**

The evolution of soil moisture at the land surface during inter-storm periods is dependent on surface characteristics such as vegetation and topography. Vegetation, as well as its dynam-

ics, plays a fundamental role in the energy and water balance, by altering surface roughness, albedo, soil aggregation and macroporosity, and intercepting rainfall. Vegetation adaptively evolves and responds to seasonal and inter-annual cycles of radiative forcing and water redistribution. The impacts of deforestation in tropics on large-scale atmospheric circulation has been documented by a number of numerical studies [Dickinson and Henderson-Sellers, 1988, Eltahir and Bras, 1993, Eltahir, 1996, Dickinson, 2000]. Wang and Eltahir [2000] demonstrated that biosphere-atmosphere system in West Africa has multiple equilibrium states with respect to vegetation perturbations. At spatial scales smaller than those used in climatological studies, vegetation-hydrology interactions are crucial [Rodriguez-Iturbe et al., 2001]. Eagleson [1978] was the first to study the complex dynamics of vegetation-hydrology in a water-limited system under stochastic climate forcing at a point-scale. Using an ecological optimality theory of water-limited systems, Eagleson [1982] argued that such systems can reach equilibrium state at shorter timescales by minimizing water demand stress. Protopapas and Bras [1987] developed a point model of a plant physiology to investigate conditions for optimal plant growth, while accounting for moisture and soil salinity. In a series of papers by Rodriguez-Iturbe et al. [2001], Laio et al. [2001b,a], Porporato et al. [2001], the probabilistic structure of steady-state soil moisture and water balance was explored by linking soil moisture deficit to vegetation water stress at point scale.

Topography also exerts control on the hydrological processes, like soil moisture redistribution, runoff response and incoming radiation, [Western and Grayson, 2000]. Capturing this control within a land surface hydrologic models is central to accurate prediction of catchment response [Beven and Kirkby, 1979, Wood et al., 1990, 1997]. The topographic data is readily available at high-resolution (30m or less), yet progress in incorporating the effect of topography explicitly in a regional climate model (RCM) has been slow. Additionally topography influences the organization of plant species and functional types [Florinsky and Kuryakova, 1996, Hack and Goodlett, 1960] and plants in turn dynamically modulate the spatial variability of soil moisture by preferentially uptaking water from different depths. Ivanov et al. [2008b] presented a quantitative evidence of the interactions between vegeta-

tion and topography occurring at basin scale in New Mexico through a local mechanism of radiation and soil moisture redistribution, using a fully distributed hydrology and dynamic vegetation model.

#### **4.1.4 The role of high performance computing in Earth system models**

Spatial variability of soils, topography and vegetation at sub-meter spatial scales are significant in determining the response of watershed states (soil moisture) and fluxes (runoff, evapotranspiration); but their explicit accounting within the land surface models in regional climate model is computationally expensive. Thus, numerous simplifications are made regarding the physical processes while applying these models. Also, challenging the computation capabilities is the large amount of readily available remote sensing data that can be assimilated to constrain and improve predictive capabilities of regional climate models. Use of RCMs with an operational framework involves additional computational cost, since these models are required to produce an ensemble of model simulations rather than a single simulation. Recently, high performance computing (HPC) has become ubiquitous tool for conducting simulations across wide-range of scientific disciplines. IBM's Roadrunner machine of the Los Alamos National Laboratory became the first ever computer to cross the petaflop/s ( $10^{15}$  floating point operations per second) barrier in June 2008, while the Oak Ridge National Laboratory's Jaguar supercomputer is presently rated as fastest in the world for open science as of Nov., 2009. A report by a committee of scientists clearly identified hydrologic models as of the scientific frontiers that would benefit from large computing systems, [UCAR/JOSS 2005]:

*“High-performance computing and petascale machines provide an opportunity to enhance spatial and temporal resolutions in hydrologic models that operate in a stand-alone mode or are coupled with atmospheric codes to address the societal-relevant questions that have been posed.”*

Washington et al. [2008] presented a report reviewing research challenges and opportunities for climate change science, and made recommendations about the role of computing

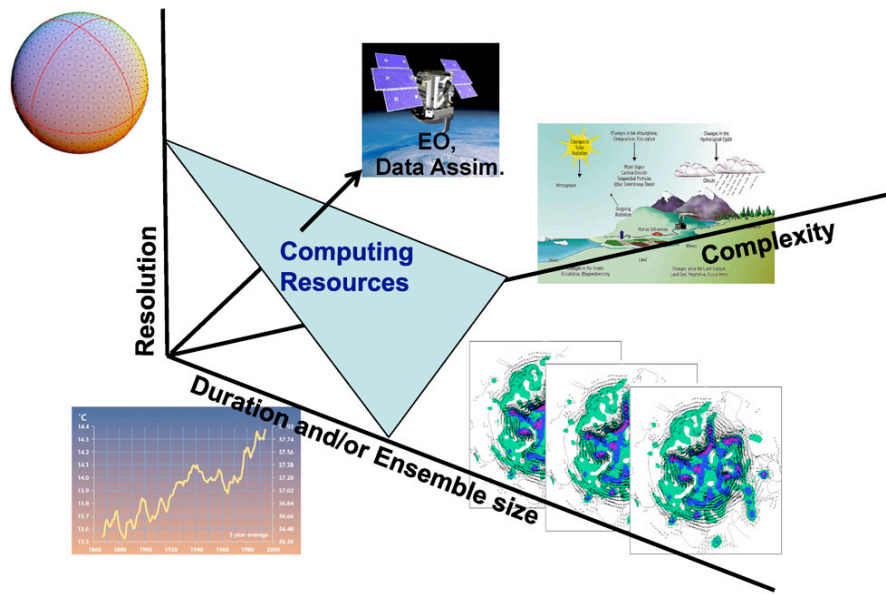


Figure 4-4: Computational resources tradeoff (From [Washington et al., 2008])

for achieving the research goals. The report suggested that it is necessary to identify which components (i.e., physical, chemical, and biological) of the climate system are needed to be modeled, at what resolution, and how large of an ensemble of predictions is needed. In other words, how do we best balance resolution versus complexity versus ensemble size to give current and future computational resources (see Figure 4-4)? The report also acknowledged the important role of continued and vigorous effort in model improvement. The advancement in the computer industry presents excellent opportunities for researchers to incorporate more physical processes in next generation Earth system models.

## 4.2 Modeling overview of land surface processes

### 4.2.1 Land surface models in climate models

The land surface model (LSM) in a global or regional climate model provides the lower boundary conditions of the transport of heat, momentum and moisture. The latent heat

flux from the Earth's surface determines the amount of water evaporated and transpired, while sensible heat flux warms the planetary boundary layer, transporting the evaporated water up in the atmosphere, causing condensation and finally producing precipitation. Thus, the partitioning of net radiation into sensible and latent heat has a strong influence on the evolution of climate. In a pioneering work, Charney [1975] proposed the bidirectional relationship between the atmosphere and the ecosystem by explaining that the lack of vegetation in Sahara sustains itself and its arid climate. Lack of vegetation cover in the Sahel leads to higher surface albedo values, thereby reducing the net incoming solar radiation at the surface. Cooling of the land surface affects the overlying atmosphere so as to reduce rainfall, which further reduces the vegetation.

One of the earliest attempts to study the role of hydrologic cycle through numerical simulation in a GCM was done by Manabe et al. [1965]. In those simulations, the Earth's surface was assumed completely wet with no heat storage capacity and the model was referred as a "moist general circulation model". In the subsequent study, the assumption of a completely wet land surface was revised and soil moisture and snow depth were accounted for in the model, which was referred to as the "bucket" model [Manabe, 1969]. Precipitation replenished the bucket, while evaporation occurring at a potential rate (scaled down by a factor to account for dry soils) depleted the bucket. The second generation of LSMs included functions that describe the role of soil and vegetation in land-atmosphere interactions. The interactions that were incorporated in those models are biophysical control of evapotranspiration through an introduction of a canopy layer, radiation absorption by leaves and canopy, alteration of roughness in boundary layer due to canopy height, precipitation interception by the canopy and soil moisture availability due to root depth and root density. These models represented vegetation as a big-leaf, where a single leaf is used to scale the fluxes for the whole canopy [Dickinson et al., 1986, Sellers et al., 1986].

Avissar and Pielke [1989] developed a parameterization scheme to account for sub-grid vegetation heterogeneity within the grid cells of the land surface model by subdividing the grid cell into homogeneous vegetation types. A complicated micrometeorological model of

soil-vegetation-atmosphere was separately applied for each of the vegetation type present to compute surface temperature and heat fluxes. The heat fluxes at the grid cell level were obtained by area-weighted averaging of heat fluxes from each vegetation type in proportion of their presence within the grid cell. The third generation of LSMs incorporated the relation between photosynthesis and transpiration, along with the role of stomatal conductance in energy, momentum and carbon fluxes [Bonan, 1996].

In the late 1980s and early 1990s, the scientific community became increasingly interested in investigating how climate change would affect the ecosystem structure and the feedbacks of those changes on the atmosphere. The third-generation LSMs operated globally with prescribed vegetation and soil characteristics and were thus inadequate for modeling the effects of transient vegetation cover on climate [Piekle and Avissar, 1990, Solomon and Cramer, 1993]. This led to the development of the fourth generation of land models, termed as Dynamic Global Vegetation Models (DGVMs) [Foley et al., 1996, Dickinson et al., 1998], which have a mechanistic model of photosynthesis simulating the flux of carbon and water; along with a biogeochemistry model to track the fate of carbon in above- and below-ground pools. In recent years, DGVMs have started to incorporate the role of soil carbon dynamics and nitrogen cycling with varying degree of complexity to study feedbacks in the climate systems [Cox, 2000, Sitch et al., 2003, Krinner et al., 2005, Michle et al., 2006, Sokolov et al., 2008, Xu-Ri and Prentice, 2008, Thornton et al., 2009].

Following the development of a more realistic treatment of surface processes (interaction of energy fluxes and vegetation dynamics) within LSMs, the importance of soil moisture transport in the subsurface has also been recognized [Famiglietti and Wood, 1994, Peters-Lidard et al., 1997]. The effect of subgrid topographic variability on land-atmosphere interactions of a climate model have been incorporated in basin-scale hydrologic models, at “catchment” scale [Koster et al., 2000] and “large area basin scale” [Chen and Kumar, 2001]. Chen and Kumar [2001] showed that the inclusion of topographic attributes had a significant impact on water table dynamics and predictability of soil moisture. Choi et al. [2007] incorporated a three dimensional volume-averaged soil moisture transport model in a regional

climate model and the effects of subgrid topographic variability were noticeable in both the vertical and lateral drainage over most moist conditions.

Groundwater influences soil moisture in regions where the water is shallow, thus incorporation of groundwater components in the LSMs has also gained attention in the recent years. Using atmospheric forcings (real or projected under climate change scenarios), several studies have demonstrated the importance of groundwater on simulated streamflow, soil moisture, recharge and surface fluxes [Liang et al., 2003, Maxwell and Miller, 2005, Yeh and Eltahir, 2005, Gulden et al., 2007, Niu et al., 2007, Maxwell and Kollet, 2008]. While other studies have explicitly coupled water table dynamics within the atmospheric models [Gutowski et al., 2002, York et al., 2002, Georgescu et al., 2003]. In a further effort to develop LSMs, Kollet and Maxwell [2008] coupled a three-dimensional subsurface flow and overland flow with the Community Land Model (CLM). Janetos [2009] envisions that with the advancement in computing capabilities will allow future global climate models to run at cloud resolving resolution ( $\approx 1$  km) and increase our understanding of the Earth system.

#### **4.2.2 Distributed hydrologic models**

The early generation of hydrologic models represented the whole catchment by a single bucket and were appropriately called lumped models. They captured the integrated behavior of the whole catchment. An example of such a model is Sacramento Soil Moisture Accounting (SAC-SMA), developed by National Weather Service (NWS) [Burnash et al., 1973]. The spatio-temporal dynamics of precipitation, soil moisture, topography, soil properties were shown as key factors for predicting the timing and magnitude of streamflow events [Pessoa et al., 1993, Goodrich et al., 1995]. Beven [1985] envisioned that the advantage of a distributed approach over a lumped one would be in their capability to capture effects due to land-use change, spatially variable inputs, pollutant and sediment movement and hydrologic response at the basin interior. Studies have shown that the fine-scale dynamics of soil moisture arising due to spatial heterogeneity of topography, land-use and vegetation are among the major predictors of landslides and fire occurrences [Pelletier et al., 1997, Taylor

and Solem, 2001]. A plethora of new data sources, such as the Shuttle Radar Topography Mission (SRTM) for topography, Soil Survey Geographic (SSURGO) database for soil types, the United States Geological Survey (USGS) Land Use and Land Cover (LULC) database and rainfall maps from the Next Generation Weather Radar (NEXRAD), were motivating factors responsible for the development of distributed rainfall-runoff hydrologic models.

Freeze and Harlan [1969] pioneered the idea of a physically-based distributed hydrologic model. The distributed models accounts for spatial heterogeneity in a catchment by discretizing model processes in space. Two kinds of distributed models have emerged: conceptually and physically-based models, where the philosophical difference between them is that the parameters of latter approach can be measured directly in the field. Beven and Kirkby [1979] presented a conceptual model, TOPMODEL, based on a topographic wetness index obtained from topographic analysis. The working assumption for physically based distributed models is that such explicit representation of spatial heterogeneities, particularly topography, soils and vegetation should enhance predictability at season to inter-annual time scales. A variety of such models exists [Abbott et al., 1986, Beven et al., 1987, Grayson et al., 1992, B., 1991, Wigmosta et al., 1994, Garrote and Bras, 1995, Berger and Entekhabi, 2001, Ivanov et al., 2008a, Qu and Duffy, 2007].

The Hydrology Laboratory of the National Weather Service (HL-NWS) undertook a comparison study of many distributed and lumped models during the Distributed Model Intercomparison Project (DMIP) [Smith et al., 2004]. One of the conclusions drawn from the study was that distributed models produced reasonable results at interior points, but not as statistically satisfactory as those obtained from parent basins. Among the criticisms against distributed models are a large number of parameters [Refsgraard, 1996, 1997] and an absence of a general framework for evaluating the simulated dynamics against spatial observations [Grayson et al., 2002]. Numerous model calibration methodologies have been used, not only to improve model performance [Gupta et al., 1998, Madsen, 2003, Leavesley et al., 2003], but also to detect and resolve model shortcomings [Yilmaz et al., 2008]. Physically-based hydrologic models are playing an increasingly important role in understanding and predicting



the impacts of climate change on hydrological processes and water resources [VanRheenen et al., 2004, Kollet and Maxwell, 2008]; while still continuing to serve more traditional needs of river and flash flood forecasting [Foody et al., 2004]. Owing to their explicit representation of spatially varying forcing and state fields, physically-based hydrologic models are promising candidates to represent land-surface processes and thereby lead to advances in hydrologic forecasts [Lyon et al., 2008].

### 4.3 Conclusion

The aforementioned studies have looked at the soil moisture-vegetation-climate, soil moisture-topography-climate or soil-vegetation-topography interactions. This work will focus on the role of vegetation modulated by topography and soil moisture in seasonal to inter-annual climatic patterns. Figure 4-5 presents a schematic illustration of the scope of proposed research work. Climate models (regional or global) at the land surface allow for two-way feedback between soil moisture and vegetation dynamics; but they usually neglect the role of topography (in lateral soil moisture redistribution and local radiation budget due to slope/aspect) in the evolution soil moisture (as shown in Figure 4-5 (a)). Distributed hydrologic models account for role of topography explicitly in soil-moisture and vegetation dynamics, but do not provide feedbacks to the atmosphere. In this research, we propose a **two-way** coupling of a regional climate model with a physically based eco-hydrology model that accounts for topography in soil moisture and vegetation dynamics (see Figure 4-5 (c)). Description of the eco-hydrology and regional climate model is presented in the next chapter; along with an overview of model coupling, domain modification to enable the usage of high performance computing and a new one-dimensional ground heat flux scheme.

Before proceeding to couple a fully distributed hydrological model, incorporating dynamic vegetation, with a regional climate model, we need to ascertain the performance of the hydrologic model under consideration. A rigorous benchmarking of the eco-hydrology model, driven with observed meteorological data, to correctly represent hydrologic and vegetation states is performed in Chapter 6. The eco-hydrology model is applied in a highly

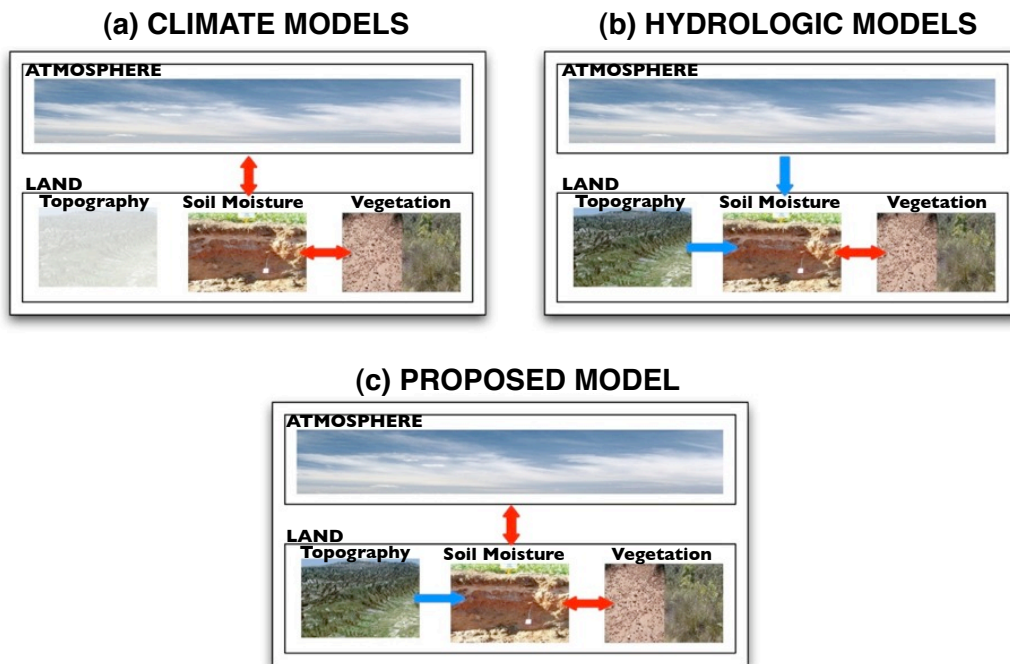


Figure 4-5: A schematic representation of land-atmosphere modeling, illustrating how the feedbacks (one- or two-way) within the various land surface components (topography, soil moisture and vegetation) are considered. (a) Within climate models (regional or global), the atmosphere, soil moisture and vegetation are two-way coupled; while role of topography in lateral redistribution and surface radiation is neglected. (b) In hydrologic modeling, the atmospheric forcings drive the model, and topography influences soil moisture and vegetation dynamics. (c) The proposed model of regional climate will explicitly account for the role of topography in the evolution of soil moisture and vegetation.

instrumented semiarid USDA-Agricultural Research Services (ARS) Walnut Gulch Experimental Watershed in southeast Arizona for a period of 11 years. The model performance is examined with respect to several key hydrologic variables: energy balance, distributed soil moisture with the watershed at three depths, and land surface temperature. Additionally, the model's capability to capture vegetation dynamics for two generic plant functional types, C4 grasses and C3 shrubs, is also evaluated against the MODIS leaf area index product.

Three different experiments are conducted in Chapter 7 to examine the impacts of regional scale feedbacks between atmosphere and dynamic vegetation modulated by topography and soil moisture at seasonal to inter-annual timeseries. The following cases of vegetation and topography are considered:

- Flat topography with static vegetation
- Observed topography with static vegetation
- Observed topography with dynamic vegetation

The results from the experiments are explained within the framework of soil moisture-rainfall feedback hypothesis of Eltahir [1998]. The results demonstrates the role of explicitly accounting for topography and vegetation dynamics in coupled land-atmosphere model.



# CHAPTER 5

## MODELS

The core of this research relies on two numerical models: an ecohydrology model and a regional climate model. This chapter presents an overview of both the models individually and describes how they are coupled together to address one of the questions raised in this thesis. The modification in domain representation of the ecohydrology model in order to utilize high performance computing is also described. Additionally, a brief description of the new one-dimensional ground heat flux scheme incorporated within the ecohydrology model is also presented.

### 5.1 tRIBS+VEGGIE Model

Natural and anthropogenic changes in climate have been shown to significantly impact the hydrologic cycle [DeWalle et al., 2000, Porporato et al., 2004, Milly et al., 2005, Oki and Kanae, 2006, Scibek and Allen, 2006, Weiskel et al., 2007]. A recent report summarizing the impacts of climate change on the United States has recognized that the southwest United States has seen some of the longest documented mega-droughts on Earth [Karl et al., 2009]. Ecosystems throughout the southwestern United States have been significantly altered by the encroachment of shrubs into grasslands [Buffington and Herbel, 1965, Grover and Mutschick, 1990, Bahre and Shelton, 1993]; which not only out-competes the native species, but

provides additional fuel for forest fires [Weiss and Overpeck, 2005]. Physically-based hydrologic models are playing an increasingly important role in understanding and predicting the impacts of climate change on hydrological processes and water resources [VanRheenen et al., 2004, Kollet and Maxwell, 2008, Liuzzo et al., 2010]; while still continuing to serve more traditional needs of river and flash flood forecasting [Foody et al., 2004]. Owing to their explicit representation of spatially varying forcing and state fields, physically-based hydrologic models are promising candidates to represent land-surface processes and thereby lead to advances in hydrologic forecasts [Lyon et al., 2008].

One of the models used in this thesis is the Triangulated Irregular Network (TIN) based Real-time Integrated Basin Simulator (tRIBS), a fully distributed physically based hydrologic model [Ivanov et al., 2004]; integrated with a plant physiology and spatial dynamics component, VEGetation Generation for Interactive Evolution (VEGGIE) [Ivanov et al., 2008a,b]. Unlike the use of regular mesh adopted by most hydrologic models [Wigmosta et al., 1994, Downer et al., 2002, Kollet and Maxwell, 2006], the tRIBS+VEGGIE model uses a triangulated irregular network (TIN) representation of land surface topography (Figure 5-1). The TINs capture topographic detail with fewer computational nodes as compared to the traditional grid based representation, thus allowing to simulate basin hydrologic response in a computationally efficient manner [Vivoni et al., 2004]. Elevation data from the Shuttle Radar Topography Mission (SRTM) [Farr et al., 2007] can be used to construct a TIN representation of the watershed under consideration. The Voronoi polygons are the fundamental computational element of the tRIBS+VEGGIE model, where the energy and water budgets are solved numerically (see Figure 5-1(a) and (b)). The Voronoi polygon can have both vegetated and non-vegetated surfaces simultaneously within it. The model allows for spatially varying precipitation forcing to be intercepted by vegetation (if present), or reach the ground surface directly; where it may infiltrate into the soil or produce surface runoff. The Rutter et al. [1971] scheme is used to model canopy interception and the intercepted water can evaporate from the leaf surface or drain to the surface as leaf dripping. A finite-element solution of the  $\psi$ -based form of 1-D Richards formulation of infiltration process,

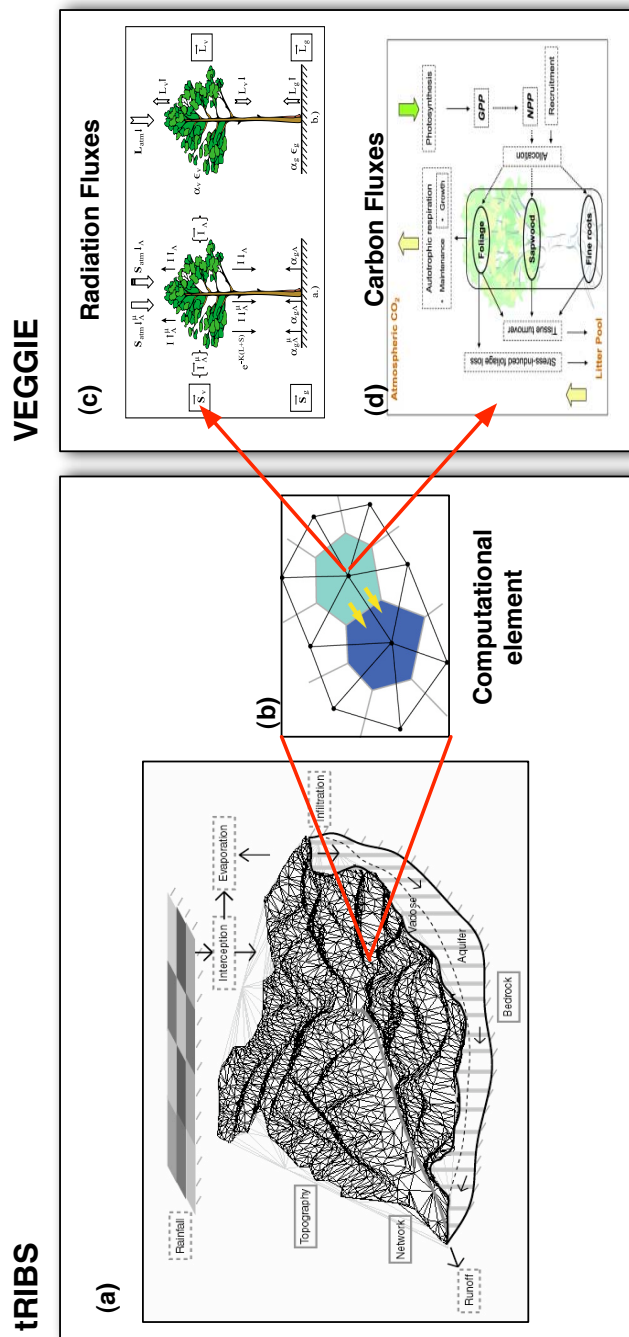


Figure 5-1: A schematic representation of the fully distributed eco-hydrology model: the tRIBS+VEGGIE is shown. (a) The various hydrologic process represented in tRIBS and the TIN representation of the surface, (b) The basic computational voronoi element of tRIBS, (c) The partitioning of radiation fluxes, and (d) The carbon fluxes simulated by the model (tRIBS+VEGGIE). [Adapted from Ivanov [2006]]

with a varying vertical mesh resolution, is implemented within the model [Ivanov, 2006]. The model uses the Brooks and Corey [1964] parameterization for soil water retention curve. The surface (runoff) and subsurface (unsaturated zone) mass flux exchange occurs along the steepest-descent direction. The surface runoff can be produced in the model as saturation excess or infiltration excess. Hydrologic runoff routing is performed on the hillslope; while hydraulic kinematic wave routing is performed in the channel network. The model can account for spatially varying hydraulic, thermal and albedo properties of soil types within the watershed.

The dynamic vegetation component of the tRIBS+VEGGIE model is a “big-leaf” model that operates on specified plant functional types (PFTs) [Bonan, 1996]. The various biophysical and biochemical processes that are accounted for with the coupled vegetation-hydrology system include absorption, reflection and transmittance of radiative fluxes (shortwave and longwave); sensible and ground heat fluxes; partitioning of latent heat into bare soil evaporation and canopy transpiration; photosynthesis and primary production; plant respiration; tissue turnover and stress-induced foliage loss; carbon allocation and vegetation phenology (for details see [Ivanov et al., 2008a]). The exchange of CO<sub>2</sub> flux between the atmosphere and land surface contribute to the dynamics in three carbon pools modeled within tRIBS+VEGGIE: foliage, sapwood, and fine roots. Assimilation of CO<sub>2</sub> through photosynthesis is coupled to surface energy and water balance through the stomatal resistance model. A conceptual map of the VEGGIE model is shown in Figure 5-1 (c) and (d). The simulated physical processes allow for numerous dynamic feedbacks among various components of the coupled vegetation-hydrology system. These physical processes within the model operate at different time scales: simulation of infiltration, lateral moisture distribution and runoff is carried out at a finer time step of  $\approx 7.5 - 15$  minutes; while meteorological forcings and biophysical processes operate at 1 hour time step. Vegetation responds to environmental conditions of water and energy through stomata dynamics at an hourly time scale. At daily time scale, the vegetation affects the land-surface state through the change of its structural attributes and vegetation fraction.



## 5.2 Weather Research and Forecasting Model

The Weather Research and Forecasting (WRF) model is a state-of-the-art numerical weather prediction (NWP) system, developed from the collaborative efforts between various US agencies, including National Center for Atmospheric Research (NCAR) and National Oceanic and Atmospheric Administration (NOAA), and universities. There are two dynamics solvers in the WRF: the Advanced Research WRF (ARW) solver developed primarily at NCAR, and the NMM (Nonhydrostatic Mesoscale Model) solver developed at NOAA's National Centers for Environmental Prediction (NCEP). The WRF-NMM replaced the Eta model in the North American Mesoscale (NAM) modeling system as of June 2006 to be used in operational forecast mode.

The atmospheric dynamics of the WRF core are based around full set of primitive differential equations, advancing three-dimensional fields of momentum, heat and moisture [Skamarock et al., 2008]. The vertical grid of the model is terrain-following with the top of the model being a constant pressure surface, while the horizontal grid is the Arakawa-C grid. The time integration scheme in the model uses the third-order Runge-Kutta scheme, and the spatial discretization employs 2nd to 6th order schemes. The model supports one-way, two-way and moving nest options. It runs on single-processor, shared- and distributed-memory computers. The latest release of WRF version 3.0 in April, 2008, includes global modeling capabilities. WRF has five physics categories, namely microphysics, cumulus parameterization, planetary boundary layer, LSM and radiation, each of which has several options as listed in Table 5.1.

## 5.3 Domain Representation

### 5.3.1 Domain decomposition for tRIBS+VEGGIE

Topography and drainage network of a domain within the tRIBS+VEGGIE model is represented via a triangulated irregular network (TIN) of points [Vivoni et al., 2004, Ivanov

Table 5.1: Various physics options available in WRF-ARW v3.0

Microphysics	<p>Kessler scheme  Purdue Lin scheme  WRF Single-Moment 3-class(WSM3) scheme  WSM5 scheme  WSM6 scheme  Eta Grid-scale Cloud and Precipitation scheme  Thompson scheme  Goddard Cumulus Ensemble model scheme  Morrison 2-Moment scheme</p>
Cumulus parameterization	<p>Kain-Fritsch scheme  Betts-Miller-Janjic scheme  Grell-Devenyi ensemble scheme  Grill-3 scheme</p>
Surface layer	<p>Similarity Theory - MM5  Similarity Theory - Eta  Similarity theory - PX</p>
Land surface model	<p>5-layer thermal diffusion  Noah LSM  Rapid Update Cycle model LSM  Pleim-Xiu LSM  Urban Canopy Model  Ocean Mixed-Layer Model  Specified Boundary conditions</p>
Planetary boundary layer	<p>Medium Range Forecast Model (MRF)  Yonsei University (YSU)  Mellor-Yamada-Janjic (MYJ)  Asymmetrical Convective Model version 2 (ACM2)</p>
Atmospheric radiation	<p>Rapid Radiative Transfer Model (RRTM) Longwave  Eta Geophysical Fluid Dynamics Laboratory Longwave  CAM Longwave  Eta Geophysical Fluid Dynamics Laboratory Shortwave  MM5 (Dudhia) Shortwave  Goddard Shortwave  CAM Shortwave</p>

et al., 2004]. The primary motivation for the use of TINs is the multiple resolutions offered by the irregular domain. The fundamental computational element is a voronoi polygon, which is defined by two axes:  $p$  in the direction parallel to the plane along the maximum slope,  $\alpha_{\nabla}$ , (positive downslope) and  $n$  in the direction normal to the plane (positive downwards). The state variable of the one-dimensional mass flow equations, when applied to a voronoi polygon, are a function of the direction  $n$ . The surface (overland-flow) and subsurface (unsaturated-zone) mass flux exchange occurring between upstream and steepest downstream cell occurs in the plane parallel to  $p$ . Details regarding the geometric representation of the computational element can be found in Vivoni et al. [2004] and Ivanov et al. [2004]. In the following section, we describe the extension of the basic tRIBS+VEGGIE domain to accommodate the use high performance computing architecture and coupling of the tRIBS+VEGGIE model with a regional climate model.

### 5.3.2 Domain decomposition for Parallel tRIBS+VEGGIE

High performance computing (HPC) has become ubiquitous tool for conducting simulations. Modeling large spatial domains in distributed hydrologic models at fine resolution over long period of time can now be achieved using HPC. Vivoni et al. [2005] successfully parallelized an early version of the tRIBS model [Ivanov et al., 2004]. During the implementation of VEGGIE component within the tRIBS model [Ivanov, 2006], the representation of hydrologic processes underwent improvements, including development of finite-element based formulation of the Richards equation. The implementation of Vivoni et al. [2005] served as guide to develop parallel tRIBS+VEGGIE (*ptRIBS+VEGGIE* henceforth) model. *ptRIBS+VEGGIE* uses the Message Passing Interface (MPI) for distributed memory computer system.

Within a given *ptRIBS+VEGGIE* domain, the lateral exchange in the subsurface and overland occurs along the steepest decent downstream. Thus, a watershed domain can be interpreted as a *directed-graph*, where each computational element interacts with its downstream neighbor only. The watershed domain is decomposed into sub-watersheds or reaches

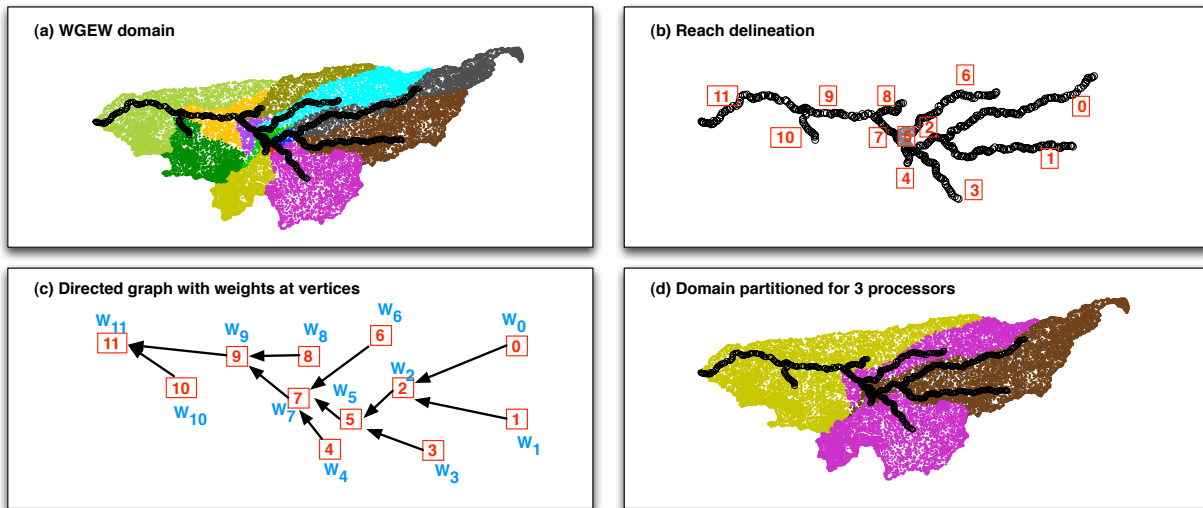


Figure 5-2: (a) Domain representation for the Walnut Gulch Experimental Watershed, AZ. The computational elements in black are the stream nodes, while elements with same color belong to a common reach. (b) Delineation of reaches within the watershed. (c) Directed graph that shows the connectivity of reaches and contains weights at the vertices. The weights corresponds to the number of computational elements draining into a given reach. (d) Partition of the WGEW domain for a simulation with three processors.

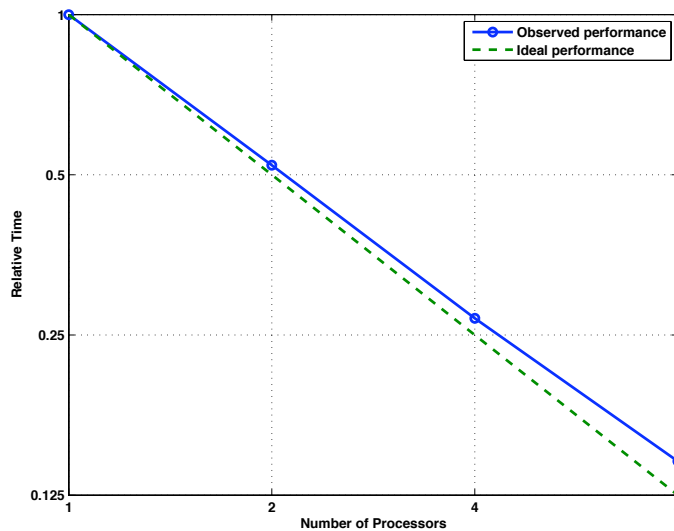


Figure 5-3: Performance of the *ptRIBS*+*VEGGIE* model for a 240-hours simulation experiment.

along the stream-network. Each reach is assigned a weight corresponding to the number of computational elements that flow directly into the reach under consideration. Freely available graph partitioning software, METIS [Karypis and Kumar, 1999], is used to partition the weighted directed graph over the specified number of processors during runtime, while trying to balance the load on each processor. An example of the *ptRIBS+VEGGIE* domain is shown for the Walnut Gulch Experimental Watershed (WGEW) in Arizona in Figure 5-2(a). In Figure 5-2(a) the computational elements classified as streams are shown in black, while those elements that belong to a common reach are displayed with a similar color. The delineated reaches within the watershed are shown in Figure 5-2(b); while the resulting directed graph with weights on each vertices is shown in Figure 5-2(c). The resulting domain after partitioning using METIS for three processors is illustrated in Figure 5-2. In order to test the performance of the *ptRIBS+VEGGIE* model a 240 hours simulation experiment was conducted for the WGEW with varying number of processors. The simulation was conducted on an AMD Quad-core Opteron 2.1GHz with 8Gb RAM. The performance of the *ptRIBS+VEGGIE* model is shown in Figure 5-3 and the model scales well with the increasing number of processors.

### 5.3.3 Domain representation for WRF - *ptRIBS+VEGGIE*

The WRF and the *ptRIBS+VEGGIE* model use different horizontal discretization, a rectangular grid and a watershed domain, respectively (see Figure 5-4). When a simulation is run on multiple processors (say 4 processors), the WRF domain gets broken into rectangular tiles, as shown in Figure 5-4 with four different solid colors; while the watershed of *ptRIBS+VEGGIE* gets partitioned along stream reaches (shown with filled colors in Figure 5-4). One immediate challenge that arises during the simulation of the coupled model running on multiple processors is demonstrated in Figure 5-4 : Reach-3 of the watershed for the *ptRIBS+VEGGIE* model resides entirely on one processor; while the atmospheric conditions corresponding to it within the WRF model are present on all 4 processors. Thus, while running a simulation in a parallel mode, additional care has to be taken to ensure that

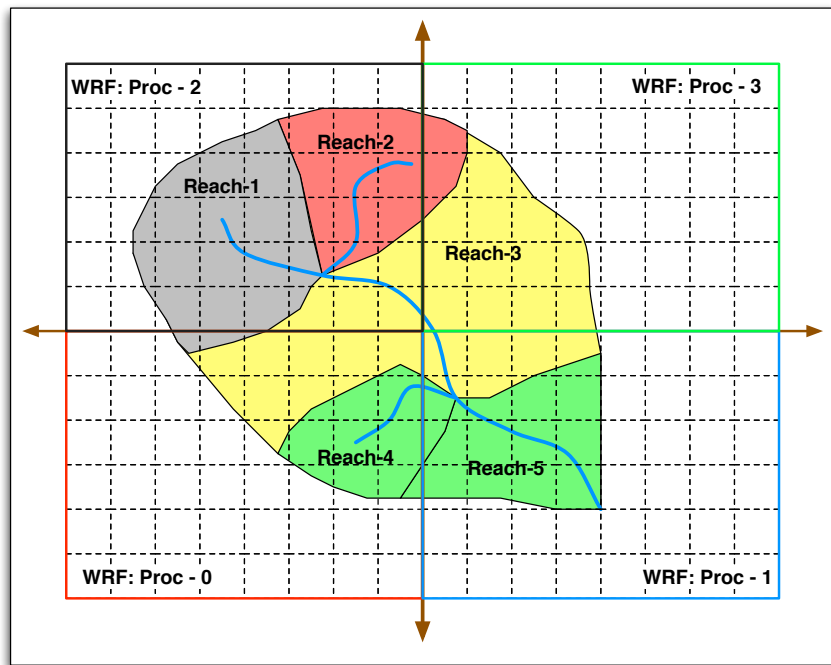


Figure 5-4: Horizontal domain representation for WRF and *ptRIBS+VEGGIE* model. WRF employs a rectangular grid, while *ptRIBS+VEGGIE* works on a watershed domain.

both models receive and return correct information while communicating with each other.

The coupling between WRF - *ptRIBS+VEGGIE* models is graphically represented in Figure 5-5. The two models are separated via a “buffer” which communicates instantaneous values of atmospheric forcing and land surface boundary state variables, heat and moisture fluxes between models. As the first step, on each processor, the buffer receives atmospheric forcings from the WRF model (Figure 5-5 a.1). The buffer on each processor then communicates its individual atmospheric forcings to other processors, until buffers on processors have atmospheric forcings for the entire simulation domain (Figure 5-5 a.2). After the *ptRIBS+VEGGIE* model has updated the land surface fluxes and state variables for the portion of watershed domain active on the given processor, the buffers communicate among themselves to reconstruct the fluxes and state variable for the entire watershed domain (Figure 5-5 b.1). Finally, each buffer returns the corresponding fluxes to the WRF model (Figure 5-5 b.2).

The *ptRIBS+VEGGIE* model was initially developed to represent a single watershed and simulate hydrological processes occurring within the watershed boundary. In order to obtain estimates from *ptRIBS+VEGGIE* regarding land surface state (temperature, albedo) and heat and moisture fluxes over the entire WRF domain of atmospheric processes simulation, it was necessary to extend *ptRIBS+VEGGIE* to operate on several watersheds simultaneously. Multiple watersheds were implemented in a parallel computing framework that allowed certain watersheds to reside entirely on a single processor, while simultaneously allowing for larger watersheds to be distributed over multiple processors.

## 5.4 Ground heat flux

Ground heat flux transfers heat from the surface to subsurface via conduction and Wang and Bras [1999] method was used within the original *tRIBS+VEGGIE* model. In this work, a one-dimensional heat diffusion model within the soil is incorporated. The heat diffusion model in a vertical soil column,  $z$ [m], for soil temperature,  $T$ [K], can be described as

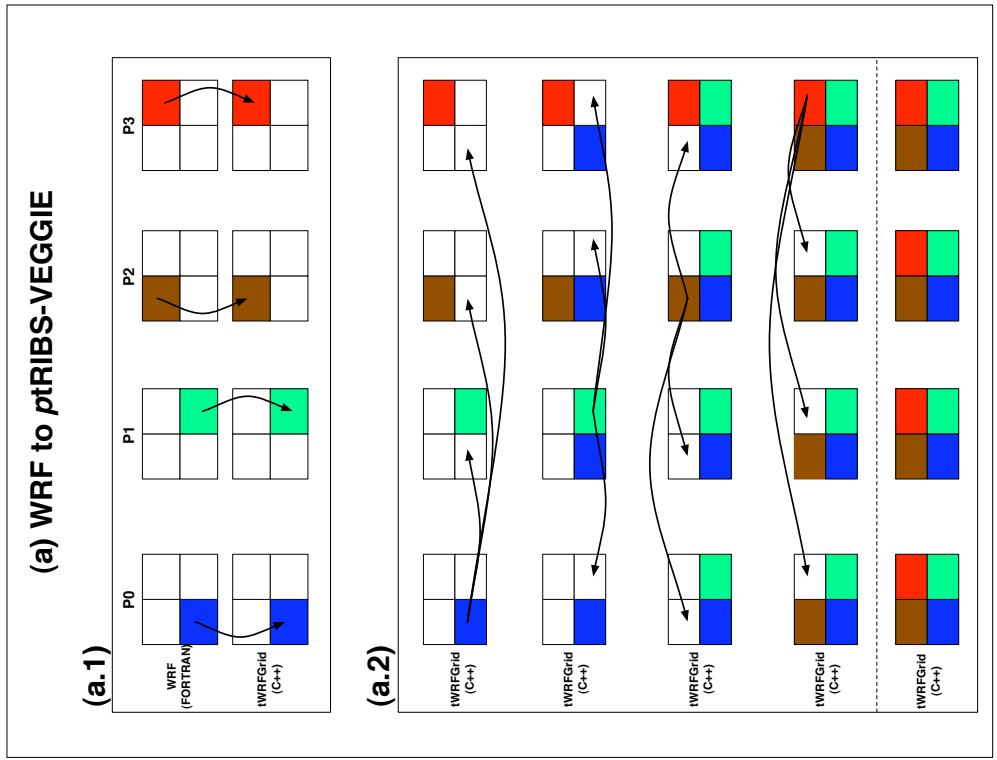
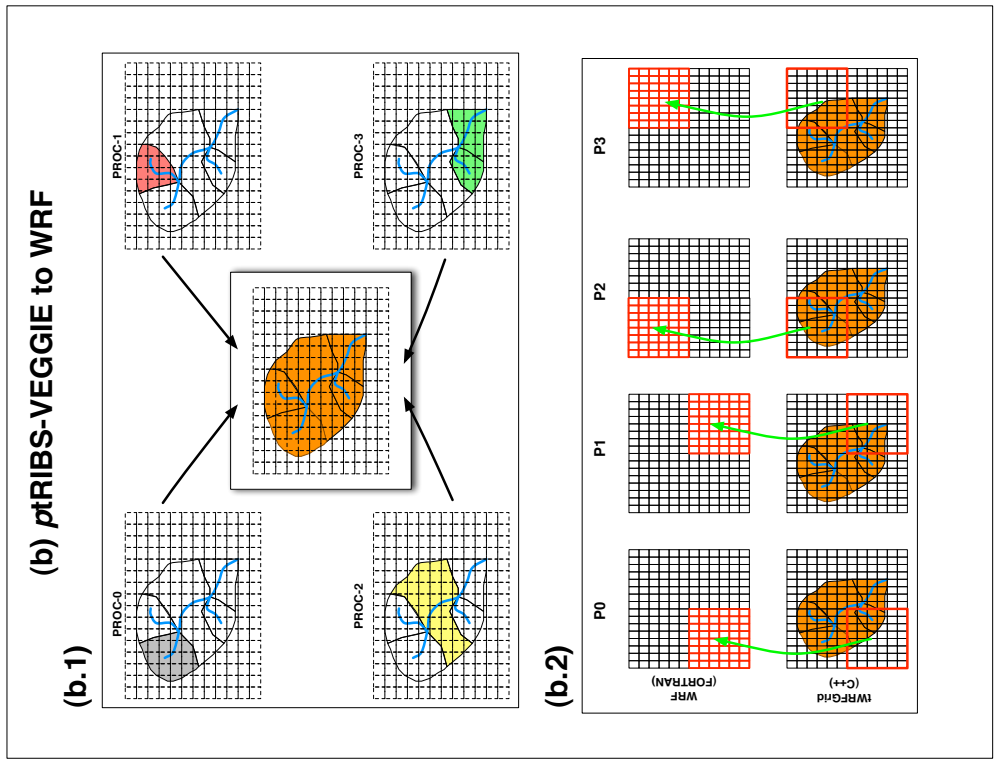


Figure 5-5: A schematic representation of WRF *pt*RIBS+VEGGIE coupling for a simulation run with 4 processors (P0, P1, P2 and P3).



$$C(\theta) \frac{\partial T}{\partial t} = \frac{\partial}{\partial z} \left( \kappa(\theta) \frac{\partial T}{\partial z} \right) \quad (5.1)$$

where  $C(\theta)$  [ $\text{J m}^{-3} \text{K}^{-1}$ ] and  $\kappa(\theta)$  [ $\text{J m}^{-3} \text{s}^{-1} \text{K}^{-1}$ ] are volumetric soil heat capacity and volumetric soil heat conductivity respectively. Soil moisture ( $\theta$ ) directly impacts both the volumetric soil heat capacity and volumetric soil heat conductivity.

In this study, the soil heat conductivity parameterization scheme of Farouki [1981] is used. The volumetric soil heat conductivity is given as a combination of dry ( $\kappa_{dry}$ ) and saturated ( $\kappa_{sat}$ ) conductivities, weighted by a normalized conductivity ( $K_e$ , Kersten number) as

$$\kappa(\theta) = \begin{cases} K_e(\kappa_{sat} - \kappa_{dry}) + \kappa_{dry} & \text{if } \theta/\theta_s \geq 10^{-7}; \\ \kappa_{dry} & \text{if } \theta/\theta_s < 10^{-7}. \end{cases} \quad (5.2)$$

and

$$K_e = \ln \left( \frac{\theta}{\theta_s} \right) + 1.0 \quad (5.3)$$

where  $\theta_s$  [ $\text{mm}^3 \text{mm}^{-3}$ ] is saturated volumetric soil moisture. The volumetric soil heat capacity is assumed to vary linearly with soil moisture as

$$C(\theta) = (1 - \theta_s)C_{soil} + \theta C_{water} \quad (5.4)$$

where  $C_{soil}$  [ $\text{J m}^{-3} \text{K}^{-1}$ ] is soil heat capacity of dry soil and  $C_{water} = 4.188 \times 10^6$  [ $\text{J m}^{-3} \text{K}^{-1}$ ] is the specific heat capacity of water. The current formulation of the heat diffusion is only applicable to unfrozen soil conditions, but the extension to frozen soils is straight-forward.

The ground heat flux at the surface,  $G$  [ $\text{Wm}^{-2}$ ], defined as positive into the ground, and

its partial derivative with respect to soil surface temperature,  $T_{surf}[\text{K}]$ , are given by

$$\begin{aligned} G &= \left( \kappa \frac{\partial T}{\partial z} \right) \Big|_{z=0} \\ &= \kappa_1 \left( \frac{T_{surf} - T_1}{(\Delta z_1)/2} \right) \end{aligned} \quad (5.5a)$$

$$\frac{\partial G}{\partial T_{surf}} = \frac{2\kappa_1}{\Delta z_1} \quad (5.5b)$$

The numerical approximation for solving 1-D heat diffusion model in this study closely follows the approach of Bonan [1996] and is detailed in Appendix A.

## 5.5 Conclusion

This chapter has discussed the two numerical models that are used in this thesis. A brief description of the modifications carried out in the ecohydrology model (domain representation for HPC and 1-D ground heat diffusion formulation) were summarized. An overview of how the two numerical models coupled together was also presented. Before proceeding to simulations with WRF - *ptRIBS*+*VEGGIE* model to study the importance of incorporating dynamic vegetation and topography within a regional climate model, one needs to assess how capable the ecohydrology model (in an offline mode) is in accurately resolving hydro-climatic signatures and vegetation dynamics in a semiarid region. In the next chapter, we discuss the results from the application of the *ptRIBS*+*VEGGIE* model (driven by measured atmospheric forcings) in a highly instrumented semiarid catchment, Walnut Gulch Experimental Watershed in Arizona for a period of 11 years (1997-2007). The model performance is examined with respect to several key hydrologic variables: energy fluxes, distributed soil moisture within the watershed at three depths and land surface temperature. Additionally, the model's capability to capture vegetation dynamics for two generic plant functional types,  $C_4$  grass and  $C_3$  shrubs, is also evaluated against the MODIS leaf area index product.

## CHAPTER 6

# APPLICATION OF *pt*RIBS+VEGGIE OVER A SEMI-ARID REGION

### 6.1 Walnut Gulch Experimental Watershed

The USDA-ARS Walnut Gulch Experimental Watershed (WGEW) is located in the San Pedro River Basin of southeastern Arizona, a transition zone between the Sonoran and Chihuahuan Deserts. It is one of the most highly instrumented semi-arid experimental watershed in the world [Renard et al., 2008]. The WGEW has a total area of approximately 150 km<sup>2</sup> and the elevation of the watershed ranges from 1220m to 1950m above mean sea level, as shown in Figure 6-1. The North American monsoon (NAM) is responsible for supplying two-thirds of the region's annual precipitation during the summer [Goodrich et al., 2008]. Primary surface condition measurements were made in 1953 and are continuing to the present, including various locations throughout the WGEW and surrounding area. The WGEW has an extensive database of precipitation, runoff, soil hydrology, meteorological, vegetation, geographic information system, carbon dioxide and water flux [Goodrich et al., 2008, Stone et al., 2008, Keefer et al., 2008, Skirvin et al., 2008, Emmerich and Verdugo, 2008, Moran et al., 2008, Heilman et al., 2008].

Lucky Hills and Kendall are two intensive rangeland study areas with small (<10 ha) within the WGEW. They are representative of the two main vegetation cover types, shrubs in Lucky Hills and grasses in Kendall. The Kendall sub-watershed includes rain gage 82

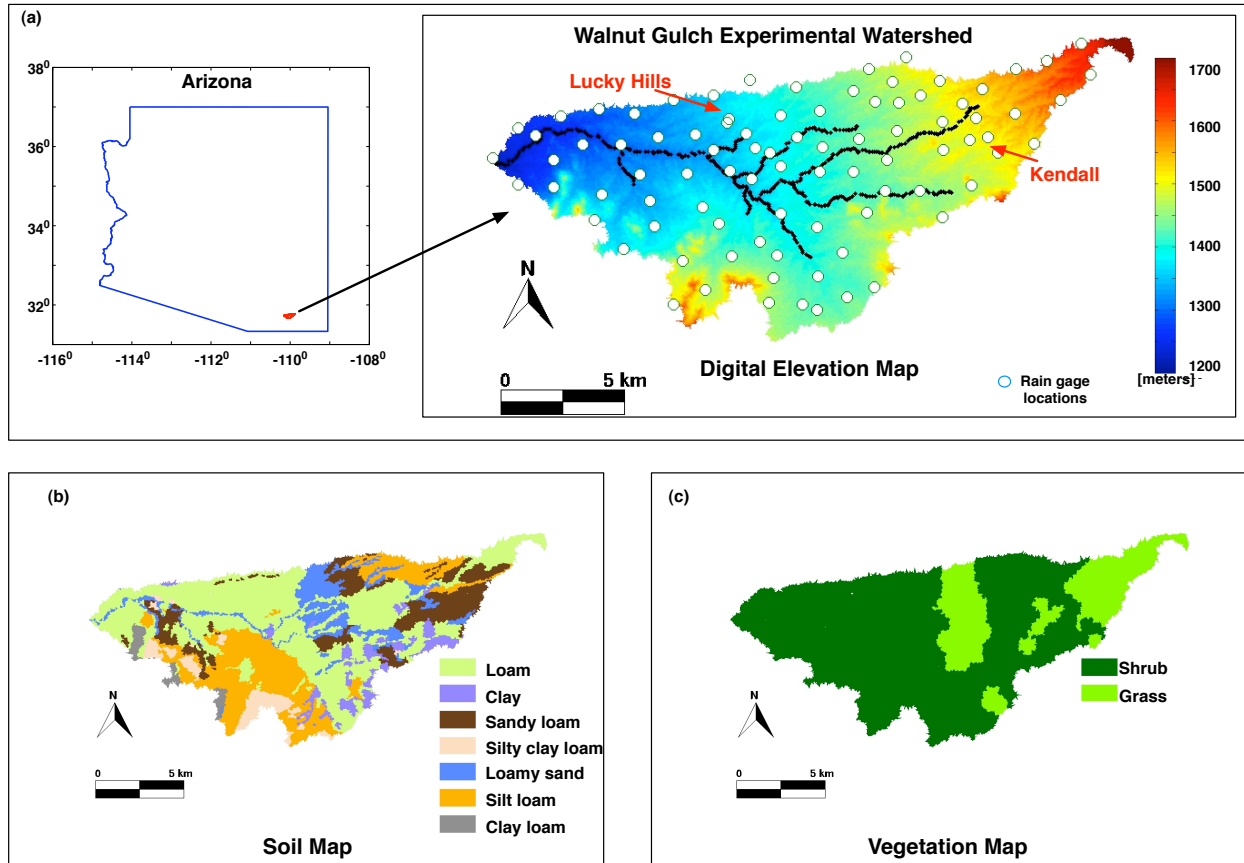


Figure 6-1: (a) Location of the USDA-ARS Walnut Gulch Experimental Watershed in south-east Arizona and the digital elevation map of the WGEW along with rain gage locations from which data is used. Kendall and Lucky Hills are station 82 and 83, respectively. (b) Soil types within the Walnut Gulch Experimental Watershed provided by Soil Survey Geographic (SSURGO) database. (c) Spatial distribution of the two dominant vegetation types, grass and shrub, within the WGEW.

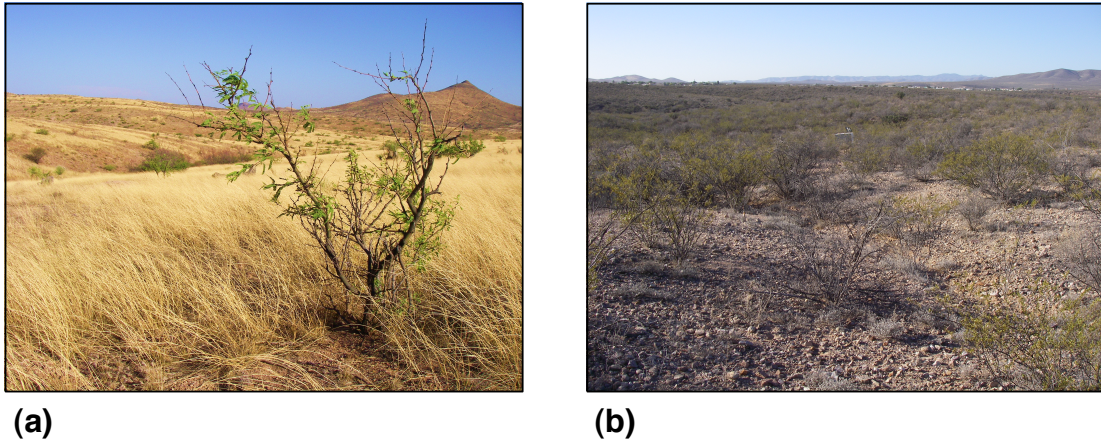


Figure 6-2: Illustrations of surface conditions at sites Kendall (grass-dominated) and Lucky Hills (shrub-dominated), respectively. [Pictured in June, 2008]

and Lucky Hills is near rain gage 83 (Figure 1a) and their dominant vegetation cover can be seen in photographs presented in Figures 6-2(a) and (b). The Lucky Hills site is located at  $110^{\circ}3'5''\text{W } 31^{\circ}44'37''\text{N}$  with an elevation of 1372 meters. The dominant shrubs present at the site are creosotebush (*Larrea tridentata*), hitethorn Acacia (*Acacia constricta*), tarbush (*Flourensia Cernua*), and desert zinnia (*Zinnia pumila*) with some mariola (*Parthenium incanum*) and little leaf sumac (*Rhus microphylla*) [King et al., 2008]. The soil at this site is Lucky Hills series (coarse-loamy, mixed, thermic Ustochreptic Calciorthids) with 3 to 8% slopes [Heilman et al., 2008]. The Kendall site is located at  $109^{\circ}56'28''\text{W } 31^{\circ}44'10''\text{N}$  with an elevation of 1526 meters. Dominant grasses are sideoats grama (*Bouteloua curtipendula*), black grama (*Bouteloua eriopoda*), three-awn (*Aristida sp.*) and cane beard grass (*Bothriochloa barbinodis*) [King et al., 2008]. The soils at the site are a complex of Stronghold (coarse-loamy, mixed, thermic Ustollic Calciorthids) with 4-9% slopes [Heilman et al., 2008].

Table 6.1: Station number in Walnut Gulch and data type used either for model forcing or evaluation.

	Model forcing data		Model evaluation data				
	Meteorological data (except precipitation)	Precipitation data	Energy fluxes	Soil moisture (at following depths)			Soil surface temperature
				5 cm	15 cm	30 cm	
Station number	82	14	82	3	46	46	46
	83	7-72	83	13	82	82	69
		74		14	83	83	92
		76		18			100
		79-83		20			
		87-92		28			
		100		34			
		384		37			
		398-399		40			
				46			
				57			
				69			
				70			
				76			
				82			
				83			
				89			
			92				
			100				

### 6.1.1 Hydro-Meteorological in situ data

Both, Kendall and Lucky Hills sites in the WGEW have automated weather stations to collect meteorological data [Keefer et al., 2008]. The meteorological variables used by the *ptRIBS+VEGGIE* model include atmospheric pressure, relative humidity, wind speed, air temperature, solar radiation and precipitation. In this study, 11 years (1997-2007) of hourly meteorological data was used to force the *ptRIBS+VEGGIE* simulation. Precipitation data from 88 rain gage stations during the study period are used for the simulations. The measurements of net radiation, latent, sensible and ground heat flux at Kendall and Lucky Hills from 1998 to 2007, are used to evaluate the simulation results. Soil moisture and soil surface temperature observations are also employed to assess the model performance. Soil moisture observations are available for the 2002-2007 period at three depths: 5 cm (at 19 stations), 15 cm (at 3 stations) and 30 cm (at 3 stations); while surface soil temperature observations are available at 4 stations for the time-period of 2004-2007. A summary of the different data types, available at the various stations, used in this study are presented in Table 6.1.

### 6.1.2 Remote sensing data

Remote sensing provides data with a high spatial and temporal coverage, which can be used not only to evaluate the performance of a distributed hydrologic model but also improve model estimates through data assimilation. One such source is the MODerate-resolution Imaging Spectroradiometer (MODIS) instrument onboard of the Earth Observing System (EOS) Terra and Aqua satellites. Terra and Aqua satellites were launched in Dec., 1999 and May, 2002 respectively. With 36 spectral bands and a global coverage of 1 to 2 days, the MODIS sensor provides various atmospheric, land, cryospheric and ocean data products. The MODIS products used in this study include the level-3 land surface temperature (LST) product and the level-4 leaf area index (LAI) product.

The MODIS 5-minute swath LST day/night data product is a level-2 product and is produced by the generalized split-window LST algorithm [Wan and Dozier, 1996] for pixels whose emissivities are known in the MODIS band 31 and 32. In the case of pixels with

variable or unknown emissivities, the Day/Night LST Algorithm [Wan and Li, 1997] is used to simultaneously retrieve band emissivities and temperature from a pair of daytime and nighttime the MODIS observations in bands 20, 22, 23, 29, 31, 32 and 33. The MODIS LST data product used in this study is 11A1, a daily level-3 LST product, produced by reprojecting 5-minute swath LST product in 1 km sinusoidal projection.

The MODIS LAI data product, MOD15A2 from the Terra satellite, was used in this study to evaluate the model's performance in capturing vegetation dynamics. The MOD15A2 is a level-4 product, produced at 1 km spatial resolution and composited over 8 days. The retrieval algorithm producing this product is based on a three dimensional radiative transfer model tuned for six main biome classes [Knyazikhin et al., 1998]. The inputs for the retrieval algorithm include atmospherically corrected bidirectional reflectance values for two wavelength bands, red and near-infrared; the Sun and satellite viewing angle for reflectance data; a land cover classification map and a lookup table for a radiative transfer coefficient [Knyazikhin et al., 1998]. The algorithm compares observed and modeled canopy reflectances for a range of canopy structures and soil patterns expected in natural conditions. The LAI is retrieved as the mean value from all possible solutions within a specific level of input satellite data and model uncertainties [Knyazikhin et al., 1998]. Both MODIS data products, LST and LAI, are available in EOS-hierarchical data format and were obtained from NASA's Warehouse Inventory Search Tool (WIST) website and are subsetted to spatially cover the WGEW.

## 6.2 Model setup and calibration

The Bowen ratio measurements at Kendall and Lucky Hills began in July, 1996 and starting from 1997 the measurements were quality controlled. Thus, a study period of 11 years, 1997-2007, was selected to evaluate whether the *pt*RIBS+VEGGIE model is able to resolve hydrologic variables and vegetation dynamics in a semiarid region. The model is initialized with spatially homogenous (horizontally as well as vertical) soil moisture at 20% saturation. As the study period spans over a decade, we believe that the initial conditions will not bias



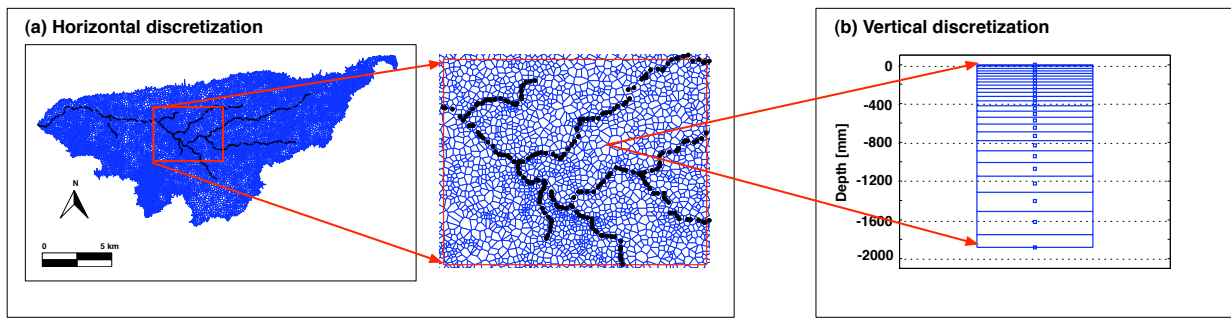


Figure 6-3: Domain discretization of the WGEW (a) Horizontal discretization (19,443 Voronoi polygons); and (b) Vertical discretization (25 exponentially varying soil layers)

the results of this study. Furthermore, the results obtained during the first year of study (i.e. 1997) were neglected while making any comparisons between the modeled outputs and observations. A 30-meter Digital Elevation Model (DEM) from the U.S. Geological Survey was used to construct the mesh for the WGEW. An efficient TIN mesh was constructed using the ArcInfo Geographic Information System package developed by ESRI following the approach outlined by Vivoni et al. [2005]. The final TIN mesh comprised of 19,433 computational elements in the horizontal; while the vertical discretization comprising of 25 soil layers (whose thickness varies exponentially, increasing with depth) extending  $\approx 2$  m deep. Figure 6.2 illustrates the horizontal and vertical discretizations for the domain. The Soil Survey Geographic (SSURGO) database, maintained and published by the USDA, was used to determine the spatial distribution of soils within the WGEW, as shown in Figure 6-1(b). The soil parameterizations used by the *ptRIBS+VEGGIE* model corresponding to the various soil types present within the WGEW are listed in Table 6.2. Since the groundwater has been shown to be deep [Goodrich et al., 2004], the simulations do not include saturated dynamics. The bottom boundary condition of each computational element is specified as the open flow boundary approximated as the gravity-driven drainage.

The vegetation cover map was obtained from a publicly accessible website of the Southwest Watershed Research Center, Tucson, Arizona [Skirvin et al., 2008]. The vegetation map included six classes and for this study we further simplified the classification into grass and

shrub only, as shown in Figure 6-1(c). Vegetation is simulated by the *ptRIBS+VEGGIE* model as *spatially-static*, but *temporally dynamic*. Tables 6.3, 6.4 and 6.5 summarize the various vegetation parameters used by the model, which include biophysical, biochemical, allocation, phenology, water uptake and interception. A detailed description of these vegetation parameters for C<sub>4</sub> grass is provided in Ivanov et al. [2008a]. The corresponding vegetation parameters for C<sub>3</sub> shrubs were obtained from the Community Land Model (CLM) parameterization [Oleson et al., 2004].

Manual model calibration was performed to accurately capture the vegetation dynamics of C<sub>4</sub> grass and C<sub>3</sub> shrubs for smaller sub-watersheds nested within the WGEW at Kendall and Lucky Hills respectively. The goal of the calibration exercise was to better capture the start of growing season, duration of growing season and peak LAI during the growing season for both vegetation types. Simulations for sub-watersheds at Kendall and Lucky-Hills are carried out for the 11 years period (1997-2007) and basin average simulated vegetation dynamics were compared with the mean of the MODIS LAI pixels, lying within the sub-watersheds, for the period of 2000-2007. Several parameters were varied during the calibration procedure from the reported values in Ivanov et al. [2008a] and Oleson et al. [2004]. These parameters include: soil matric potential at which the stomatal closure begins,  $\Psi^*$ ; soil matric potential at which vegetation starts to wilt,  $\Psi_w$ ; temperature threshold below which cold-induced leaf loss begins,  $T_{cold}$ ; minimum days for which conditions of transition from/to the dormant season have to be met,  $\Delta T_{min,Fav}$ ; maximum drought induced foliage,  $\gamma_{Wmax}$ ; and maximum cold induced foliage,  $\gamma_{Cmax}$ . These parameters control the range over which photosynthesis uptake occurs and the stress caused by cold and drought, curtails growth activity. After the manual calibration was completed, the model simulations for the entire WGEW are carried using hourly meteorological variables from Kendall and Lucky Hills stations (except rainfall) at hourly time-step. Hourly rainfall data from 88 rain gages within the WGEW were used to drive the simulation.

Table 6.2: Soil parameterizations: Saturated hydraulic conductivity in the surface normal direction,  $K_{sn}$  [mm hr<sup>-1</sup>]; saturation moisture content,  $\theta_s$  [mm<sup>3</sup> mm<sup>-3</sup>]; residual moisture content,  $\theta_r$  [mm<sup>3</sup> mm<sup>-3</sup>]; pore size distribution,  $\lambda_o$  [dimensionless]; air entry bubbling pressure,  $\psi_b$  [mm]; dry soil thermal conductivity, porosity,  $n$  [mm<sup>3</sup> mm<sup>-3</sup>];  $k_{s,dry}$  [J m<sup>-1</sup> K<sup>-1</sup>]; saturated soil thermal conductivity,  $k_{s,sat}$  [J m<sup>-1</sup> K<sup>-1</sup>]; and soil heat capacity  $C_{s,soi}$  [J m<sup>-3</sup> K<sup>-1</sup>].

	Clay	Clay loam	Silty clay loam	Silty loam	Loam	Sandy loam	Loamy sand
$K_{sn}$	3.0	4.5	5.7	6.8	13.2	48	85
$\theta_s$	0.385	0.390	0.423	0.486	0.434	0.412	0.401
$\theta_r$	0.020	0.075	0.056	0.015	0.027	0.041	0.035
$\lambda_o$	0.165	0.242	0.15	0.234	0.553	0.755	0.553
$\psi_b$	-400	-260	-340	-210	-110	-140	-90
$n$	0.475	0.464	0.479	0.501	0.463	0.453	0.437
$k_{s,dry}$	0.189	0.196	0.196	0.196	0.196	0.196	0.214
$k_{s,sat}$	1.706	2.250	2.250	2.250	2.250	2.250	2.639
$C_{s,soi}$	2320750	2205100	2205100	2205100	2205100	2205100	2148443

Table 6.3: Vegetation biophysical and interception parameters:  $\chi_L$  is departure of leaf angles from a random distribution; Leaf reflectance and transmittance,  $\alpha_{\Lambda}^{leaf}$  [-] and  $\tau_{\Lambda}^{leaf}$  [-] respectively; Stem reflectance and transmittance,  $\alpha_{\Lambda}^{stem}$  [-] and  $\tau_{\Lambda}^{stem}$  [-] respectively; VIS and NIR denote visible and near-infrared spectral bands; Canopy water drainage rate coefficient,  $K_c$  [mm h<sup>-1</sup>]; Exponential decay parameter of canopy water drainage rate,  $g_c$  [mm<sup>-1</sup>]; and Specific leaf area,  $S_{la}$  [m<sup>2</sup> leaf area kg C<sup>-1</sup>] (For detail descriptions of the parameters, the reader is referred to Ivanov et al. [2008a].)

	C <sub>3</sub> Shrub	C <sub>4</sub> Grass
$\chi_L$	0.01	-0.30
$\alpha_{\Lambda}^{leaf}$ - VIS	0.10	0.11
$\alpha_{\Lambda}^{leaf}$ - NIR	0.45	0.58
$\alpha_{\Lambda}^{lstem}$ - VIS	0.16	0.36
$\alpha_{\Lambda}^{stem}$ - NIR	0.39	0.58
$\tau_{\Lambda}^{leaf}$ - VIS	0.05	0.07
$\tau_{\Lambda}^{leaf}$ - NIR	0.25	0.25
$\tau_{\Lambda}^{lstem}$ - VIS	0.001	0.22
$\tau_{\Lambda}^{stem}$ - NIR	0.001	0.38
$K_c$	0.18	0.10
$g_c$	3.90	3.20
$S_{la}$	0.011	0.020

Table 6.4: Biochemical parameters: Maximum catalytic capacity of Rubisco at 25<sup>0</sup>C,  $V_{max,25}$  [ $\mu\text{mol CO}_2 \text{ m}^{-2} \text{ leaf s}^{-1}$ ]; Mean time PAR extinction coefficient parameterizing decay of nitrogen content in canopy,  $\bar{K}$  [-]; Slope parameter,  $m$ [-]; Minimum stomatal conductance,  $b$  [ $\mu\text{mol CO}_2 \text{ m}^{-2} \text{ leaf s}^{-1}$ ]; Intrinsic quantum efficiency for CO<sub>2</sub> uptake for C<sub>3</sub> and C<sub>4</sub> plants,  $\epsilon_{3,4}$  [ $\mu\text{mol CO}_2 \mu\text{mol}^{-1} \text{ photons}$ ]; Sapwood and root tissue respiration at 10<sup>0</sup>C,  $r_{sapw}$  [g C g C<sup>-1</sup> s<sup>-1</sup>] and  $r_{root}$  [g C g C<sup>-1</sup> s<sup>-1</sup>], respectively; Fraction of canopy assimilation less maintenance respiration utilized for tissue growth,  $\omega_{sapw}$  [-]; Leaf turnover rate,  $d_{leaf}$  [year<sup>-1</sup>]; Stem turnover rate,  $d_{stem}$  [year<sup>-1</sup>]; and Root turnover rate,  $d_{root}$  [year<sup>-1</sup>]. (For detail descriptions of the parameters, the reader is referred to Ivanov et al. [2008a].)

	C <sub>3</sub> Shrub	C <sub>4</sub> Grass
$V_{max,25}$	35.0	30.0
$\bar{K}$	0.30	0.30
$m$	9	4
$b$	10000	40000
$\epsilon_{3,4}$	0.053	0.053
$r_{sapw}$	$9.61 \times 10^{-10}$	-
$r_{root}$	$1.09 \times 10^{-8}$	$4.0 \times 10^{-8}$
$\omega_{sapw}$	0.25	0.25
$d_{leaf}$	1	1
$d_{sapw}$	0.1	-
$d_{root}$	0.33	1.0

Table 6.5: Vegetation allocation, phenology and water uptake parameters: Maximum drought induced foliage,  $\gamma_{Wmax}$  [ $\text{day}^{-1}$ ]; Maximum cold induced foliage,  $\gamma_{Cmax}$  [ $\text{day}^{-1}$ ]; Shape parameter reflecting sensitivity for drought,  $b_W$  [-], and cold,  $b_C$  [-]; Temperature threshold below which cold-induced leaf loss begins,  $T_{cold}$  [ $^{\circ}\text{C}$ ]; Base allocation fraction for canopy,  $e_{leaf}$  [-], sapwood,  $e_{sapw}$  [-] and root,  $e_{root}$  [-]; Sensitivity parameter of allocation fractions to changes in light and soil availability,  $\varpi$  [-]; Parameters controlling the relation between carbon content in the above and below ground biomass,  $\xi$  [-] and  $\epsilon_s$  [-]; Mean daily soil temperature,  $\bar{T}_{soil}$  [ $^{\circ}\text{C}$ ], and day length,  $D_{LH}^C$  [hour], that have to be exceeded for the growing season to start; Minimum duration of period for which the conditions of transition from/to the dormant season have to be continuously met,  $\Delta T_{min,Fav}$  [day]; Fraction of structural biomass,  $f_{C,init}$  [-], and leaf area index,  $L_{init}$  [-], used to initiate the leaf onset; Soil matric potential at which stomatal closure,  $\Psi^*$  [Mpa], and plant wilting,  $\Psi_w$  [MPa], begins. (For detail descriptions of the parameters, the reader is referred to Ivanov et al. [2008a].)

	C <sub>3</sub> Shrub	C <sub>4</sub> Grass
$\gamma_{Wmax}$	1/10	1/15
$b_W$	4.0	4.0
$\gamma_{Cmax}$	1/6.67	1/6.67
$b_C$	3.0	3.0
$T_{cold}$	12	9.0
$e_{leaf}$	0.25	0.45
$e_{sapw}$	0.1	-
$e_{root}$	0.65	0.55
$\varpi$	0.8	0.7
$\xi$	1.6.0	1.0
$\epsilon_s$	2.0	1.25
$\bar{T}_{soil}$	5.0	5.0
$D_{LH}^C$	10.0	10.0
$\Delta T_{min,Fav}$	5.0	2.0
$f_{C,init}$	0.025	-
$L_{init}$	0.22	0.25
$\Psi^*$	-0.01	-0.01
$\Psi_w$	-2.8	-3.0

## 6.3 Model evaluation

### 6.3.1 Energy fluxes

At the Earth's surface, conservation of energy for snow-free surface (neglecting the energy of photosynthesis and storage effects), is given by:

$$R_{net} = LE + H + G \quad (6.1)$$

where  $R_{net}$  [ $\text{Wm}^{-2}$ ] is the net radiation,  $LE$  [ $\text{Wm}^{-2}$ ] is latent heat flux,  $H$  is sensible heat flux [ $\text{Wm}^{-2}$ ] and  $G$  [ $\text{Wm}^{-2}$ ] is the ground heat flux. Traditionally, soil moisture and streamflow are used as primary benchmarks to appraise the performance of a distributed hydrologic model. In this study, we use energy fluxes as additional benchmarking information to evaluate the ecohydrology model. The intention here is to demonstrate that the *ptRIBS+VEGGIE* model can potentially serve as a land surface parameterization scheme within a regional climate model. Therefore, it is important for this ecohydrology model to provide accurate estimates of net radiation, but also have the ability to correctly quantify the partitioning of net radiation into latent, sensible and ground heat fluxes. Additionally, vegetation type and amount impacts the energy and water balances by altering surface characteristics. The model thus has to demonstrate the capability to reasonably reproduce vegetation dynamics.

The ability of the *ptRIBS+VEGGIE* model to correctly quantify net radiation and its components is separately demonstrated over the grass-dominated Kendall and shrub-dominated Lucky Hills sub-watersheds in WGEW. The comparison between the modeled fluxes and the observations at the two stations is carried out at an hourly scale over the 10 years of study period (excluding 1997), except for days when the instruments malfunctioned and no data were recorded. The bias, root mean square error (RMSE) and correlation ( $R^2$ ) between hourly observed and simulated net radiation, latent heat, sensible heat and ground heat flux for Kendall and Lucky Hills are summarized in Table 6.6. In this study, the bias is computed as the modeled output minus observation for the variable under consideration.

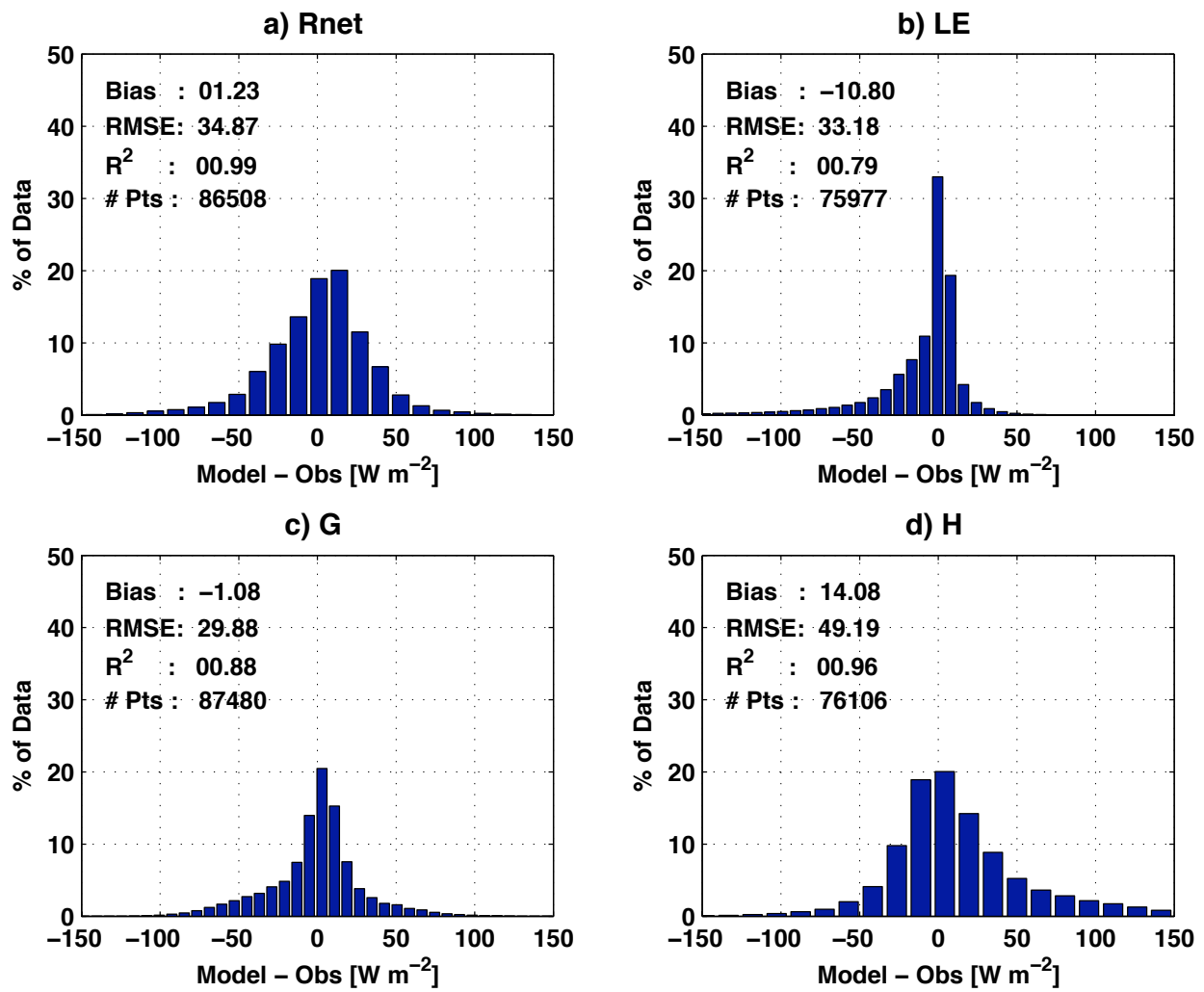


Figure 6-4: Hourly difference between *ptRIBS*+*VEGGIE* model and observations at grass-dominated Kendall station for (a) Net radiation; (b) Latent heat flux; (c) Ground heat flux; and (d) Sensible heat flux.



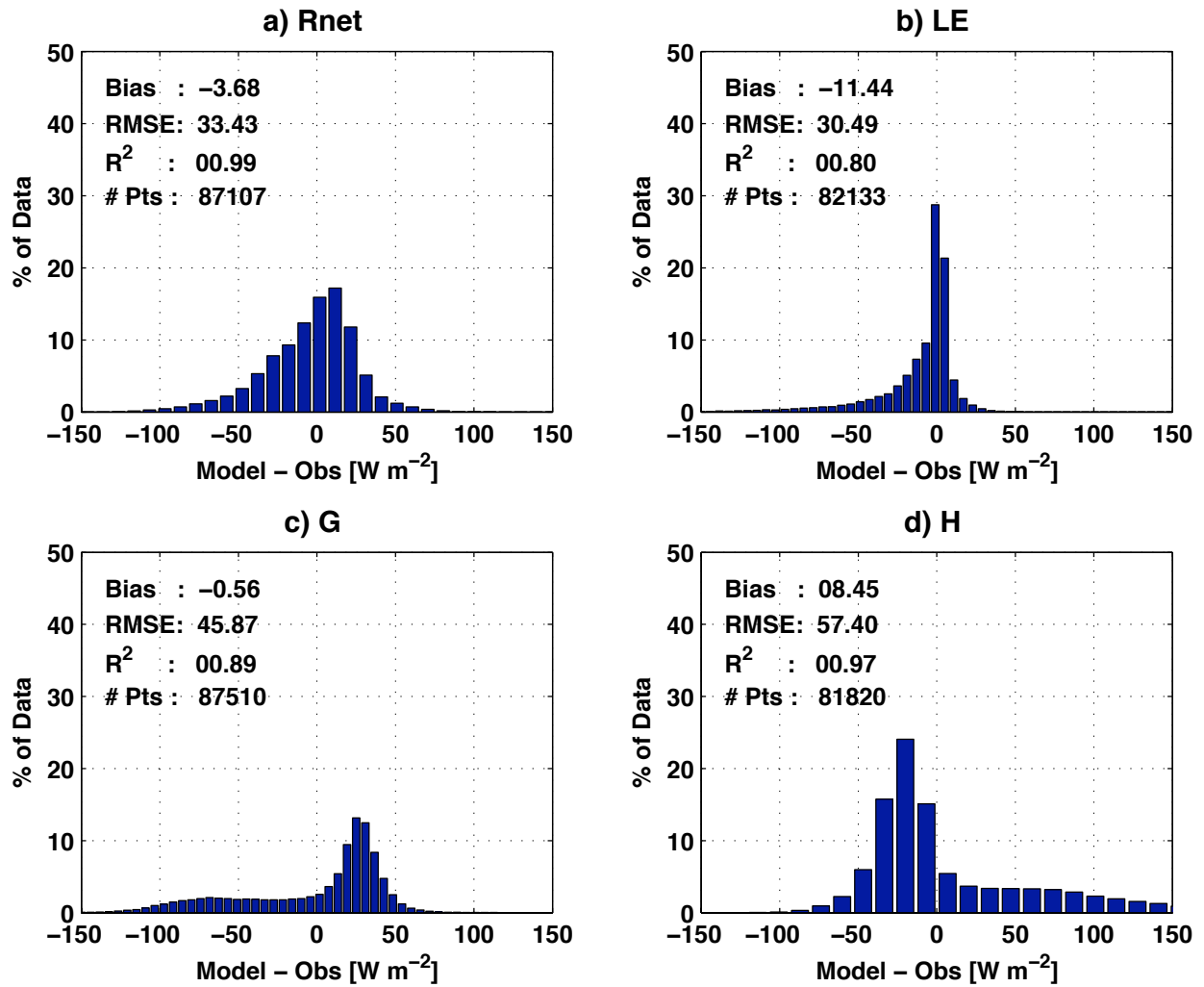


Figure 6-5: Same as Figure 6-4, except for shrub-dominated Lucky Hills station.

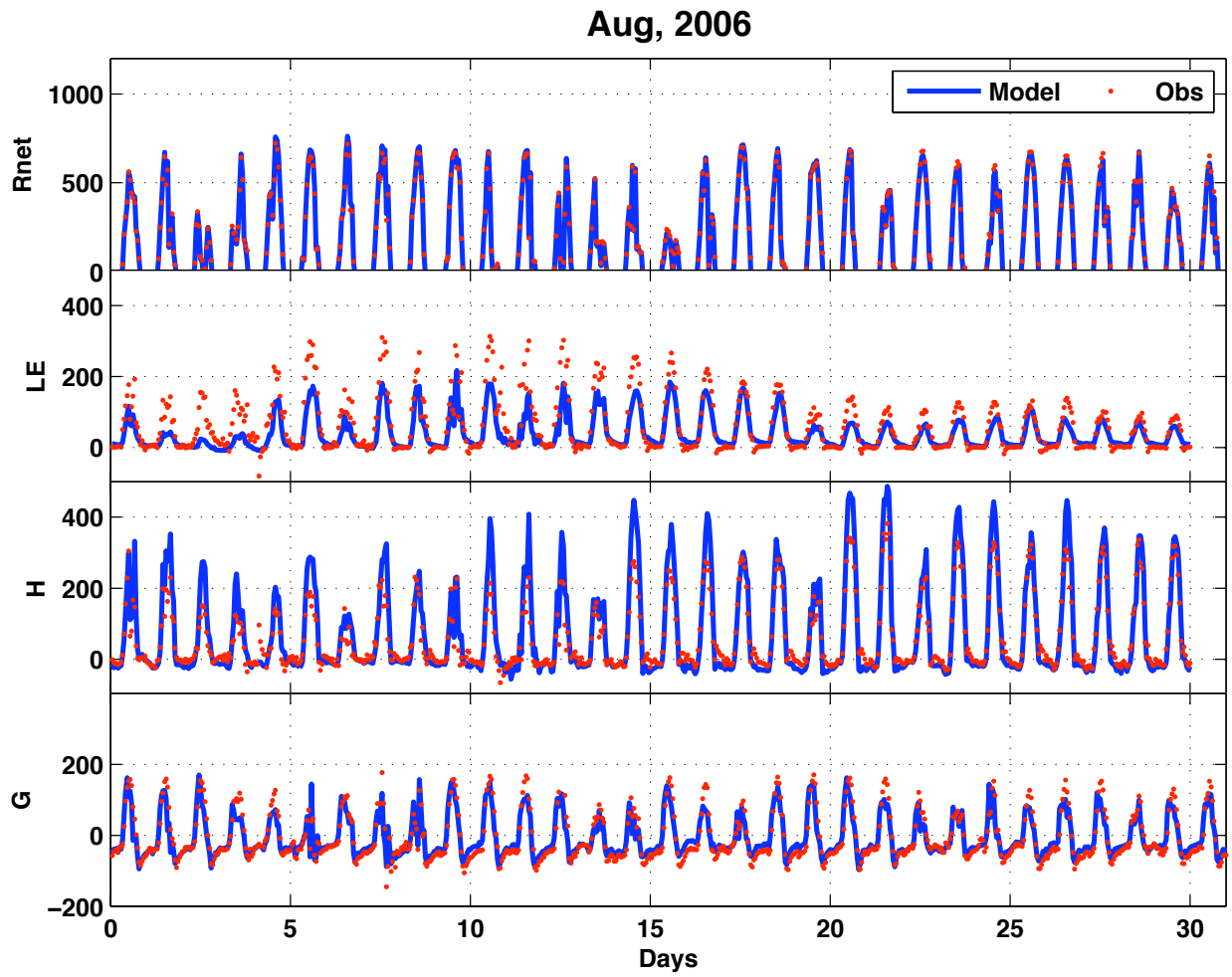


Figure 6-6: Hourly time-series for August, 2006 simulated by the *pt*RIBS+VEGGIE model (red) and observations (blue) at grass-dominated Kendall station for (a) Net radiation, (b) Latent heat flux (c) Sensible heat flux; and (d) Ground heat flux.

Aug, 2006

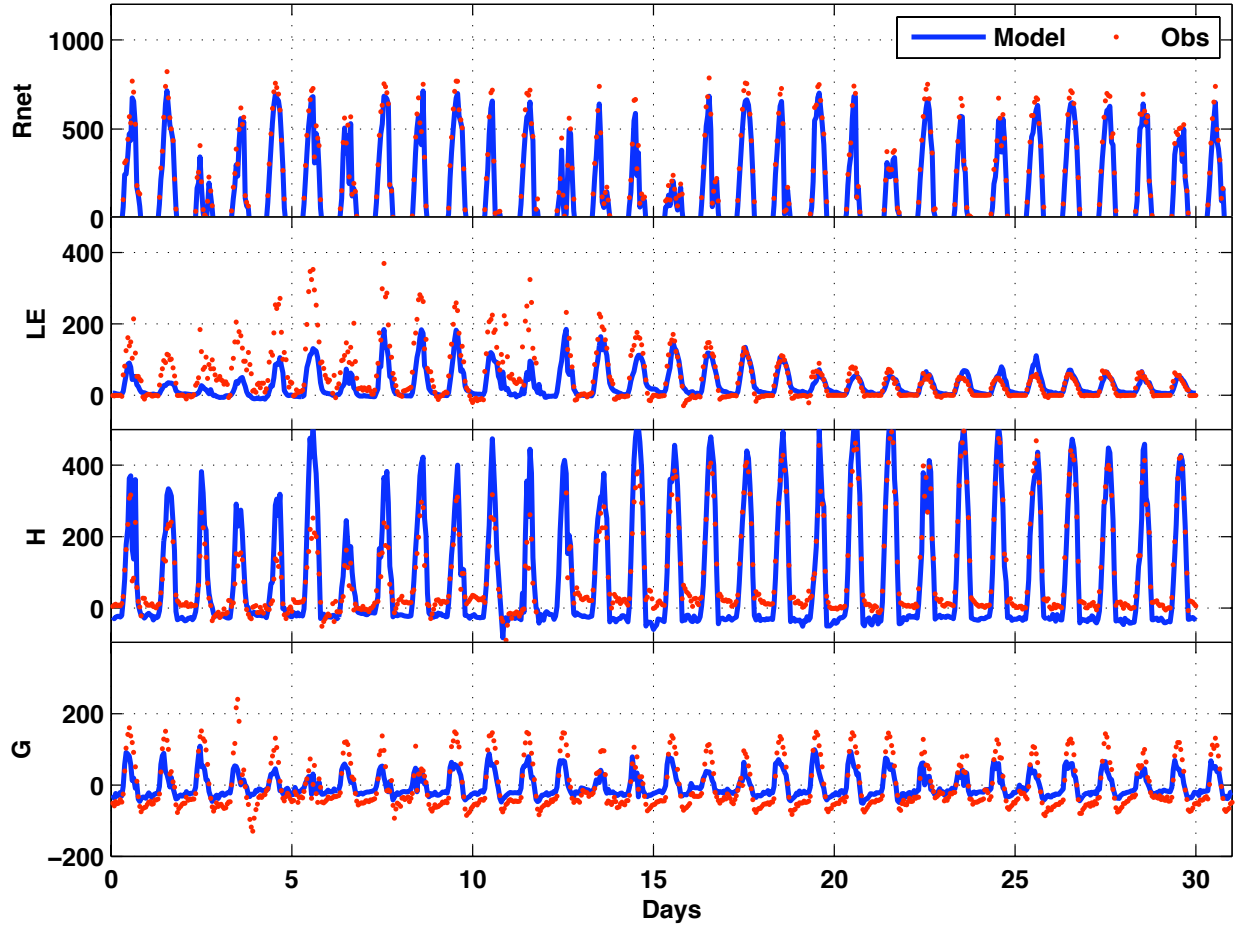


Figure 6-7: Same as Figure 6-6 except for Lucky Hills station.

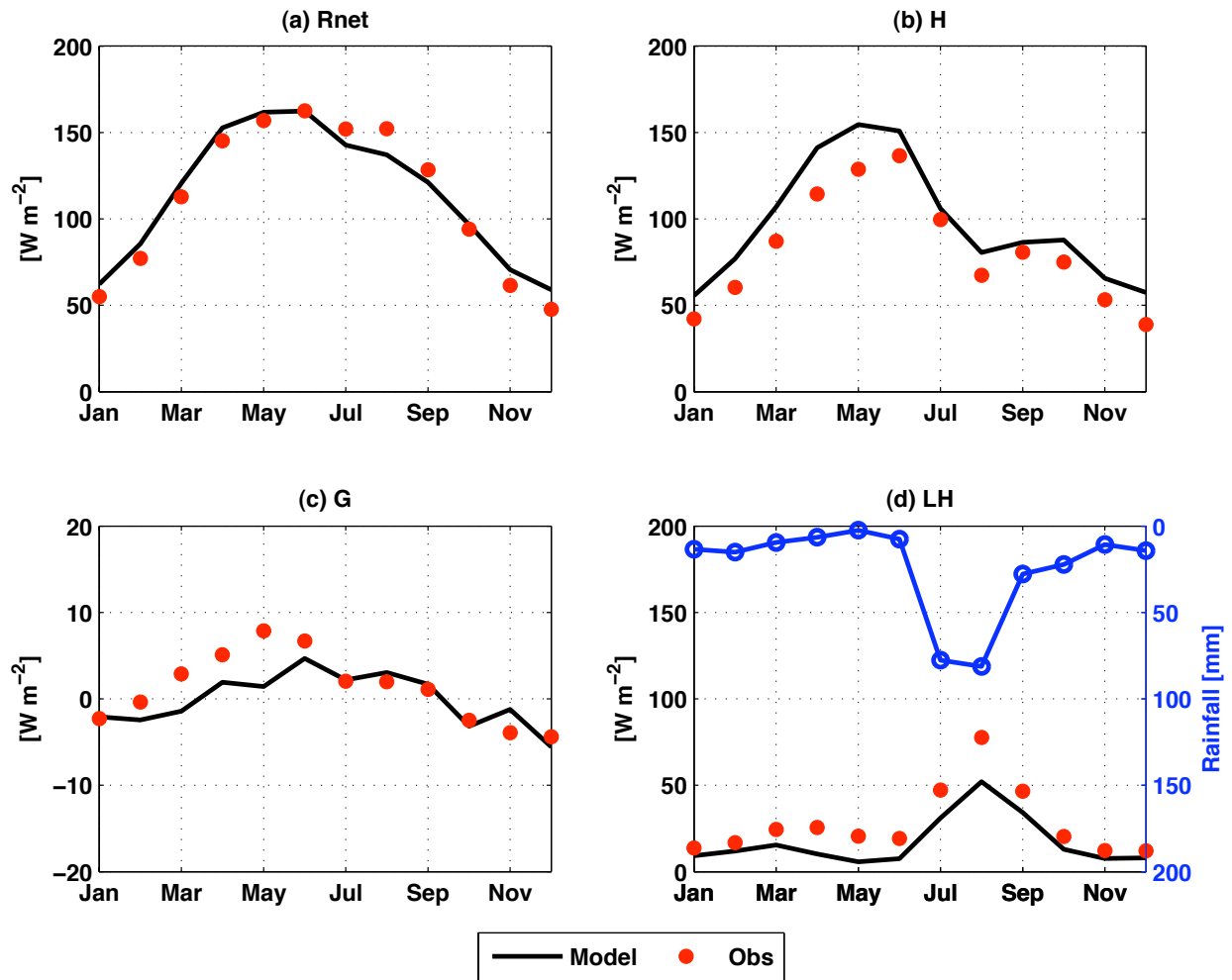


Figure 6-8: Monthly energy fluxes at grass-dominated Kendall: (a) Net radiation; (b) Latent heat flux; (c) Ground heat flux; and (d) Sensible heat flux

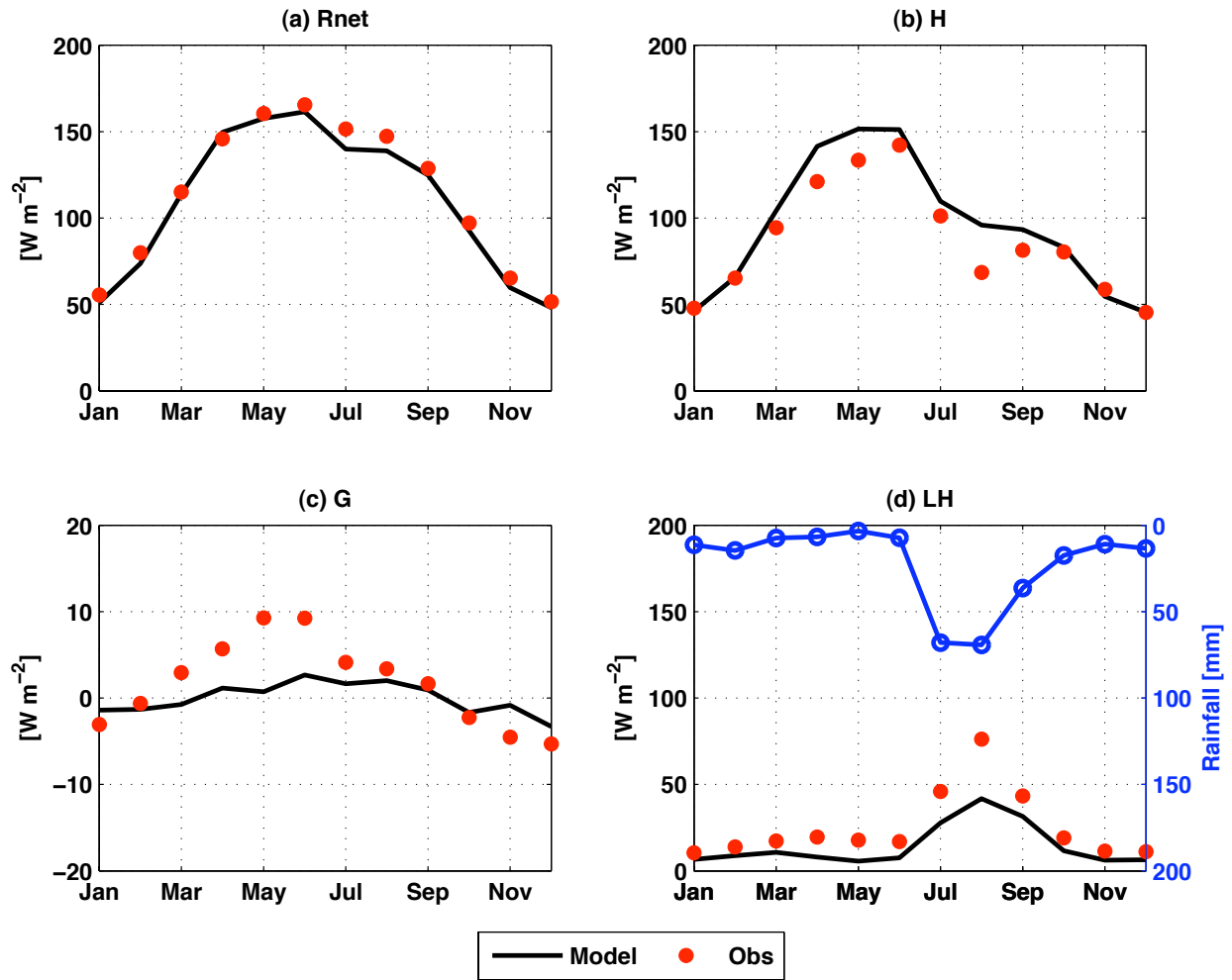


Figure 6-9: Same as Figure 6-8, except for shrub-dominated Lucky Hills station.

The point-scale measurements of energy fluxes show good agreement with the simulated energy fluxes over the period of 10 years. Histograms of the hourly error between modeled and observations energy fluxes are shown in Figure 6-4 and 6-5 for Kendall and Lucky Hills, respectively. Examples of the time-series of energy fluxes simulated and observed for Kendall and Lucky Hills stations are shown in Figure 6-6 and 6-7 for August, 2006.

In order to gain a better understanding of the model performance at a larger integration scale, we computed daily mean values for all energy fluxes. Subsequently, monthly-mean of mean daily values are computed across the 10 years of the study period (neglecting 1997) for both modeled and observed energy fluxes. The mean monthly energy fluxes for Kendall and Luck Hills are shown in Figure 6-8 and 6-9, respectively. As expected, the daily mean ground heat flux is close to zero. The latent heat flux of the semiarid climate of the study sites is also insignificant for most part of the year, except for pronounced monsoon in July and August. The model tends to underestimate latent heat flux when compared to observations in August at both, Kendall and Lucky Hills.

Table 6.6: Bias, RMSE and  $R^2$  for hourly net radiation ( $R_{net}$ ), latent heat flux (LH), ground heat flux (G) and sensible heat flux (H) for Kendall and Lucky Hills between the hourly observations and *ptRIBS+VEGGIE* simulations for 1997-2007.

	Kendall			Lucky Hills		
	Bias [ $Wm^{-2}$ ]	RMSE [ $Wm^{-2}$ ]	$R^2$	Bias [ $Wm^{-2}$ ]	RMSE [ $Wm^{-2}$ ]	$R^2$
Rnet	-1.2	$\pm 34$	0.99	-5.7	$\pm 33$	0.99
LH	-10.8	$\pm 33$	0.79	-11.4	$\pm 30$	0.77
G	-1.1	$\pm 30$	0.88	-0.6	$\pm 46$	0.94
H	14.1	$\pm 49$	0.96	8.5	$\pm 57$	0.97

### 6.3.2 Soil moisture

In this section, we present a comparison between the observed and simulated daily volumetric soil moisture at 19 stations within the WGEW, spanning over a period of six years, 2002-2007. Data that were used are summarized in Table 6.1. The number of stations representing

Table 6.7: Bias, RMSE and  $R^2$  for the daily volumetric soil moisture between modeled and observations for 2002-2007 at various soil depths. The comparison was carried for all station within each of the four soil-type classes and separately for Kendall and Lucky Hills site.

	Depth [cm]	Bias [mm <sup>3</sup> mm <sup>-3</sup> ]	RMSE [mm <sup>3</sup> mm <sup>-3</sup> ]	R <sup>2</sup>
Sandy loam	5	0.01	±0.03	0.84
	15	-0.05	±0.06	0.57
	30	-0.03	±0.07	0.42
Loam	5	0.02	±0.04	0.86
	15	0.02	±0.03	0.83
	30	0.00	±0.03	0.61
Clay	5	0.01	±0.04	0.84
	15	-	-	-
	30	-	-	-
Silty clay loam	5	0.04	±0.04	0.86
	15	-	-	-
	30	-	-	-
Kendall	5	0.02	±0.04	0.83
	15	0.02	±0.02	0.83
	30	0.00	±0.03	0.61
Lucky Hills	5	0.01	±0.03	0.80
	15	0.00	±0.03	0.71
	30	0.03	±0.03	0.45

a particular soil type varies: sandy loam (3, 13, 40, 46, 57, 69, 70, 76, 83, 92), clay (28, 37), loam (18, 82), and silty clay loam (14, 20, 34, 89, 100). All of the 19 stations had soil moisture measurements at 5 cm depth, but only 3 stations (46, 82 and 83) had measurements at the depths of 15 and 30 cm. For the purpose of this analysis, we compare the point observations of soil moisture with the closest Voronoi polygon within the computational domain. The quantitative comparisons of simulated and point-scale soil moisture observations for the four soil types and separately for Kendall and Lucky Hills sites are reported in Table 6.7. The agreement between the model and observations is best at 5 cm and slightly deteriorates for deeper soil depths. The time-series of rainfall and volumetric soil moisture, observed as well as simulated, at depth of 5, 15 and 30 cm, at Kendall and Lucky Hills are shown in

Figure 6-10 and 6-11 respectively. Overall, the model captures the timing and magnitude of the observed soil moisture with depth at both locations. It should also be noted that it is very difficult to make highly accurate, replicated observations of soil moisture due to the high percentage of rocks (>2mm) in the soil matrix and associated problems of contact between continuously sensing soil moisture monitoring probes [Paige and Keefer, 2004]. This results in substantial uncertainties in the observed soil moisture values. These results indicate that the physically-based distributed model is able to reproducing consistent soil moisture conditions for different soil types. Note that only a minimum calibration effort has been carried out, thus holds the promise for using the model for less studied watersheds with little observational information.

### **6.3.3 Land surface temperature**

Land surface temperature is another key parameter in the physics of land-surface processes and in this section we contrast our model simulated LST against ground-based and space-based observations. The four ground stations that recorded skin surface temperature over 2004-2007 in the WGEW are listed in Table 6.1. The comparison of hourly the modeled LST and observations is carried out for the day and night hours separately. The scatter plot and accompanying error histogram are shown in Figure 6-12; while the bias, RMSE and  $R^2$  are summarized in Table 6.8. The result shows that the model tends to under-estimate the peak surface temperature during the day; while over-estimating the surface temperature at night. The RMSE for surface temperature at night is much lower than during the night.

Space-based observations of LST have an advantage of a large spatial coverage, though being temporally sparse. The MODIS LST product is generally available twice during the day and twice during the night, provided the region had clear-sky conditions at the overpass time. We examined the performance of our model estimated LST against MODIS LST product. Before undertaking such a comparative analysis, we evaluated the performance of the MODIS LST product against the point observations of surface temperature. Figure 6-13 (a) and (b) show the error histogram between the MODIS LST product and point-observations for 2004-



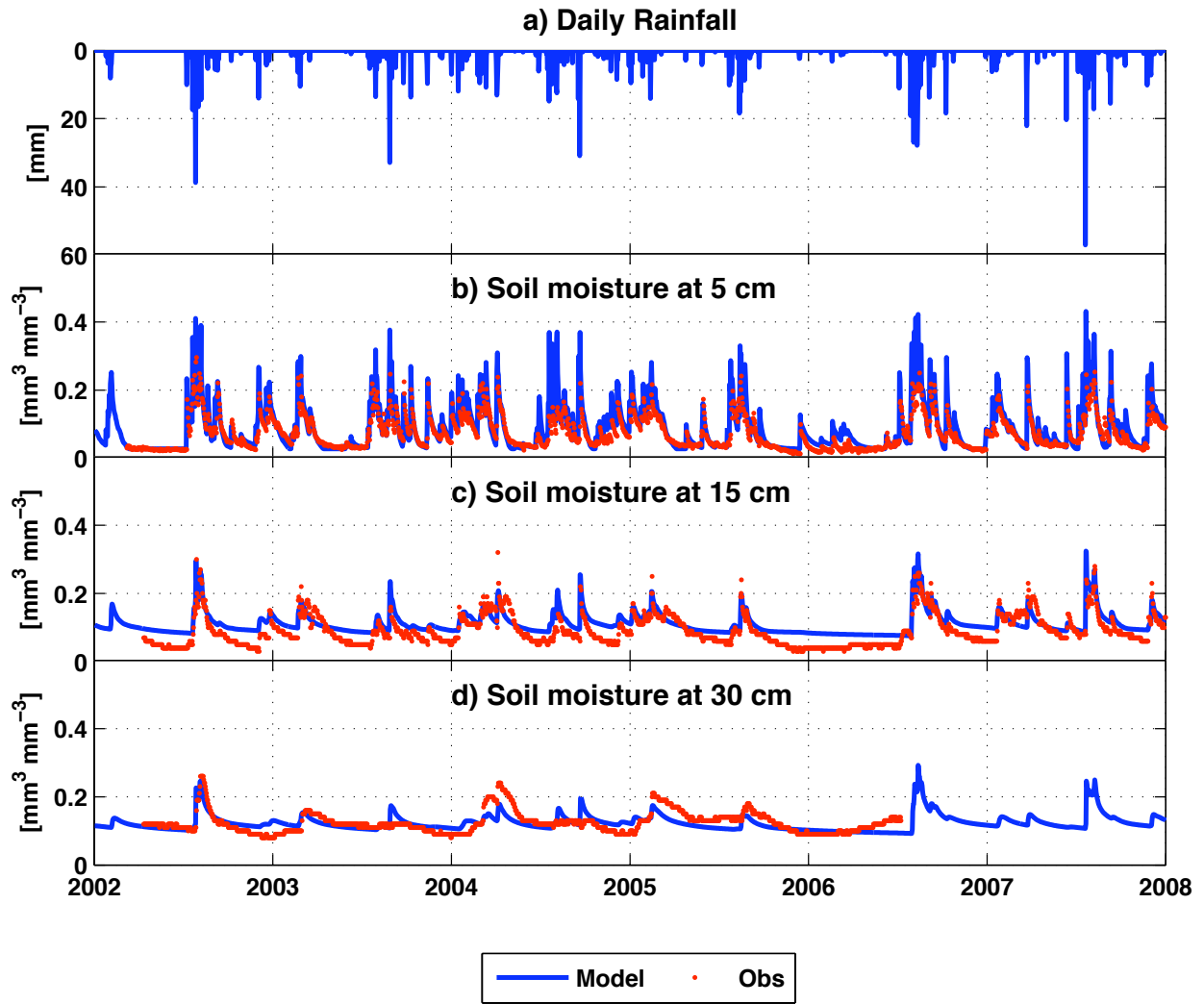


Figure 6-10: Time-series of (a) daily rainfall; and daily volumetric soil moisture, modeled along with observations, at Kendall station at varying soil depths: (b) 5cm; (c) 15cm; and (d) 30cm respectively.

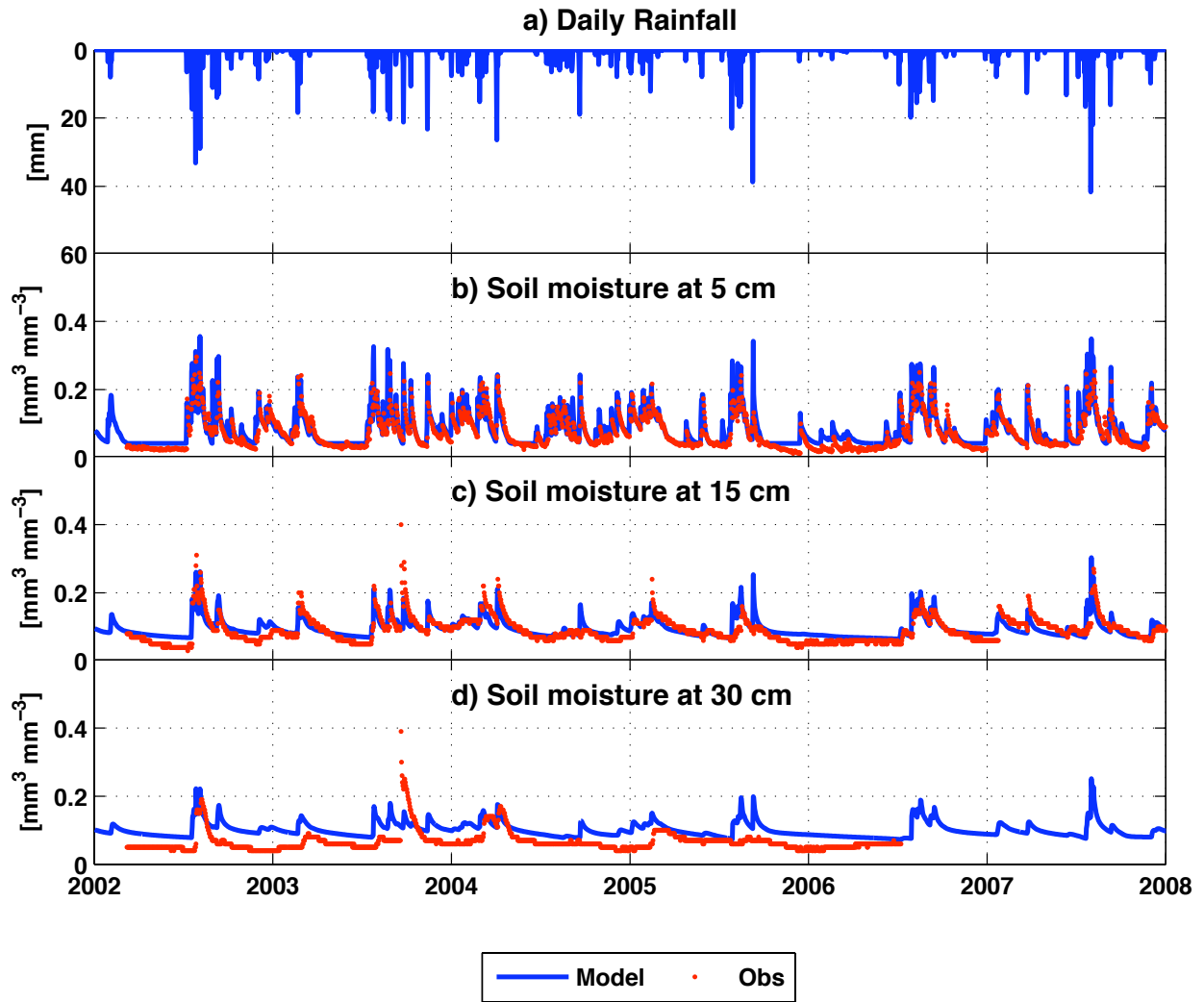


Figure 6-11: Same as Figure 6-10, except for Lucky Hills.

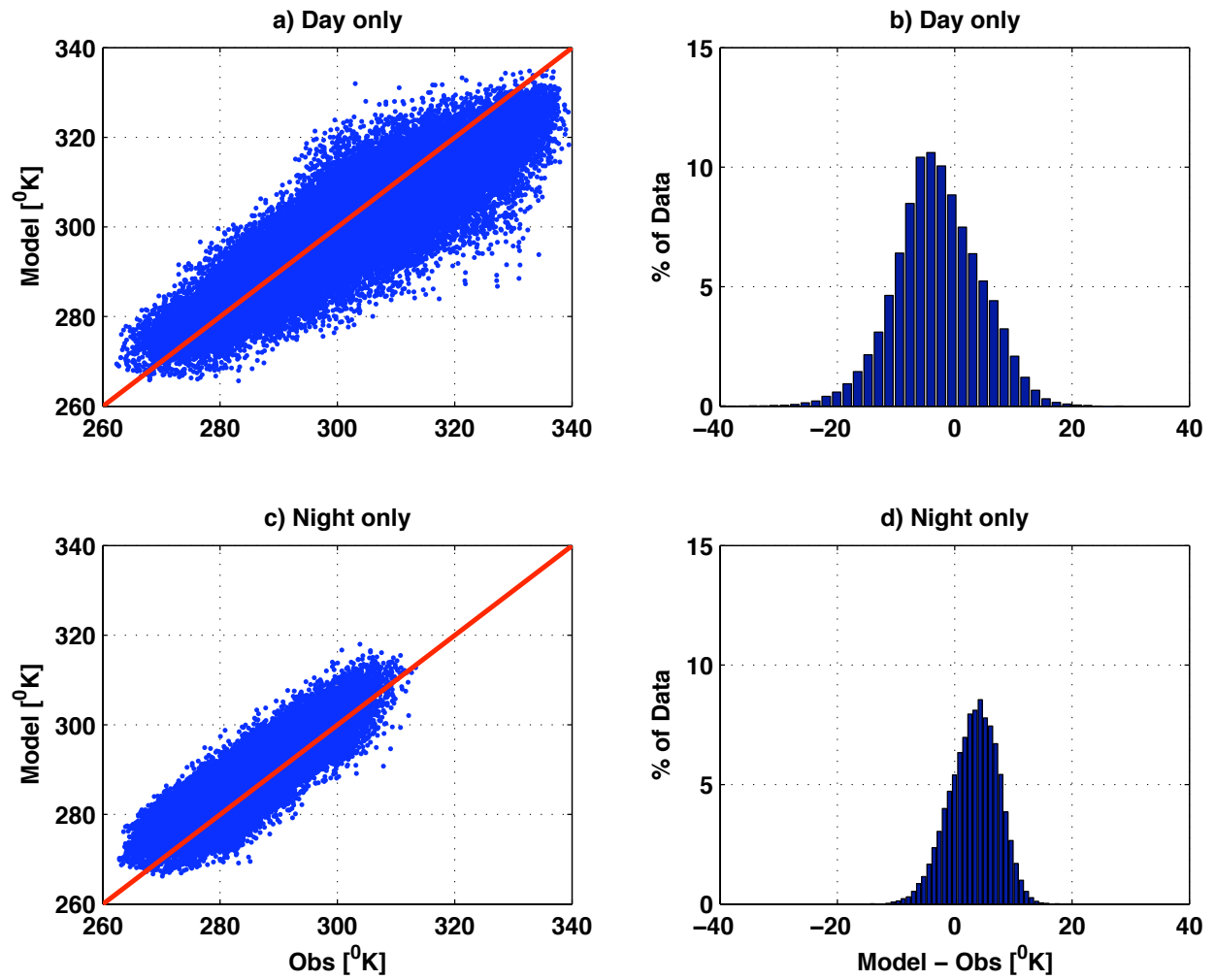


Figure 6-12: Hourly surface temperature comparison between the modeled and ground observations. Scatter plots and error histogram during daytime are shown in (a) and (b), respectively; while (c) and (d) comparison during nighttime.

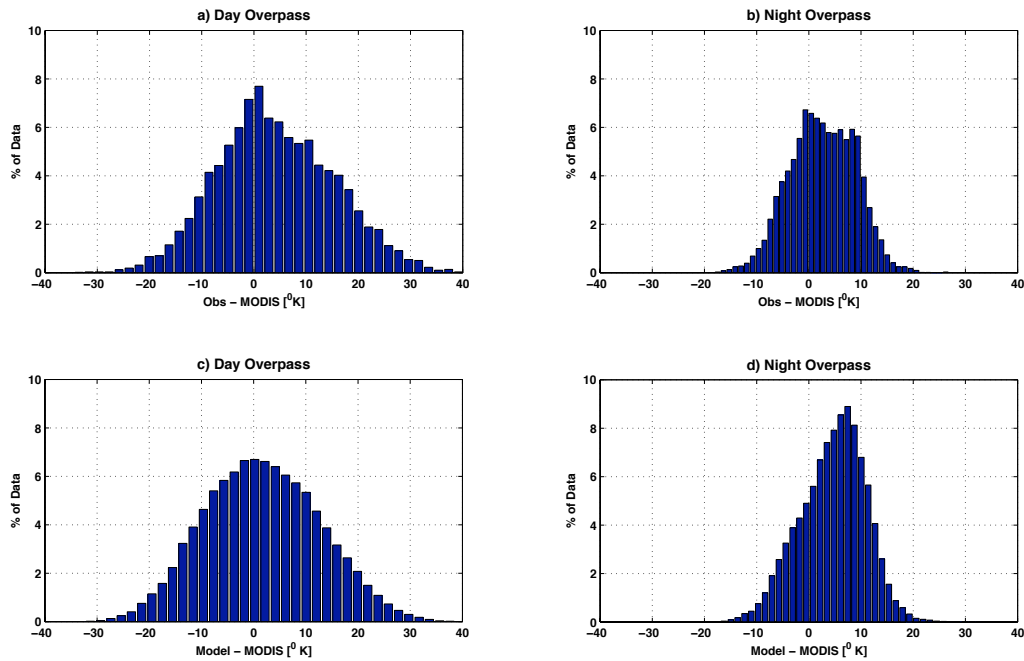


Figure 6-13: Evaluation of the MODIS-derived land surface temperature (LST) product. Error histogram for the MODIS-LST with respect to ground observations for day and night overpasses shown in (a) and (b) respectively; while (c) and (d) show the error histogram for the MODIS-LST with respect to upscaled modeled surface temperature for day and night overpasses.

Table 6.8: Bias, RMSE and  $R^2$  for land surface temperature: (a) *ptRIBS+VEGGIE* modeled output against ground observations at hourly interval (2004-2007); (b) MODIS LST product against ground observation for day and night overpasses (2004-2007); and (c) *ptRIBS+VEGGIE* modeled output against MODIS LST product for day and night overpasses (2001-2007); (d) Upscaled *ptRIBS+VEGGIE* modeled output at 1km resolution against MODIS LST product for day and night overpasses (2001-2007).

		Bias [°K]	RMSE [°K]	$R^2$
(a) Modeled - Observation	Day only	-3.0	$\pm 7.2$	0.87
	Night only	3.2	$\pm 4.1$	0.89
(b) Observation - MODIS	Day only	4.0	$\pm 11.0$	0.46
	Night only	3.0	$\pm 6.3$	0.60
(c) Modeled - MODIS	Day only	-0.4	$\pm 10.0$	0.37
	Night only	5.0	$\pm 6.3$	0.54
(d) Upscaled Modeled - MODIS	Day only	1.2	$\pm 11.0$	0.40
	Night only	5.2	$\pm 6.3$	0.56

2007; while Table 6.8 quantifies the results. The results show high RMSE for day and night overpasses; while the correlation is low, especially for the day overpasses. The comparison of the upscaled modeled LST to match with the MODIS LST at 1km resolution did not provide any significant improvements. Figure 6-13 (c) and (d) show the error histogram between the MODIS LST and upscaled modeled surface temperature. Even though modeled LST compared well with point observations, the MODIS-LST products did not have significant agreement with point observations, as well as, upscaled modeled LST.

### 6.3.4 Vegetation dynamics

The North American monsoon contributes the majority of annual rainfall in the southwest U.S. and the northwest Mexico, which leads to a dramatic vegetation response in the region [Watts et al., 2009, Vivoni et al., 2008]. These vegetation dynamics are known to strongly impact the surface energy balance of radiation, heat and moisture. In this section, we evaluate the performance of the *ptRIBS+VEGGIE* in capturing the vegetation dynamics

for two plant functional types:  $C_4$  grass and  $C_3$  shrubs, present within the WGEW. The MODIS LAI eight-days product from the Terra satellite was used to compare the model performance over the period of 7 years, 2001-2007. Time-series of modeled LAI (mean value as a solid black line, with gray region denoting one standard deviation from the mean) and the MODIS-LAI product (as red dots) for grass-dominated and shrub-dominated region are shown in Figure 6-14 (a) and (b), respectively. The model was able to capture the timing of the start of the growing season, the magnitude of peak LAI, and the length of the growing season quite well over the analysis period. The *ptRIBS+VEGGIE* model simulates live-biomass and thus during dry months the near-zero LAI corresponds to absence of any live biomass. The model reproduced the trend of decreasing maximum LAI from 2000 to 2004 and increasing maximum biomass from 2004 onwards. The model was able to replicate the response vegetation to spring rainfall in 2001 and 2004 as observed by the MODIS data. The overall  $R^2$  between the simulated and the MODIS LAI are 0.77 and 0.76 for grasses and shrubs, respectively. Recognizing the uncertainty in the derived LAI products, the above mentioned results imply that the *ptRIBS+VEGGIE* model is able to successfully capture the amount, as well as, the dynamics of vegetation.

Recognizing the uncertainty in the derived LAI products, the above mentioned results imply that the *ptRIBS+VEGGIE* model is able to successfully capture the amount, as well as, the dynamics of vegetation.

## 6.4 Conclusion

Distributed, physically-based ecohydrologic models are key tools in understanding land-surface processes and their interaction with the atmosphere. High performance computing has enabled the application of hydrologic models at large spatio-temporal scales. In this study, we investigate whether the framework that combines a dynamic vegetation and a physically-based hydrologic model (*ptRIBS+VEGGIE*), that takes advantage of HPC, is capable of capturing hydrologic signatures and vegetation dynamics in a semi-arid region. The WGEW in Arizona was chosen as the study site and simulations were carried out for a

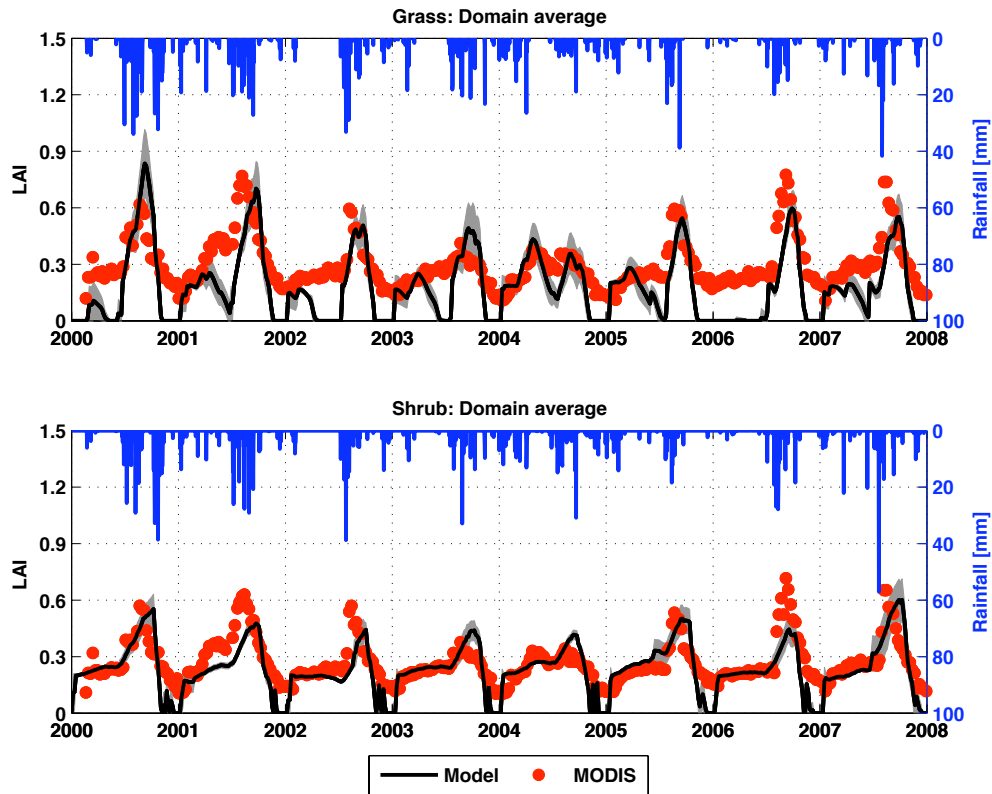


Figure 6-14: Comparison between modeled leaf area index (LAI) and MODIS-LAI for grass-dominated Kendall and shrub-dominated Lucky-Hills sites.

period of 11 years (1997-2007). Weather station data from two sites in the WGEW: grass-dominated Kendall and shrub-dominated Lucky Hills; along with 88 distributed rain gages is used as forcing data for the model simulation. The model performance was benchmarked with respect to various hydrologic variables: energy fluxes, soil moisture and land surface temperature. The model is not only able to estimate net radiation at the land surface accurately, but also correctly quantified the partitioning of it into latent, sensible and ground heat fluxes at Kendall and Lucky Hills.

Quantitative comparison between simulated and measured soil moisture at 5, 15 and 30 cm depth were in good agreement for different soil types. High correlation was observed between simulated land surface temperature and measurements, including day and night observations. The model was however unable to capture the diurnal range of surface temperature by under-predicting during day and over-predicting during night. The MODIS LST 1-km product did not show a good agreement with ground-observations. The MODIS LST product did not have a significant agreement with the point scale and upscaled 1-km modeled LST. The *ptRIBS+VEGGIE* model was able to capture the timing of the start of the growing season; magnitude of peak LAI; and the length of the growing season when compared against the MODIS LAI product. The results presented here demonstrate the ability of the *ptRIBS+VEGGIE* model to successfully capture hydrologic and ecologic signatures.

This study also shows that the *ptRIBS+VEGGIE* model transcends classical hydrology applications and has the potential of being used as a land surface parameterization scheme within a RCM to study land-atmosphere interactions. At the same time, we need to acknowledge the limitations of the present version of the *ptRIBS+VEGGIE* model. Ground water table dynamics, which are not modeled presently, are shown to have significant impact on soil moisture in certain geographical locations [Chen and Kumar, 2001]. The lack of snow dynamics also curtails the application of the current version of the model to snow-free regions. Though, it should be pointed out that a snow module is available for the *tRIBS* model [Rinehart et al., 2008] and has not been presently incorporated within the *ptRIBS+VEGGIE* model. Nutrient cycling is also not accounted for as a possible limiting



resource in vegetation dynamics. These limitations of the *ptRIBS+VEGGIE* model were not important during its application in the WGEW, which being a semi-arid region has little influence of water table on surface processes. It is also assumed that water-limitation is the dominant factor controlling vegetation growth in the WGEW. Though runoff observations are available from various locations within the WGEW, in this study modeled runoff was not compared against observations. The reason for not performing the runoff comparison is that ephemeral channel transmission losses play an important role in the WGEW [Goodrich et al., 2004]; and these channel losses are currently not modeled within the *ptRIBS+VEGGIE*. These present limitations of the *ptRIBS+VEGGIE* model need to be addressed in the future in order to expand the geographical regions where the model could be used to study hydrologic and vegetation dynamics. Nonetheless, the *ptRIBS+VEGGIE* model is able to capture hydro-climatic signature and vegetation dynamics in a semi-arid region.



# CHAPTER 7

# WRF - *pt*RIBS+VEGGIE SIMULATIONS

This chapter describes a series of synthetic experiments that investigate the effect of incorporating vegetation dynamics and topography on hydro-climatology over large river basins. The configuration of the three synthetic experiments conducted is explained first, followed by a description of the coupled model (WRF - *pt*RIBS+VEGGIE) setup. Results are presented for each of the three cases next, followed by a discussion.

## 7.1 Synthetic experiments

### 7.1.1 Design of synthetic experiments

The land and atmosphere are fundamentally coupled through the exchange of heat, momentum and water at the the boundary. Prior studies have looked at the feedbacks between soil moisture, vegetation, topography, and climate by considering either two or three of the

Table 7.1: Description of synthetic experiments

Experiment	Description
FLAT-STAT	Flat Earth and Static vegetation
TOPO-STAT	Observed topography and Static vegetation
TOPO-DYN	Observed topography and Dynamic vegetation

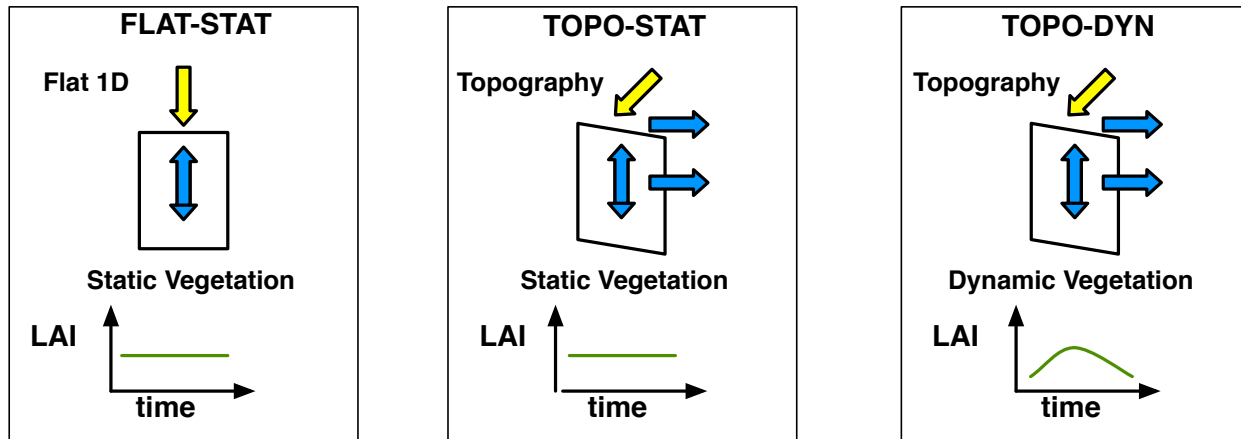


Figure 7-1: Schematic representation of physical processes accounted within the three synthetic experiments. (a) Static vegetation with flat Earth assumption. (b) Topographic effects on surface radiation and lateral redistribution of moisture (above- and below-ground) are accounted, while keeping static vegetation cover. (c) Accounting for both, vegetation dynamics and topographic effects.

components coupled together. In this work, a series of three experiments (see Table 7.1) are designed to investigate the impacts of regional scale feedbacks between vegetation (modulated by topography and soil moisture) and atmosphere at seasonal to inter-annual timescale. In the first experiment, it is assumed that the Earth’s surface is flat and vegetation cover is prescribed, static in time and space. In this work, the term “flat Earth” does not imply an absence of orography within the computational domain, but it mainly refers to the lack of accounting for two physical processes at the land surface: lateral redistribution of soil moisture (via subsurface and overland flow); and the impact of local terrain (through slope and aspect) on downwelling solar shortwave radiation. In the second experiment, we use observed topography available from the Digital Elevation Models (DEMs), while keeping the vegetation static. The second experiment investigates how explicitly accounting for topography influence the hydro-climatic patterns within the coupled model. The third experiment allows vegetation to respond to climate, while simultaneously using the observed topography. A schematic representation of the various physical processes accounted for within the three synthetic experiments is shown in Figure 7-1.

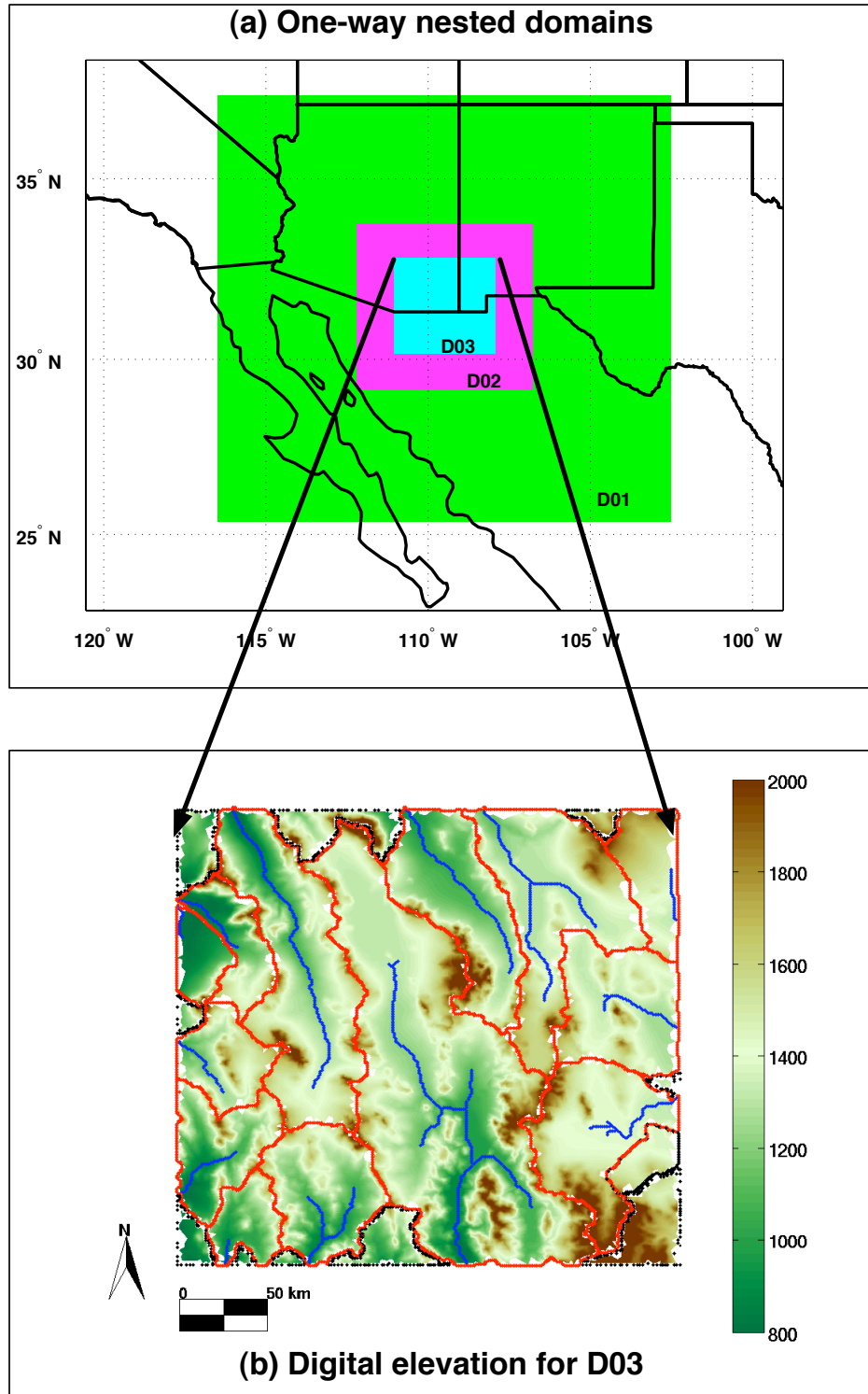


Figure 7-2: Modeling domain over the Southwestern United States. (a) One-way nested domains for simulations. Domain 1 (D01), Domain 2 (D02) and Domain 3 (D03) have grid spacing of 27-km, 9-km and 4.5-km, respectively. (b) Delineated watersheds used by the *ptRIBS+VEGGIE* model for D03.

### 7.1.2 Nested domains

In this study, we perform one-way nested simulations using the WRF model version 3.0 over the Southwestern United States and part of Mexico at a spatial resolutions of 27, 9 and 4.5 km respectively, as shown in Figure 7-2 (a). Several studies have documented the role of soil moisture in promoting rainfall during the North American Monsoon (NAM) over the Southwestern United States [Hong and Pan, 2000, Kurc and Small, 2007, Vivoni et al., 2007, 2008]. On the two outer domains, D01 and D02, simulations are carried using the Noah land surface scheme; while on the innermost D03 domain simulation are performed using the *ptRIBS+VEGGIE* model as the land surface scheme. Thirty vertical levels in the atmosphere are used. The initial and lateral boundary conditions are derived from the North American Regional Reanalysis (NARR) dataset for the outermost domain [Mesinger et al., 2006]. The other physics parameterization options used for the coupled model include: (i) microphysics scheme by Lin et al. [1983], (ii) cumulus parameterization scheme by Kain and Fritsch [1990], (iii) the Yonsei University Planetary Boundary Layer scheme [Hong and Pan, 1996], (iv) longwave radiation based on the Rapid Radiative Transfer Model scheme [Mlawer et al., 1997] and (v) shortwave radiation based on the Goddard scheme [Chou and Suarez, 1994]. No convective parameterization scheme is used for the D03 domain.

One-way nested simulations on domains, D01 and D02, are carried out from 1 Jan, 2000 to 1 Jan, 2004 with the WRF model using the Noah land surface scheme. Year long simulations on the innermost D03 domain are carried, separately for years 2001 and 2003, using the WRF - *ptRIBS+VEGGIE* model. The reason for not performing a continuous simulation spanning 2001 to 2003 on D03 is due to the computational demand the WRF - *ptRIBS+VEGGIE* model. Separate simulation runs for two different years on the D03 allowed the simulations to be started simultaneously. The results presented in section 7.2 will only focus on those obtained from the WRF - *ptRIBS+VEGGIE* model on D03.

Table 7.2: Soil hydraulic and thermal properties: Saturated hydraulic conductivity in the surface normal direction,  $K_{sn}$ [mm hr<sup>-1</sup>]; saturation moisture content,  $\theta_s$ [mm<sup>3</sup> mm<sup>-3</sup>]; residual moisture content,  $\theta_r$ [mm<sup>3</sup> mm<sup>-3</sup>]; pore size distribution,  $\lambda_o$  [dimensionless]; air entry bubbling pressure,  $\psi_b$ [mm]; dry soil thermal conductivity,  $k_{s,dry}$ [J m<sup>-1</sup> K<sup>-1</sup>]; saturated soil thermal conductivity,  $k_{s,sat}$ [J m<sup>-1</sup> K<sup>-1</sup>]; and soil heat capacity  $C_{s,soi}$ [J m<sup>-3</sup> K<sup>-1</sup>] (Obtained from Ivanov [2006]).

Parameter	$K_{sn}$	$\Theta_s$	$\Theta_r$	$\lambda_0$	$\Psi_b$	$k_{s,dry}$	$k_{s,sat}$	$C_s$
Sand	235.0	0.417	0.02	5.92	-73	0.214	2.789	1202632

### 7.1.3 Topography data

The input mesh, required by the *ptRIBS+VEGGIE* model for the D03, is generated from a 1-km DEM using a watershed delineation package. The watershed delineation package consists of several modules within the ESRI ArcGIS and is developed to delineate watersheds within a rectangular domain. The delineation of watersheds and constructing TINs describing topography and extracting channel network within the watersheds, is a tedious process and ArcGIS modules automate this process fully. The D03 domain consists of 24 watersheds, which have connectivity between nodes based on flow direction as shown in Figure 7-2 (b). A channel network (shown in blue), based on a flow accumulation threshold, is also overlaid on the figure and each watershed has an outlet where the channel network intersects the boundary of the rectangular domain. Figure 7-2 (b) also shows watersheds with black boundaries, where it is not possible to designate a single outlet with sufficient upstream contributing area.

### 7.1.4 Soils and vegetation type

In order to keep the number of independent factors influencing the outcome of this study, we assume homogeneous soil and vegetation type within the entire the D03 domain for simulations with the WRF - *ptRIBS+VEGGIE* model. The soils are assumed to sandy soils, whose hydraulic and thermodynamic properties are obtained from Ivanov [2006], and are provided in Table 7.2. The vegetation is assumed to be a generic C<sub>4</sub> grass and the various vegetation parameters required by the model, are obtained from the validation exercise of

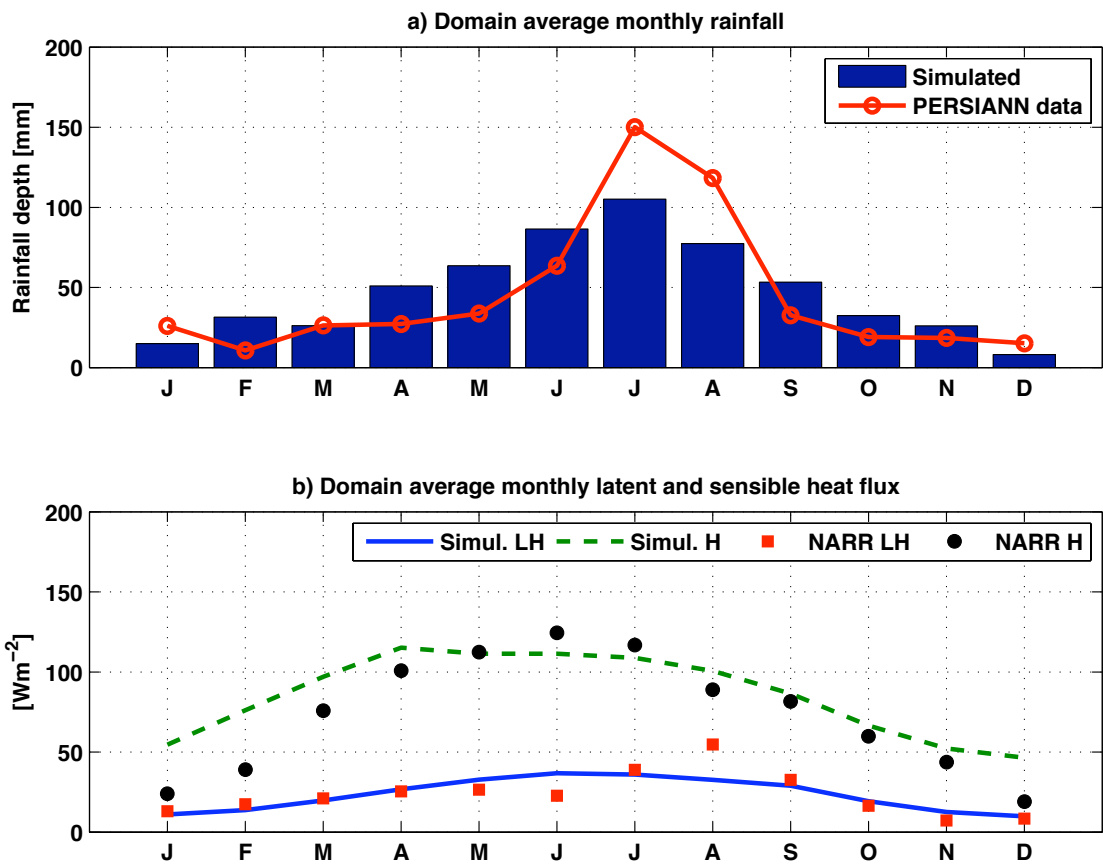


Figure 7-3: Timeseries of various simulated quantities for 2001 by the WRF - *pt*RISB+VEGGIE model. Panel (a) shows domain average simulated monthly precipitation, along with the estimates obtained from the PERSIANN data over the same region. Panel (b) shows simulated domain average latent and sensible heat fluxes, along with the estimates from the NARR data.



the *ptRIBS+VEGGIE* model over the WGEW (see Chapter 6). It is acknowledged here that spatial heterogeneity in soil types and vegetation types does exist in nature, nonetheless the goal of this study is investigate the influence of topography and vegetation dynamics on regional scale atmospheric feedbacks, and as a first step such heterogeneities are ignored in this study.

## 7.2 Results

As mentioned earlier, the simulations with the WRF - *ptRIBS+VEGGIE* model over D03 domain is carried out for two separate years, 2001 and 2003. Results from the two years are similar. In the following sections, we present the results from 2001, while results for 2003 are given in the Appendix B.

### 7.2.1 Flat Earth with static vegetation experiment

To reiterate, only results from the WRF - *ptRIBS+VEGGIE* model on the D03 are presented, since the focus of this work is to investigate the impact of explicit accounting of topography and vegetation dynamics on hydro-climatology. We begin this section with an analysis of simulated monthly timeseries of precipitation and surface fluxes. The NAM occurs from July through September and is responsible for bringing rain to the southwest United States and northwest Mexico [Douglas et al., 1993]. Figure 7-3 shows the simulated domain average monthly timeseries of precipitation; along with sensible and latent heat flux for the year 2001. Along with the simulated rainfall timeseries, estimates from the Precipitation Estimation from the Remotely Sensed Information Using Artificial Neural Networks (PERSIANN) system [Hsu et al., 1997, 1999] are presented in Figure 7-3(a). The PERSIANN product estimates rainfall at  $0.25^0 \times 0.25^0$  using geosynchronous satellites longwave infrared (GOES-IR) bands along with instantaneous rain-rate estimates from the Tropical Rainfall Measurement Mission (TRMM) microwave images [Sorooshian et al., 2000]. The goal of this work is not to more accurately reproduce the NAM system. Nevertheless, considering that

homogeneous soil and vegetation type are assumed for the current simulation, the model is able to reasonably reproduce the monthly precipitation behavior over the study domain for 2001.

Domain average simulated latent and sensible heat fluxes, along with the NARR model outputs of the surface fluxes for 2001 are presented in Figure 7-3 (b). The NARR model uses the NCEP Eta Model (32km/45 layer) together with the Regional Data Assimilation System (RDAS), which assimilates precipitation along with other variables. The NARR outputs are available 8 times daily data at 29 levels for most of the model variables. A complete list of model output variables is available at [http://www.emc.ncep.noaa.gov/mmb/rreanl/narr\\_archive\\_contents.pdf](http://www.emc.ncep.noaa.gov/mmb/rreanl/narr_archive_contents.pdf). The simulated sensible heat flux is over predicted at the start of simulation when compared to the NARR outputs. The peak latent heat flux in August, 2001 is under estimated by the WRF - *pt*RIBS+VEGGIE. Separate analysis of the MODIS LAI data over the D03 domain for 2001 (not shown here) indicates that vegetation shows peak values in August. The static vegetation within the FLAT-STAT simulation experiment is thus expected to under-predict the latent heat flux. Once again, acknowledging that the homogenous soil and vegetation, the domain average simulated surface fluxes are reasonable when compared to the NARR outputs.

Spatial maps of monthly average precipitation, 10-cm soil moisture and downwelling surface shortwave radiation for 2001 are presented in Figure 7-4, 7-5 and 7-6, respectively; while the correlation coefficient ( $R^2$ ) of rainfall with 10-cm soil moisture and downwelling surface shortwave radiation for each month of 2001 are shown in Figure 7-7. During the monsoon months, higher rainfall occurs diagonally in the domain from south-east to north-west. Downwelling surface shortwave radiation exhibits a strong negative correlation with rainfall patterns and has a  $R^2$  value of less than  $-0.60$  from April to October. Vegetation needs sufficient amount of incoming solar radiation, along with available water, to grow. In the third synthetic experiment, where vegetation is allowed to respond dynamically to the climate forcings and surface conditions, the spatial pattern of downwelling shortwave radiation plays a significant role.

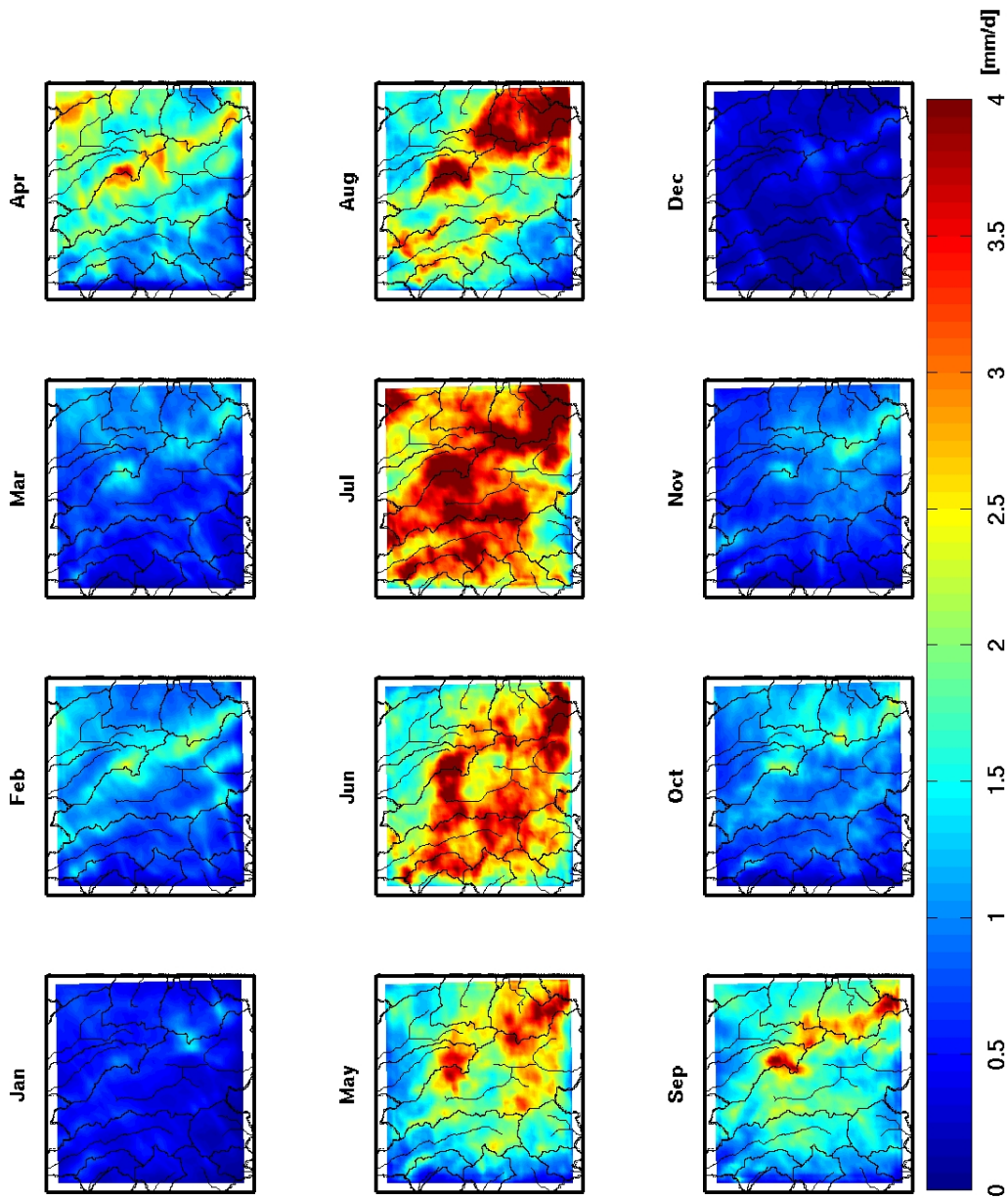


Figure 7-4: Spatial distribution of simulated monthly precipitation for 2001 by the WRF - *ptRISB+VEGGIE* model for the FLAT-STAT case.

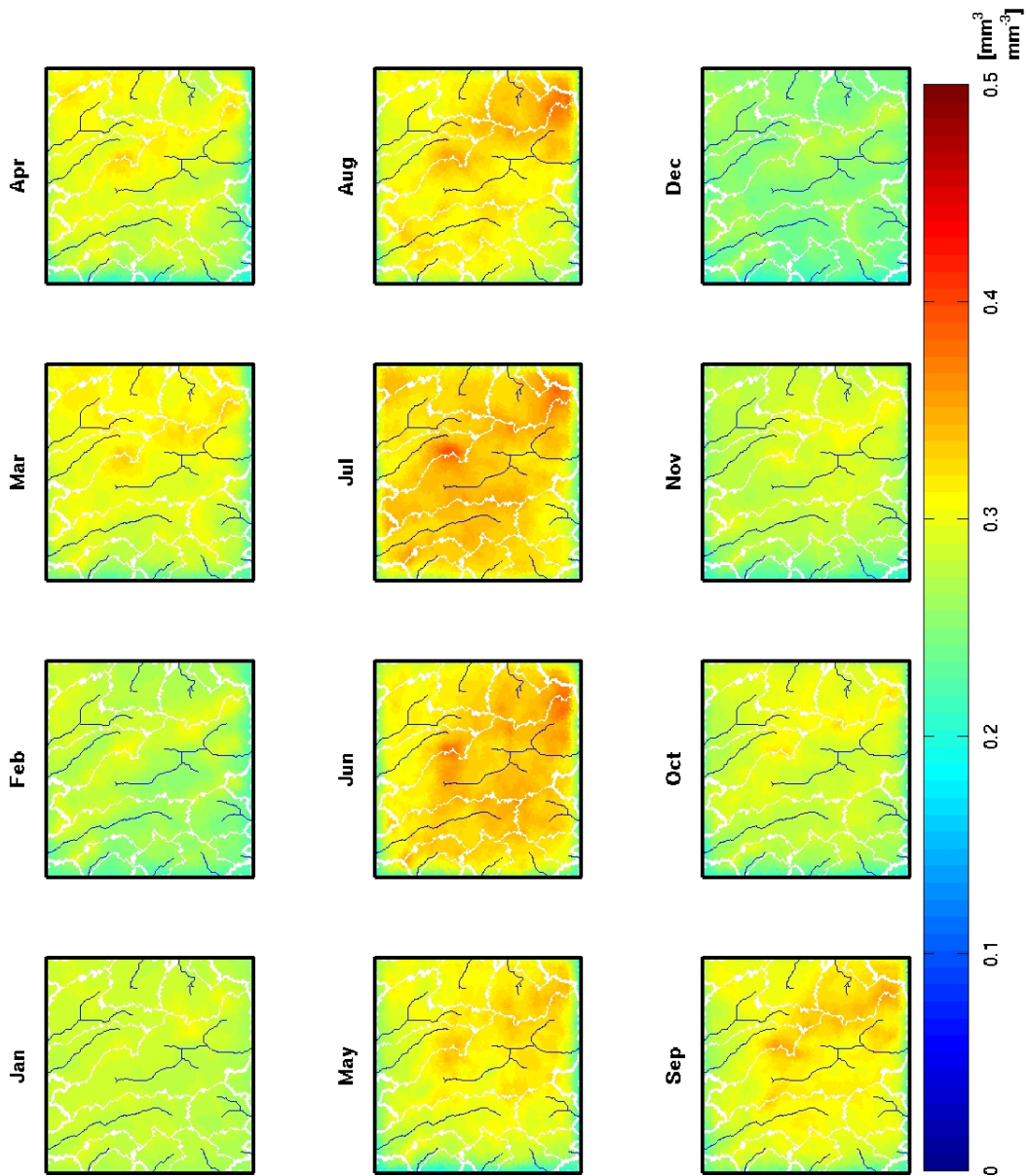


Figure 7-5: Spatial distribution of simulated monthly volumetric root-zone soil moisture for 2001 by the WRF - *pt*RISB+VEGGIE model for the FLAT-STAT case.

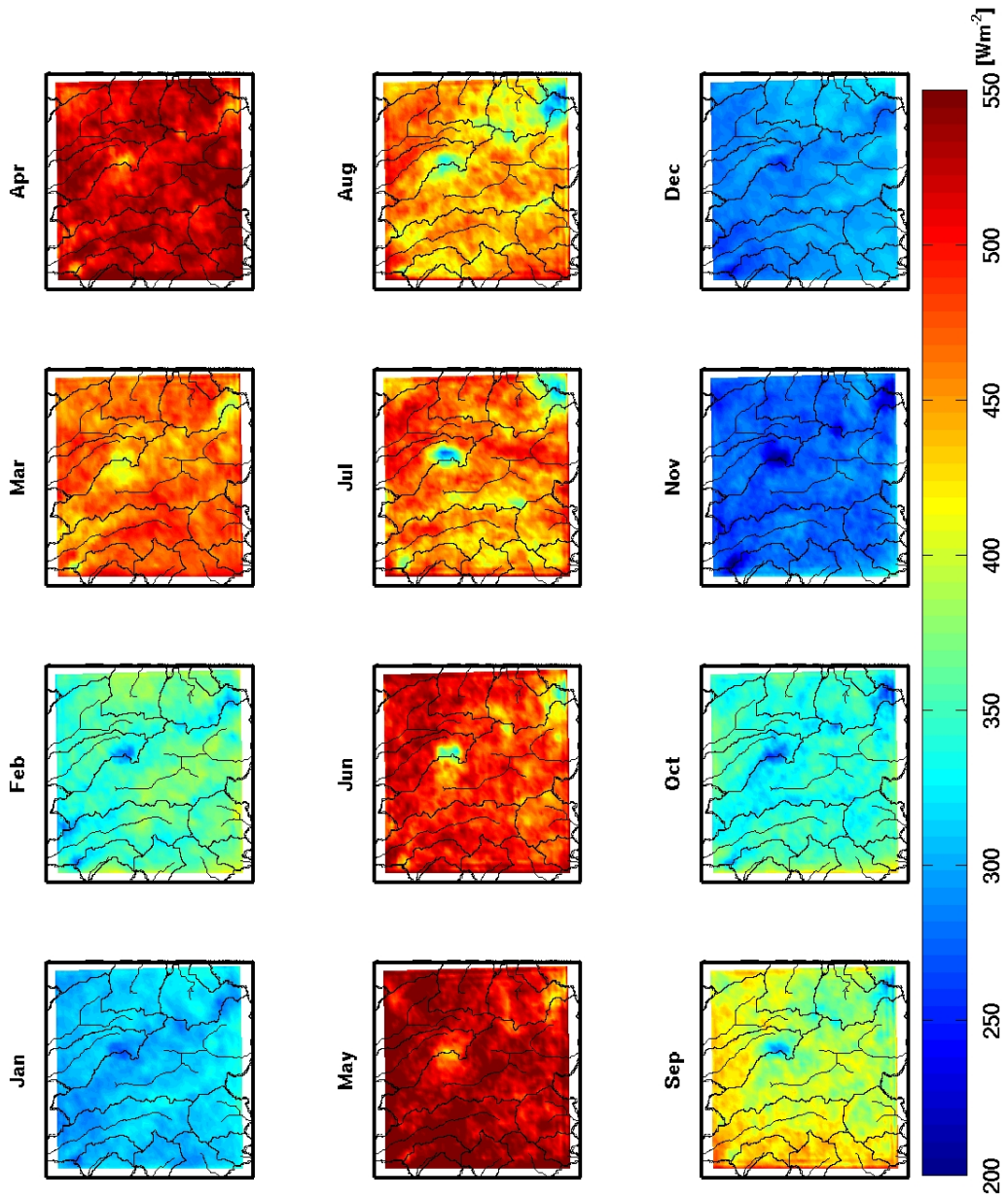


Figure 7-6: Spatial distribution of simulated monthly downwelling surface shortwave radiation for 2001 by the WRF - *ptRISB+VEGGIE* model for the FLAT-STAT case.

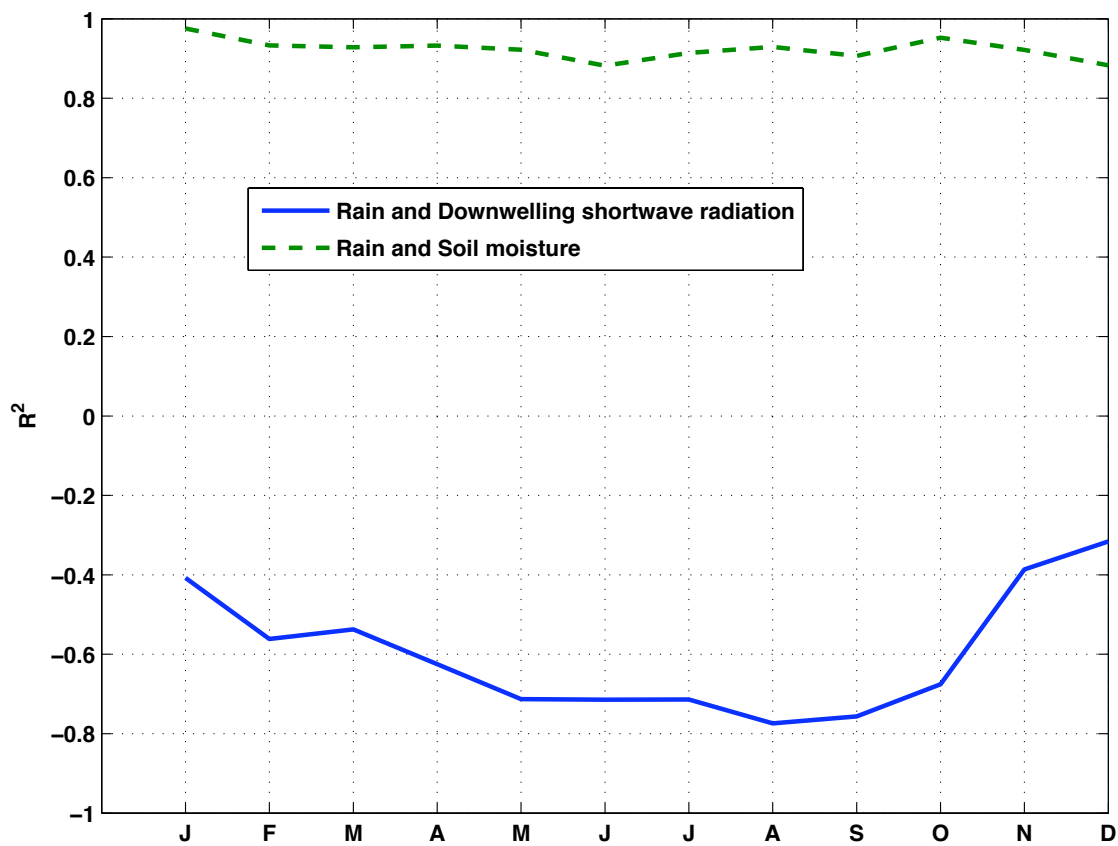


Figure 7-7: Correlation coefficient for various months in 2001 simulated by the WRF - *pt*RISB+VEGGIE model for FLAT-STAT case among the following quantities: (i) rainfall and downwelling surface shortwave radiation; and (ii) rainfall and soil moisture.

## 7.2.2 TOPO-STAT: Observed topography with static vegetation experiment

The second synthetic experiment attempts to elucidate the impact of explicitly representing topography on land-atmosphere interactions through lateral redistribution of moisture (above- and below-ground) and local radiation budget (via slope and aspect of the terrain). The domain average simulated quantities (for eg. rainfall, latent and sensible heat flux) for the TOPO-STAT are similar to those obtain in the FLAT-STAT case; but their spatial distribution are quite different in the two cases. It is expected that the influence of land on atmospheric states through the local mechanism of convection would be strongest during the monsoon, thus like many other previous studies [Eltahir, 1998, Koster et al., 2004b, Jiang et al., 2009], we limit our analysis to months of June, July, and August (JJA) in this section. Figure 7-8 shows the monthly percentage anomalies during JJA between the TOPO-STAT and the FLAT-STAT case for rainfall, latent and sensible heat fluxes, respectively. Percentage anomalies for all quantities are computed as the TOPO-STAT value minus the FLAT-STAT value with respect to the FLAT-STAT value. A large portion of the domain has rainfall anomalies with magnitude larger than 10% for JJA; while anomalies in latent and sensible heat are generally less than 5% in the domain.

Eltahir [1998] proposed a theoretical framework of positive feedback mechanisms between soil moisture conditions and subsequent rainfall, shown in Figure 7-9. Following the framework of Eltahir [1998], we identified six variables of interest: rainfall, 10-cm soil moisture, Bowen ratio (the ratio of sensible to latent heat flux), surface temperature, planetary boundary layer height, and wet bulb depression (difference between dry bulb temperature and wet bulb temperature). Higher rainfall lead to wetter soil conditions, which in turn influence the energy partitioning at the surface by reducing the Bowen ratio [Molders and Ruhaak, 2007] and causing a decrease in surface temperature. Cooler surface temperature tends to lower the planetary boundary layer height. Maxwell et al. [2007] demonstrated through a simulation of a coupled groundwater and atmospheric model that boundary layer height was lower in regions with shallower water table. Eltahir [1998] argued that wet bulb depression

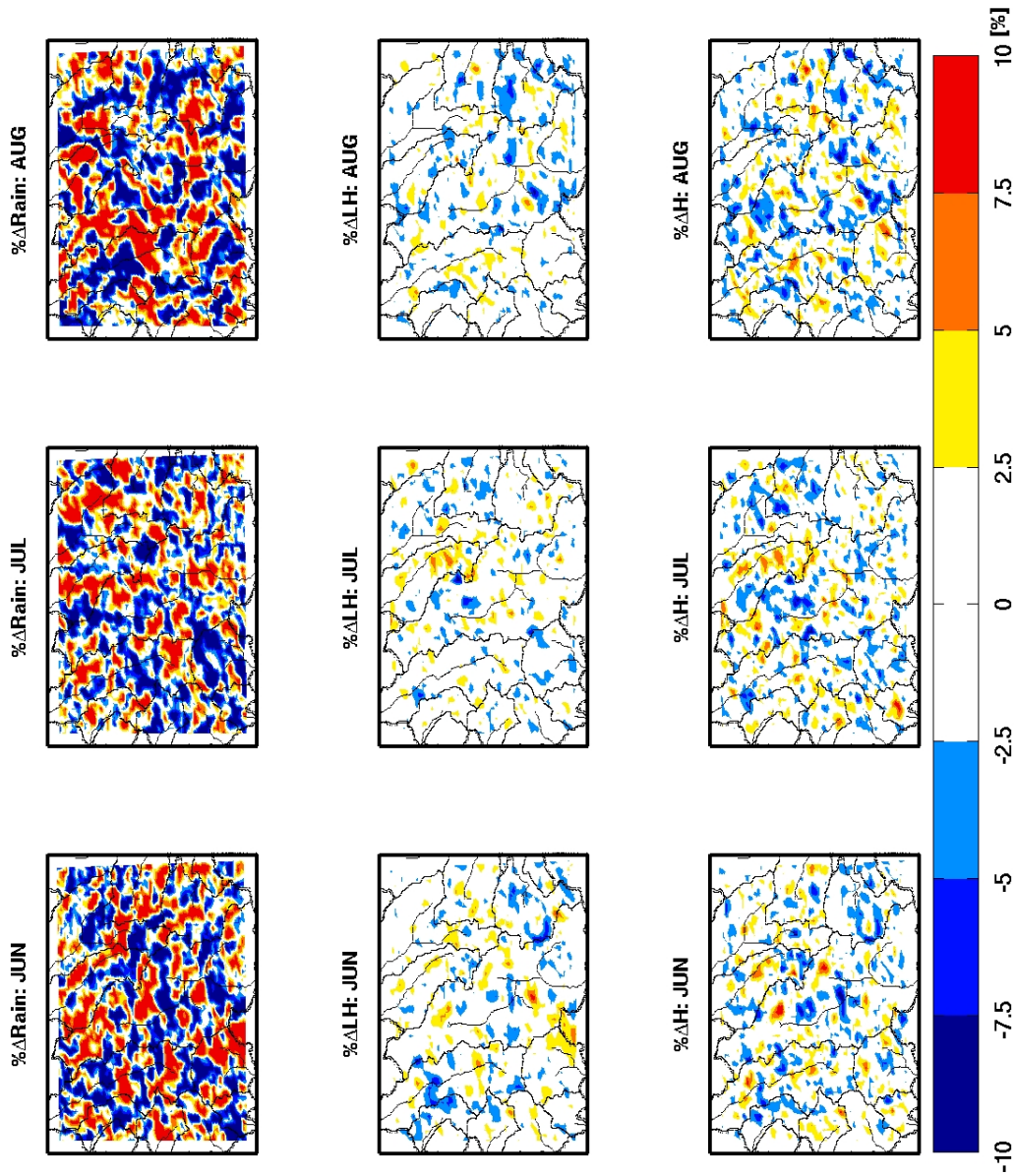


Figure 7-8: Monthly average anomalies between the TOPO-STAT and the FLAT-STAT case during the months of June, July and August, 2001 for: (a) Rainfall; (b) Latent heat flux; and (c) Sensible heat flux. (Percentage anomalies are computed as the TOPO-STAT value minus the FLAT-STAT value with respect to the FLAT-STAT value).



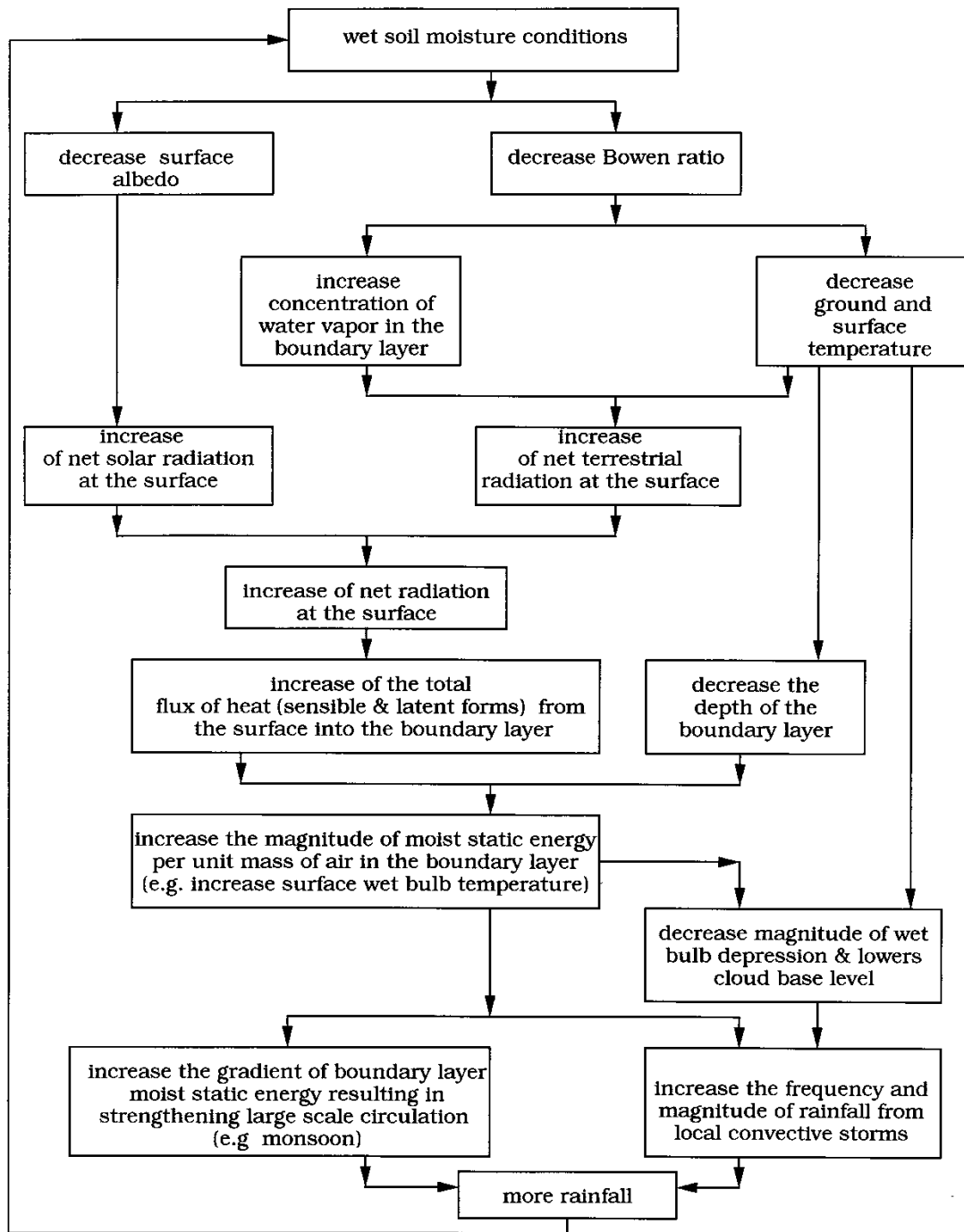


Figure 7-9: Soil moisture-rainfall feedback hypothesis proposed by Eltahir [1998].

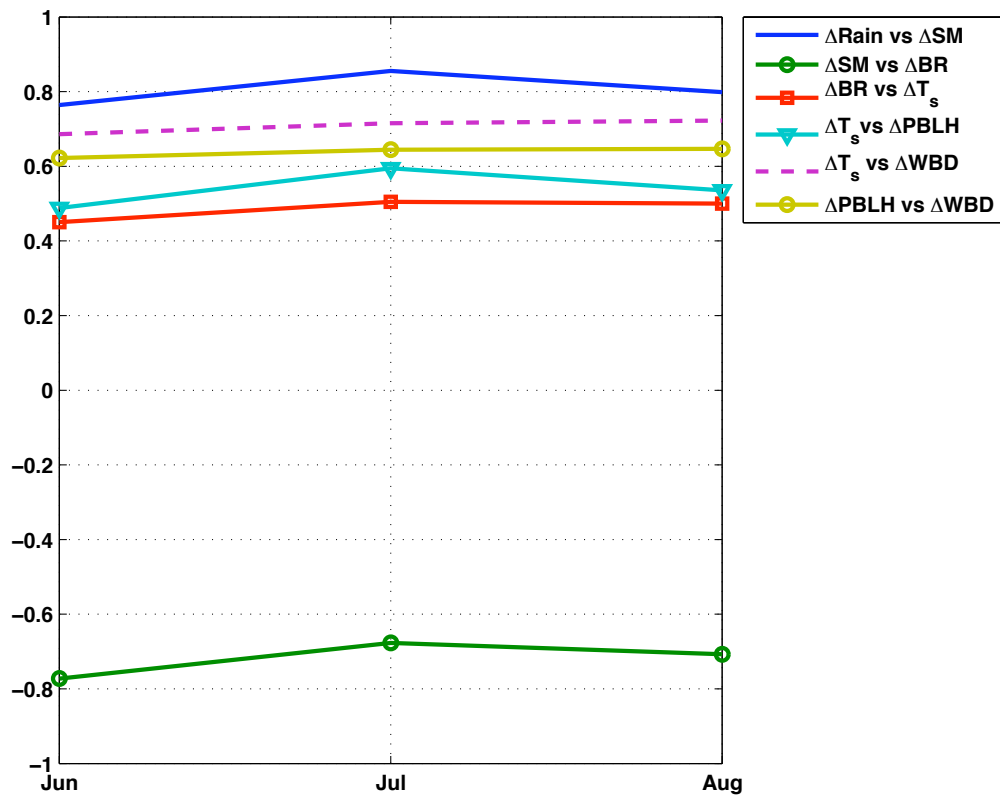


Figure 7-10: Correlation coefficient in June, July and August, 2001, among anomalies between the TOPO-STAT and the FLAT-STAT case for various quantities: rainfall, 10-cm soil moisture (SM), Bowen ratio (BR), surface temperature ( $T_s$ ), planetary boundary layer height (PBLH), and wet-bulb depression (WBD).

Table 7.3: Average correlation during June, July and August, 2001, among the various anomalies: rainfall, 10-cm soil moisture (SM), Bowen ratio (BR), surface temperature ( $T_s$ ), planetary boundary layer height (PBLH), and wet-bulb depression (WBD). The first and second column corresponds to anomalies between the TOPO-STAT and the TOPO-DYN cases with respect to the FLAT-STAT case. The third column corresponds to anomalies in the TOPO-DYN with respect to the FLAT-STAT case, after neglecting the “radiation-limited” points within the domain (see Section 7.2.3)

	TOPO-STAT vs FLAT-STAT	TOPO-DYN vs FLAT-STAT	TOPO-DYN vs FLAT-STAT*
$\Delta$ Rain and $\Delta$ SM	+0.88	+0.82	+0.84
$\Delta$ SM and $\Delta$ BR	-0.71	-0.43	-0.44
$\Delta$ BR and $\Delta T_s$	+0.49	-0.01	+0.25
$\Delta T_s$ and $\Delta$ PBLH	+0.54	+0.37	+0.46
$\Delta T_s$ and $\Delta$ WBD	+0.71	+0.71	+0.71
$\Delta$ PBLH and $\Delta$ WBD.	+0.64	+0.51	+0.62

is more sensitive to soil moisture conditions as compared to either dry- or wet-bulb temperatures. In order to investigate the differences in the spatial pattern of simulated quantities between the TOPO-STAT and the FLAT-STAT case,  $R^2$  is computed among the anomalies of six variables of interest for all the points within the simulation domain for each month in JJA. Figure 7-10 show the monthly variation of  $R^2$  for the six quantities during JJA, while their average values for JJA are summarized in Table 7.3.

Rainfall anomalies are very strongly related to top layer (10-cm) soil moisture anomalies with an average  $R^2$  of 0.88; while wetter soil conditions do tend to reduce the Bowen ratio. The  $R^2$  between anomalies of Bowen ratio and surface soil temperature is the lowest (in absolute value). Surface temperature anomalies are positively correlated to the depth of planetary boundary layer (PBL) and wet-bulb depression. PBL height and wet-bulb depression anomalies also show a positive correlation. The direction of co-dependence (positive or negative) among various anomalies agrees with the soil moisture-rainfall feedback mechanism proposed by Eltahir [1998].

### 7.2.3 Observed topography with dynamic vegetation experiment

In the third synthetic experiment, vegetation is allowed to respond to climatic and surface conditions, while simultaneously accounting for the impacts of topography on soil moisture and local radiation budget. Analogous to the previous case, the domain average values of the simulated quantities for the TOPO-DYN case are similar to those obtain in the FLAT-STAT case; but their spatial distribution are quite different in the two cases. We limit our analysis similarly to JJA and anomalies of the six quantities identified in Section 7.2.2 are studied. Figure 7-11 shows the spatial distribution of the monthly percentage anomalies between the TOPO-DYN and the FLAT-STAT case JJA for rainfall, latent and sensible heat fluxes. Similarly to the previous case, a large portion of the domain has rainfall anomalies with magnitude larger than 10% for JJA. Unlike the anomalies of latent and sensible heat flux obtained in the previous case, a greater portion of the domain exhibits anomalies larger than 2.5% (in absolute value). The latent heat anomalies are mostly negative in June because the average vegetation cover for the TOPO-DYN case is less than the prescribed value for the FLAT-STAT case. In August, the TOPO-DYN case has more vegetation cover as compared to the FLAT-STAT case, thus the latent heat flux anomalies are positive, especially along the river channel network. In June, the vegetation cover in the TOPO-DYN is closer to the prescribed value for the FLAT-STAT case; and the anomalies in sensible and latent heat are lower in absolute magnitude in comparison to June and August. Thus, in July, when vegetation cover is similar in the two cases, accounting for processes controlled by topography have large impact on spatial distribution of rainfall, but lower impact on latent and sensible heat flux. This is consistent with the results obtained in the previous section 7.2.2, where keeping vegetation static, inclusion of topography shows a lesser impact of spatial distribution of heat fluxes as compared to rainfall.

Spatial distribution of simulated monthly average LAI by the WRF - *ptRIBS+VEGGIE* model is shown in Figure 7-12. The *ptRIBS+VEGGIE* model only tracks live above-ground biomass and does not account for standing dead biomass. Thus, at the beginning (January to March) and end (November and December) of the simulation time-period, the model

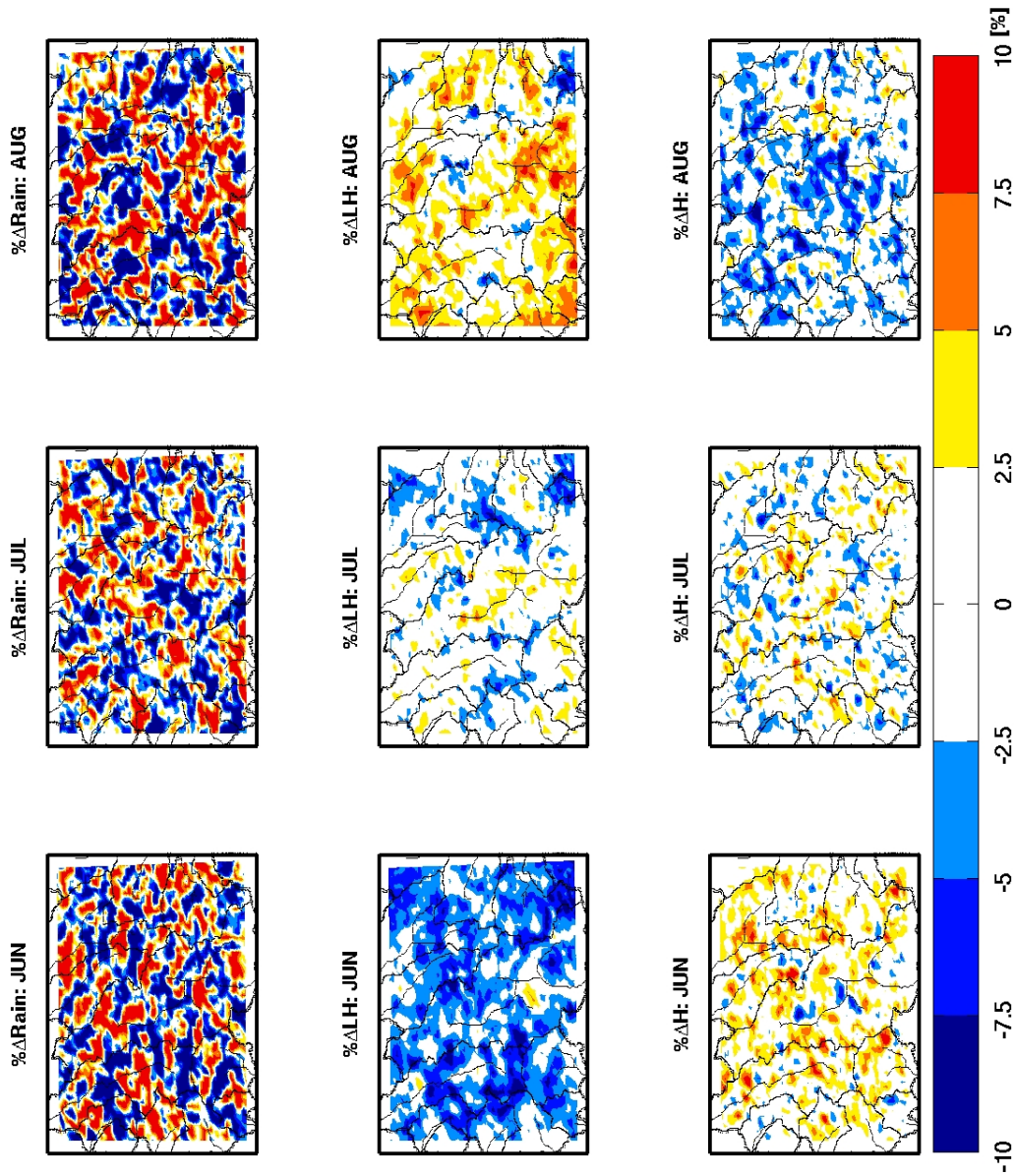


Figure 7-11: Monthly average anomalies between TOPO-DYN and FLAT-STAT case during the months of June, July and August, 2001 for: (a) Rainfall; (b) Latent heat flux; and (c) Sensible heat flux. (Percentage anomalies are computed as TOPO-DYN minus FLAT-STAT with respect to FLAT-STAT).

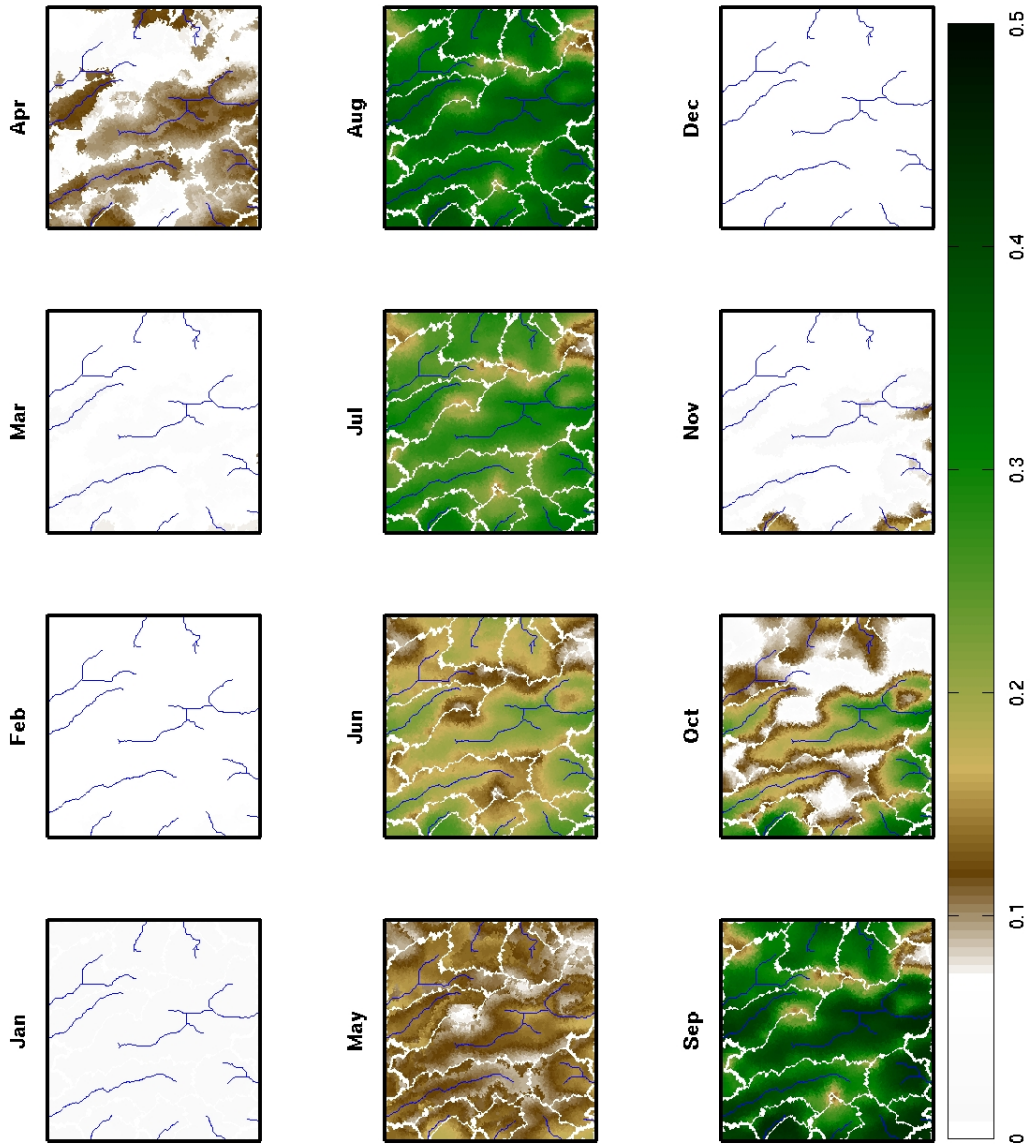


Figure 7-12: Spatial distribution of simulated monthly average leaf area index for 2001 by the WRF - *pt*RISB+VEGGIE model for the TOPO-DYN case.

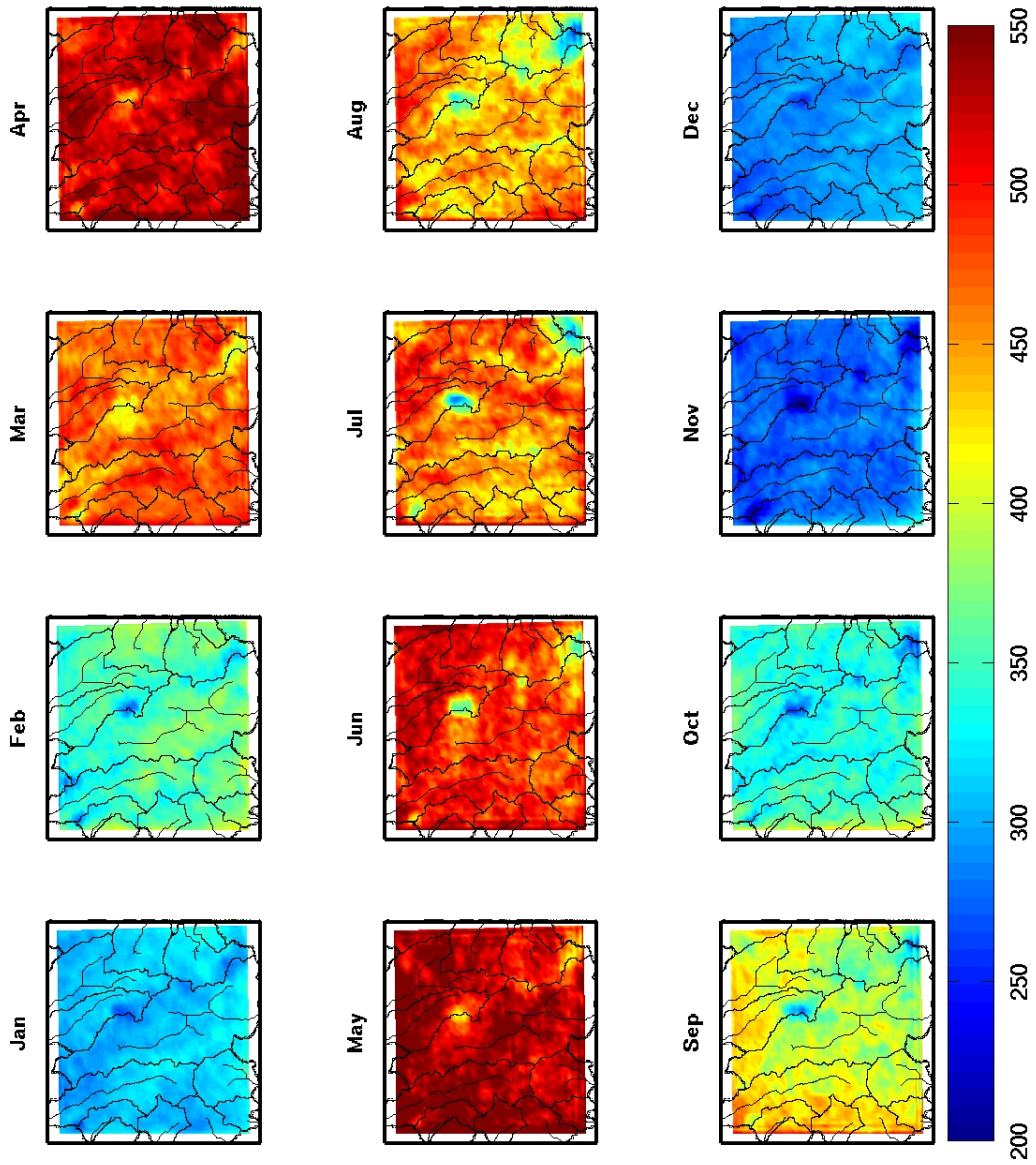


Figure 7-13: Spatial distribution of simulated monthly average downwelling surface short-wave radiation for 2001 by the WRF - *ptRISB+VEGGIE* model for the TOPO-DYN case.

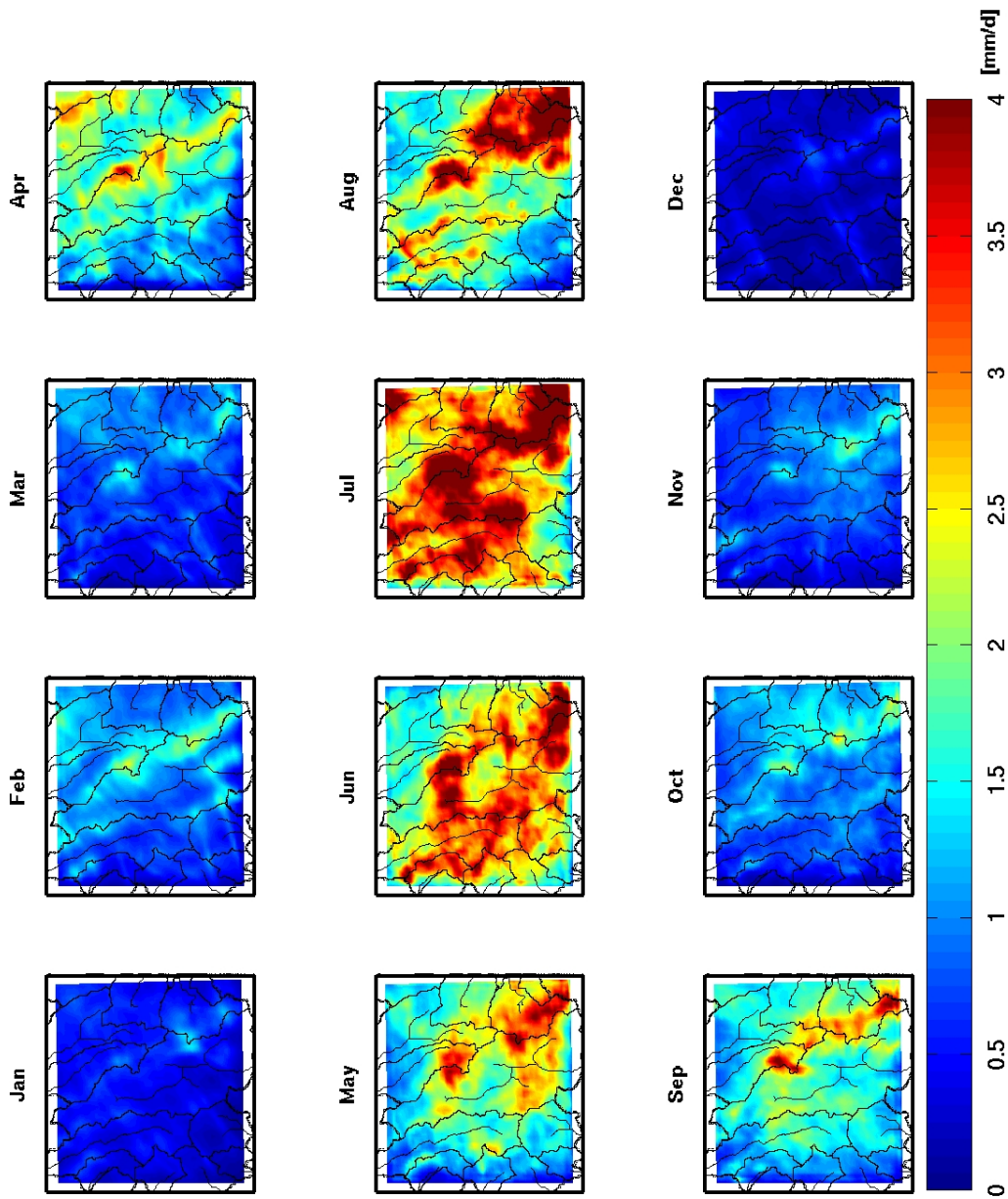


Figure 7-14: Spatial distribution of simulated monthly average rainfall for 2001 by the WRF - *ptRISB+VEGGIE* model for the TOPO-DYN case.



Monthly Average LAI for June

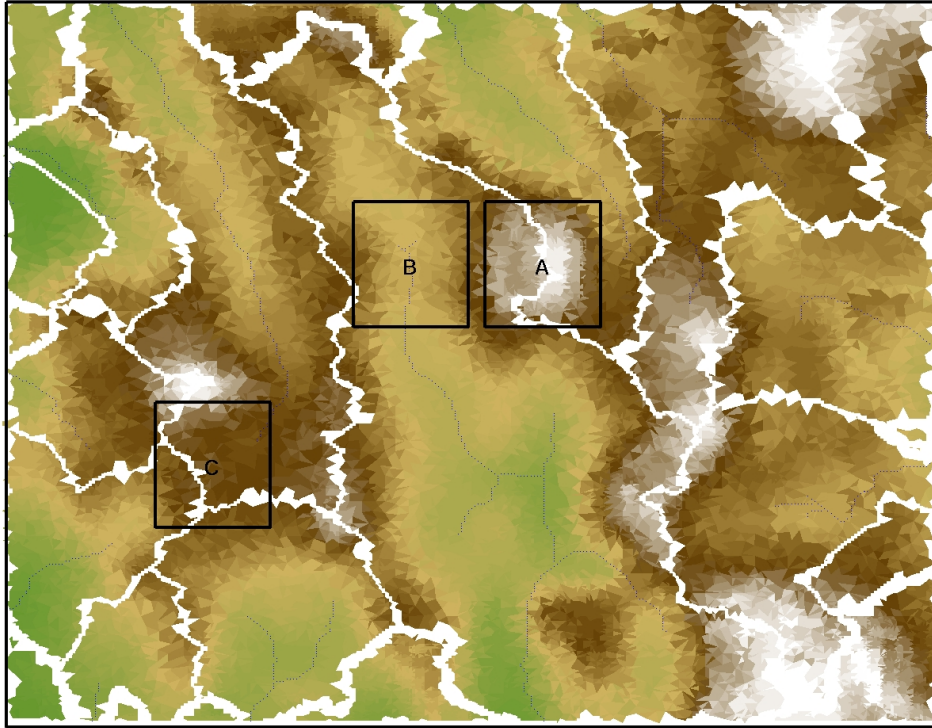


Figure 7-15: Simulated monthly average LAI for June, 2001, along with three sub-regions within the domain.

predicts zero LAI values, which corresponds to an absence of live biomass. It is also evident from Figure 7-12, that vegetation first emerges along the river channel network in April, and stays for a longer duration within the river channel, until the end of October. Additionally, there are regions (shown in brown) within the simulation domain, where LAI values remain lower as compared to the rest of the domain throughout the year. The regions of low LAI values correspond to regions that receive lower downwelling surface shortwave radiation and higher rainfall, as shown in Figure 7-13 and 7-14, respectively. Thus, the regions with lower LAI values are “radiation-limited” as compared to other parts of the domain. This highlights the co-dependence of vegetation dynamics on water and radiation availability.

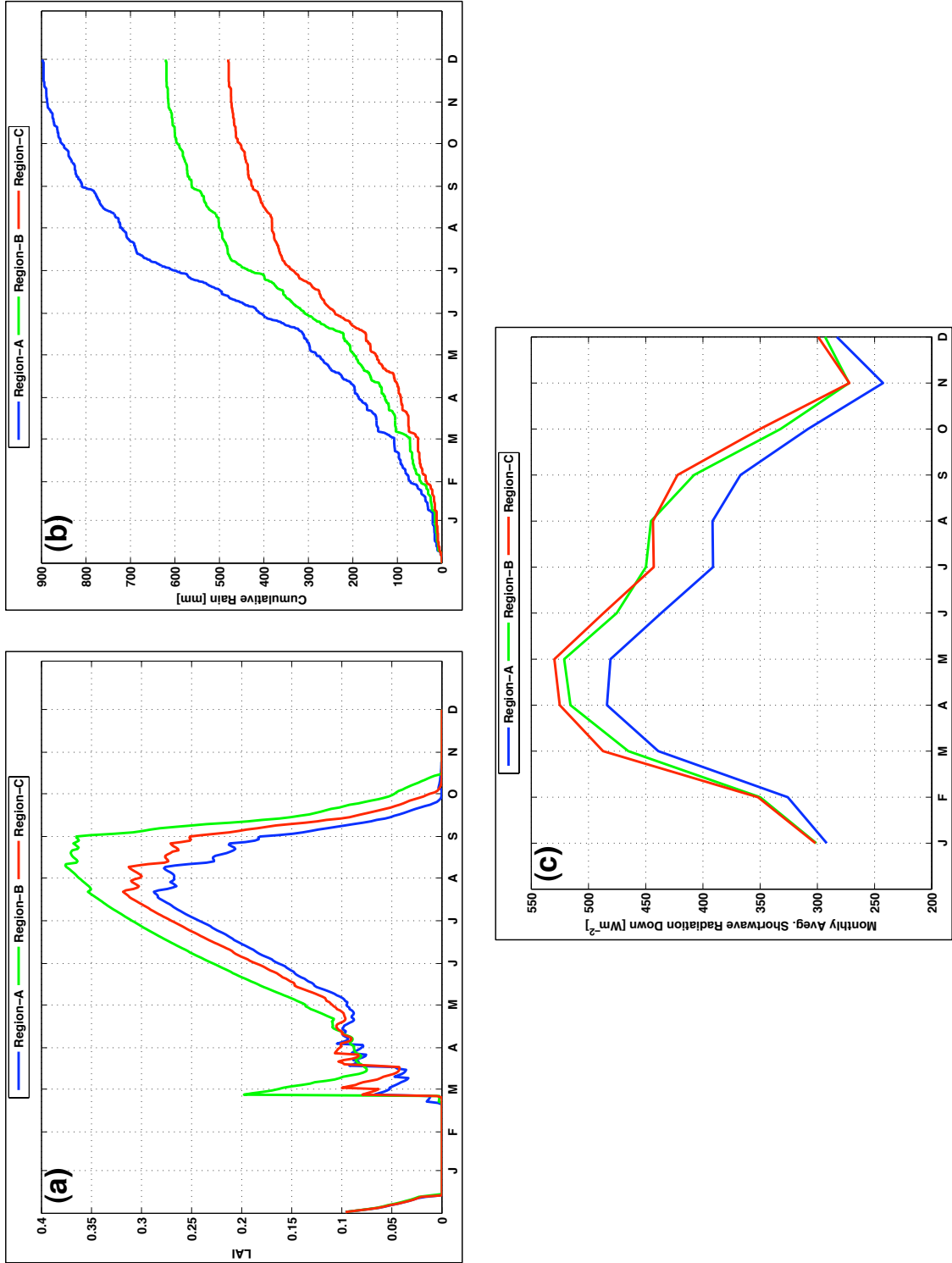


Figure 7-16: Timeseries of simulated (a) LAI; (b) Cumulative rainfall; and (c) Monthly average downwelling shortwave radiation for three sub-regions within the D03 domain.

In order to further examine the “radiation-limited” regions, we focused our analysis on sub-regions A, B and C within the D03 domain, as shown in Figure 7-15. A timeseries of simulated LAI, cumulative rainfall and downwelling shortwave radiation for the three sub-regions are shown in Figure 7-16. The *pt*RIBS+VEGGIE model accounts for downwelling shortwave incident on a non-flat surface, through slope and aspect of the local terrain. The values of downwelling shortwave radiation plotted in Figure 7-15 are before the local effects of terrain are accounted for within the *pt*RIBS+VEGGIE model. Sub-regions B and C receive similar downwelling shortwave radiation values; while B receives larger rainfall and higher simulated LAI as compared to C. Thus, higher water availability, without a significant decrease in downwelling shortwave radiation, leads to a positive feedback on vegetation growth as suggested by Eltahir [1998].

Sub-region A receives highest rainfall and lowest downwelling shortwave radiation, due to cloudiness, and results in lowest overall vegetation growth. An observational study by Mendez-Barroso and Vivoni [2010] over northwest Mexico also support these results. Mendez-Barroso and Vivoni [2010] used the eddy covariance data from the 2007 summer season and created two composites on the basis of cloud conditions for the day following a rainfall event or high soil moisture conditions. Mendez-Barroso and Vivoni [2010] found that there exists a positive vegetation-rainfall feedback, as long as, clouds do not decrease the net solar radiation. Cloudy conditions weakened the positive vegetation-rainfall feedback, thus Mendez-Barroso and Vivoni [2010] suggested modification to the soil moisture-rainfall hypothesis proposed by Eltahir [1998].

To further investigate how vegetation impacts the partitioning of energy flux at the land surface, diurnal monthly average timeseries of net radiation, latent and sensible heat flux for June, July and August, 2001 are shown in Figure 7-17. Sub-regions B and C having received similar downwelling shortwave radiation, produce similar net radiation. Nonetheless, the partition of net radiation for sub-regions B and C is different, with B producing more latent heat flux as compared to C and vice-versa for sensible heat flux. The higher evapotranspiration over B can be explained with the higher vegetation cover and more rainfall when

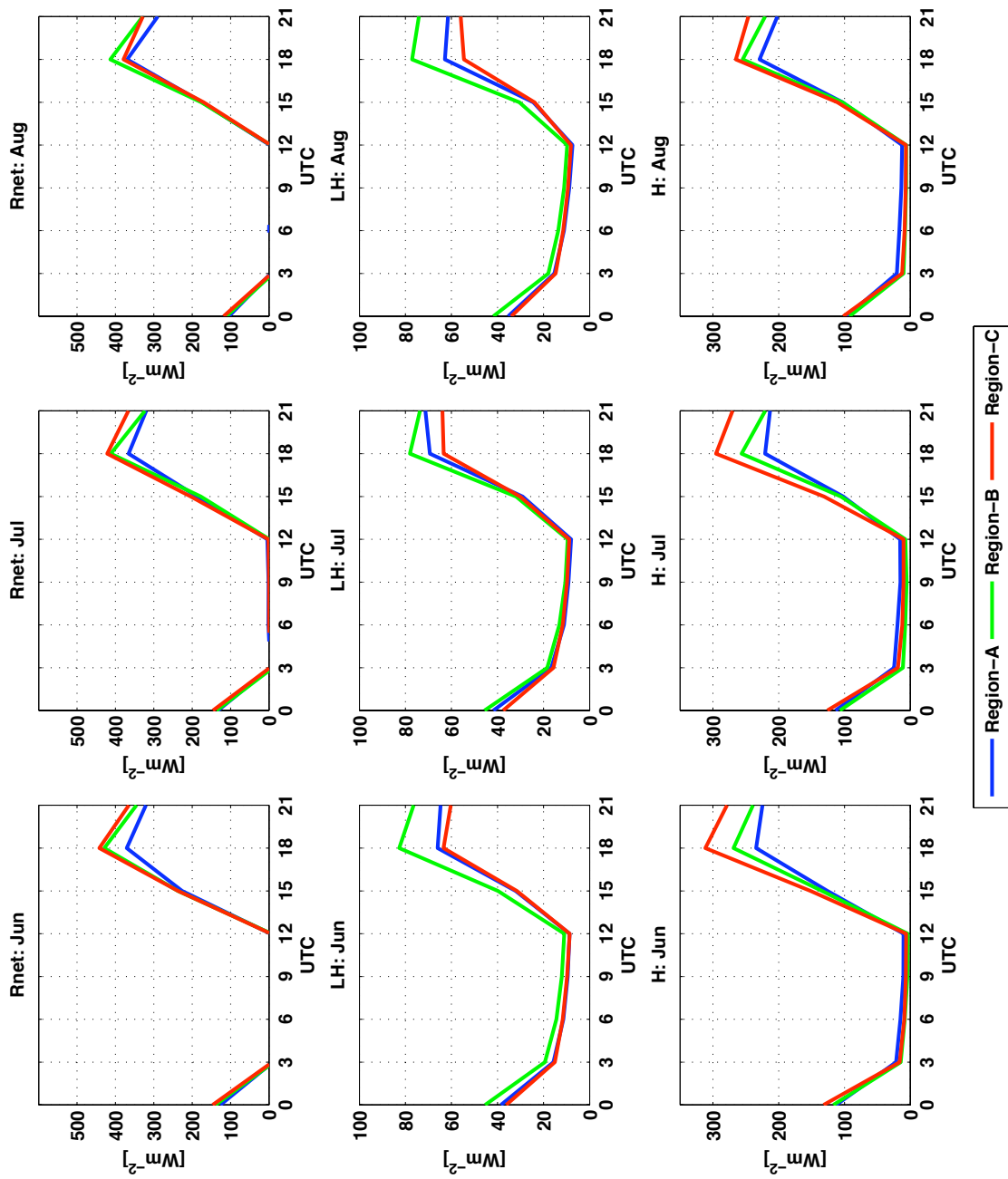


Figure 7-17: Average diurnal cycle for (a) Net radiation; (b) Latent heat flux; and (c) Sensible heat flux for June, July and August, 2001.

compared to C. It is also interesting to note that latent heat flux for A is higher as compared to C, even though the vegetation biomass for C is higher than A. It is expected that bare soil evaporation from A is able to compensate for lower transpiration values as compared to C, given that A does receives much higher rainfall.

The correlation coefficients among the anomalies of the six index quantities during JJA are summarized in the second column of Table 7.3, and are generally lower (in absolute value) than those obtained in the TOPO-STAT case. Anomalies of Bowen ratio and surface temperature shown no correlation at all. The soil moisture-rainfall feedback hypothesis of Eltahir [1998] did not account for changes in vegetation cover. As mentioned earlier, soil moisture conditions, along with downwelling solar radiation reaching the surface, exert control on vegetation dynamics. Thus, the  $R^2$  for the six anomalies are recomputed by neglecting the “radiation-limited” points within the domain (which constitute approximately 13% of all the points) and summarized in the last column of Table 7.3.  $R^2$  values are higher (in absolute value) when “radiation-limited” points are neglected.

### 7.3 Discussion

This work demonstrates the role of explicitly accounting for topography and vegetation dynamics in coupled land-atmosphere model. A series of three experiments are performed for two separate years over the southwestern United States. Results show that monthly domain average quantities (eg. rainfall, latent and sensible heat flux) do not show significant change when topography and vegetation dynamics are accounted for within the coupled land-atmosphere model, but their spatial distributions show differences. Accounting for processes influenced by topography only (namely redistribution of soil moisture and changes in local solar radiation budget) as demonstrated by the TOPO-STAT case, resulted in precipitation anomalies of magnitude larger than 10% during JJA; while anomalies in latent and sensible heat flux are generally less than 5%. The anomalies among six variables of interest: rainfall, 10-cm soil moisture, Bowen ratio, surface temperature, planetary boundary layer height, and wet bulb depression, were explained within the framework of soil moisture-rainfall feedback

hypothesis of Eltahir [1998].

Incorporation of dynamic vegetation along with topography within the coupled land-surface model shows that the latent heat flux anomalies (with respect to static vegetation and flat Earth case) for most of the domain are negative in June and positive in August. The reason for the switch in sign of the latent heat flux anomalies is due to the fact that vegetation cover in the dynamic vegetation case is less as compared to that prescribed in the static vegetation case in June and vice-versa in August. Additional analysis of three sub-regions within the D03 domain for the TOPO-DYN case illustrate the role of rainfall and cloudiness on vegetation growth. Positive vegetation-rainfall feedback is observed as suggested by Eltahir [1998] with an additional constraint that downwelling shortwave radiation remains nearly unaffected by increased rainfall. Further increase in rainfall at the expense of decreasing downwelling shortwave radiation leads to lower vegetation growth, as suggested by Mendez-Barroso and Vivoni [2010]. Impact of vegetation on the partitioning of net radiation at the land surface is also demonstrated.

The results presented in this work demonstrate the need to explicitly account for topography and vegetation dynamics within the coupled land-atmosphere models. Given the assumption of homogeneous soil and vegetation types made, additional experiments need to be performed using the observed vegetation and soil types. Several studies have recently demonstrated the impact of accounting for groundwater on surface fluxes and soil moisture within the regional climate models (RCMs) [Gutowski et al., 2002, Liang et al., 2003, Yeh and Eltahir, 2005, Maxwell et al., 2007, Niu et al., 2007, Gan et al., 2007, Maxwell et al., 2007, Kollet and Maxwell, 2008, Anyah et al., 2008, Jiang et al., 2009]. An earlier version of the tRIBS model included a quasi three-dimensional cascade groundwater module [Ivanov et al., 2004], though the current version of the *ptRIBS+VEGGIE* model does not include it. Incorporation of the groundwater module within the *ptRIBS+VEGGIE* model would not only extend the eco-hydrology model's applicability in an offline mode, but would also allow the WRF - *ptRIBS+VEGGIE* model to study the influence of groundwater dynamics on the regional climate.

It should be acknowledged here that vegetation requires nutrients, along with water and radiation, for growth, as demonstrated by several studies [Vitousek and Howarth, 1991, Elser et al., 2007, LeBauer and Treseder, 2008]. Accounting for the nitrogen cycle within the global climate models has recently been shown as a crucial factor in simulating the response terrestrial ecosystem to increasing atmospheric CO<sub>2</sub> concentration by Thornton et al. [2009]. At the present, the *ptRIBS+VEGGIE* model does not account for nutrients, and the vegetation growth is controlled by water and radiation availability only. Thus, accounting for nutrients while modeling could lead to more non-linear interactions within the soil moisture - vegetation hypothesis proposed by Eltahir [1998].





# CHAPTER 8

## CONCLUSIONS

In order to improve our understanding of the Earth system, advancement in both, observations and modeling, are necessary. The first part of this work focused on estimating the surface radiation budget from existing satellite data under all-sky conditions, while not relying on study-site specific ancillary ground data. In the second part of this work, the impact of explicitly accounting for topography and vegetation dynamics on hydro-climatology using a coupled ecohydrology and atmospheric model was examined. This final chapter summarizes the original contribution of this work, along with some potential future research directions.

### 8.1 Contribution

#### 8.1.1 Satellite-based estimates of surface radiation budget

Retrieval algorithms to estimate net radiation and its components from the MODIS data have recently been developed by numerous investigators [Bisht et al., 2005, Wang et al., 2005, Tang et al., 2006, Zhou et al., 2007, Tang and Li, 2008, Kim and Hogue, 2008, Wang and Liang, 2009, Wang et al., 2009, Formann and Margulis, 2009]. Most retrieval algorithms to estimate the surface radiation budget (SRB) generally suffer from two major shortcomings: difficulty in dealing with cloudy-sky conditions and reliance on study-site specific ancillary ground data. In this work, a retrieval algorithm to estimate various components of SRB

under all sky conditions was presented. Comparisons of estimated SRB components were performed against ground measurements within the Southern Great Plains and seven additional stations within United States for the entire 2006. The remotely sensed data from the MODIS sensor from both Aqua and Terra satellites is used. The results indicate that the proposed methodology was successful in retrieving various components of the SRB under all-sky conditions while not relying on any ancillary ground data. In order to estimate net radiation over the Continental United States (CONUS) using the proposed algorithm, two adaptations were incorporated. The first was related to the computation of temperature offsets necessary for estimating near-surface air and dew temperatures from the 5-km LST values given by the cloud product; while the second addressed the issue of missing surface albedo values in the MOD43B2 product. Finally, monthly radiation maps for the Continental United States were presented.

### **8.1.2 Coupled WRF - *pt*RIBS+VEGGIE modeling framework**

The second part of this work required coupling of a physically-based, distributed ecohydrology model with a numerical atmospheric model. One of the biggest hurdles that was evident from the beginning of this work was the additional computational cost associated in using a sophisticated ecohydrology model within the WRF model. Recent advances in high performance computing and its adaptation within the earlier version of the tRIBS model [Vivoni et al., 2005] served as a blueprint for developing the parallel version of the tRIBS+VEGGIE model. Additionally, a restart capability was added in the *pt*RIBS+VEGGIE model to ensure that if any simulation was terminated unexpectedly, it can be restarted from the time-step prior to termination. The restart capability within the *pt*RIBS+VEGGIE also complements the WRF restart capability and allows year-long simulations to be split as several shorter monthly runs.

The present work also enabled the *pt*RIBS+VEGGIE model to now serve as a new LSM option with the WRF model. The two models are written in different programming languages, C++ (*pt*RIBS+VEGGIE model) and FORTRAN (WRF model); and they were

coupled via a “buffer” that communicates instantaneous values of atmospheric forcing and land surface states between the two models. Furthermore, the tRIBS+VEGGIE model was initially developed to represent a single watershed and simulate hydrological processes occurring within the watershed boundary; while the WRF model works on a rectangular horizontal grid. In order to obtain *pt*RIBS+VEGGIE estimates of land surface states and surface fluxes over the rectangular WRF domain, it was necessary to enable the *pt*RIBS+VEGGIE model to operate on multiple watersheds simultaneously, which covered the entire WRF domain. The ability of the *pt*RIBS+VEGGIE model to handle multiple watersheds was implemented in a fashion that allowed watersheds to be distributed on to different computational nodes when using a parallel computing framework.

The capability of the ecohydrology model (in an offline mode) to accurately resolve hydro-climatic signatures and vegetation dynamics within a semiarid region was examined. The ecohydrology model was applied in a highly instrumented semiarid catchment, Walnut Gulch Experimental Watershed in Arizona for a period of 11 years (1997-2007). The model performance is examined with respect to several key hydrologic variables: energy fluxes, distributed soil moisture within the watershed at three depths and land surface temperature. Additionally, the model’s capability to capture vegetation dynamics for two generic plant functional types,  $C_4$  grass and  $C_3$  shrubs, was also evaluated against the MODIS leaf area index product.

A series of three experiments were performed for two separate years over the southwestern United States with the WRF - *pt*RIBS+VEGGIE model. The work demonstrated the role of explicitly accounting for topography and vegetation dynamics in coupled land-atmosphere model. Results show that monthly domain average quantities (eg. rainfall, latent and sensible heat flux) do not show significant change when topography and vegetation dynamics are accounted for within the coupled land-atmosphere model, but their spatial distributions show differences. Accounting for processes influenced by topography (namely redistribution of soil moisture and changes in local solar radiation budget) resulted in precipitation anomalies of magnitude larger than 10% during JJA; while anomalies in latent and sensible heat flux are

generally less than 5%. The anomalies among six variables of interest: rainfall, 10-cm soil moisture, bowen ratio, surface temperature, planetary boundary layer height, and wet bulb depression, were explained within the framework of soil moisture-rainfall feedback hypothesis of Eltahir [1998].

Incorporation of dynamic vegetation along with topography within the coupled land-surface model shows that the latent heat flux anomalies (with respect to static vegetation and flat Earth case) for most of the domain are negative in June and positive in August. The reason for the switch in sign of the latent heat flux anomalies is due to the fact that vegetation cover in the dynamic vegetation case is less as compared to that prescribed in the static vegetation case in June and vice-versa in August. Additionally, the control of solar radiation and rainfall in vegetation growth is demonstrated. Regions with increases in rainfall without significant decreases in downwelling shortwave radiation have higher vegetation growth. Although, an increase in rainfall with a decrease in downwelling shortwave radiation, leads to lower vegetation.

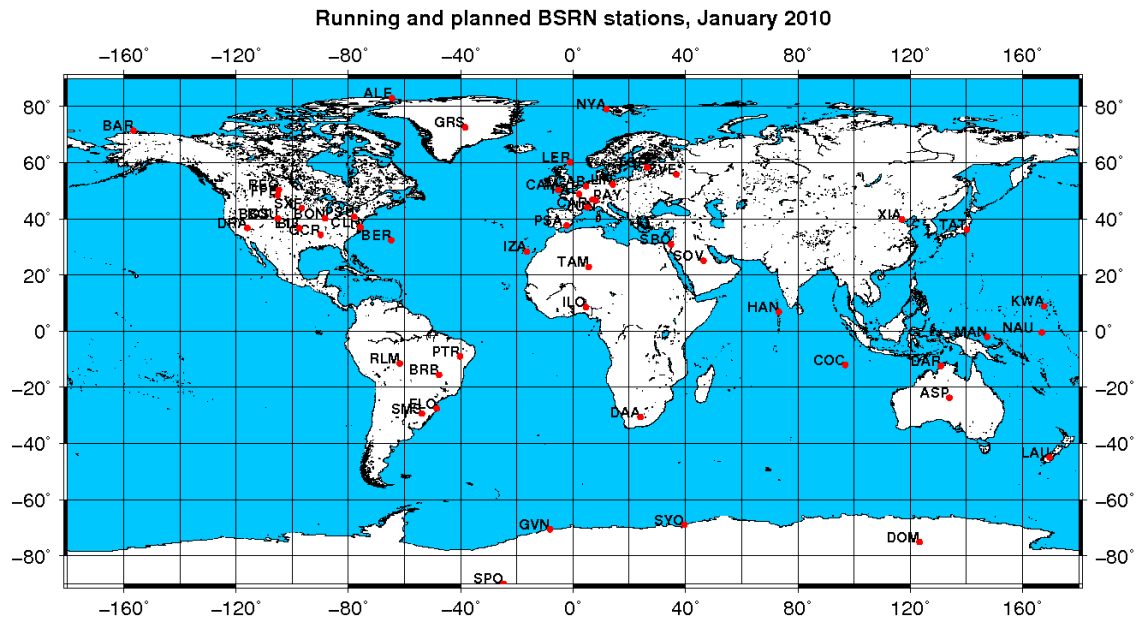
## **8.2 Future research**

### **8.2.1 Satellite-based estimates of surface radiation budget**

In order to achieve better accuracy and broaden the scope of application of satellite-based estimation of the SRB, several potential future improvements have been enumerated.

1. Estimation of downwelling shortwave radiation had the largest error among all the components of surface radiation budget, thus future efforts should focus on reducing that error. A statistical regression approach between the MODIS Top Of the Atmosphere (TOA) reflectance to estimate net surface shortwave radiation by Tang et al. [2006] for clear and cloudy days has shown to have a lower RMSE than the proposed methodology in this work. Use of TOA data for shortwave radiation; while employing near-surface data products for longwave component of the SRB, is one of the avenues to be pursued.

2. Distributed hydrologic models [Ivanov et al., 2004], that could potential benefit from the current approach, require separate estimation of diffuse and direct components of shortwave radiation. Currently, the use of Zillman's [1972] parameterization to estimate downwelling shortwave radiation, lumps diffuse and direct components together. Kim and Hogue [2008] computed direct and diffuse shortwave radiation separately using the MODIS data regarding total ozone amount (MOD07\_L2), angstrom turbidity factor (MOD04\_L2) and precipitable water (MOD05\_L2); and their approach could serve as a guidance for future improvements.
3. Retrieval of the diurnal cycle of the SRB and its components can also be used by distributed hydrologic models. The diurnal cycle of downwelling components of the SRB could be used to force the hydrologic models; while upwelling components of the radiation could be used to evaluate or improve (via data-assimilation approaches) model forecasts. Data from polar-orbiting satellites only is unable to capture the diurnal cycle of radiation as shown in Figure 3-22 and incorporation of additional remote sensing data from geostationary satellites should be pursued.
4. Estimation of SRB over the CONUS was made feasible by computing temperature offsets over  $5^{\circ} \times 5^{\circ}$  sub-domains. An alternate approach could involve computation of temperature offsets for the different vegetation types present within the sub-domains by using the MODIS Land Cover Yearly Level 3 data product (MCD12Q1).
5. The current spatio-temporal technique of filling the missing surface albedo from the MCD43B3 product is a simplistic one. Integration of a 1-km continuous surface albedo product, being developed by the MODIS land surface team, will be straight forward.
6. Finally, MODIS data from the Terra satellite are available from March, 2000 onwards; while data from the Aqua satellite are available from July, 2002 onwards. Furthermore, there exists a global network of ground stations, Baseline Surface Radiation Network (BSRN), shown in Figure 8-1, which record various components of the radiation budget at the surface. This presents an excellent opportunity to extend the temporal and



AWI  Alfred-Wegener-Institut  
für Polar- und Meeresforschung  
in der Helmholtz-Gemeinschaft

Figure 8-1: Global locations of Baseline Surface Radiation Network. (Obtained from <http://www.gewex.org/bsrn.html>)

spatial application of the current SRB retrieval methodology using the MODIS data.

## 8.2.2 Coupled WRF - *pt*RIBS+VEGGIE modeling framework

### Ensemble runs

In order to further bolster the results from this study, ensemble runs with the WRF - *pt*RIBS+VEGGIE model need to be performed. The southwest of the United States was under a drought from 2001-2004 [Webb et al., 2005], thus to see how results of this study change under wet conditions, additional simulation runs must be performed. Hourly model diagnostics pertaining to various components of the water and energy budget (such as bare soil evaporation, under-canopy soil evaporation, transpiration and shortwave radiation within the PAR) should be outputted so as to gain a better understanding of the system when topographic related processes and vegetation dynamics is accounted for within the coupled model.

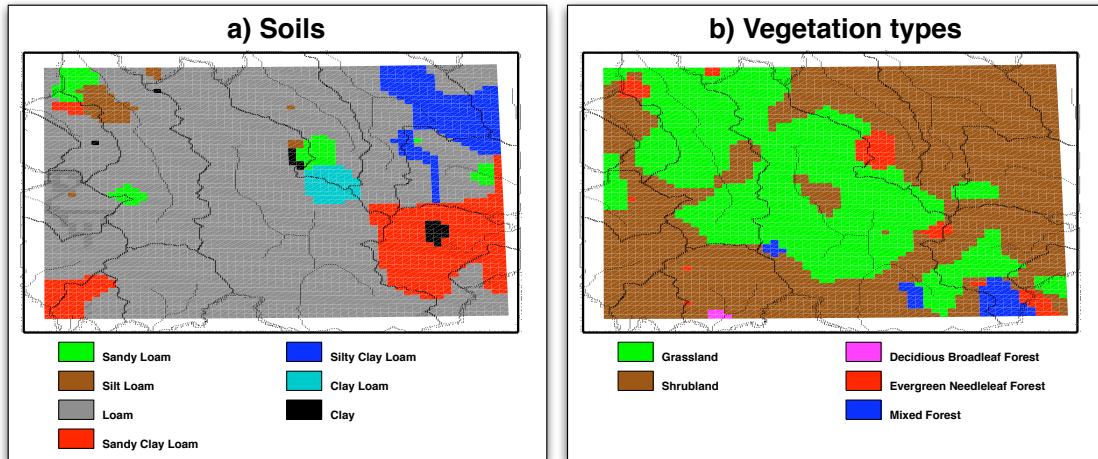


Figure 8-2: Spatial distribution of soil and vegetation types within the D03 domain, as obtained from the NARR data.

### Incorporation of heterogeneous soil and vegetation types

In the present work, the assumption of homogeneous soil and vegetation types was made in order to keep the number of independent factors influencing the outcome of this study. Figure 8-2 shows the distribution of soils and vegetation types within the D03 domain, as obtained from the NARR data. The impact of explicitly accounting for topography and vegetation dynamics in the coupled land-atmosphere model has been demonstrated, and additional experiments need to be performed using the observed vegetation and soil types. Offline runs of the *ptRIBS+VEGGIE* model also need to be undertaken to obtain relevant vegetation parameters required by the VEGGIE module for the different vegetation types present within the domain.

### Dynamical downscaling of regional climate change prediction

IPCC AR4 acknowledged that due to the complexity of AOGCMs and computational constraints, the horizontal resolution of such AOGCMs generally range from 400-km to 125-km. Even though AOGCM projections provide plausible future global climate scenarios, methods to establish reliable estimates of regional scale climate change are still not mature [Chris-

tensen et al., 2007]. Regional climate models (RCMs), which have been traditionally used for numerical weather prediction, are now serving as useful tools in dynamically downscaling information from AOGCMs [Leung et al., 2003, Wood et al., 2004, Castro et al., 2005, Lo et al., 2008]. A recent report summarizing the impacts of climate change on the United States has recognized that the southwest United States has seen some of the longest documented megadroughts on the Earth [Karl et al., 2009]. Ecosystems throughout the southwestern United States have been significantly altered by the encroachment of shrubs into grasslands [Buffington and Herbel, 1965, Grover and Musick, 1990, Bahre and Shelton, 1993]; which not only out-competes the native species, but provides additional fuel for forest fires [Weiss and Overpeck, 2005]. Physically-based hydrologic models are playing an increasingly important role in understanding and predicting the impacts of climate change on hydrological processes and water resources [VanRheenen et al., 2004, Kollet and Maxwell, 2008, Liuzzo et al., 2010]. The WRF - *pt*RIBS+VEGGIE model, a combination of RCM with a physically-based eco-hydrology model, thus presents an excellent opportunity to study regional impact of climate change with emphasis on water resources and vegetation distribution.

### **Incorporation of groundwater dynamics**

Groundwater is estimated to be approximately 50% of potable water [Foster and Chilton, 2003] and is replenished by precipitation that escapes evaporation, transpiration, and surface runoff. The land surface schemes within the RCMs have commonly ignored groundwater dynamics. Recently several studies have demonstrated the impact of accounting for groundwater on surface fluxes and soil moisture within RCMs [Gutowski et al., 2002, Liang et al., 2003, Yeh and Eltahir, 2005, Maxwell et al., 2007, Niu et al., 2007, Gan et al., 2007, Maxwell et al., 2007, Kollet and Maxwell, 2008, Anyah et al., 2008, Jiang et al., 2009]. The complexity of groundwater model coupled with RCMs shows quite a range of variation: use of water table as a lower boundary condition [Yeh and Eltahir, 2005, Niu et al., 2007]; a TOPMODEL [Beven and Kirkby, 1979] based lateral redistribution [Famiglietti and Wood, 1994]; a full integration of variably-saturated groundwater flow modeling [Maxwell et al.,



2007, Maxwell and Kollet, 2008]. RCMs coupled with groundwater models have been applied at spatial scale ranging from catchment [Maxwell et al., 2007] to continental [Anyah et al., 2008, Yuan et al., 2008]. An earlier version of the tRIBS model included a quasi three-dimensional cascade groundwater module [Ivanov et al., 2004], though the current version of the *ptRIBS+VEGGIE* model does not include it. Incorporation of the groundwater module within the *ptRIBS+VEGGIE* model would not only extend the eco-hydrology model's applicability, but would also allow the WRF - *ptRIBS+VEGGIE* model to study the influence of groundwater dynamics on regional climate. Climate change is expected to alter precipitation patterns (amount and timing of rainfall), thus affecting the moisture supply for recharge. Increased temperatures could lead to higher evaporative demands, thereby lowering the amount of recharge. A number of studies have started to look at the impacts of climate change on recharge in various watersheds [Krishnen, 2002, II and Luukkonen, 2003, Scibek and Allen, 2006, Green et al., 2007, Herrera-Pantoja and Hiscock, 2008, Ng, 2009]. Thus, incorporating the groundwater modeling capability within *ptRIBS+VEGGIE* could further enable the use the WRF - *ptRIBS+VEGGIE* model to study regional impacts of climate change on groundwater recharge.



# APPENDIX A

## 1-D HEAT DIFFUSION MODEL

The implementation of 1-D heat diffusion model in this study closely follows the approach of Bonan [1996]. The heat flux,  $F[\text{W m}^{-2}]$ , at depth  $z[\text{m}]$  with soil temperature,  $T[\text{K}]$ , is given as

$$F = -\kappa(\theta)\frac{\partial T}{\partial z} \quad (\text{A.1})$$

and 1-D heat diffusion model for is

$$C(\theta)\frac{\partial T}{\partial t} = -\frac{\partial F}{\partial z} \quad (\text{A.2})$$

$$= \frac{\partial}{\partial z} \left( \kappa(\theta)\frac{\partial T}{\partial z} \right) \quad (\text{A.3})$$

where  $C(\theta)$  [ $\text{J m}^{-3} \text{K}^{-1}$ ] and  $\kappa(\theta)$  [ $\text{J m}^{-3} \text{s}^{-1} \text{K}^{-1}$ ] are volumetric soil heat capacity and volumetric soil heat conductivity respectively. The details about the parameterization scheme used for  $C(\theta)$  and  $\kappa(\theta)$  are given in Section 5.4.

## A.1 Spatial discretization

For the finite-volume formulation of 1-D heat diffusion equation, the mesh used is shown in Figure A-1. The spatial domain is discretized into *grid cells*, where i-th grid cell ( $C_i$ ) is denoted by  $[z_{i-1/2}, z_{i+1/2}]$ .

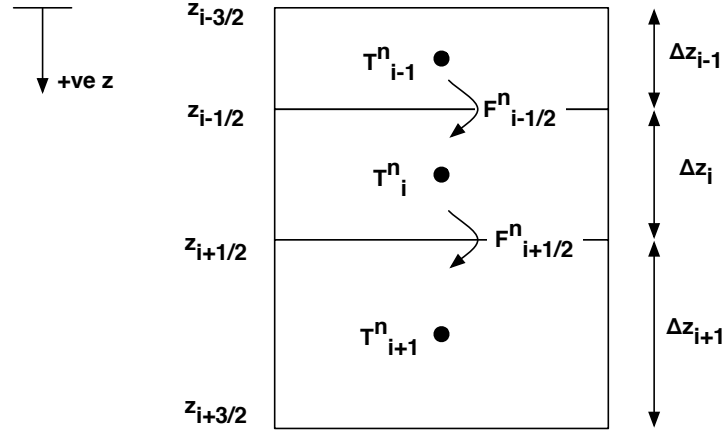


Figure A-1: Vertical mesh used of soil profile used in solving 1-D heat diffusion model

The value of average soil temperature ( $T_i$ ) will be approximated over the  $i$ -th interval at  $n$ -th time interval as

$$T_i^n \approx \frac{1}{\Delta z_i} \int_{z_{i-1/2}}^{z_{i+1/2}} T(z, t_n) dz \equiv \frac{1}{\Delta z_i} \int_{C_i} T(z, t_n) dz$$

where  $\Delta z_i = z_{i+1/2} - z_{i-1/2}$  is the length of the grid cell.

Integrating Eq A.2 over the control volume  $C_i$  gives

$$\begin{aligned} \int_{C_i} C(\theta) \frac{\partial T}{\partial t} dz &= \int_{C_i} -\frac{\partial F}{\partial z} dz \\ \Delta z_i C(\theta_i) \frac{\partial T}{\partial t} &= -F_{i+1/2} + F_{i-1/2} \end{aligned} \quad (\text{A.4})$$

Assuming the heat flux from depth  $z_i$  to interface  $z_{i+1/2}$  is equal to heat flux from the interface  $z_{i+1/2}$  to depth  $z_{i+1}$  i.e.

$$F_{i+1/2} = -\kappa_i \left( \frac{T_{i+1/2} - T_i}{\Delta z_i/2} \right) \quad (\text{A.5a})$$

$$= -\kappa_{i+1} \left( \frac{T_{i+1} - T_{i+1/2}}{\Delta z_{i+1}/2} \right) \quad (\text{A.5b})$$

$$= -\kappa_{i+1/2} \left( \frac{T_{i+1} - T_i}{\Delta z_i/2 + \Delta z_{i+1}/2} \right) \quad (\text{A.5c})$$

Using algebraic manipulation, the interface soil temperature and interface soil thermal conductivity are

$$T_{i+1/2} = \frac{1}{\frac{2\kappa_i}{\Delta z_i} + \frac{2\kappa_{i+1}}{\Delta z_{i+1}}} \left[ \frac{T_i}{\frac{\Delta z_i}{2\kappa_i}} + \frac{T_{i+1}}{\frac{\Delta z_{i+1}}{2\kappa_{i+1}}} \right] \quad (\text{A.6})$$

$$\frac{(\Delta z_i + \Delta z_{i+1})/2}{\kappa_{i+1/2}} = \frac{(\Delta z_i)/2}{\kappa_i} + \frac{(\Delta z_{i+1})/2}{\kappa_{i+1}} \quad (\text{A.7})$$

Combining A.5c and A.7, the interface heat flux is given as

$$F_{i+1/2} = - \left( \frac{T_{i+1} - T_i}{\frac{\Delta z_i}{2\kappa_i} + \frac{\Delta z_{i+1}}{2\kappa_{i+1}}} \right) \quad (\text{A.8})$$

## A.2 Temporal discretization

Crank-Nicolson method, second-order accurate method in time, is used for time discretization. The method combines the explicit method fluxes evaluated at n-th time level and the implicit method fluxes evaluated at n+1-th time level as

$$\Delta z_i C(\theta_i) \left( \frac{T_i^{n+1} - T_i^n}{\Delta t} \right) = \frac{1}{2} (-F_{i+1/2}^n + F_{i-1/2}^n) + \frac{1}{2} (-F_{i+1/2}^{n+1} + F_{i-1/2}^{n+1}) \quad (\text{A.9})$$

The above results in a tri-diagonal system of equations that can be given in the form of

$$a_i T_{i-1}^{n+1} + b_i T_i^{n+1} + c_i T_{i+1}^{n+1} = r_i \quad (\text{A.10})$$

where  $a_i$ ,  $b_i$ ,  $c_i$  and  $r_i$  are described in the following section.

### A.3 Derivation for the system of equations

Let us define three following variables

$$m_1 = \frac{\Delta z_{i-1}}{\kappa_{i-1}} + \frac{\Delta z_i}{\kappa_i} \quad (\text{A.11})$$

$$m_2 = \frac{\Delta z_i}{\kappa_i} + \frac{\Delta z_{i+1}}{\kappa_{i+1}} \quad (\text{A.12})$$

$$m_3 = \frac{\Delta t}{\Delta z C_i} \quad (\text{A.13})$$

For first layer,  $i = 1$ ,  $F_{-1/2} = G$ , where  $G$  is the ground heat flux into the soil (positive into the soil).

$$\begin{aligned} \Delta z_1 C_1 \left( \frac{T_1^{n+1} - T_1^n}{\Delta t} \right) &= G - \frac{1}{2} \left( F_{1+1/2}^n + F_{1+1/2}^{n+1} \right) \\ &= G + \frac{1}{2} \left( \frac{T_2^n - T_1^n + T_2^{n+1} - T_1^{n+1}}{\frac{\Delta z_1}{2\kappa_1} + \frac{\Delta z_2}{2\kappa_2}} \right) \end{aligned}$$

Rearranging the above equation and multiplying both sides by  $m_3$ , one obtains the following equation

$$\left( 1 + \frac{m_3}{m_2} \right) T_1^{n+1} - \frac{m_3}{m_2} T_2^{n+1} = T_1^n + G m_3 + \frac{m_3}{m_2} (T_2^n - T_1^n) \quad (\text{A.14})$$

Comparing A.14 with A.10, the coefficients of the tri-diagonal system are given as

$$a_1 = 0 \quad (\text{A.15a})$$

$$b_1 = 1 + \frac{m_3}{m_2} \quad (\text{A.15b})$$

$$c_1 = -\frac{m_3}{m_2} \quad (\text{A.15c})$$

$$r_1 = T_1^n + Gm_3 + \frac{m_3}{m_2}(T_2^n - T_1^n) \quad (\text{A.15d})$$

For the last soil layer,  $i = N$ , zero flux boundary condition is implemented i.e.  $F_{N+1/2} = 0$

$$\begin{aligned} \Delta z_N C_N \left( \frac{T_N^{n+1} - T_N^n}{\Delta t} \right) &= \frac{1}{2} \left( F_{N-1/2}^n + F_{N-1/2}^{n+1} \right) \\ &= \frac{1}{2} \left( \frac{-T_N^n + T_{N-1}^n - T_N^{n+1} + T_{N-1}^{n+1}}{\frac{\Delta z_{N-1}}{2\kappa_{N-1}} + \frac{\Delta z_N}{2\kappa_N}} \right) \end{aligned}$$

Rearranging the above equation and multiplying both side by  $m_3$ , one obtains the following equation

$$-\frac{m_3}{m_1} T_{N-1}^{n+1} + \left( 1 + \frac{m_3}{m_1} \right) T_N^{n+1} \Psi = T_N^n + \frac{m_3}{m_1} (T_{N-1}^n - T_N^n) \quad (\text{A.16})$$

Comparing A.16 with A.10, the coefficients of the tri-diagonal system are given as

$$a_N = -\frac{m_3}{m_1} \quad (\text{A.17a})$$

$$b_N = 1 + \frac{m_3}{m_1} \quad (\text{A.17b})$$

$$c_N = 0 \quad (\text{A.17c})$$

$$r_N = T_N^n + \frac{m_3}{m_1} (T_{N-1}^n - T_N^n) \quad (\text{A.17d})$$

For the all other layers,  $1 < i < N$ ,

$$\begin{aligned}
\Delta z_i C_i \left( \frac{T_i^{n+1} - T_i^n}{\Delta t} \right) &= \frac{-1}{2} \left( F_{i+1/2}^n + F_{i+1/2}^{n+1} \right) \\
&+ \frac{1}{2} \left( F_{i-1/2}^n + F_{i-1/2}^{n+1} \right) \\
&= \frac{1}{2} \left( \frac{T_{i+1}^n - T_i^n + T_{i+1}^{n+1} - T_i^{n+1}}{\frac{\Delta z_i}{2\kappa_i} + \frac{\Delta z_{i+1}}{2\kappa_{i+1}}} \right) \\
&+ \frac{1}{2} \left( \frac{-T_i^n + T_{i-1}^n - T_i^{n+1} + T_{i-1}^{n+1}}{\frac{\Delta z_{i-1}}{2\kappa_{i-1}} + \frac{\Delta z_i}{2\kappa_i}} \right)
\end{aligned}$$

Rearranging the above equation and multiplying by  $m_3$  on both sides, one obtains

$$\begin{aligned}
-\frac{m_3}{m_1} T_{i-1}^{n+1} + \left( 1 + \frac{m_3}{m_1} + \frac{m_3}{m_2} \right) T_i^{n+1} - \frac{m_3}{m_2} T_{i+1}^{n+1} = \\
T_i^n + \frac{m_3}{m_1} (T_{i-1}^n - T_i^n) - \frac{m_3}{m_2} (T_i^n - T_{i+1}^n)
\end{aligned} \tag{A.18}$$

Comparing A.18 with A.10, the coefficients of the tri-diagonal system are given as

$$a_i = -\frac{m_3}{m_1} \tag{A.19a}$$

$$b_i = 1 + \frac{m_3}{m_1} + \frac{m_3}{m_2} \tag{A.19b}$$

$$c_i = -\frac{m_3}{m_2} \tag{A.19c}$$

$$r_i = T_i^n + \frac{m_3}{m_1} (T_{i-1}^n - T_i^n) - \frac{m_3}{m_2} (T_i^n - T_{i+1}^n) \tag{A.19d}$$



## APPENDIX B

# RESULTS FROM THE WRF - *pt*RIBS+VEGGIE SIMULATION IN 2003

This appendix provides results with the WRF - *pt*RIBS+VEGGIE model over the D03 domain for 2003. The sequence of results presented here, follow closely those presented in Section 7.2.

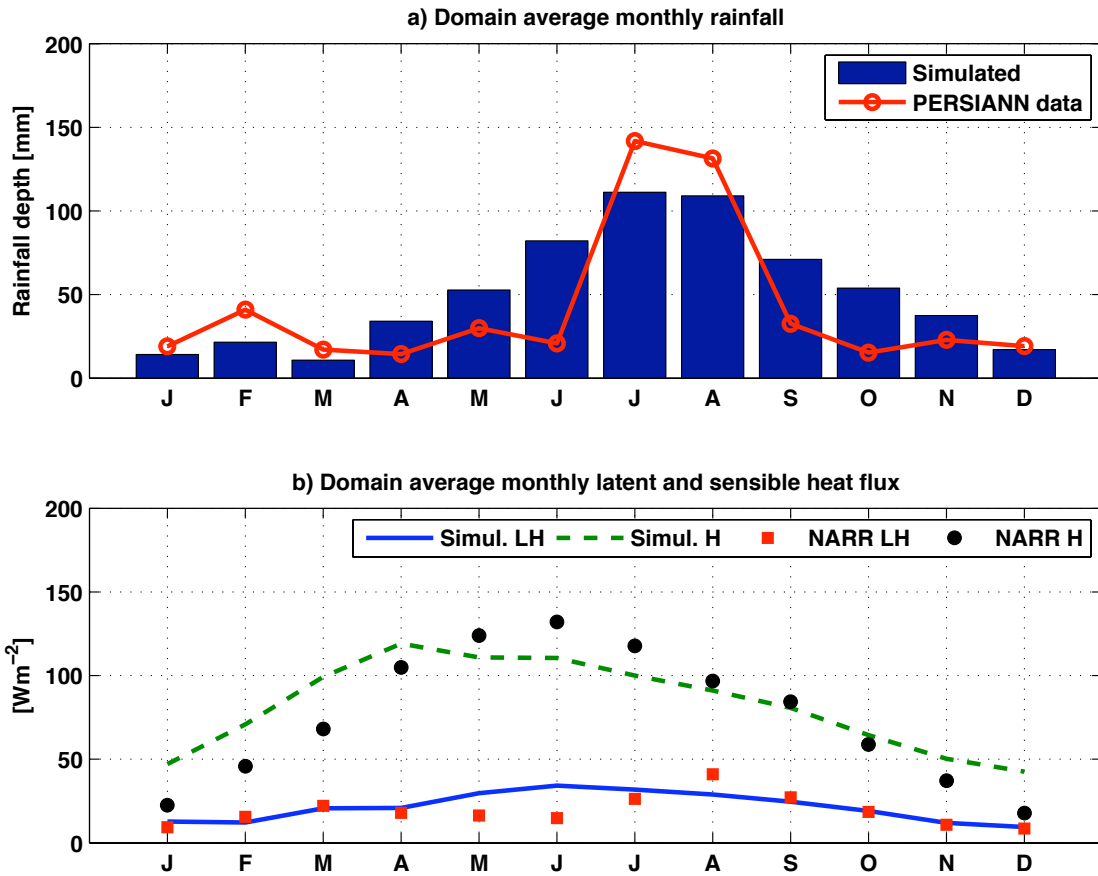


Figure B-1: Timeseries of various simulated quantities for 2003 by the WRF - *ptRISB+VEGGIE* model. Panel (a) shows domain average simulated monthly precipitation, along with the estimates obtained from the PERSIANN data over the same region. Panel (b) shows simulated domain average latent and sensible heat fluxes, along with the estimates from the NARR data.

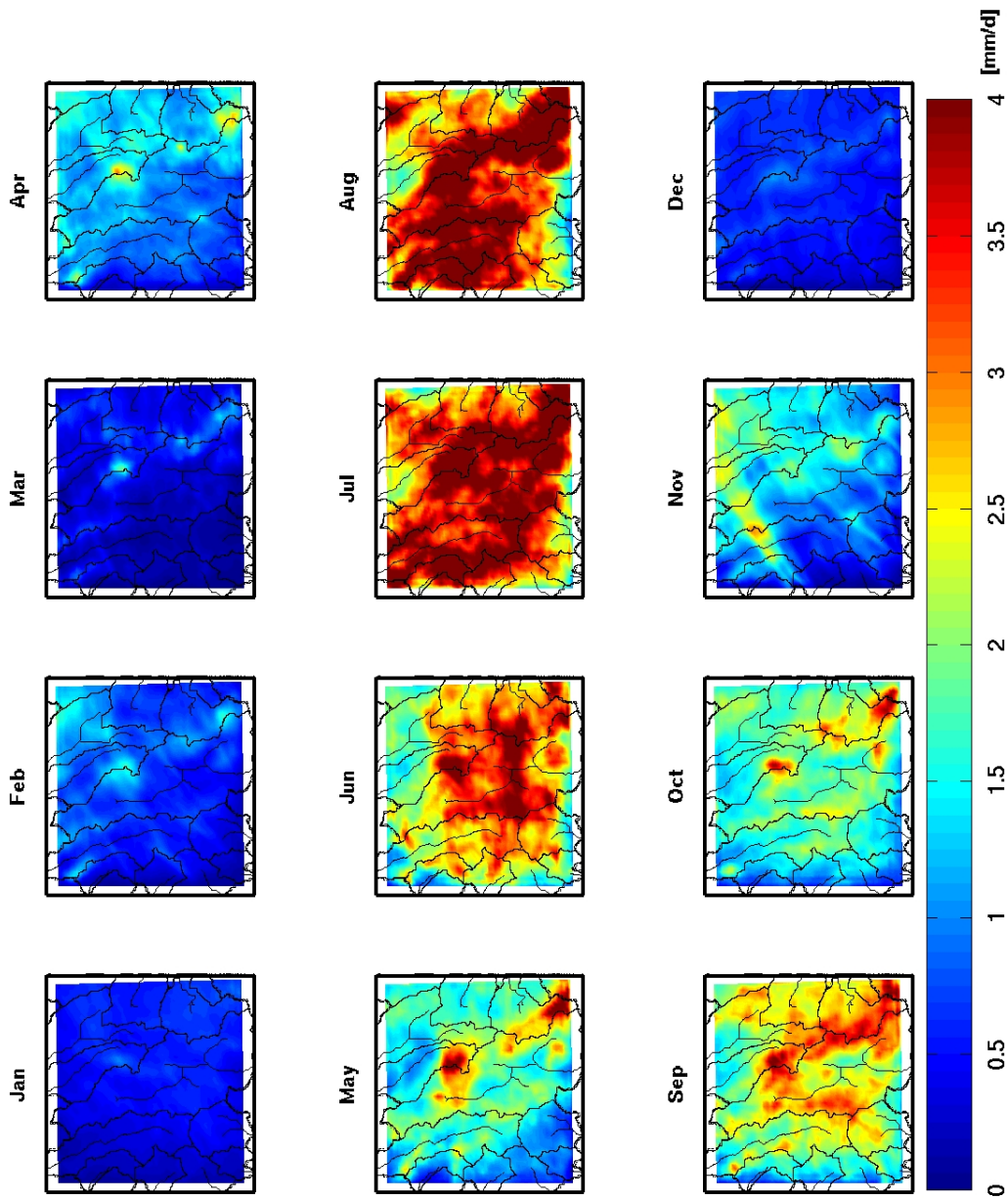


Figure B-2: Spatial distribution of simulated monthly precipitation for 2003 by the WRF - *pt*RISB+VEGGIE model for the FLAT-STAT case.

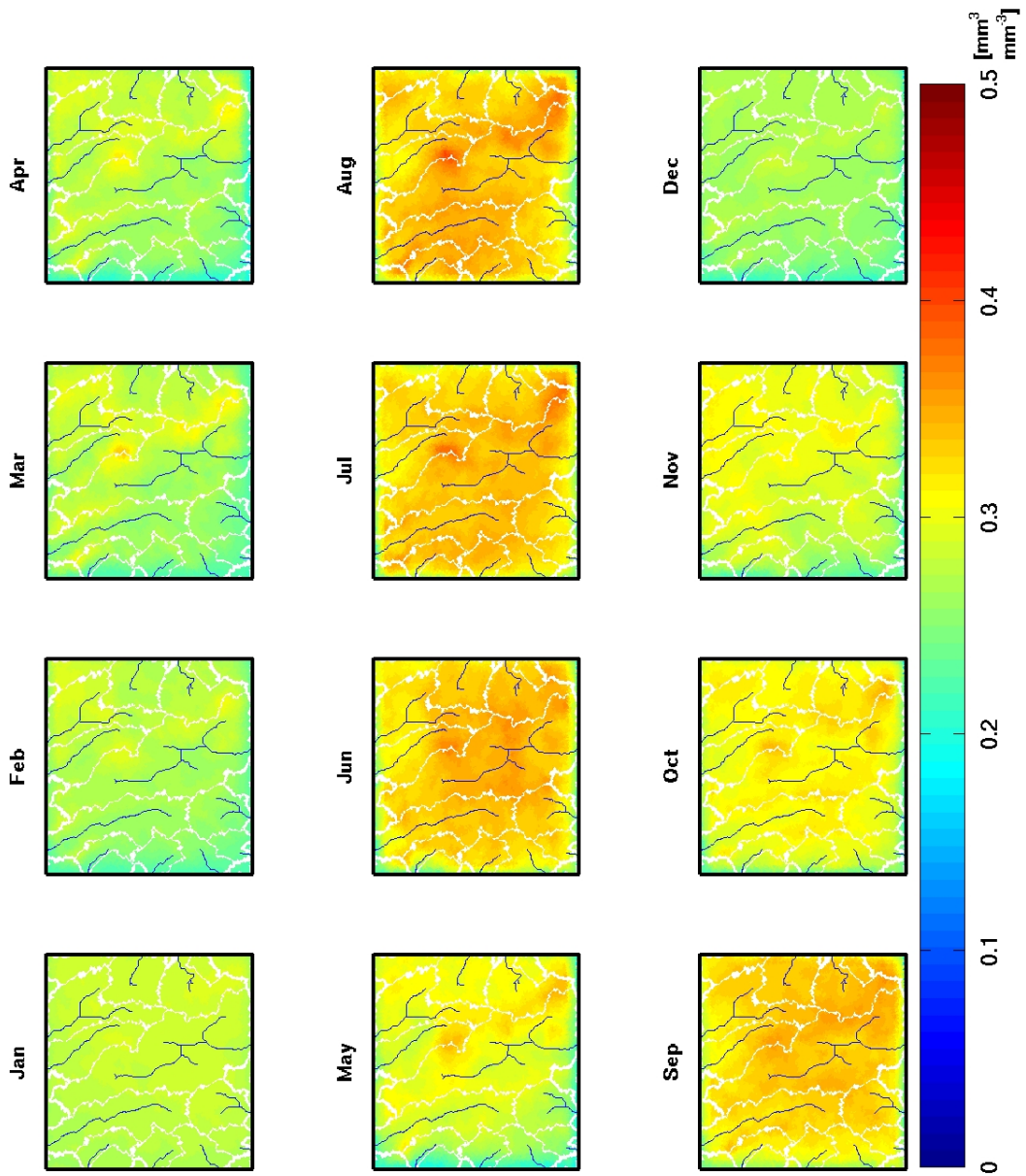


Figure B-3: Spatial distribution of simulated monthly volumetric root-zone soil moisture for 2003 by the WRF - *pt*RISB+VEGGIE model for the FLAT-STAT case.

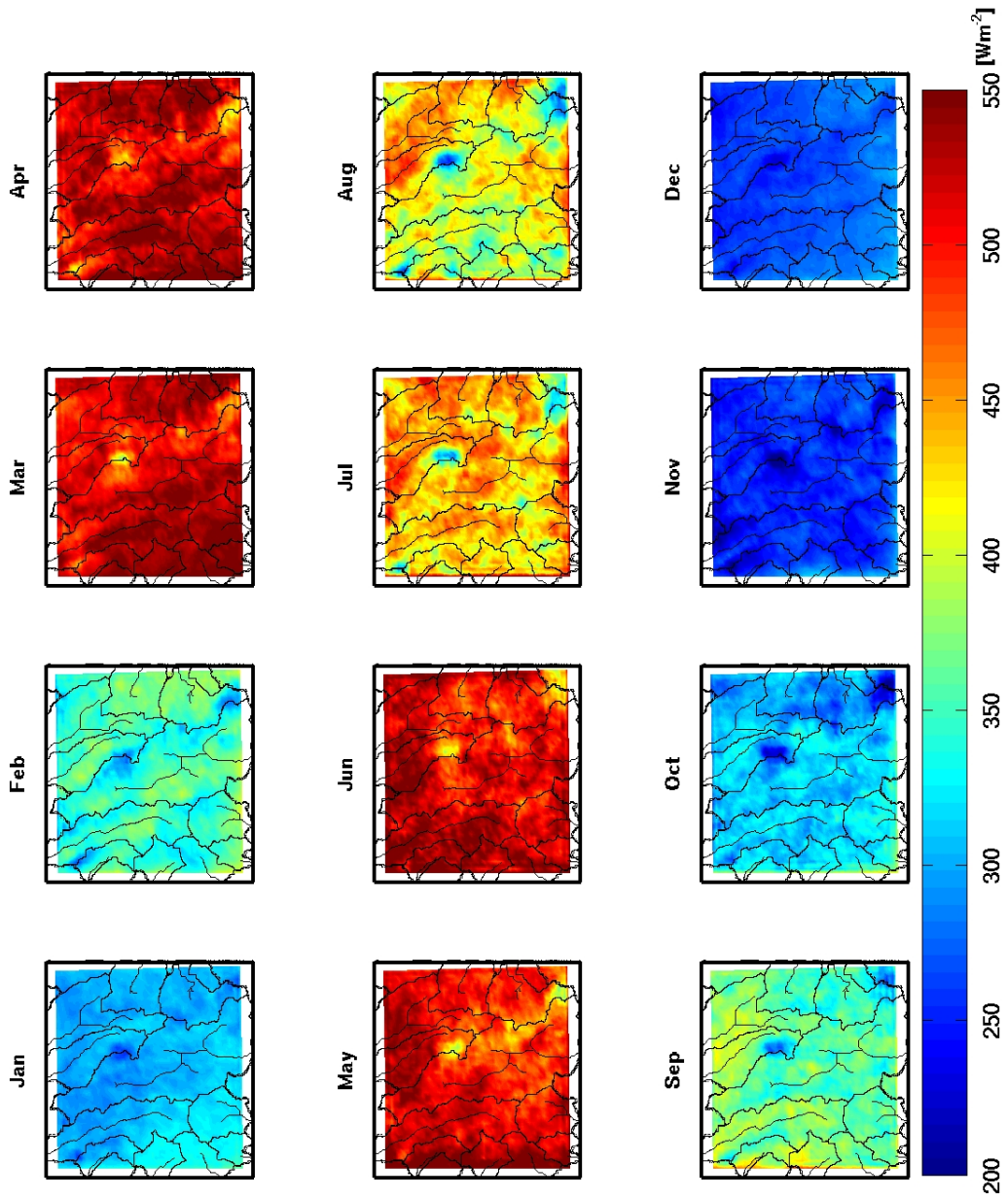


Figure B-4: Spatial distribution of simulated monthly downwelling surface shortwave radiation for 2003 by the WRF - *pt*RISB+VEGGIE model for the FLAT-STAT case.

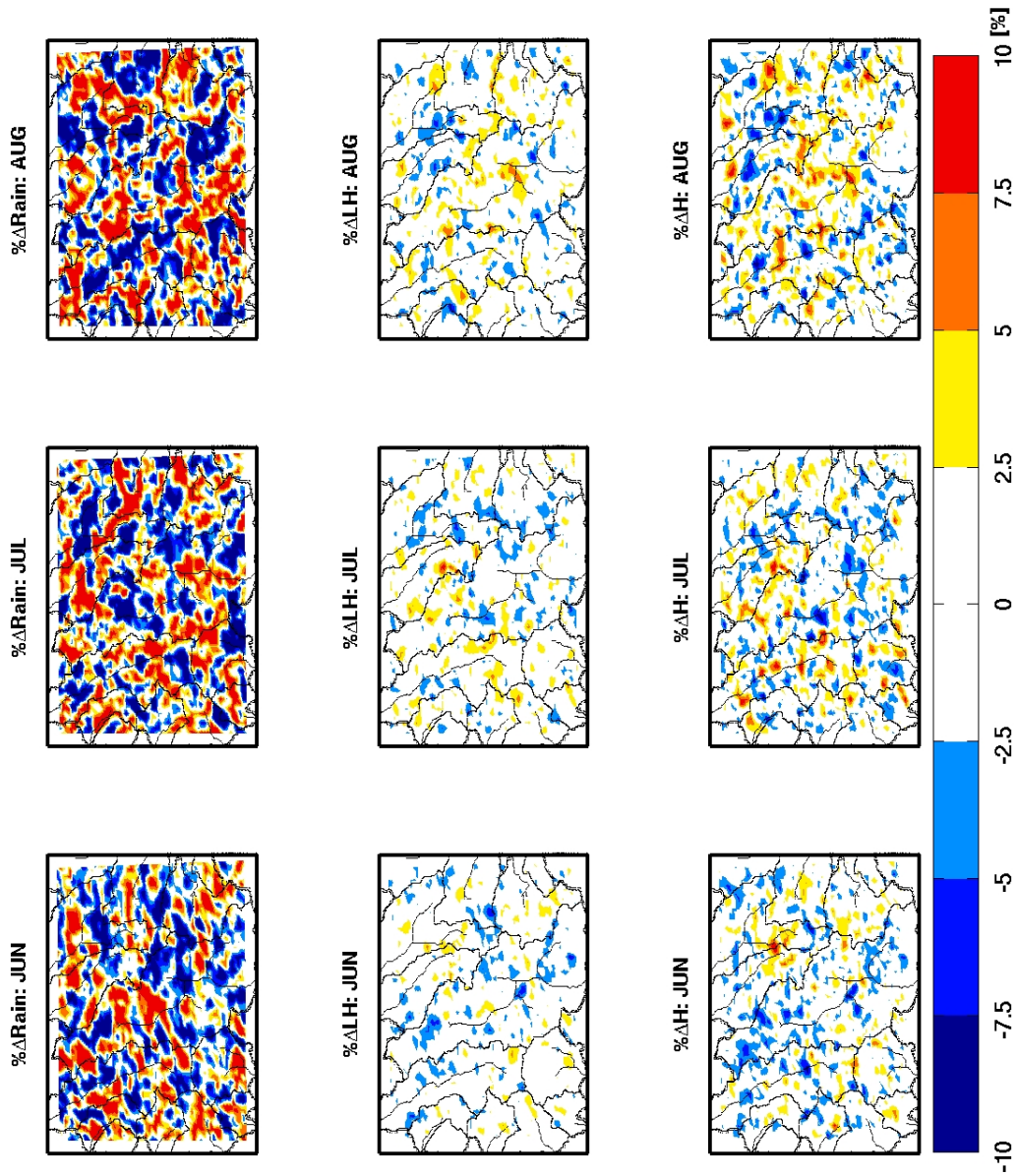


Figure B-5: Monthly average anomalies between the TOPO-STAT and the FLAT-STAT case during the months of June, July and August, 2003 for: (a) Rainfall; (b) Latent heat flux; and (c) Sensible heat flux. (Percentage anomalies are computed as the TOPO-STAT value minus the FLAT-STAT value with respect to the FLAT-STAT value).

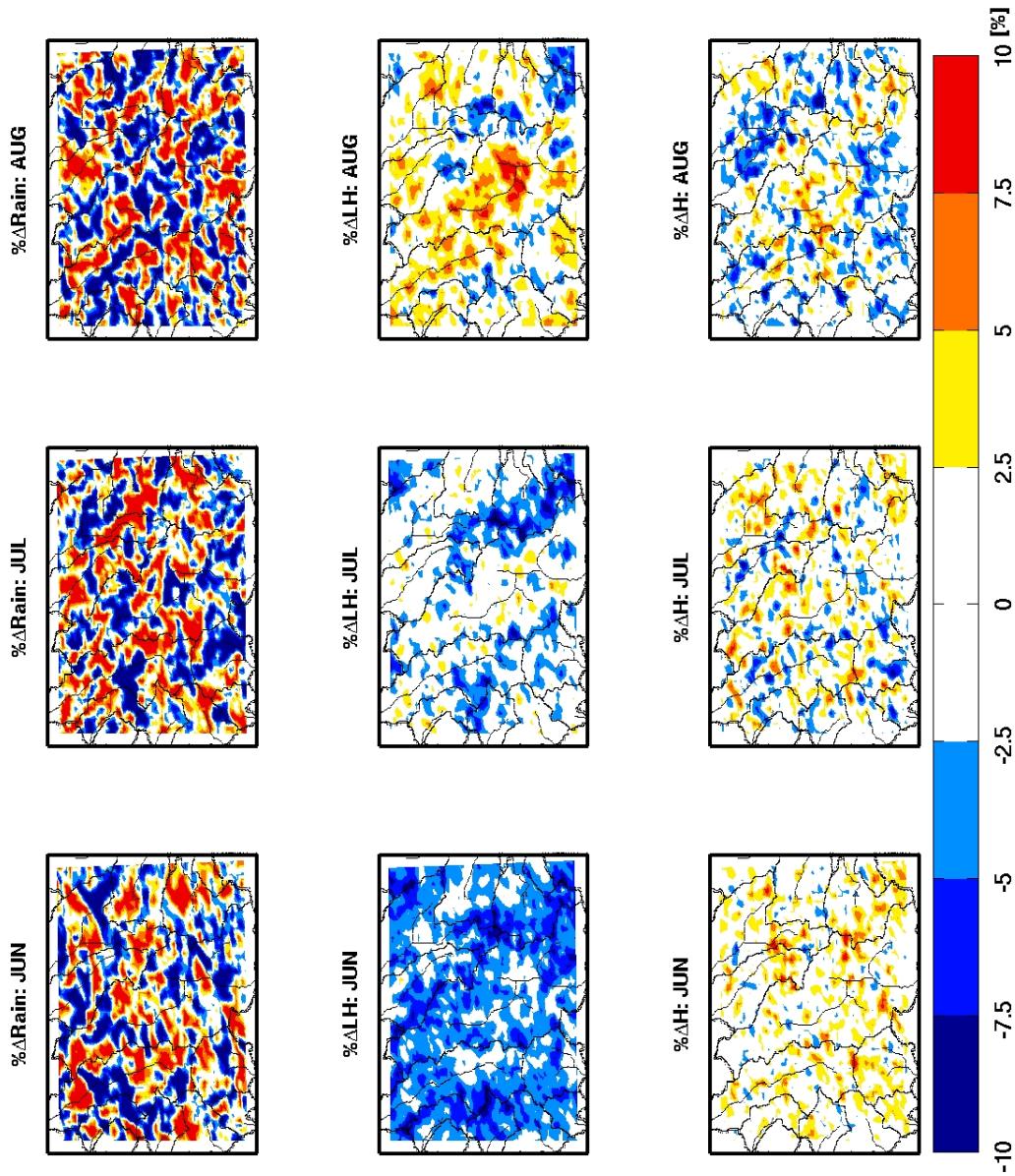


Figure B-6: Monthly average anomalies between the TOPO-DYN and the FLAT-STAT case during the months of June, July and August, 2003 for: (a) Rainfall; (b) Latent heat flux; and (c) Sensible heat flux. (Percentage anomalies are computed as the TOPO-DYN value minus the FLAT-STAT value with respect to the FLAT-STAT value).

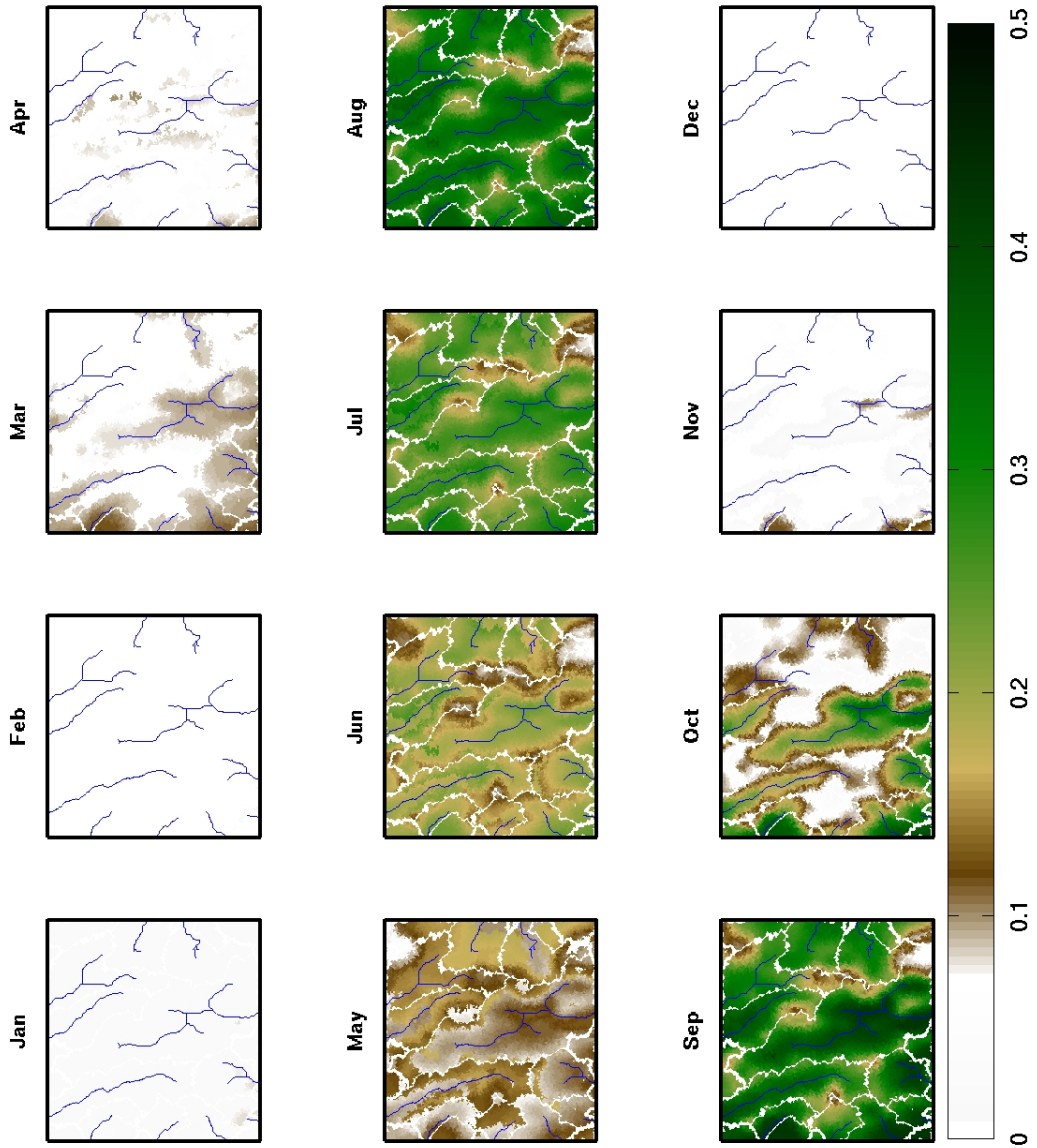


Figure B-7: Spatial distribution of simulated monthly average leaf area index for 2003 by the WRF - *pt*RISB+VEGGIE model for the TOPO-DYN case.



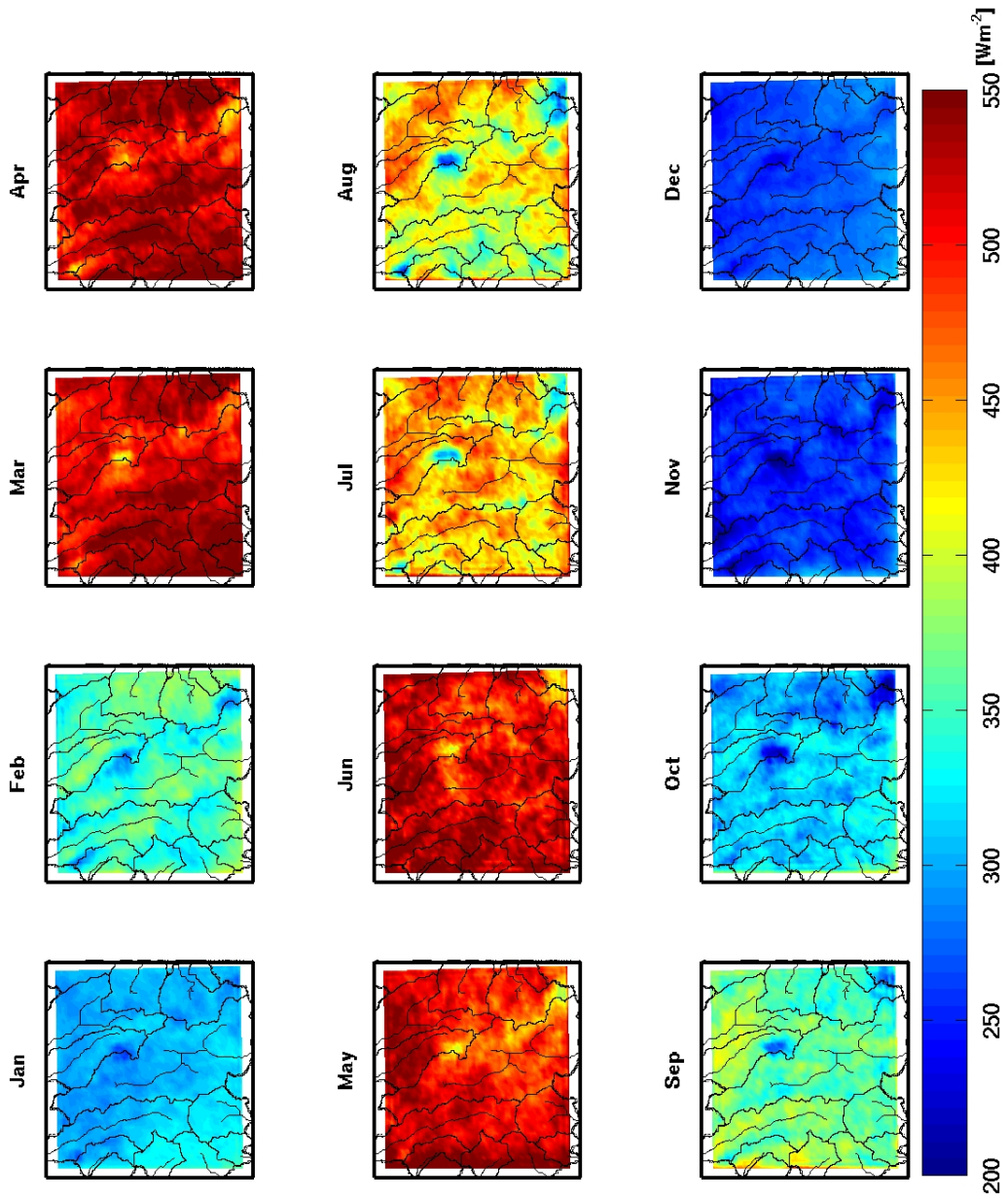


Figure B-8: Spatial distribution of simulated monthly average downwelling surface shortwave radiation for 2003 by the WRF - *ptRISB+VEGGIE* model for the TOPO-DYN case.

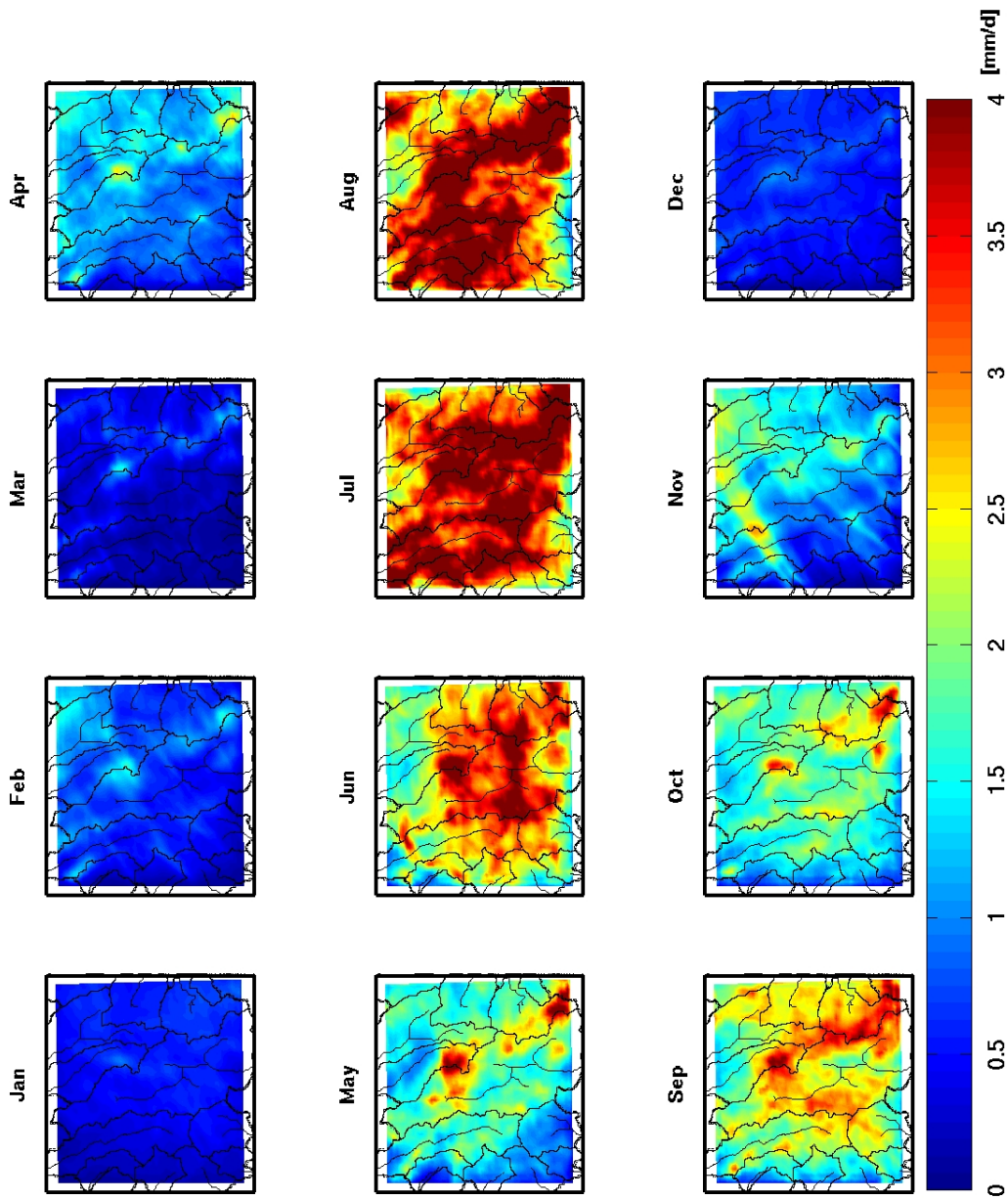


Figure B-9: Spatial distribution of simulated monthly average rainfall for 2003 by the WRF - *ptRISB+VEGGIE* model for the TOPO-DYN case.

Table B.1: Average correlation during June, July and August, 2003, among the various anomalies: rainfall, 10-cm soil moisture (SM), bowen ratio (BR), surface temperature ( $T_s$ ), planetary boundary layer height (PBLH), and wet-bulb depression (WBD). The first and second column corresponds to anomalies between the TOPO-STAT and the TOPO-DYN cases with respect to the FLAT-STAT case. The third column corresponds to anomalies in the TOPO-DYN with respect to the FLAT-STAT case, after neglecting the “radiation-limited” points within the domain (see Section 7.2.3)

	TOPO-STAT vs FLAT-STAT	TOPO-DYN vs FLAT-STAT	TOPO-DYN vs FLAT-STAT*
$\Delta$ Rain and $\Delta$ SM	+0.88	+0.87	+0.88
$\Delta$ SM and $\Delta$ BR	-0.69	-0.36	-0.47
$\Delta$ BR and $\Delta T_s$	+0.53	-0.06	+0.17
$\Delta T_s$ and $\Delta$ PBLH	+0.54	+0.40	+0.46
$\Delta T_s$ and $\Delta$ WBD	+0.74	+0.74	+0.74
PBLH and $\Delta$ WBD.	+0.63	+0.54	+0.60



# REFERENCES

- M. B. Abbott, J. C. Bathurst, L. A. Cunge, P. E. O’Connell, and J. Rasmussen. An introduction to the European Hydrological System-Systeme Hydrologique European, ‘SHE’. *Journal Hydrology*, 87:61–77, 1986.
- E. A. Aligo, W. A. Gallus, and M. Segal. Summer rainfall forecast spread in an ensemble initialized with different soil moisture analysis. *Weather Forecasting*, 22:299–314, 2007.
- M. C. Anderson and W. P. Kustas. Mapping evapotranspiration and drought at local to continental scales using thermal remote sensing. In *Proc. IEEE International Geoscience & Remote Sensing Symposium*, Boston, MA, July 2008.
- A. Ångström. A study of the radiation of the atmosphere. *Smithsonian Institution Miscellaneous Collections*, 65:1–159, 1918.
- R. O. Anyah, C. P. Weaver, G. Miguez-Macho, Y. Fan, and A. Robock. Incorporating water table dynamics in climate modeling: 3. Simulated groundwater influence on coupled land-atmosphere variability. *J. Geophys. Res.*, 113(D07103, doi:1029/2007JD009087), 2008.
- J. A. Augustine, J. J. DeLuisi, and C. N. Long. SURFRAD-A National Surface Radiation Budget Network for Atmospheric Research. *Bulletin of the American Meteorological Society*, 81(10):2341–2357, 2000.
- J. A. Augustine, G. B. Hodges, C. R. Cornwall, J. J. Michalsky, and C. I. Medina. An update on SURFRADThe GCOS surface radiation budget network for the continental United States. *J. Atmos. Oceanic Technol.*, 22:1460–1472, 2005.

- R. Avissar and Y. Liu. Three-dimensional numerical study of shallow convective clouds and precipitation induced by land surface forcing. *J. Geophys. Res.*, 101:7499–7518, 1996.
- R. Avissar and R. Pielke. A parameterization of heterogeneous land-surface for atmospheric numerical models and its impact on regional meteorology. *Monthly Weather Review*, 117: 2113–2136, 1989.
- P. Y. Julien B. Saghaian B. CASC2D Users Manual. Technical Report, Department of Civil Engineering, Colorado State University, Fort Collins, 1991.
- C. J. Bahre and M. L. Shelton. Historic vegetation change, mesquite increases, and climate in southwestern Arizona. *Journal of Biogeography*, 20:489–504, 1993.
- B.C. Bates, Z.W. Kundzewicz, S. Wu, and J.P. Palutikof. Climate Change and Water. Technical report, Technical Paper of the Intergovernmental Panel on Climate Change, IPCC Secretariat, Geneva, 2008.
- N. Batra, S. Islam, V. Venturini, G. Bisht, and L. Jiang. Estimation and comparison of evapotranspiration from MODIS and AVHRR sensors for clear sky days over the Southern Great Plains. *Remote Sens. Environ.*, 103(1):1–15, 2006.
- A. C. M. Beljaars, P. Viterbo, M. J. Miller, and A. K. Betts. The anomalous rainfall over the United States during July 1993: Sensitivity to land surface parameterization and soil moisture. *Monthly Weather Review*, 124:362–383, 1996.
- T. J. Bennett. A coupled atmosphere-sea ice model study of the role of sea ice in climatic prediction. *J. Atmos. Sci.*, 39:1456–1465, 1982.
- K. P. Berger and D. Entekhabi. Basin hydrologic response relations to distributed physiographic descriptors and climate. *Journal of Hydrology*, 247(3-4):169–182, 2001.
- T. C. Berliand. Method of climatological estimation of global radiation. *Meteorol. Gridrol.*, 6:9–12, 1960.

- A. K. Betts. Understanding hydrometeorology using global models. *Bulletin of American Meteorological Society*, 85(11):1673–1688, 2004.
- K. J. Beven. *Distributed Models*, chapter 13. Wiley, New York, 1985.
- K. J. Beven and M. J. Kirkby. A physically based variable contributing area model of basin hydrology. *Hydrological Sciences Bulletin*, 24:43–69, 1979.
- K. J. Beven, , A. Calver, and E. M. Morris. A physically based variable contributing area model of basin hydrology. Technical Report 24, Hydrological Sciences Bulletin, 1987.
- G. Bisht, V. Venturini, J. Liang, and S. Islam. Estimation of the net radiation using MODIS (moderate resolution imaging spectroradiometer) data for clear sky days. *Remote Sens. Environ.*, 97(1):52–67, 2005.
- G. B. Bonan. A land surface model (LSM version 1.0) for ecological, hydrological and atmospheric studies: Technical description and user’s guide. NCAR Technical Note, NCAR/TN-417+STR, 1996.
- G. B. Bonan and L. M. Stillwell-Soller. Soil water and the persistence of oods and droughts in the Mississippi River Basin. *Water Resources Research*, 34(10):2693–2701, 1998.
- M. G. Bosilovich and W. Y. Sun. Numerical simulations of the 1993 Midwestern flood: Land-atmosphere interactions. *Journal of Climate*, 12:1490–1505, 1999.
- R. H. Brooks and A. T. Corey. Hydraulic Properties of Porous Media, Hydrol. Pap. 3. Technical report, Colo. Satat Uno., Fort Collins, 1964.
- K. L. Brubaker and D. Entekhabi. An analytical approach to modeling land atmosphere interaction, 1. Construct and Equilibrium behavior. *Water Resources Research*, 31(3): 619–632, 1995a.
- K. L. Brubaker and D. Entekhabi. An analytical approach to modeling land atmosphere interaction, 2. Stochastic formulation. *Water Resources Research*, 31(3):633–643, 1995b.

- K. L. Brubaker and D. Entekhabi. Analysis of feedback mechanism in land-atmosphere interaction. *Water Resources Research*, 32(5):107–136, 1996.
- D. Brunt. Notes on radiation in the atmosphere. *Quarterly Journal of the Royal Meteorological Society*, 58:389–420, 1932.
- W. Brutsaert. On a derivable formula for long-wave radiation from clear skies. *Water Resources Research*, 11:742–744, 1975.
- L. C. Buffington and C. H. Herbel. Vegetational changes on a semidesert grassland range from 1858 to 1963. *Ecological Monographs*, 35:139–164, 1965.
- R. J. C. Burnash, R. L. Ferral, and R. A. McGuire. A generalized streamflow simulation system-conceptual modeling for digital computers. Technical report, U.S. Department of Commerce, National Weather Service and State of California, Department of Water Resources, 1973.
- C. L. Castro, R. A. Pielke Sr., and G. Leoncini. Dynamical downscaling: Assessment of value retained and added using the Regional Atmospheric Modeling System (RAMS). *J. Geophys. Res.*, 110(D05108, doi:10.1029/2004JD004721), 2005.
- F. J. F. Chagnon. *Patterns of Shallow Clouds and Rainfall over the Amazon: Climatic Impacts of Deforestation*. PhD dissertation, Massachusetts Institute of Technology, Department of Civil and Environmental Engineering, February 2005.
- J. G. Charney. Dynamics of deserts and drought in the Sahel. *Quarterly Journal of the Royal Meteorological Society*, 101:193–202, 1975.
- J. Chen and P. Kumar. Topographic influence on the seasonal and inter-annual variation of water and energy balance of basins in North America. *Journal of Climate*, 14(9):1989–2014, 2001.



- H. I. Choi, P. Kumar, and X.-Z. Liang. Three-dimensional volume-averaged soil moisture transport model with a scalable parameterization of subgrid topographic variability. *Water Resources Research*, 43, W04414, doi:10.1029/2007WR005134, 2007.
- M.-D. Chou and M. J. Suarez. An efficient thermal infrared radiation parameterization for use in general circulation models. Technical report, NASA Tech. Memo. 104606, 3, 1994.
- J. H. Christensen, B. Hewitson, and coauthors. *Regional Climate Projections. In: Climate Change 2007: The Physical Science Basis. Contribution of Working Group I to the Fourth Assessment Report of the Intergovernmental Panel on Climate Change.* Cambridge University Press, Cambridge, United Kingdom and New York, NY, USA., 2007.
- T. M. Church. An underground route for the water cycle. *Nature*, 380:579–580, 1996.
- B. A. Cosgrove, D. Lohmann, K. E. Mitchell, P. R. Houser, E. F. Wood, J. C. Schaake, A. Robock, C. Marshall, J. Sheffield, Q. Duan, L. Luo, R. W. Higgins, R. T. Pinker, and J. D. Tarpley. Real-time and Retrospective Forcing in the North American Land Data Assimilation System (NLDAS) Project. *J. Geophys. Res.*, 108(D22), 8842, doi:10.1029/2002JD003118, 2003.
- P. M. Cox. Description of the 'TRIFFIRD' dynamic global vegetation model. Technical report, Hadley Center Technical Note, 24, 2000.
- D. R. DeWalle, B. R. Swistock, T. E. Johnson, and K. J. McGuire. Potential effects of climate change and urbanization on mean annual streamflow in the United States. *Water Resour. Res.*, 36(9):2655-2664, 2000.
- G. Diak and C. Gautier. Improvements to a simple physical model for estimating insolation from GOES data. *Journal of Climate and Applied Meteorology*, 22:505–508, 1983.
- G. Diak, J. Mecikalski, M. Anderson, J. Norman, W. Kustas, R. D. Torn, and R. L. DeWolf. Estimating Land Surface Energy Budgets From Space: Review and Current Efforts at the

- University of Wisconsin-Madison and USDA-ARS. *Bull. Amer. Meteorol. Soc.*, 85:65–78, 2004.
- G. R. Diak, W. L. Bland, J. R. Mecikalski, and M. C. Anderson. Satellited-based Estimates of Longwave Radiation for Agricultural Applications. *Agr. Forest Meteorol.*, 103(4):349–355, 2000.
- R. E. Dickinson. How the coupling of the atmosphere to ocean and land helps determine the timescales of interannual variability of climate. *Journal of Geophysical Research*, 105(D20):20115–20119, 2000.
- R. E. Dickinson and A. Henderson-Sellers. Modeling tropical deforestation: A study of GCM land surface parameterizations. *Quarterly Journal of the Royal Meteorological Society*, 144:439–462, 1988.
- R. E. Dickinson, A. Henderson-Sellers, P. J. Kennedy, and M. F. Wilson. Biosphere-atmosphere transfer scheme (bats) for the near community climate model. Technical report, NCAR Technical Note NCAR/TN-275+STR, Boulder, CO, 1986.
- R. E. Dickinson, M. Shaikh, R. Bryant, and L. Graumlich. Interactive Canopies for a Climate Model. *Journal of Climate*, 11(11):2823–2836, 1998.
- P. A. Dirmeyer. The Hydrologic Feedback Pathway for Land-Climate Coupling. *Journal of Hydrometeorology*, 7(5):857–867, 2006.
- P. A. Dirmeyer. Problems in initializing soil wetness. *Bulletin of American Meteorological Society*, 76:2234–2240, 1995.
- M. W. Douglas, R. A. Maddox, K. W. Howard, and S. Reyes. The mexican monsoon. *Journal of Climate*, 6(6):1665–1677, 1993.
- C. W. Downer, F. L. Ogden, W. D. Martin, and R. S. Harmon. Theory, development, and applicability of the surface water hydrologic model CASC2D. *Hydrological Processes*, 16(2):255–275, 2002.

- P. Eagleson. Climate, Soil and Vegetation 1. Introduction to water balance dynamics. *Water Resources Research*, 15(5):705–712, 1978.
- P. Eagleson. Ecological optimality in water-limited natural soil-vegetation systems. 1. Theory and hypothesis. *Water Resources Research*, 18(2):325–340, 1982.
- R. G. Ellingson. Surface Longwave Fluxes from Satellite Observations: A Critical Review. *Remote Sens. Environ.*, 51:89–97, 1995.
- J. J. Elser, M. E. S. Bracken, E. E. Cleland, D. S. Gruner, W. S. Harpole, H. Hillebrand, J. T. Ngai, E. W. Seabloom, J. B. Shurin, and J. E. Smith. Global analysis of nitrogen and phosphorus limitation of primary producers in freshwater, marine, and terrestrial ecosystem. *Ecological Letters*, 10.1111/j.1461-0248.2007.01113.x, 2007.
- E. A. B. Eltahir. A feedback mechanism in annual rainfall, Central Sudan. *Journal of Hydrology*, 110:323–334, 1989.
- E. A. B. Eltahir. The role of vegetation in sustaining large-scale atmospheric circulations in the tropic. *Journal of Geophysical Research*, 101(D2):4255–4268, 1996.
- E. A. B. Eltahir. A soil moisture-rainfall feedback mechanism, 1. *Water Resources Research*, 34(4):765–776, 1998.
- E. A. B. Eltahir and R. L. Bras. On the response of the tropical atmosphere to large-scale deforestation. *Quarterly Journal of the Royal Meteorological Society*, 119:779–793, 1993.
- E. A. B. Eltahir and R. L. Bras. Precipitation recycling in the Amazon basin. *Quarterly Journal of the Royal Meteorological Society*, 120:861–880, 1994.
- W. E. Emmerich and C. L. Verdugo. Long-term carbon dioxide and water flux database, Walnut Gulch Experimental Watershed, Arizona, United States. *Water Resources Research*, 44, W05S09, doi:10.1029/2006WR005693, 2008.
- D. Entekhabi, I. Rodríguez-Iturbe, and F. Castelli. Mutual interaction of soil moisture state and atmospheric processes. *Journal of Hydrology*, 184:3–7, 1996.

- J. K. Entin, A. Robock, K. Y. Vinnikov, S. E. Hollinger, S. Liu, and A. Namkhai. Temporal and spatial scales of observed soil moisture variations in the extratropics. *Journal of Geophysical Research*, 105(D9):11865–11877, 2000.
- J. S. Famiglietti and E. F. Wood. Multi-scale modeling of spatially variable water and energy balance processes. *Water Resources Research*, 30(11), 1994.
- H. Fang, S. Liang, H.-Y. Kim, J. R. Townshend, C. L. Schaaf, A. H. Strahler, and R. E. Dickinson. Developing a spatially continuous 1 km surface albedo data set over North America from Terra MODIS products. *J. Geophys. Res.*, 112, D20206, doi:10.1029/2006JD008377, 2007.
- O. T. Farouki. The thermal properties of soils in cold regions. Technical report, Cold Regions Sci. and Tech., 1981.
- T. G. Farr, P. A. Rosen, and Coauthors. The shuttle radar topography mission. *Rev. Geophys.*, 45, RG2004, doi:10.1029/2005RG000183, 2007.
- K. Findell and E. A. B. Eltahir. Atmospheric controls on soil moisture-boundary layer interactions. Part I: Framework development. *Journal of Hydrometeorology*, 4(3):552–569, 2003a.
- K. Findell and E. A. B. Eltahir. Atmospheric controls on soil moisture-boundary layer interactions. Part II: Feedbacks within the continental United States. *Journal of Hydrometeorology*, 4(3):570–583, 2003b.
- K. Findell and E. A. B. Eltahir. An analysis of the soil moisture-rainfall feedback, based on direct observations from Illinois. *Water Resources Research*, 33(4):725–735, 1997.
- K. Findell and E. A. B. Eltahir. An analysis of the pathways relating soil moisture and subsequent rainfall in Illinois. *Journal of Geophysical Research*, 104:31565–31574, 1999.
- I. V. Florinsky and G. A. Kuryakova. Influence of topography on some vegetation cover properties. *Catena*, 27:12–141, 1996.

- J. A. Foley, I. C. Prentice, S. Levis, D. Pollard, S. Stich, and A. Haxeltine. An integrated biosphere model of land-surface processes, terrestrial carbon balance and vegetation dynamics. *Global Biogeochemical Cycles*, 10(4):603–628, 1996.
- G. M. Foody, E. M. Ghoneim, and N. W. Arnell. Predicting locations sensitiv to flash flooding in a rid environment. *Journal of Hydrology*, 292(1-4), 2004.
- B. Formann and S. A. Margulis. High-resolution satellite-based cloud-coupled estimates of total downwelling surface radiation for hydrologic modelling applications. *Hydrol. Earth Syst. Sci.*, 13:969–986, 2009.
- S. S. D. Foster and P. J. Chilton. Groundwater: the processes and global significance of aquifer degradation. *Phil. rans. R. Soc. Lond. B*, 358:1957–1972, 2003.
- R. A. Freeze and R. L. Harlan. Blueprint for a physically-based, digitally-simulated hydrologic response model. *Journal of Hydrology*, 173(237-258), 1969.
- S. Fritz, P. Rao, and M. Weinstein. Satellite measurements of reflected solar energy and energy received at the ground. *J. Atmos. Sci.*, 21:141–151, 1964.
- Y. Gan, G. Miguez-Macho, C. Weaver, R. Walko, and A. Robock. Incorporating water table dynamics in climate modeling, Part I: Water table observations and the equilibrium water table. *J. Geophys. Res.*, 112, D10125, doi:10.1029/2006JD008111, 2007.
- L. Garrote and R. L. Bras. A distributed model for real-time ood forecasting using digital elevation model. *Journal of Hydrology*, 167:279–306, 1995.
- C. Gautier, G. Diak, and S. Masse. A simple physical model to estimate incident solar radiation at the surface from GOES satellite data. *Journal of Applied Meteorology*, 19: 1005–1012, 1980.
- M. Georgescu, C. P. Weaver, R. Avissar, R. L. Walko, and G. Miguez-Macho. The Boreal Ecosystem-Atmosphere Study (BOREAS): An overview and early results from the 1994 field year. *J. Geophys. Res.*, 108, 855, doi:10.1029/2002JD003107, 2003.

- D. J. Gochis, W. J. Shuttleworth, and Z. L. Yang. Sensitivity of the modeled North American monsoon regional climate to convective parameterization. *Monthly Weather Review*, 130: 1282–1298, 2002.
- D. J. Gochis, W. J. Shuttleworth, and Z. L. Yang. Hydrometeorological response of the modeled North American monsoon to convective parameterization. *Journal of Hydrometeorology*, 4:235–250, 2003.
- D. C. Goodrich, J. M. Faurés, D. A. Woolhiser, L. J. Lande, and S. Sorooshian. Measurement and analysis of small-scale convective storm rainfall variability. *Journal of Hydrology*, 173: 283–308, 1995.
- D. C. Goodrich, D. G. Williams, C. L. Unkrich, J. F. Hogan, R. L. Scott, K. R. Hultine, D. Pool, A. L. Coes, and S. N. Miller. Comparison of Methods to Estimate Ephemeral Channel Recharge, Walnut Gulch, San Pedro River Basin, Arizona. In F.M. Phillips, J.F. Hogan, and B. Scanlon, editors, *Recharge and Vadose Zone Processes: Alluvial Basins of the Southwestern United States*. American Geophysical Union, 2004.
- D. C. Goodrich, T. O. Keefer, C. L. Unkrich, M. H. Nichols, J. J. Stone H. B. Osborn, and J. R. Smith. Long-term precipitation database, Walnut Gulch Experimental Watershed, Arizona, United States. *Water Resources Research*, 44, W05S04, doi:1029/2006WR005782, 2008.
- D. J. Gratton, P. J. Howarth, and D. J. Marceau. Using Landsat-5 thematic mapper and digital elevation data to determine the net radiation eld of a Mountain Glacier. *Remote Sens. Environ.*, 43:315–331, 1993.
- R. B. Grayson, I. D. Moore, and T. A. McMahon. Physically-based hydrologic modeling I, A terrain-based model for investigative purposes. *Water Resources Research*, 28:2639–2658, 1992.
- R. B. Grayson, G. Bloschl, A. W. Western, and T. A. McMahon. Advances in the use of ob-

- served spatial patterns of catchment hydrological response. *Advances in Water Resources*, 25:1313–1334, 2002.
- T. R. Green, B. C. Bates, S. P. Charles, and P. M. Fleming. Physically based simulation of potential effects of carbon dioxide-altered climates on groundwater recharge. *Vadose Zone Journal*, 6:597–609, 2007.
- H. D. Grover and H. B. Musick. Shrubland encroachment in southern New Mexico, USA: an analysis of desertification processes in the American Southwest. *Climate Change*, 17: 305–330, 1990.
- L. E. Gulden, E. Rosero, Z.-L. Yang, M. Rodell, C. S. Jackson, G.-Y. Niu, P. J.-F. Yeh, and J. Famiglietti. Improving land-surface model hydrology: Is an explicit aquifer model better than a deeper soil profile. *Geophysical Research Letters*, 34, L09402, doi:10.1029/2007GL029804, 2007.
- H. V. Gupta, S. Sorooshian, and P. O. Yapo. Towards improved calibration of hydrological models: Multiple and non-commensurable measures of information. *Water Resources Research*, 34(4):751–763, 1998.
- W. J. Gutowski, C. J. Vörösmarty, M. Person, Z. Ötles, B. Fekete, and J. York. A Coupled Land-Atmosphere Simulation Program (CLASP): Calibration and validation. *Journal of Geophysical Research*, 107(D16), 4283, 10.1029/2001JD000392, 2002.
- J. T. Hack and J. C. Goodlett. Geomorphology and forest ecology of a mountain region in the Central Appalachians. *U.S. Geological Survey*, 347:66, 1960.
- K. J. Hanson. Studies of cloud and satellite parameterization of solar irradiation at the Earth’s surface. In *Proc. Miami Workshop on Remote Sensing Symposium on the Theory of Computing*, pages 133–148, Washington, D.C., 1971. U.S. Dept. Commerce.
- P. Heilman, M. H. Nichols, D. C. Goodrich, S. N. Miller, and D. P. Guertin. Geographic information systems database, Walnut Gulch Experimental Watershed, Arizona. *Water Resources Research*, 44, W05S09, doi:10.1029/2006WR005777, 2008.

- M. Herrera-Pantoja and K. M. Hiscock. The effects of climate change on potential groundwater recharge in Great Britain. *Hydrol. Process.*, 22:73–86, 2008.
- S.-Y. Hong and H.-L. Pan. Impact of soil moisture anomalies on seasonal, summertime circulation over North America in a regional climate model. *Journal of Geophysical Research*, 105:29625–29634, 2000.
- S.-Y. Hong and H.-L. Pan. Nonlocal boundary layer vertical diffusion in a medium-range forecast model. *Mon. Weather Rev.*, 124:2322–2339, 1996.
- K. L. Hsu, X. Gao, S. Sorooshian, and H. V. Gupta. Precipitation estimation from remotely sensed information using artificial neural networks. *Journal of Applied Meteorology*, 36:1176–1190, 1997.
- K. L. Hsu, H. V. Gupta, and S. Sorooshian. Estimation of physical variables from multichannel remotely sensed imagery using neural networks: Application to rainfall estimation. *Water Resources Research*, 35(5):1605–1618, 1999.
- C. Huang, X. Li, and L. Lu. Retrieving soil temperature profile by assimilating MODIS LST products with ensemble Kalman filter. *Remote Sens. Environ.*, 112(4):1320–1336, 2008.
- L. A. Hunt, L. Kuchar, and C. J. Swanton. Estimation of Solar Radiation for Use in Crop Modelling. *Agr. Forest Meteorol.*, 91(3-4):293–300, 1998.
- S. B. Idso. A set of equations for full spectrum and 8- to 14-mm and 10.5- to 12.5-mm thermal radiation from cloudless skies. *Water Resources Research*, 17:295–304, 1981.
- T. E. Crolley II and C. L. Luukkonen. Potential effects of climate change on ground water in Lansing, Michigan. *Journal of American Water Resources Association*, 39(1):149–163, 2003.
- M. Iqbal. *An Introduction to Solar Radiation*. Academic Press, New York, USA, 1983.



- V. Y. Ivanov. *Effects of Dynamic Vegetation and Topography on Hydrological Processes in Semi-Arid Areas*. PhD dissertation, Massachusetts Institute of Technology, Department of Civil and Environmental Engineering, April 2006.
- V. Y. Ivanov, E. R. Vivoni, R. L. Bras, and D. Entekhabi. Catchment hydrologic response with a fully distributed triangulated irregular network model. *J. Hydrol.*, 40, W11102, doi:10.1029/2004WR003218, 2004.
- V. Y. Ivanov, E. R. Vivoni, R. L. Bras, and D. Entekhabi. Vegetation-hydrology dynamics in complex terrain of semiarid areas: 1. A mechanistic approach to modeling dynamic feedbacks . *Water Resources Research*, 44, W03429, doi:10.1029/2006WR005588, 2008a.
- V. Y. Ivanov, R. L. Bras, and E. R. Vivoni. Vegetation-hydrology dynamics in complex terrain of semiarid areas: 2. Energy-water controls of vegetation spatiotemporal dynamics and topographic niches of favorability. *Water Resources Research*, 44, W03430, doi:10.1029/2006WR005595, 2008b.
- J. Jacobs. Radiation climate of Broughton Islands. In *Energy budget studies in relation to fast-ice breakup processes in Davis Strait : A climatological overview*, volume 26, pages 105–120. Boulder, CO: University of Colorado, Institute of Arctic and Alpine Research, 1978.
- J. M. Jacobs, D. A. Myers, M. C. Anderson, and G. R. Diak. GOES surface insolation to estimate wetlands evapotranspiration. *J. Hydrol.*, 266(1-2):53–65, 2002.
- A. C. Janetos. Science challenges and future directions: Climate change integrated assessment research. Technical report, Report from the U.S. Department of Energy, PNNL-18417, U.S. DOE, Office of Science, 2009.
- X. Jiang, G.-Y. Niu, and Z.-L. Yang. Impacts of vegetation and groundwater dynamics on warm season precipitation over the Central United States. *Journal of Geophysical Research*, 114, D06109,doi:10.1029/2008JD010756, 2009.

- J. S. Kain and M. Fritsch. A one-dimensional entraining/detraining plume model and its application in convective parameterization. *J. Atmos. Sci.*, 47:2784–2802, 1990.
- T. R. Karl, J. M. Melillo, and T. C. Peterson. Global Climate Change Impacts in the United States. Cambridge University Press, 2009.
- G. Karypis and V. Kumar. A fast and high quality multilevel scheme for partitioning irregular graphs. *SIAM Journal on Scientific Computing*, 20(1):359–392, 1999.
- T. O. Keefer, M. S. Moran, and G. B. Paige. Long-term meteorological and soil hydrology database, Walnut Gulch Experimental Watershed, Arizona, United States. *Water Resources Research*, 44, W05S07, doi:10.1029/2006WR005702, 2008.
- J. Kim and T. S. Hogue. Evaluation of a MODIS-based Potential Evapotranspiration Product at the Point-scale. *J. of Hydrometeorology*, 9:444–460, 2008.
- Y. Kim and G. Wang. Impact of initial soil moisture anomalies on subsequent precipitation over North America in the coupled land-atmosphere model CAM3-CLM3. *J. of Hydrometeorology*, 8:513–533, 2007.
- D. M. King, S. M. Skirvin, C. D. Holifield Collins, M. S. Moran, S. H. Biedenbender, M. R. Kidwell, M. A. Weltz, and A. Diaz-Gutierrez. Assessing vegetation change temporally and spatially in south-eastern Arizona. *Water Resources Research*, 44, W05S09, doi:10.1029/WR005850, 2008.
- M. D. King, S.-C. Tsay, S. E. Platnick, M. Wang, and K.-N. Liou. Cloud Retrieval Algorithms for MODIS: Optical Thickness, Effective Particle Radius, and Thermodynamic Phase. ATBD Reference Number: ATBD-MOD-05, [http://modis-atmos.gsfc.nasa.gov/\\_docs/atbd\\_mod05.pdf](http://modis-atmos.gsfc.nasa.gov/_docs/atbd_mod05.pdf) (accessed on 05/05/2008), 1998.
- D. Kirk and W.. Hwu. *CUDA textbook*. unpublished.
- Y. Knyazikhin, J. V. Martonchik, D. J. Diner, R. B. Myeni, M. Verstraete, B. Pinty, and N. Gobron. Estimation of leaf area index and fraction absorbed photosynthetically active

- radiation from atmosphere corrected MISR data. *Journal of Geophysical Research*, 103: 32239–32256, 1998.
- S. J. Kollet and R. M. Maxwell. Integrated surfacegroundwater flow modeling: A free-surface overland flow boundary condition in a parallel groundwater flow model. *Advances in Water Resources*, 29(7):945–958, 2006.
- S. J. Kollet and R. M. Maxwell. Capturing the influence of groundwater dynamics on land surface processes using an integrated, distributed watershed model. *Water Resources Research*, 44, W02402, doi:10.1029/2007WR006004, 2008.
- V. I Kozun. World Water Balance and Water Resources of the Earth. Studies and Reports in Hydrology, UNESCO, Paris, 1978.
- R. D. Koster and M. J. Suarez. Soil moisture memory in climate models. *Journal of Hydrometeorology*, 2(6):558–570, 2001.
- R. D. Koster, M. J. Suarez, A. Ducharne, M. Stieglitz, and P. Kumar. A catchment-based approach to modeling land surface processes in a general circulation model: 1. Model structure. *Journal of Geophysical Research*, 105(D20):24809–24822, 2000.
- R. D. Koster, P. A. Dirmeyer, and Coauthors. Regions of strong coupling between soil moisture and precipitation. *Science*, 305(5687):1138–1140, 2004a.
- R. D. Koster, M. J. Suarez, and Coauthors. Realistic Initialization of Land Surface States: Impacts on Subseasonal Forecast Skill. *Journal of Hydrometeorology*, 5(6):1049–1063, 2004b.
- R. D. Koster, Z. C. Guo, and Coauthors. Glace: the global landatmosphere coupling experiment. Part I: Overview. *Journal of Hydrometeorology*, 7(4):590–610, 2006.
- G. Krinner, N. Vivoy, N. de Noblet-Ducoudré, J. Ogée, J. Polcher, P. Friedlingstein, P. Ciais, S. Sitch, and I. C. Prentice. A dynamic global vegetation model for studies

- of the coupled atmosphere-biosphere system. *Global Biogeochemical Cycles*, 19, GB1015, doi:10.1029/2003GB002199, 2005.
- P. H. Krishnen. Potential impacts of global warming on groundwater in eastern Massachusetts. *Journal of Water Resources*, 128(3):216–226, 2002.
- P. Kumar and A. L. Kaleita. Assimilation of near-surface temperature using extended Kalman filter. *Advances in Water Resources*, 26:79–93, 2003.
- S. A. Kurc and E. E. Small. Soil moisture variations and ecosystem-scale fluxes of water and carbon in semiarid grassland and shrubland. *Water Resources Research*, 43, W06416, doi:10.1029/2006WR005011, 2007.
- T. Laevastu. Factors affecting the temperature of the surface layer of the sea. *Commentat. Phys.-Math.*, 25:907–925, 1960.
- J. P. Lagouarde and Y. Brunet. A simple model for estimating the daily upward longwave surface radiation flux from NOAA AVHRR data. *Int. J. of Remote Sens.*, 14(5):907–925, 1983.
- F. Laio, A. Porporato, C. P. Fernandez-Illescas, and I. Rodríguez-Iturbe. Plants in water-controlled ecosystems: active role in hydrologic processes and response to water stress IV. Discussion of real cases. *Advances in Water Resources*, 24:745–762, 2001a.
- F. Laio, A. Porporato, L. Ridolfi, and I. Rodríguez-Iturbe. Plants in water-controlled ecosystems: active role in hydrologic processes and response to water stress II. Probabilistic soil dynamics. *Advances in Water Resources*, 24:707–723, 2001b.
- V. Lakshmi. A simple surface temperature assimilation scheme for use in land surface models. *Water Resources Research*, 36(12):3687–3700, 2000.
- G. H. Leavesley, L. E. Hay R. J. Viger, and S. L. Markstrom. *Use of a priori parameter-estimation methods to constrain calibration of distributed-parameter models*. Calibration

- of Watershed Models: Water, Science and Application 6. American Geophysical Union, 2003.
- D. S. LeBauer and K. K. Treseder. Nitrogen limitation of net primary productivity in terrestrial ecosystems is globally distributed. *Ecology*, 89:371–379, 2008.
- H.-T. Lee and R. G. Ellingson. Development of a nonlinear statistical method for estimating the downward longwave radiation at the surface from satellite observations. *Journal of Atmospheric and Oceanic Technology*, 19(10):1500–1515, 2002.
- L. R. Leung, L. O. Mearns, F. Giorgi, and R. L. Wilby. Workshop on regional climate research: Needs and opportunities. *Bulletin of American Meteorological Society*, 84:89–95, 2003.
- Z. Li, H. G. Leighton, K. Masuda, and T. Takashima. Estimation of shortwave flux absorbed at the surface from TOA reflected flux. *Journal of Climate*, 6:1764–1772, 1993.
- Z. Li, M. C. Cribb, F.-L. Chang, A. Trishchenko, and Y. Luo. Natural Variability and Sampling Errors in Solar Radiation Measurements for Model Validation over the Atmospheric Radiation Measurement Southern Great Plains Region. *J. Geophys. Res.*, 110, D15S19, doi:10.1029/2004JD005028, 2005.
- X. Liang, Z. Xie, and M. Huang. A new parameterization for surface and groundwater interactions and its impact on water budgets with the variable infiltration capacity (VIC) land surface model. *Journal of Geophysical Research*, 108(D16), 8613, doi:10.1029/2002JD003090,, 2003.
- Y.-L. Lin, R. D. Rarley, and H. D. Orville. Bulk parameterization of the snow field in a cloud model. *J. Appl. Meteorol.*, 22:1065–1092, 1983.
- K.-N. Liou. *An Introduction to Atmospheric Radiation*, volume 84 of *International Geophysics Series*. Academic Press, 525 B Street, Suite 1900, San Diego, California 92101, USA, second edition, 2002.

- L. Liuzzo, L. V. Noto, E. R. Vivoni, and G. La Loggie. Basin-scale Water Resources Assessment in Oklahoma under Synthetic Climate Change Scenarios using a Fully-Distributed Hydrologic Model. *Journal of Hydrology*, 15(2):107–122, 2010.
- J. C.-F. Lo, Z.-L. Yang, and R. A. Pielke Sr. Assessment of three dynamical climate downscaling methods using the Weather Research and Forecasting (WRF) model. *J. Geophys. Res.*, 113(D09112, doi:10.1029/2007/JD009216), 2008.
- C. N. Long, E. G. Dutton, J. A. Augustine, W. Wiscombe, M. Wild, S. A. McFarlane, and C. J. Flynn. Significant decadal brightening of downwelling shortwave in the continental United States. *J. Geophys. Res.*, 114(D06):1460–1472, 2009.
- L. Lu, R. A. Pielke, G. E. Liston, W. J. Parton, D. Ojima, and M. Hartman. Implementation of a two-way interactive atmospheric and ecological model and its application to the central United States. *Journal of Climate*, 14:900–919, 2001.
- W. Lucht, C. B. Schaaf, and A. H. Strahler. An algorithm for the retrieval of albedo from space using semiempirical BRDF models. *IEEE Trans. Geosci. Remote Sens.*, 38(2):997–998, 2000.
- S. W. Lyon, F. Dominguez, and coauthors. Coupling Terrestrial and Atmospheric Water Dynamics to Improve Prediction in a Changing Environment. *Bulletin of the American Meteorological Society*, 89(9):1275–1279, 2008.
- Y. Ma, Z. Su, Z. Li, T. Koike T, and M. Menenti. Determination of regional net radiation and soil heat flux over a heterogeneous landscape of the Tibetan Plateau. *Hydrological Processes*, 16:2963–2971, 2002.
- H. Madsen. Parameter estimation in distributed hydrological catchment modelling using automatic calibration with multiple objectives. *Advances in Water Resources*, 26:205–216, 2003.
- J.-F. Mahfouf. Analysis of soil-moisture from near-surface parameters-A feasibility study. *Journal of Applied Meteorology*, 30:1534–1547, 1991.

- S. Manabe. Climate and the ocean circulation I. The atmospheric circulation and the hydrology of the Earth's surface. *Monthly Weather Review*, 97(11):739–774, 1969.
- S. Manabe, J. Smagorinsky, and R. F. Strickler. Simulated climatology of a general circulation model with a hydrologic cycle. *Monthly Weather Review*, 93(12):769–798, 1965.
- K. Masuda, H. G. Leighton, and Z. Li. A New Parameterization for the Determination of Solar Flux Absorbed at the Surface from Satellite Measurements. *Journal of Climate*, 8: 1615–1629, 1995.
- R. M. Maxwell and S. J. Kollet. Interdependence of groundwater dynamics and land-energy feedbacks under climate change. *Nature Geoscience*, 1:665–669, 2008.
- R. M. Maxwell and N. L. Miller. On the development of a coupled land surface and groundwater model. *Journal of Hydrometeorology*, 6:233–247, 2005.
- R. M. Maxwell, F. K. Chow, and S. J. Kollet. The groundwater-land-surface-atmosphere connection: Soil moisture effects on the atmospheric boundary layer in full-coupled simulations. *Advances in Water Resources*, 30:2447–2466, 2007.
- G. A. Maykut and P. F. Church. Radiation climate of Barrow, Alaska, 1962-66. *J. Appl. Meteorol.*, 12:620–628, 1973.
- L. A. Mendez-Barroso and E. R. Vivoni. Observed shifts in land surface conditions during the North American Monsoon: Implications for a vegetation-rainfall feedback mechanism. *Journal of Arid Environment*, 74:549–555, 2010.
- W. P. Menzel, R. A. Frey, B. A. Baum, and H. Zhang. Cloud Top Properties and Cloud Phase - Algorithm Theoretical Basis Document. ATBD Reference Number: ATBD-MOD-04. [http://modis-atmos.gsfc.nasa.gov/MOD06\\_L2/atbd.html](http://modis-atmos.gsfc.nasa.gov/MOD06_L2/atbd.html) (accessed on 05/05/2008), 2006.
- F. Mesinger, G. DiMego, E. Kalnay, P. Shafran, W. Ebisuzaki, D. Jovic, J. Woollen, K. Mitchell, E. Rogers, M. Ek, Y. Fan, R. Grumbine, W. Higgins, H. Li, Y. Lin,

- G. Manikin, D. Parrish, and W. Shi. North American Regional Reanalysis. *Bull. Am. Meteorol. Soc.*, 87:343–360, 2006.
- P. Michle, S. J. Livesley, C. Li, P. M. Feikema, M. A. Adams, and S. K. Arndt. Quantifying uncertainty from large-scale model predictions of forest carbon dynamics. *Global Change Biology*, 12:1421–1434, 2006.
- P. C. D. Milly, L. A. Dunne, and A. V. Vecchia. Global pattern of trends in streamflow and water availability in a changing climate. *Nature*, 438:347–350, 2005.
- J. B. Minster, J. W. Campbell, J. Dozier, J. R. Fleming, J. C. Gille, D. L. Hartmann, K. Jezek, S. Kidder, N. Ramankutty, A. Thompson, S. L. Ustin, J. Yoder, and C. Mengelt. *Committee on Scientific Accomplishments of Earth Observations from Space*. The National Academies Press, Washington, D. C., 2008.
- E. J. Mlawer, S. J. Taubman, P. D. Brown, M. J. Iacono, and S. A. Clough. Radiative transfer for inhomogeneous atmospheres: RRTM, a validated correlated-k model for the longwave. *J. Geophys. Res.*, 102(D14):16663–16682, 1997.
- K. C. Mo, J. E. Schemm, H. Kim, and W. R. Higgins. Influence of initial conditions on summer precipitation simulations over the United States and Mexico. *Journal of Climate*, 19:3640–3658, 2006.
- N. Molders and W. Ruhaak. On the impact of explicitly predicted runoff on the simulated atmospheric response to small-scale land-use changes-an integrated modeling approach. *Atmospheric Research*, 30:2447–2466, 2007.
- M. S. Moran, C. D. Holifield Collins, D. C. Goodrich, J. Qi, D. T. Shannon, and A. Olsson. Long-term remote sensing database, Walnut Gulch Experimental Watershed, Arizona, United States. *Water Resources Research*, 44, W05S09, doi:10.1029/2006WR005689, 2008.
- R. E. Moritz. A model for estimating global solar radiation. In *Energy budget studies in relation to fast-ice breakup processes in Davis Strait : A climatological overview*, volume 26,



- pages 121–142. Boulder, CO: University of Colorado, Institute of Arctic and Alpine Research, 1978.
- D. R. Myers. Solar Radiation Modeling and Measurements for Renewable Energy Applications: Data and Model Quality. *Energy*, 30:1517–1531, 2005.
- J. Namias. The annual course of month-to-month persistence in climatic anomalies. *Bulletin of American Meteorological Society*, 33:279–285, 1952.
- G.-H. C. Ng. *Probabilistic Estimation and Prediction of Groundwater Recharge in a Semi-Arid Environment*. PhD dissertation, Massachusetts Institute of Technology, Department of Civil and Environmental Engineering, February 2009.
- S. Niemelä, P. Räisänen, and H. Savijärvi. Comparison of surface radiative flux parameterizations Part I: Longwave radiation. *Atmospheric Research*, 58:1–18, 2001a.
- S. Niemelä, P. Räisänen, and H. Savijärvi. Comparison of surface radiative flux parameterizations Part II: Shortwave radiation. *Atmospheric Research*, 58:141–154, 2001b.
- K. Nishida, R. R. Nemani, S. W S. W. Running, and J. M. Glassy. An operational remote sensing algorithm of land evaporation. *J. Geophys. Res.*, 108(D09):4270, 2003.
- G.-Y. Niu, Z.-L. Yang, R. E. Dickinson, L. E. Gulden, and H. Su. Development of a simple groundwater model for use in climate models and evaluation with Gravity Recovery and Climate Experiment data. *Journal Geophysical Research*, 112, D07103, doi:10.1029/2006JD007522, 2007.
- J. M. Norman, M. C. Anderson, W. P. Kustas, A. N. French, J. Mecikalski, R. Torn, G. R. Diak, T. J. Schmugge, and B. C. W. Tanner. Remote sensing of surface energy fluxes at 10-m pixel resolutions. *Water Resources Research*, 39(8):1221, 2003.
- R. J. Oglesby. Springtime soil moisture, natural climatic variability and North American drought as simulated by the NCAR Community Climate Model, 1. *Journal of Climate*, 4: 890–897, 1991.

- R. J. Oglesby and D. J. Erickson III. Soil moisture and the persistence of North American drought. *Journal of Climate*, 2:1362–1380, 1989.
- R. J. Oglesby, S. Marshall, D. J. Erickson III, J. O. Roads, and F. R. Robertson. Thresholds in atmosphere-soil moisture interactions: Results from climate mode studies. *J. Geophys. Res.*, 107, 4244, doi:10.1029/2001JD001045:1362–1380, 2002.
- T. Oki. *Encyclopedia of Hydrological Sciences*, volume 1. Wiley, New York, 2005.
- T. Oki and S. Kanae. Global Hydrological Cycles and World Water Resources. *Science*, 313: 1068–1072, 2006.
- K. W. Oleson, Y. Dai, and coauthors. Technical Description of the Community Land Model (CLM),. Technical report, Tech. Note NCAR/TN-461+STR, 2004.
- J. Paegle, K. C. Mo, and J. Nogés-Paegle. Dependence of simulated precipitation on surface evaporation during the 1993 United States summer floods. *Monthly Weather Review*, 124: 345–361, 1996.
- G. B. Paige and T. O. Keefer. Comparison of field performance of multiple soil moisture sensors in a semi-arid rangeland. *Journal of American Water Resources Association*, 44(1):121-135. DOI: 10.1111/j.1752-1688.2007.00142.x, 2004.
- J. S. Pal and E. A. B. Eltahir. Pathways relating soil moisture conditions to future summer rainfall within a model of the land-atmosphere system. *Journal of Climate*, 14(6):1227–1242, 2001.
- G. W. Paltridge and C. M. R. Platt. *Radiative Processes in Meteorology and Climatology*. Elsevier, Amsterdam, 1976.
- J. D. Pelletier, B. D. Malamud, T. Blodgett, and D. L. Turcotte. Scale-invariance of soil moisture variability and its implications for the frequency-size distribution of landslides. *Engineering Geology*, 48(3-4):255–268, 1997.

- M. L. Pessoa, R. L. Bras, and E. R. William. Use of weather radar for flood forecasting in the Sieve river basin: A sensitivity analysis. *Journal of Applied Meteorology*, 32(3):462–475, 1993.
- C. D. Peters-Lidard, M. S. Zion, and E. F. Wood. A soil-vegetation atmosphere transfer scheme for modeling spatially variable water and energy balance processes. *Journal of Geophysical Research*, 102(D4):4304–4324, 1997.
- R. A. Pielke. Influence of the spatial distribution of vegetation and soils on the prediction of cumulus convective rainfall. *Reviews of Geophysics*, 39(2):151–177, 2001.
- R. A. Pielke and R. Avissar. Influence of landscape structure on local and regional climate. *Landscape Ecology*, 4:133–155, 1990.
- R. T. Pinker, R. Frouin, and Z. Li. A Review of Satellite Methods to Derive Surface Short-wave Irradiance. *Remote Sens. Environ.*, 51:108–124, 1995.
- A. Porporato, F. Laio, L. Ridolfi, and I. Rodríguez-Iturbe. Plants in water-controlled ecosystems: active role in hydrologic processes and response to water stress III. Vegetation water stress. *Advances in Water Resources*, 24:725–744, 2001.
- A. Porporato, E. Daly, and I. Rodríguez-Iturbe. Soil water balance and ecosystem response to climate change. *American Naturalist*, 144(5):352–365, 2004.
- A. J. Prata. A new long-wave formula for estimating downward clear sky radiation at the surface. *Quarterly Journal of the Royal Meteorological Society*, 122:1127–1151, 1996.
- A. L. Protopapas and R. L. Bras. A model for water uptake and development of root systems. *Soil Science*, 144(5):352–366, 1987.
- Y. Qu and C. J. Duffy. A semidiscrete finite volume formulation for multiprocess watershed simulation. *Water Resource Research*, 43, W08419, doi:10.29/2006WR005752, 2007.

- D. A. Randall, R. A. Wood, S. Bony, R. Colman, T. Fichefet, J. Fyfe, V. Kattsov, A. Pitman, J. Shukla, J. Srinivasan, R. J. Stouffer, and A. Sumi and K. E. Taylor. *Climate Models and Their Evaluation. In: Climate Change 2007: The Physical Science Basis. Contribution of Working Group I to the Fourth Assessment Report of the Intergovernmental Panel on Climate Change.* Cambridge University Press, Cambridge, United Kingdom and New York, NY, USA, 2007.
- J. V. Ratnam and K. K. Kumar. Sensitivity of the simulated monsoons of 1987 and 1988 to convective parameterizations schemes in MM5. *Journal of Climate*, 18:2724–2743, 2005.
- J. C. Refsgaard. *Terminology, modelling protocol and classification of hydrological model codes.* Distributed Hydrological Modelling . Kluwer Academic, 1996.
- J. C. Refsgaard. Parameterization, calibration and validation of distributed model. *Journal of Hydrology*, 198:69–97, 1997.
- K. Renard, M. H. Nichols, D. A. Woolhiser, and H. B. Osborn. A brief background on the U.S. Department of Agriculture Agricultural Research Service Walnut Gulch Experimental Watershed. *Water Resources Research*, 44, W05S02, doi:10.1029/2006WR005691, 2008.
- D. Rind. The influence of ground moisture conditions in North America on summer climate as modeled in the GISS GCM. *Monthly Weather Review*, 110:1487–1494, 1982.
- D. Rind, R. Goldberg, J. Hansen, C. Rosenzweig, and R. Ruedy. Potential Evapotranspiration and the Likelihood of Future Drought. *J. Geophys. Res.*, 95(D7):9983–10,004, 1990.
- A. Rinehart, E. R. Vivoni, and P. D. Brooks. Effects of vegetation, albedo, and solar radiation sheltering on the distribution of snow in the Valles Caldera, New Mexico. *Ecohydrology*, 1(3):253–270, 2008.
- I. Rodriguez-Iturbe, D. Entekhabi, and R. L. Bras. Nonlinear dynamics of soil moisture at climate scales 1, Stochastic analysis. *Water Resources Research*, 27:1889–1906, 1991.

- I. Rodriguez-Iturbe, A. Porporato, F. Lai, and L. Ridolfi. Plants in water-controlled ecosystems: active role in hydrologic processes and response to water stress I. Scope and general outline. *Advances in Water Resources*, 24:695–705, 2001.
- R. R. Rogers and M. K. Yau. *A Short Course in Cloud Physics*. Butterworth Heinemann, third edition, 1989.
- A. J. Rutter, K. A. Kershaw, P. C. Robins, and A. J. Morton. A predictive model of rainfall interception in forests. 1. Derivation of the model from observation in a plantation of Corsican pine. *Agric. Meteorol.*, 9:367–384, 1971.
- H. H. G. Savenije. New definitions of moisture recycling and the relationship with land-use changes in the Sahel. *Journal of Hydrology*, 167:57–78, 1995.
- C. B. Schaaf and coauthors. First operational BRDF, albedo nadir reflectance products from MODIS. *Remote Sens. Environ.*, 83(1-23):135–148, 2002.
- C. Schär, D. Lüthi, U. Beyerle, and E. Heise. The soil-precipitation feedback: A process study with a regional climate model. *Journal of Climate*, 12:722–741, 1999.
- J. Schmetz. Towards a surface radiation climatology: Retrieval of downward irradiances from satellites. *Atmospheric Research*, 23(3-4):287–321, 1989.
- J. Scibek and D. M. Allen. Modeled impacts of predicted climate change on recharge and groundwater levels. *Water Resources Research*, 42, W11405, doi:10.1029/2005WR004742, 2006.
- P. J. Sellers, Y. Mintz, Y. C. Sud, and A. Dalcher. A simple biosphere model (SiB) for use within general circulation models. *Journal of Atmospheric Science*, 43:505–531, 1986.
- P. J. Sellers, F. G. Hall, and Coauthors. The Boreal Ecosystem-Atmosphere Study (BOREAS): An overview and early results from the 1994 field year. *Bulletin of the American Meteorological Society*, 76:1549–1577, 1995.

- A. Seth and F. Giorgi. The effects of domain choice on summer precipitation simulation and sensitivity in a regional climate model. *Journal of Climate*, 11:2698–2712, 1998.
- I. A. Shiklomanov. Assessment of Water Resources and Water Availability in the World. World Meteorological Organization/Stockholm Environment Institute, Geneva, 1997.
- I. A. Shiklomanov. World Water Resources: Modern Assessment and Outlook for the 21st Century, 1999. (Summary of World Water Resources at the Beginning of the 21st Century, prepared in the framework of the IHP UNESCO). Federal Service of Russia for Hydrometeorology & Environment Monitoring, State Hydrological Institute, St. Petersburg, 1999.
- J. Shukla and Y. Minz. Influence of the land surface evapotranspiration on the earth's climate. *Science*, 215:1077–1099, 1982.
- S. Sitch, B. Smith, and Coauthors. Evaluation of ecosystem dynamics, plant geography and terrestrial carbon cycling in the LPJ dynamics global vegetation model. *Global Change Biology*, 9:161–185, 2003.
- W. C. Skamarock, J. B. Klemp, J. J. Dudhia, D. O. Gill, D. M. Barker, W. Wang, and J. G. Powers. A description of the Advanced Research WRF Version 3. NCAR Technical Note, 2008.
- S. M. Skirvin, M. Kidwell, S. Biedenbender, J. P. Henley, D. King, C. H. Collins, S. Moran, and M. Weltz. Vegetation data, Walnut Gulch Experimental Watershed, Arizona, United States. *Water Resources Research*, 44, W05S08, doi:10.1029/2006WR005724, 2008.
- A. Slingo. A GCM parameterization for the shortwave radiative properties of water clouds. *Journal of the Atmospheric Sciences*, 46(10):1419–1427, 1989.
- M. B. Smith, D.-J. Seo, V. I. Koren, S. Reed, Z. Zhang, Q.-Y. Duan, S. Cong, and F. Moreda. The distributed model intercomparison project (DMPI): motivation and experiment design. *Journal of Hydrology*, 298(1-4):4–26, 2004.

- A. P. Sokolov, D. W. Kicklighter, J. M. Mehilllo, B. S. Felzer, C. A. Schlosser, and T. W. Cronin. Consequences of considering carbon-nitrogen interactions on the feedbacks between climate and the terrestrial carbon cycle. *Journal of Climate*, 21:3776–3796, 2008.
- A. M. Solomon and W. Cramer. *Biosphere implications of global environmental change*. Chapman & Hall, New York, New York, USA, 1993.
- S. Sorooshian, K. L. Hsu, X. Gao, H. V. Gupta, B. Iman, and D. Braithwaite. Evaluation of PERSIANN System Satellite-Based Estimates of Tropical Rainfall. *Bulletin of the American Meteorological Society*, 81(9):2035–2046, 2000.
- D. Stensrud. *Parameterization Schemes: Keys to Understanding Numerical Weather Prediction Models*. Cambridge University Press, The Edinburg Building, Cambridge, CB2 8RU, UK, first edition, 2007.
- G. L. Stephens. Radiation profiles in extended water clouds. Part II: Parameterization schemes. *J. Atmos. Sci.*, 35(11):2123–2132, 1978.
- J. J. Stone, M. H. Nichols, D. C. Goodrich, and J. Buono. Long-term runoff database, Walnut Gulch Experimental Watershed, Arizona, United State. *Water Resources Research*, 44, W05S05, doi:10.1029/2006WR005733, 2008.
- Y. C. Sud, D. M. Mocko, K.-M. Lau, and R. Atlas. Simulating the midwestern U.S. drought of 1988 with a GCM. *Journal of Climate*, 16:3946–3965, 2003.
- B. Tang and Z.-L. Li. Estimation of instantaneous net surface longwave radiation from MODIS cloud-free data. *Remote Sens. Environ.*, 112(9):3482–3492, 2008.
- B. Tang, Z.-L. Li, and R. Zhang. A direct method for estimating net surface shortwave radiation from MODIS data. *Remote Sens. Environ.*, 103(1):115–126, 2006.
- A. H. Taylor and M. N. Solem. Fire regimes and stand dynamics in a upper mountain forest landscape in the southern Cascades, Caribou Wilderness, California. *Journal of Torrey Botany Society*, 128(4):350–361, 2001.

- C. M. Taylor, D. J. Parker, and P. P. Harris. An observational case study of mesoscale atmospheric circulations induced by soil moisture. *Geophysical Research Letters*, 34, L15801, doi:10.1029/2007GL030572, 2007.
- P. E. Thornton, J.-F. Lamarque, N. A. Rosenbloom, and N. M. Mahowald. Influence of carbon-nitrogen cycle coupling on land model response to CO<sub>2</sub> fertilization and climate variability. *Global Biogeochemical Cycles*, 21:1–15, 2007.
- P. E. Thornton, S. C. Doney, K. Kindsay, J. K. Moore, N. Mahowald, J. T. Randerson, I. Fung, J.-F. Lamarque, J. J. Feddema, and Y.-H. Lee. Carbon-nitrogen interactions regulate climate-carbon cycle feedbacks: results from an atmosphere-cocean general circulation model. *Biogeosciences*, 6:2099–2120, 2009.
- H. R. Le Treut, R. Somerville, U. Cubasch, Y. Ding, C. Mauritzen, A. Mokssit, T. Peterson, and M. Prather. Historical Overview of Climate Change. In: *Climate Change 2007: The Physical Science Basis. Contribution of Working Group I to the Fourth Assessment Report of the Intergovernmental Panel on Climate Change*. [Solomon, S., D. Qin, M. Manning, Z. Chen, M. Marquis, K.B. Averyt, M. Tignor and H.L. Miller (eds.)], Cambridge University Press, Cambridge, United Kingdom and New York, NY, USA., 2007.
- N. T. VanRheenen, A. W. Wood, R. N. Palmer, and D. Lettermaier. Potential Implications of PCM Climate Change Scenarios for Sacramento San-Joaquin River Basin Hydrology and Water Resources. *Climate Change*, 62:257–281, 2004.
- V. Venturini, S. Islam, and L. Rodriguez. Estimation of evaporative fraction and evapotranspiration from MODIS products using a complementary based model. *Remote Sens. Environ.*, 112(1):132–141, 2008.
- P. M. Vitousek and R. W. Howarth. Nitrogen limitation on land and in the sea: How can it occur? *Biogeochemistry*, 13:87–115, 1991.
- E. R. Vivoni, V. Y. Ivanov, R. L. Bras, and D. Entekhabi. Generation of triangulated



- irregular networks based on hydrological similarity. *Journal of Hydrologic Engineering*, 9 (4):288–302, 2004.
- E. R. Vivoni, S. Mniszewski, P. Fasel, E. S. Springer, V. Y. Ivanov, and R. L. Bras. Parallelization of a Fully-Distributed Model using Sub-basin Partitioning. San Francisco, December 2005. American Geophysical Union.
- E. R. Vivoni, H. A. Gutierrez-Juardo, C. A. Aragon, L. A. Mendez-Barroso, A. J. Rinehart, R. L. Wyckoff, J. C. Rodriguez, C. J. Watts, J. D. Bolten, V. Lakshmi, and T. J. Jackson. Variation of Hydrometeorological Conditions along a Topographic Transect in Northwestern Mexico during the North American Monsoon. *Journal of Climate*, 2-(9):1792–1809, 2007.
- E. R. Vivoni, H. A. Moren, G. Mascaro, J. C. Rodriguez, C. J. Watts, J. Garatuza-Payan, and R. L. Scott. Observed Relation between Evapotranspiration and Soil Moisture in the North American Monsoon Region. *Geophysical Research Letters*, 35:L22403, doi:10.1029/2008GL036001, 2008.
- E. R. Vivoni, K. Tai, and D. J. Gochis. Effects of Initial Soil Moisture on Rainfall Generation and Subsequent Hydrologic Response during the North American Monsoon. *Journal of Hydrometeorology*, 10:644–664, 2009.
- Z. Wan and J. Dozier. A generalized split-window algorithm for retrieving land-surface temperature from space. *IEEE Transactions of Geoscience and Remote Sensing*, 34(4): 892–905, 1996.
- Z. Wan and Z. Li. A physics-based algorithm for retrieving land-surface emissivity and temperature from EOS/MODIS data. *IEEE Transactions of Geoscience and Remote Sensing*, 35(4):980–996, 1997.
- G. Wang and E. A. B. Eltahir. Biosphere-atmosphere interactions over West Africa, II, Multiple climate equilibria. *Quarterly Journal of the Royal Meteorological Society*, 126: 1261–1280, 2000.

- J. Wang and R. L. Bras. Ground heat flux estimated from surface soil temperature. *Journal of Hydrology*, 216:214–226, 1999.
- K. Z. Wang, P. Wan, M. Wang, J. L. Sparrow, X. Zhou, and S. Haginoya. Estimation of surface long wave radiation and broadband emissivity using Moderate Resolution Imaging Spectroradiometer (MODIS) land surface temperature/emissivity products. *J. Geophys. Res.*, 110, D11109, doi:10.1029/2004JD005566, 2005.
- W. Wang and S. Liang. Estimation of high-spatial resolution clear sky longwave downward and net radiation over land surfaces from MODIS data. *Remote Sens. Environ.*, 113: 745–754, 2009.
- W. Wang, S. Liang, and T. Meyers. Validating MODIS land surface temperature products using long-term nighttime ground measurements. *Remote Sens. of Environ.*, 112:623–635, 2008.
- W. Wang, S. Liang, and J. A. Augustine. Estimating High Spatial Resolution Clear-Sky Land Surface Upwelling Longwave Radiation From MODIS data. *IEEE Trans. Geosci. Remote Sens.*, 47(5):1559–1570, 2009.
- W. Washington, D. Bader, B. Collins, J. Drake, M. Taylor, B. Kirtman, D. Williams, and D. Middleton. Scientific Grand Challenges: Challenges in Climate Change Science and the Role of Computing at the Extreme Scale. Technical report, U.S. Department of Energy, Office of Biological and Environmental Research and the Office of Advanced Scientific Computing Research, November 2008.
- C. J. Watts, R. L. Scott, J. Garatuza-Payan, J. C. Rodrigues, J. H. Prueger, W. P. Kustas, and M. Douglas. Changes in vegetation condition and surface fluxes during NAME 2004. *Journal of Climate.*, 20:1810–1820, 2009.
- C. P. Weaver. Coupling between large-scale atmospheric processes and mesoscale land-atmosphere interactions in the U.S. Southern Great Plains during summer. Part I: Case studies. *Journal of Hydrometeorology* , 5:1223–1246, 2004.

- R. H. Webb, R. Hereford, and G. J. McCabe. Climatic fluctuations, drought, and flow in the Colorado River. In S. P. Gloss, J. E. Lovich, and T. S. Melis, editors, *The state of the Colorado River ecosystem in Grand Canyon: U.S. Geological Survey Circular*, pages 59–69. 2005.
- P. K. Weiskel, R. M. Vogel, P. A. Steeves, P. J. Zarriello, L. A. DeSimone, and K. G. Riess III. Water use regimes: Characterizing direct human interaction with hydrologic systems. *Quarterly Journal of the Royal Meteorological Society*, 43, W04402, doi:10.1029/2006WR005062, 2007.
- J. L. Weiss and J. Overpeck. Is the Sonoran Desert losing its cool? *Global Change Biology*, 11(12):2065 – 2077, 2005.
- A. W. Western and R. B. Grayson. *Soil moisture and runoff processes at Tarrawarra*, chapter 9. Spatial Patterns in Catchment Hydrology: Observations and Modeling. Cambridge University Press, 2000.
- M. S. Wigmosta, W. V. Lance, and D. P. Lettenmaier. A distributed hydrology-vegetation model for complex terrain. *Water Resources Research*, 30(6):1665–1679, 1994.
- A. W. Wood, L. R. Leung, V. Sridhar, and D. P. Lettenmaier. Hydrologic implications of dynamical and statistical approaches to downscaling climate model outputs. *Climatic Change*, 62(1-3):189–216, 2004.
- E. F. Wood, M. Sivapalan, and K. Beven. Similarity and scale in catchment storm response. *Review of Geophysics*, 28(1):1–18, 1990.
- E. F. Wood, D. Lettenmaier, X. Liang, B. Nijssen, and S. W. Wetzel. Hydrologic modeling of continental scale basins. *Annual Reviews of Earth and Planetary Sciences*, 25:279–300, 1997.
- J. J. Xu and E. E. Small. Simulating summertime rainfall variability in the North American monsoon region: The influence of convection and radiation parameterizations. *Journal of Geophysical Research*, 107, 4727, doi10.1029/2001JD002047, 2002.

- Xu-Ri and I. C. Prentice. Terrestrial nitrogen cycle simulation with a dynamic global vegetation model. *Global Change Biology*, 14(8):1745–1764, 2008.
- P. J. F. Yeh and E. A. B. Eltahir. Representation of water table dynamics in a land surface scheme, Part I: Model development. *Journal of Climate*, 18(12):1861–1880, 2005.
- L. L. Yilmaz, H. V. Gupta, and T. Wagener. A process-based diagnostic approach to model evaluation: Application to the NWS distributed hydrologic model. *Water Resources Research*, 44, W09417, doi:10.1029/2007WR006716, 2008.
- J. P. York, M. Person, W. J. Gutowski, and T. C. Winter. Putting aquifers into atmospheric simulation models: An example from the Mill Creek Watershed, northeastern Kansas. *Advances in Water Resources*, 25(2):221–238, 2002.
- X. Yuan, Z. Xie, J. Zheng, X. Tian, and Z. Yang. Effects of water table dynamics on regional climate: A case study over east Asian monsoon area. *Journal of Geophysical Research*, 113(D21112, doi:10.1029/2008JD010180), 2008.
- Y. Zhou, D. P. Kratz, A. C. Wilber, S. K. Gupta, and R. D. Cess. An improved algorithm for retrieving surface downwelling longwave radiation from satellite measurements. *J. Geophys. Res.*, 112, D15102, doi:10.1029/2006JD008159, 2007.
- J. W. Zillman. A study of some aspects of the radiation and heat budgets of the southern hemisphere oceans. Meteorological study 26, Commonwealth Bureau of Meteorology, Canberra, Australia, 1972.